UNIVERSITÀ DELLA CALABRIA

UNIVERSITA' DELLA CALABRIA

Dipartimento di Fisica

Dottorato di Ricerca in

Scienze e Tecnologie Fisiche, Chimiche e dei Materiali

CICLO

XXX

PHYSICAL PROCESSES IN SINGLE AND MULTIPLE PHOTON ADDITIVE NANO-MANUFACTURING OF THREE-DIMENSIONAL POLYMERIC AND METALLIC STRUCTURES FOR ADVANCED OPTICS

Settore Scientifico Disciplinare Fisica e Scienze dei Materiali

Coordinatore: Ch.mo Prof. Vincenzo CARBONE

Vincenzo Carbone

Supervisore/Tutor: Egr. Dott. Michele GIOCONDO

Firma _____

Ch.mo Prof. Pasquale PAGLIUSI

Firma _____

Dottorando: Dott.ssa Tiziana RITACCO

Firma Tiziana Ritacco

When I was a child, I read of fairy tales in which mystical creatures and beautiful fairies swept their wand in the air, creating beautiful trails of light and fairy dust made of gold.

During my PhD, I discovered that if you sweep a laser inside of a metal precursor you can create gold nanoparticles in the trajectory and build structures made of gold.

I don't believe in fairy tales anymore, but I believe in science and it's just as magic.

Alternatively, I'm a fairy.

Index

Abbreviations

1D	One-dimensional
2D	Bi-Dimensional
3D	Three-Dimensional
AFM	Atomic Force Microscope
BSEs	Back-Scattering Electrons
CAD	Computer-Aided design
CLC	Cholesteric Liquid Crystal
CRMs	Cholesteric Reactive Mesogens
DMOAP	Dymethiloctadecyl[3-(trimethoxysilyl)propyl]ammonium chloride
DLW	Direct Laser Writing
GNPs	Gold Nanoparticles
EBL	Electron Beam Lithography
EDL	Electric Double Layer
EDX	Energy Dispersive X-Ray
EF	Enhancement Factor
IPA	Isopropyl Alcohol
ITO	Indium Tin Oxide
LC	Liquid Crystal
LCE	Liquid Crystalline Elastomer
LCP	Liquid Crystalline Polymer
LP	Laser Power
LSPR	Localized Surface Plasmon Resonance
NIR	Near Infra-Red
NLCs	Nematic Liquid Crystals
NPs	Nanoparticles
PBG	Photonic Band Gap

PDSM	Polydimethylsiloxane
PL	Photo-luminescence
PVA	Polyvinyl Alcohol
QR	Quick Responsive
RMs	Reactive Mesogens
SEs	Secondary Electrons
SEM	Scanning Electron Microscopy
SERS	Surface-Enhanced Raman Scattering
SPA	Single Photon Absorption
SS	Scan Speed
STL	Stereolithography
TP-DLW	Two-Photons Direct Laser Writing
TPA	Two-Photon Absortoption
TPP	Two-Photon Polymerization
TPPR	Two-Photon Photo-Reduction
UV	Ultra-Violet
voxel	Volume pixel

Abstract

In the field of nanotechnologies the Two-Photons Direct Laser Writing (TP-DLW) is the most advanced optical technique for creating arbitrarily complex 3D structures in organic resists, featuring details down to 50 nm, well below the diffraction limit.

More recently, this technique has been used in "resists" containing a photosensitive metallic precursor, activated by the two-photon absorption (TPA) process, allowing for the creation of metallic nanoparticles clusters inside to the focus figure of a highly focused laser beam, where the TPA threshold intensity is reached.

The aim of my PhD work was the elucidation of the physical processes involved in the realization of 3D nanostructures made in different materials for applications in micro-fluidics and advanced optics. In particular, I carried out studies on both isotropic and anisotropic photoresists, and on metallic precursors.

Concerning the isotropic photoresists, I have investigated the capabilities and the limits of the TP-DLW technique, on the fabrication of microfluidic systems and elements of millimetric size, with micro- and nano-features printed inside the channels.

The best results in printing such millimetric structures in terms of geometrical compliance and fabrication time are achieved, by combining the single (SPA) and the two-photon absorption (TPA) processes. The latter one allowed for the creation of a shell, an internal structural scaffold and eventual microscopic details, whereas the former one to polymerize the bulk of the object. However, the development step of microfluidic systems (i.e. the removal of the un-polymerized resist) is quite challenging in general, due to possible swellings and consequent distortions in the structure geometry. In my PhD, I developed an effective protocol to face this issue.

The application of the TP-DLW technique to anisotropic reactive mesogens (RMs) resulted in very interesting achievements, as it allowed for the fabrication of 3D solid

structures, maintaining the optical properties of liquid crystals, in combination with the mechanical properties of polymers. Effects of the direct laser writing on the internal molecular order of the reactive mesogens have been thoroughly investigated, to ensure a fine control on the optical properties of 3D objects made in liquid crystalline elastomers. Analyses of the physical processes, which occur during TP-DLW and allow for tuning of the optical response of the printed 3D solid structures are shown. Appropriate doping of the reactive mesogens with dyes and chiral dopant agents were performed to investigate different fields of applications.

In particular, a chiral agent confers helical order to the RMs, which show selective Bragg reflection of the impinging light in both wavelength and polarization. Micro-fabrication of 3D chiral structures is a brand new field that is paving the way to the creation of photonic devices, such as micro-laser of defined shape, white light reflective object, anti-counterfeiting and data storage systems.

I performed a series of experiments aimed at demonstrating the possibility to manipulate the helical structural order of the liquid crystals during TP-DLW. As a consequence, multi-colour three-dimensional structure can be created.

Finally, the possibility to include metallic details in polymeric objects or even to create metallic structures would pave the way for the DLW of metallic/polymeric nano-composites. I performed experiments with polymeric or hydrogel matrices doped with a suitable metallic precursor, in a free surface drop cast, or in cell segregated thin film, onto a glass substrate. In such system, I was able to create 1D gratings made of GNPs stripes with single or multiple laser sweep. I demonstrated that the stripe width increases with the laser power and the exposure time, showing a behaviour similar to the photo-polymerization, as expected. I also analysed the influence of the exposure time over the nano-particles size distribution and density and showed that by suitably adjusting the exposure time it is possible to maximize the occurrence of a given diameter.

The experiments were aimed at elucidating the involved physical phenomena, beyond the bare optical absorption. In particular, the key-role of thermal and diffusive processes have been analysed. TPA leads to the photo-reduction of ions of $AuCl_4^-$ and the

creation of GNPs, but to a local heating of the sample as well. Due to the very fast heating, a thermal shock-wave is generated and is responsible of the local dehydration in the spot area. Due the concentration gradients of the ions of gold precursor and of water, different diffusive processes take place, occurring on different timescales. Therefore, different characteristic times are observed for the ion and the water diffusion, in the polymeric matrix. My experiments demonstrate that the diffusive effects can be exploited for controlling the NPs density and size when a given energy dose is delivered in multiple shots, by tuning the time interval between each shots. Preliminary experiments on the possibility to control the growth of GNPs through the application of specific electric field during TP-DLW were performed as well.

Last but not least, the possibility to use TP-DLW of metal precursor to realize smart platform rich in GNPs suitable to different application is shown. In particular, I demonstrate that, controlling the pitch and the size of GNPs stripes, it is possible to create both thermo-platform whose thermal response to external light is tuneable, and detecting substrates for Surface-Enhanced Raman Spectroscopy (SERS). The Raman spectra were recorded from samples immersed in a solution of rhodamine-6G (R6G), as well as, after exposure of the samples in xylene. SERS enhancement factors of up to ~10^4 were obtained for both rhodamine-6G and xylene.

Abstract (Italian)

Nel campo delle nuove tecnologie, la scrittura laser diretta a due fotoni (dall'inglese *two-photon direct laser writing* TP-DLW) è la tecnica ottica più avanzata per la creazione di strutture 3D complesse, che presentano dettagli inferiori al limite di diffrazione fino a 50 nm.

Solitamente, la stampa diretta a due fotoni avviene in monomeri organici fotosensibili, noti come *photoresist*, che possono polimerizzare per assorbimento a uno (*single photon absorption*, SPA) o due fotoni (*two-photon absorption*, TPA). Negli ultimi anni, questa tecnica è stata utilizzata anche per ottenere aggregati di nanoparticelle a partire da matrici polimeriche drogate con precursori metallici.

Quando un fascio laser è focalizzato all'interno di un materiale fotosensibile, nella regione del fuoco in cui la soglia di assorbimento a due fotoni è superata, si assiste all'eccitamento delle molecole, le quali possono rilasciare energia (attraverso fluorescenza o calore), o in alternativa legarsi attraverso processi di polimerizzazione (resine organiche) o ridursi (precursori metallici).

Lo scopo del mio dottorato è stato studiare i processi fisici coinvolti nella realizzazione di nano-strutture 3D composte da diversi materiali, per applicazioni in campo della micro-fluidica o dell'ottica avanzata. In particolare, i materiali usati sono stati photoresist organici, sia isotropi che anisotropi, e soluzioni acquose di alcol polivinilico drogate con acido tetracloroaurico.

Nel caso di photoresist isotropi, ho studiato le capacità e i limiti della tecnica TP-DLW, concentrandomi sulla fabbricazione di sistemi micro-fluidici di dimensioni millimetriche, ma con micro- e nano-dettagli presenti all'interno dei canali.

I migliori risultato nel processo di stampa delle suddette strutture millimetriche, in termini di conformità geometrica e tempo di fabbricazione, sono stati ottenuti combinando insieme SPA e TPA. Tramite TPA è stato possibile creare il guscio esterno (*shell*) della struttura e un'impalcatura interna (*scaffold*) atta a sorreggerla. Inoltre, tutti i dettagli

microscopici sono stati fatti tramite scrittura diretta a due fotoni. Il volume della struttura, invece, è stato polimerizzato attraverso SPA. Tuttavia, il processo di sviluppo di un sistema micro-fluidico (ad es. la rimozione di tutto il photoresist non polimerizzato) può rivelarsi una sfida e portare a deformazioni o conseguenti distorsioni della geometria del sistema. Durante il dottorato, quindi, ho sviluppato un protocollo che permette di sviluppare efficacemente il campione, superando questo ostacolo.

L'uso della TP-DLW in photoresist anisotropi, composti da mesogeni reattivi (*reactive mesogens*, RMs), ha permesso di ottenere risultati estremamente interessati. In particolare, ho realizzato strutture 3D che mantenessero le proprietà ottiche dei cristalli liquidi usati, pur acquisendo le tipiche proprietà meccaniche dei polimeri.

Al fine di ottenere un controllo fine sulle proprietà ottiche degli oggetti creati, gli effetti della scrittura laser diretta sull'ordine interno dei mesogeni reattivi sono stati analizzati con particolare attenzione. Nel corso del lavoro sono illustrati i risultati ottenuti e i processi fisici che consentono di modulare la risposta ottica di un oggetto creato in RMs, in funzione dei parametri di scrittura. Inoltre, al fine di ampliare i campi di applicazione consentiti dalla TP-DLW di strutture solide di cristallo liquido, ho drogato opportunamente l'RMs con agenti chirali o coloranti fluorescenti.

In particolare, gli agenti chirali hanno la proprietà di conferire ordine elicoidale ai mesogeni reattivi del photoresist, il quale presenterà dunque riflessione selettiva alla Bragg della lunghezza d'onda e della polarizzazione della luce incidente. La micro-fabbricazione di strutture chirali tridimensionali è un campo altamente innovativo che consente la creazione di dispositivi fotonici (ad es. micro-laser di forma arbitraria), micro-strutture in grado di riflettere la luce bianca, o sistemi di anticontraffazione e conservazione di dati.

Gli esperimenti effettuati hanno dimostrato la possibilità di manipolare l'ordine elicoidale del cristallo liquido chirale, durante la TP-DLW. Di conseguenze, sono riuscita a micro-fabbricare strutture multicolorate.

In ultimo, la possibilità di includere nano-particelle metalliche in strutture polimeriche, consentirebbe la realizzazione di oggetti nano-compositi. A questo proposito, ho svolto numerosi esperimenti in matrici metalliche o gel, opportunamente drogati con un

precursore d'oro, sia su gocce depositate su substrati di vetro o all'interno di celle elettrolitiche.

In particolare, ho creato reticoli 1D di nano particelle di oro (*gold nanoparticles*, GNPs), attraverso una o più passate del fascio laser, dimostrando che la larghezza delle strisce di GNPs ottenuta dipende dalla potenza e dal tempo di esposizione, in maniera analoga a quella prevista nel caso di foto-polimerizzazione. Inoltre, ho analizzato l'influenza del tempo di esposizione sulla taglia delle GNPs create a parità di energia, osservando come il diametro medio delle nano-particelle possa essere modulato.

Ulteriori esperimenti sono stati svolti al fine di chiarire i fenomeni fisici coinvolti durante il processo di TP-DLW, al di là del solo assorbimento ottico. In particolare, ho analizzato il ruolo fondamentale dei processi termici e diffusivi. Per TPA si ha la riduzione dello ione cloroaurico $AuCl_4^-$ e la conseguente creazione di GNPs, tuttavia al contempo si assiste ad un riscaldamento locale del campione. Questo riscaldamento è responsabile della formazione di un'onda d'urto termica e conseguente deidratazione locale. Si vengono così a creare gradienti di ioni cloroaurici e di acqua, che danno luogo a processi diffusivi all'interno della matrice, con diversi tempi caratteristici.

I miei esperimenti hanno mostrato che gli effetti diffusivi possono essere sfruttati per controllare la densità e le dimensioni della nanoparticelle create, frazionando la dose di energia distribuita e variando il tempo di attesa tra una esposizione (*shot*) e la successiva. Inoltre, qui presento un lavoro preliminare sulla possibilità di controllare la crescita delle nanoparticelle applicando un campo elettrico durante TP-DLW, all'interno di una cella elettrolitica.

In ultimo, ma non meno importante, l'uso della TP-DLW con un precursore metallico consente di creare delle "piattaforme" composte di nanoparticelle d'oro che possono essere usate in numerose applicazioni. In particolare, ho studiato gli effetti termo-plasmonici di reticoli fatti da GNPs, dimostrando come sia possibile modulare la variazione di temperatura in funzione del passo del reticolo. Inoltre, strutture 1D di GNPs possono essere utilizzati come substrati per la spettroscopia Raman amplificata da superfici (*Surface-Enhancement Raman Spectroscopy*, SERS). Gli spettri Raman sono stati acquisiti immergendo

il campione in soluzioni di rodamina-6G (R6G) o di xilene, ottenendo un'amplificazione del segnale di un fattore ~10^4 in entrambi i casi.

Introduction

In the last decades, micro- and nano-fabrication processes have been of great interest, both in scientific and in technological fields, due to the possibility to fabricate systems and devices featuring micrometer and nanometer resolution [1-3]. Between the different technologies, optical lithography is the most used and investigated ones [4], thanks to the possibility to use light as a tool to micro-structure a photosensitive material.

Due to their flexibility and the possibility to be employed in a wide range of applications, polymers are widely used in micro-fabrication processes [5-8]. Depending on the characteristic of to the selected polymer, ultra-violet (UV) radiation may either break the links between molecules (positive photo-resist), making the irradiated areas soluble in a developing solvent and may then be removed through chemical processes, or generate cross-linking between monomers (negative photo-resist) [9].

In both cases, a mask is usually required to cover the areas that have not to be exposed. Therefore, the structure resolution is determined by the diffraction limit. In recent years, electron-beam lithography (EBL) has been employed to overcome this limit. An electron beam is used to design the structures on a resist film, with nanometric resolution [10-12]. This process is currently used in electronics; however, it is very expensive and requires long periods of time. Moreover, no high structures can be created and only features up to two-dimensions can be obtained.

Stereolithography (STL) is a maskless additive manufacturing technique to create 3D objects, with a resolution up to few micrometers [13-16]. An UV laser beam is focused in a light-curable resin and is swept inside it line-by-line, layer after layer. The sample is then developed in the opportune solvent, to remove all the non-exposed parts. This kind of micro-fabrication process is also known as Direct Laser Writing (DLW) [17-19], since the laser beam actually "writes" the 3D object inside the resin, starting from a CAD model.

To improve the resolution of DLW, the UV laser can be substituted with a near infra-red (NIR) ultrafast laser source, with high repetition rate and peak power to excite the

compound through the simultaneous absorption of two or multiple photons. Two-photon absorption (TPA) is a non-linear optical process, whose cross-section depends on the square of the intensity of the laser beam. Therefore, polymerization is allowed only inside the focus figure of the laser beam and a resolution below hundred nanometers is achieved. Thus, two-photons direct laser writing (TP-DLW) is nowadays the best technique to nano-fabricate polymeric 3D objects [1-3, 101-109].

Until now, this technique has been applied in many technological fields; the most relevant ones may be summarized as follows:

- Optics: TP-DLW has been used to fabricate photonic crystals and metamaterials, which are able to modify and affect the flow of photons accordingly, thanks to their periodical nanostructures [20-25]; photonic platforms, made by pillar gratings with controlled period and dimension [26-27]; multi-lens objectives to be applied on optical fibre [28] or waveguide architectures for 3D integrated optics [29-30].
- Mechanical microstructures: TP-DLW is largely employed in fabrication of microstructures with interesting mechanical properties. Kadik et al. [31-32] demonstrated the possibility to obtain mechanical metamaterials, which find application in three-dimensional transformation elastodynamics, similarly to transformation optics for metamaterials. Buckmann et al. [33], in fact, created an elasto-mechanical unfeelability cloak: covering an object with pentamode metamaterials, no mechanical force can be applied upon it. Other authors [34-37], instead, showed how to fabricate micro-tissues by TP-DLW of opportune lattices in polymers, then covered by ceramics, to obtain light tissues with high elastic constant.
- Micro-fluidics: integration of nano-metric three-dimensional elements inside of microfluidic channel paved the way to large improvements in biotechnology, diagnostic or medicine. Many polymers are biocompatible and can be used to protein adsorption and cell cultivation [38-40], by creating opportune scaffolds inside a micro-fluidic system. Kim et al. [41] printed

micro-robots covered by nickel and titanium, to be magnetically manipulated by external fields and to allow cell transportations. Other possible applications are obtainable printing micro-mixer [42-43] or specific designs inside the micro-fluidic system to control diffusion.

A particular issue to be faced concerns fabrication of micro-fluidic systems, which are usually created through photolithography. TP-DLW allows the possibility to create complex three-dimensional lab-on-chips or nozzles, with sub-micrometer resolution. However, many hindrances are encountered during development of large channels with micrometric details, such as swellings or deformation of the 3D objects. In the first part of my work, is devoted to how improve the development protocol to ensure the best possible result.

For each photoresist used, a preliminary study on the resolution obtained in function of the delivered energy dose was carried out, both to define the condition to obtain high-quality TP-DLW and to achieve manufacturing in innovative materials. In fact, beyond the bare nano-fabrication, it is of high interest the possibility to obtain 3D object with exotic optical and electrical properties. TP-DLW in resins doped with dyes, quantum dots (QDs), metal nanoparticles (NPs) or liquid crystals (LCs) allows to achieve this important result [44-52].

Among LCs, Liquid Crystal Elastomers (LCE) are very interesting in the field of additive manufacturing, since they combine the liquid crystalline order with the mechanical properties of polymers. This result can be afforded thanks to the structure of their molecules, reactive mesogens (RMs), which presents two or more photo-activable reactive groups. It is then possible to fabricate solid 2D and 3D microstructures with the optical properties of LCs [53-55], such as birefringence, dichroism, or selective reflection.

In the last decades, LCs have been highly exploited in a wide range of applications, due to their extraordinary optical properties e.g.: displays [56], shutters [57], variable retarders [58], tuneable colour filters [59], photonic crystals [60], mirrorless lasers [61-63]. The possibility to transfer these properties to 3D microstructures is granting new improvements in the additive manufacturing of photonic devices. Photosensitive LCE have

been highly employed in photolithography to create micro-sized actuators and sensors [64-67], which respond to external light stimuli by contracting up to the 400% [68-69]. Adding a chiral dopant agent to the reactive mesogens, a cholesteric polymer liquid crystal (CLC) is obtained. In the nematic phase, typical of LCE, the molecules of liquid crystals are oriented along a common direction defining the director axis, a vectorial field that describes the average molecular orientation. In CLC, the director axis of the liquid crystal varies periodically, forming a helical internal structure. Depending on the pitch of the helix, the cholesteric liquid crystals reflect selectively the wavelength and polarization of light. Photolithography of CLC micro-droplet have been efficiently used in optofluidics [70], optomechanics [72], microphotonics [73-74] or e.g. to create chiral mirrors [71], chiral resonators [75] and microlasers [73, 76].

However, micro-fabrication of 3D chiral structures is a brand new field that is paving the way to the creation of photonic devices, such as micro-laser of defined shape, white light reflective object, anti-counterfeiting systems. In 2007, Sungur et al. [77] demonstrated the possibility to obtain additive manufacturing in LCs: they created 2D patterns in a cell of nematic elastomer, both by single photon and two-photon polymerization. In their conclusions, they stress on how TPA allows a better resolution, in their case from 20 μm to 7 μm. In recent years, Zeng et al. [78-79] showed how TP-DLW can be used to create three-dimensional microstructures in a liquid-crystalline monomer mixture, which maintains birefringent properties after the printing process. In their first work, they characterized the photo-resist used in function of the delivered energy dose, to obtain less than 300 nm resolution of their structures, avoiding damaging and swelling of the structures. Thanks to their results, Nocentini et al. [80] were able to print light tuneable photonic structures, obtaining high-resoluted cylinders in liquid crystalline elastomers which present mechanical deformations when light irradiated. Further improvements of this work allowed the fabrication of polymeric LCE micro-walkers [81].

I put attention on the possibility of combining additive manufacturing with the optical properties of both nematic and cholesteric liquid crystals. My experiments were aimed to investigate the effects of TPA on the internal order of the resist, and how the optical

properties of the LCE can be tuned according to the energy dose delivered. Particularly interesting were the results obtained on CLC: according to the energy dose delivered during the TP-DLW process, the reflection band can be tuned, due to a partial polymerization of the chiral structures. I was hence able to create 3D micro-objects, which selectively reflect all the spectrum of visible light, from red to blue. Nanofabrication of coloured 3D objects is extremely interesting in many fields of application; however, I put my attention on the fabrication of a new powerful anti-counterfeiting system. I printed a 3D quick responsible (QR) code, a bi-dimensional barcode containing 29x29 pixels, made of different heights, with a resolution of 400 nm. Each pixel was printed with different values of energy dose, which ascribes a 'colour code' to the QR code. The 3D micro-object obtained can be considered a four-dimensional (4D) barcode, hardly falsifiable and that can contain a huge amount of data in less than 100x100 μm^2. Therefore, I demonstrated the possibility to achieve a new generation of anti-counterfeiting and data storage systems.

Another strong point of my research was focused on the possibility to create microstructures made of gold nanoparticles by TP-DLW. Due to their extraordinary properties and diversity of applications, noble metal nanoparticles (NPs) are attracting increasing interest in many scientific and technologic fields [82-88]. Gold nanoparticles (GNPs), in particular, have shown biocompatibility and the possibility to be functionalized with organic and biological molecules, paving the way to new application in diagnostic [89], drug delivery [90], cancer therapy [91-92], and imaging [93-94]. At the nanoscale, noble metals present extraordinary optical properties: when opportunely irradiated, the incident light interacts with the nanoparticle and polarizes the conduction band electrons of the surface. The electrons oscillate like a dipole coherently with the electric field of the light, generating the well-known localized surface plasmon resonance (LSPR) [95-96]. Plasmon resonance strongly depends on the size of the nanoparticle and on the dielectric constant of the surrounding medium [97-98]. Thanks to this property, gold nanoparticles are more and more employed in ultra-fine sensors, to detect biological and chemical molecules [85, 99-100]. A crucial technological development is given by the possibility to create structures rich

in gold nanoparticles, both by including metal bricks in the polymeric structures or by fabricating 3D objects made only by GNPs.

In the last decade, many authors have tried to combine the optical properties of noble metal nanoparticles with nanofabrication [110-116]. Metal nanoparticles are usually created through synthesis processes [117-125], as a result, a colloidal solution rich of NPs is employed to cover a 3D nano-fabricated object, through a bathing process. Otherwise, NPs can be mixed with the organic photoresist before the nanofabrication process [52, 126-127]: in this way, during the photo-polymerization NPs are trapped inside the polymer, and all the bulk of the fabricated object is rich of gold nanoparticles. This kind of technique allows a fine control on the dimension and density of the NPs filling the polymeric object, actually creating a system that show the collective response of the NPs when opportunely irradiated.

However, fabrication of a pattern made solely of NPs can be extremely favourable in multiple applications. Kaneko et al. [128] demonstrated the possibility to optically micro-fabricate pattern rich in GNPs in a polymeric matrix, by the photo-reduction of a metal precursor. In their experiments, they doped a polymeric matrix of polyvinyl alcohol with an aqueous solution of tetracholorauric acid, then exposed the system to an infrared laser source, using an interferometer to obtain an intensity grating. Atomic force microscopy of the surface of their samples, revealed the ablation of the polymer in correspondence of the exposed stripes, and gold nanoparticles at the centre of the slots. From their analysis, they were able to conclude that the photoreduction of tetrachloroauric acid was possible due to the two-photon absorption process, actually demonstrating the possibility to direct laser write patterns rich in gold nanoparticles.

Many authors have investigated the possibility to control in size and density the optical creation of gold nanoparticles [113, 129-130]. In fact, TP-DLW grants the photo-reduction of the gold ions inside the voxel figure, however the GNPs created will present high polydispersity and different shape, which results in a broad peak in the absorption band. Izquierdo-Lorenzo et al. [131] afforded the issue by adding a surfactant (hexadecyltrimethyl ammonium bromide - CTAB) in the photosensitive solution, acting as a growth quencher for the NPs. TP-DLW on this compound confirmed the improvement in

the polydispersity of the photo-reduced GNPs. In this way, they were able to print three-dimensional woodpiles, created by crossing stripes of average width of 2 μm made by GNPs of ~200 nm. Cao et al. [129] were able to create well-defined 2D and 3D structures of silver NPs, with a resolution below 200 nanometers, by adding nitrogen-atom containing alkyl carboxylate n-decanoylsarcosine sodium (NDSS) to a solution of diammine silver ions in water. Varying the concentration of surfactant in the solution, they were able to control the dimension of the NPs and maximize their compactness.

Other ways to control the TP-DLW of metal precursor were proposed by Cao et al. [132]. In their work, they analysed the influence of polymeric hosting matrices during the photo-reduction, actually demonstrating how the length of the chain of the polymer may influence the dimension of single spots.

However, until now, this topic seemed to be considered as a technical curiosity and no fine analysis on the physical phenomena occurring during TP-DLW of metal precursors, beyond the bare photochemistry, was found in the literature. I investigated the physics involved during the printing process of GNPs, through several experiments, with the goal to get an effective improvement of this fabrication technique. The first step was aimed to characterize the voxel dependency on the energy dose delivered during direct laser writing. This result allows to 'select' the best condition for the fabrication of bi-dimensional and three-dimensional templates, simply by tuning the laser power and/or the exposure time, thus granting the possibility to print objects with parts showing different resolutions and dimensions. Moreover, the analysis of the dependence of the width of a stripe made in GNPs on the energy dose delivered allows defining the effective TPA cross-section of a metal precursor. This result is extremely important, because to actually combine photo-reduction with photo-polymerization of organic photo-resist, their TPA cross-sections must be comparable. A further characterization was aimed to estimate polydispersity and density of photo-reduced GNPs, in function of the exposure parameters (time and energy).

During, TP-DLW many diffusive process occurs, due to the reduction of metal ions inside the focus figure of the laser beam and to a possible water evaporation. I carried out a series of experiments to establish and control the fluid-dynamics of the system. It was

already demonstrated [128-129, 133] that two-photon photo-reduction of a metal precursor triggers the formation of metal seeds, which subsequently grow generating metal nanoparticles aggregating in clusters. Moreover, excited molecules can release energy through non-radiative process, heat, which is responsible of the thermal reduction of the ions in the surrounding material [133-135]. Furthermore, the exposure leads to a local reduction, and a gradient of ions concentration is created. As a consequence, the ions diffuse from the bulk to the exposed volume. Moreover, local heating has to be held responsible of further transport phenomena in the polymeric matrix, which may strongly affect the final results, due to damaging of the polymer, bubble formation or thermal shock-waves onset.

To analyse the behaviour of these effects, I created single spots rich in GNPs delivering the same energy dose in multiple shots, with different waiting times between them. The aim of my experiments was to determine the characteristic times of each effect and analyse their contributes during TP-DLW. In particular, gold ions diffusion can be exploited to obtain highest density of mono-disperse GNPs in areas with resolution of few hundreds of nanometers.

Further control on the optical creation of gold nanoparticles can be obtained by printing inside of an electrolytic gel. I printed structures in a solution of water and tetrachloroauric acid, applying an electric potential difference between the two electrodes, well below the reduction potential. The voltage between electrodes pushes the gold ions to travel along the longitudinal direction on one of the two surface, according to the field sign, until the total neutralization of the voltage on the electrodes. Tuning the ion concentration and the intensity of the electric field, both the photo-reduction and the growing processes can be controlled, avoiding unwanted fluid-dynamics or thermal effects.

As stated before, TP-DLW of metal nanoparticles have been employed in many fields of applications, e.g. to nano-fabricate metallic nanowires, both in flexible surface [136, 138] or inside lab-on-chips [137]. Xu et al. [138] showed in their work a micro-heater made in silver nanoparticles, opportunely designed inside a micro-fluidic system. They used silver nitrate as metal precursor in an aqueous solution, to which they added trisodium citrate as photo-reducing agent, moreover its reduction products acts as an inhibitors for the growth

of silver nanoparticles, allowing a good control on the dimensions of the structure. Applying a voltage to the micro-heater, they measured its heating capability.

Other authors [131, 139-141] have demonstrated the possibility to use two-photon photo-reduction to micro-fabricate substrates for SERS application. SERS is a powerful analytical technique for detection of trace amounts of chemical and biological active molecules adsorbed on rough metallic surfaces or on metallic nanoparticles. The possibility to control density and poly-dispersity of metallic nanoparticle allows obtaining an enhancement factor of the SERS signal ranging from 10^2 to 10^9.

Particularly relevant are applications in plasmonics [103, 142-144] and meta-materials [130, 145], as many authors focused their attention on the possibility to obtain planar layers of plasmonic resonators, obtaining in response to external light tuneable resonance in the order of 60-100 THz, according to the laser fabrication parameter.

I tackled the possibility to make thermo-smart platform. Optical excitation and non-radiative relaxation of the LSPR in GNPs create a photo-thermal effect due to the conversion of light energy into heat. Within this LSPR-mediated heating process, the light absorbed by the nanoparticle generates a non-equilibrium electron distribution that decays via electron-electron scattering. The hot electron gas equilibrates with lattice phonons, which transfer this energy into the surrounding medium, resulting in a local temperature increasing [146-147].

This effect, named photo-thermal effect in plasmonic nanoparticles, has already found applications in cancer therapy [148-149], optofluidic control [150], nano-welding [151], optical data storage [152], imaging [153] and sensing [154].

Baffau at al [155] presented an experimental and theoretical analysis on the heat generated by periodical 1D and 2D arrays of GNPs created through EBL. However, TP-DLW of devices for bio-application, it is mandatory a precise prediction on the induced temperature variations, due to thermo-plasmonics in GNPs, in the transition from nano- to macro-scale, and vice versa. Therefore, I conducted an analysis on different sample made of a planar layer of mono-dispersed GNPs chemically synthesized and randomly distributed on standard microscope glass slides through a bath in a gold NPs colloid. Similar analysis

were repeated in 1 mm^2 one-dimensional gratings of GNPs, with different periods, nanofabricated through TP-DLW. The possibility to modulate the compactness and density of gold nanoparticles in bi-dimensional templates pave the way to the fabrication of thermo-smart platforms, able to generate a desired value of temperature by controlling the number of GNPs photo-excited at the same time.

On similar structures, I also performed preliminary SERS analysis to investigate the dependence of the enhancement factor on the density and polydispersity of the GNPs.

Contents

This thesis is structured as follows:

Chapter 1

In the field of additive manufacturing, Two-photons Direct Laser Writing (TP-DLW) is the most advanced optical technique to fabricate arbitrarily complex 3D materials featuring details well below the diffraction limit, in organic resists [1, 2]. The two-photon absorption process (TPA) allows the photo-polymerization of an ellipsoidal volume (volume pixel, or 'voxel') in correspondence to the focus of the Gaussian beam of the laser, whose dimensions are of the order of 100 nm. Sweeping the laser inside the organic resist a 3D CAD model can be reproduced, with a spatial resolution defined by the voxel.

In my work, I afforded the comparison between additive manufacturing obtained by exploiting both single photon absorption (SPA) and TPA, verifying how TPA allows to improve resolution in micro-fabrication and to obtain 3D objects.

To obtain high-quality micro- and nano-manufacturing a thorough voxel characterization of standard photo-resists is required. In this section, I show the characterization made for the commercial resist IP-Dip, as well as the two-photon absorption cross section.

Eventually, I afforded the difficulties concerning the creation of millimetric structures with micro-channels, such as micro-fluidic systems, with high-resolute micrometric features inside of cavities. Hysteresis, swelling or mechanical damages typically occur during the development of such objects, so I studied how the development process can be improved.

Chapter 2

TP-DLW was then applied to create 3D structures in anisotropic photoresist. Reactive mesogens (RMs) is referred to photo-polymerizable liquid crystals (LCs), which allow the fabrication of solid 2D and 3D microstructures with the optical properties of LCs.

In my work, I investigated the effect of the direct laser writing on the birefringence of a nematic RMs. After creating 3D solid cylinders by using different value of energy dose, their optical properties were analysed.

Demonstrated that the TP-DLW does not affect the optical characteristic of nematic liquid crystals, RMs was doped with a dye, to obtain 3D photo-luminescent cylinders, and with a chiral agent. The dopant agent leads the transition from the nematic to the cholesteric phase, allowing printing 3D structures, which reflect selectively the wavelength and polarization of light.

I observed that, according to the energy dose delivered during the TP-DLW process, the reflection band can be tuned, due to a partial polymerization of the chiral structures. Therefore, I was able to create 3D micro-object, reflecting selectively all the spectrum of visible light, from red to blue.

This result introduces the possibility to nanofabricate coloured 3D object, thus leading the way to new technologies and applications. Analysing a QR code, a bi-dimensional barcode, I reproduced the structures in three dimensions, at different values of energy dose, which add a height and a 'colour' code to the QR. The micro-object obtained can be considered a four-dimensional barcode, hardly falsifiable and that can contain a huge amount of data in less than 100x100 μm^2. Therefore, a new generation of anti-counterfeiting and data storage systems can be achieved.

Chapter 3

Other than confer chiral properties to a 3D structure, I investigated the possibility to include metallic parts in polymeric structures or to create three-dimensional objects made only by metal nanoparticles. Therefore, I carried out a study on the characteristics of the voxel of a gold-doped PVA resist. My samples are made by sets of single segments, each one obtained with a single laser sweep, on a glass substrate. Upon the exposure, GNPs are created inside the swept segment. I find that the width of each segment depends on the delivered energy dose, as expected. Samples were developed in distilled water in order to

remove all the PVA from the substrate and obtained stripes of free GNPs on the glass substrate, on which I performed a basic statistical analysis based on scanning electron microscopy (SEM) images, showing the possibility to control the size and the density of the created GNPs.

These results demonstrate that beyond the bare photochemistry, other effects, which occur during the 2P-DLW process, have to be taken in account to actually describe the GNPS creation. I performed a series of experiments aimed to elucidate the involved physical phenomena, beyond the optical absorption. In particular, I pointed out the key-role of thermal and diffusive processes. TPA leads to the two-photon photo-reductions of ions of $AuCl_4^-$, to create GNPs, as well as, to a local heating of the sample that can trigger a thermal shock-wave, responsible of the local dehydration in the spot area.

Due the concentration gradients of the ions of gold precursor and of water, various diffusive processes taking place at different scale time are observed as well: respectively of 0.1 s for the ion diffusion and of 10 s for the water diffusion, in the hydro-polymer. Therefore, I created GNPs by dosing the energy in multiple shots, considering different time intervals between consecutive laser shots.

My experiments demonstrated that by waiting less than 0.1 s between consecutive shots, no relevant changes are observed. However, waiting a time between 0.1 s and 1 s, the diameter of the spot size changes considerably, as well as density of GNPs. A waiting time of 10 s or more allows the complete rehydration of the area of interest, therefore shooting again in the same spot causes repeatedly the local evaporation of water. This results in a series of thermal shock-waves whose effect cumulates and eject radially the gold nanoparticles form the spot to the near area. In this way, around the spot is formed a ring of GNPs and tetra-chloroauric acid crystals, due to precipitation of the acid in correspondence of the evaporated area. Therefore, I also made an attempt to evaluate the temperature distribution in the area of interest, as a function of the energy delivered. According to my best knowledge, it is the very first experiment that allowed for a temperature mapping at the nanoscale, and whose results are consistent with theoretical predictions present in the literature [200].

From my results, it turns out that to obtain the best resolution in the creation of 2D structures made of gold nanoparticles, thermal effects have to be minimized to avoid consistent alterations of the system, and a fine control on the ionic diffusion is required.

To this purpose, I prepared electrolytic cells made of ITO electrodes, in which I infiltrated a solution of water and HAuCl4 and direct laser wrote few 1D segments of 150 μm at an energy dose that was sufficient to activate the seeding process of TP-photo-reduced gold ions, but not the growing process of GNPs. [129]

Growing of gold nanoparticles was performed by applying an electric potential difference between the two electrodes, well below the electro-chemical reduction threshold. The resulting electric field allows controlling the surface density of the ionic species of interest, both for the seeding and the growth phases. Regarding the last, I consider that in proximity of a gold seed a tip effect is obtained, "driving" the gold ions toward the seed, where they are reduced through autocatalytic processes. Analyses on the stripes confirmed a voxel size comparable to the laser beam waist, and that the gold nanoparticles TP-photo-reduced are mono-dispersed, demonstrating that and a control on the GNPs density ad size is obtainable.

Chapter 4

Bi-dimensional structures rich in gold nanoparticles may be used in a wide range of applications, e.g. the laser-nanostructure interaction has become of great interest, in recent years, due to the application of NPs in different fields and their optical properties.

I focused my interest on photo-thermal effect in plasmonic nanoparticles: optical excitation and non-radiative relaxation of the LSPR create a photo-thermal effect due to the conversion of light energy into heat. Within this LSPR-mediated heating process, the light absorbed by the nanoparticle generates a non-equilibrium electron distribution that decays via electron-electron scattering. The hot electron gas equilibrates with lattice phonons, which transfer this energy into the surrounding medium, resulting in a local temperature increase.

In a first step, I analysed the heating effects obtained on a huge number of randomly distributed GNPs fixed on a glass substrate, after deep immersion in a gold colloidal solution.

Further thermo-plasmonic experiments were carried on two-photon direct laser written pattern of gold nanoparticles. The possibility to fix gold nanoparticles on a flat substrate, in appropriate design, with a resolution down to a few hundreds of nanometers, pave the way to the fabrication of thermo-smart platforms, able to generate a desired value of temperature by controlling the number of GNPs photo-excited at the same time. Therefore, I carried out careful analysis of the macroscopic photo-induced heat generation of four different 1D gratings of GNPs, created each of them in an area of 1 mm^2 and spaced by 0.5 – 2 – 10 and 100 μm. In particular, it was observed the possibility to tune finely the temperature variation, from 6 °C to 55 °C according to the model used and the intensity of the impinging laser.

Finally, I present preliminary results on the capability of 1D gratings, made by stripes of GNPs to work as surface-enhanced Raman spectroscopy (SERS) substrates. Multiple gratings were created by using different values of laser power and scan speed, and the SERS properties of each structure have been tested against rhodamine-6G and xylene. Enhancement factors (EF) superior to 10^4 have been quantified.

1 Micro- and Nano-fabrication through single and multiple photons absorption

1.1 Single-photon photo-lithography

Optical lithography is one of the most used and developed micro-fabrication technique [164-166]. The technique is based on the use of a photo-resist: a mixture of a reactive monomer, a solvent and a photo-initiator, spread in liquid phase onto a solid substrate. By tuning the resist viscosity when a spin-coating process is used, a thin film, of thickness finely controlled, typically in the range 0.5 - 100 μm, is deposed on a substrate. On such film, features are impressed with ultraviolet (UV) light exposure through a mask. Resists are available in positive and negative tone. A hole in the mask will create a hole in a positive tone photoresists, whereas it will create a pit in a negative tone photoresist. [166]

Let us focus on this last family (the other behaves in the symmetrical way): when a negative tone photo-resist is irradiated with ultraviolet light, the photo-initiator creates free radicals, whose interaction with the nearby monomers generates a crosslinking chain reaction. Polymerization keeps on propagating until either two different interacting radicals form a stable species, or the radicals are quenched due to interaction with non-inert gas present on the environment. To obtain high-quality results, polymerization has to occur completely during the UV light exposure. Therefore, it is mandatory to perform the process under an inert gas atmosphere and to exactly tune it according to the characteristic of the selected photo-resist.

It has to be considered that photo-lithography works efficiently if applied on thin film. Light goes through the holes inside of the mask, but diverts inside the bulk of the photoresist film, according to its thickness.

The mask screens the areas of the film that aren't to be exposed and structures 1D or 2D can be created in the photo-sensitive resin, with a resolution down to few micrometers, diffraction limited. The exposed resin polymerizes and the remaining non-exposed material

is removed bathing the sample in a solvent. As a result, it is obtained a strongly adhering layer of controlled thickness, structured in islands reproducing the shape of the uncovered areas in the mask.

This pattern can be hence used as a protective layer in a subsequent wet hatching process, as in the case of the silicon chips in the microelectronic domain, or as a mold in order to imprint the features in another material (soft lithography) [166]. The last is the standard technique used for fabricating microfluidic devices, where the microfluidic network is impressed in a polydimethylsiloxane (PDMS) block. PDMS is the most widely used silicon-based organic polymer, and is particularly known for its unusual rheological properties, allowing to fill and reproduce even the finest details, down to few nanometers. Because of his chemical-physical properties, PDMS is widely used in microfluidics [156-159], opto-fluidics [160-161] and bio-technologies [162], as it is optically clear and biocompatible.

In order to test and to assess the technique, I've prepared three different PDMS molds made as: a network of circular holes with diameter and depth of 30 μm, a network of rectangular holes (30 x 60 x 30 μm^3) and a 1D grating made by stripes oh thickness and height 30 μm.

The resist used to prepare the negative mold of the desired designs was SU-8 2050 (from MicroChem). SU-8 is a family of commercial negative photo-resist, available in different viscosities, according to the dilution of the monomer. The one used is specially tailored for creating films with thickness in the range of 40-170 μm, as a function of the spinning speed.

As substrates, I used standard 76.2 x 25.4 x 1.1 mm^3 microscope glass slides, hydroxylated through a bath in a fresh piranha solution prepared by mixing three parts of sulphuric acid (H_2SO_4) with one part of hydrogen peroxide (H_2O_2). The substrates were then rinsed with deionized water and left to dry. Before deposing 3 mL of photo-resist on each of them, the surfaces were activated through a plasma cleaning process of 5.5 W @ 8 minutes. A two step spin-coating cycle at 500 rpm for 10 s, and then at 4000 rpm for 30 s allowed to

obtain a plain film of 40 μm thickness. According to the SU-8 protocol, the film was pre-baked on a hot plate at 95 °C for 5 minutes, to let all the remaining solvent to evaporate.

A chrome on glass mask, with the desired patterns, was put upon the cooled photo-sensitive films (Figure 1.1 A), taking care to face the chrome side to the resist film. Polymerization was performed by using a led UV source (λ = 365 nm), with output intensity of 1.18 mW/cm^2 and exposure time of 10 min. A post-exposure baking at 95 °C for 5 minutes was performed in order to complete the polymerization of the exposed areas.

The film was left to cool for 10 minutes, and developed in a bath of 1-Methoxy-2-propyl acetate for 5 minutes, then the solvent was washed out with a bath in isopropyl alcohol (IPA) for 10 seconds (Figure 1.1 B). An hard-backing step at 145 °C for 30 minutes was carried out to better fix the structures on the substrates and to ensure that their mechanical properties don't change during thermal treatments.

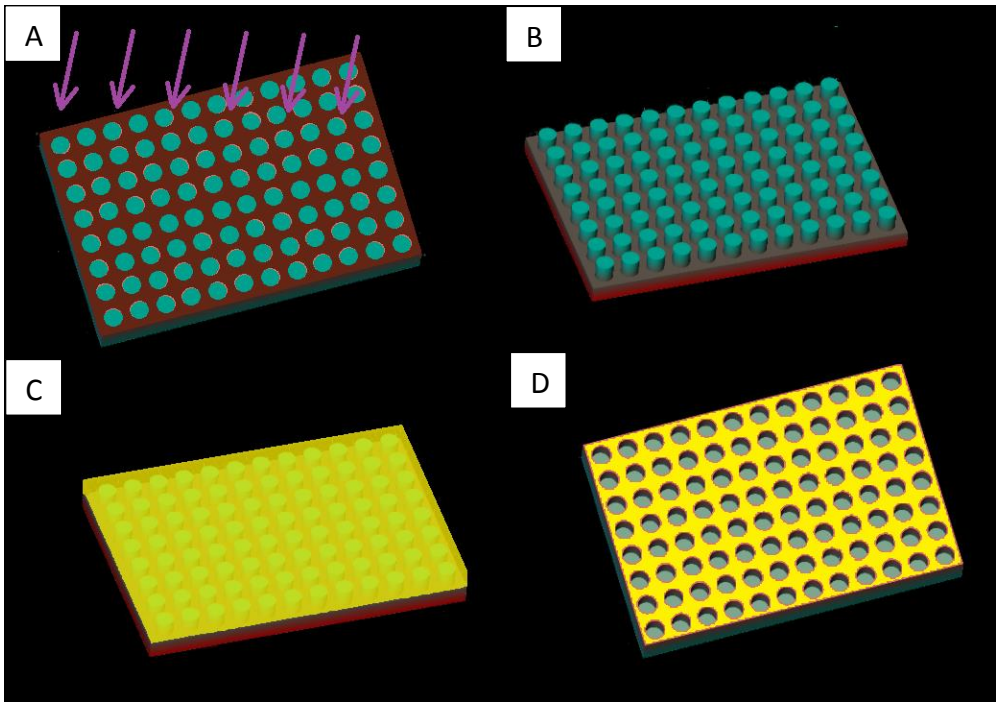

Figure 1.1 Scheme on how to prepare a PDMS mold. **A)** A mask made in chrome (indicated in brown) has to be put upon a SU-8 film (light blue in the scheme), in order to protect all the areas that have not to polymerize, during the UV exposure. **B)** The development process chemically removes all the non-exposed material, therefore a negative stamp of the mold in SU-8 is obtained.

C) PDMS (indicated in yellow) is poured on the mold to create a layer 5 mm thick and thermally cured. **D)** When hardened, the PDMS layer is peeled off from the SU-8 template.

A sufficient quantity of PDMS was prepared by mixing twelve parts in weight of base with one part of curing agent. The mix was put under low vacuum for degassing (0.37 mbar), in order to prevent the appearing of air bubbles in the bulk. Hence a PDMS layer about 5 mm thick was poured onto the SU-8 template (Figure 1.1 C) and left to cure @45 °C overnight. PDMS blocks were finally peeled off from the molds (Figure 1.1 D).

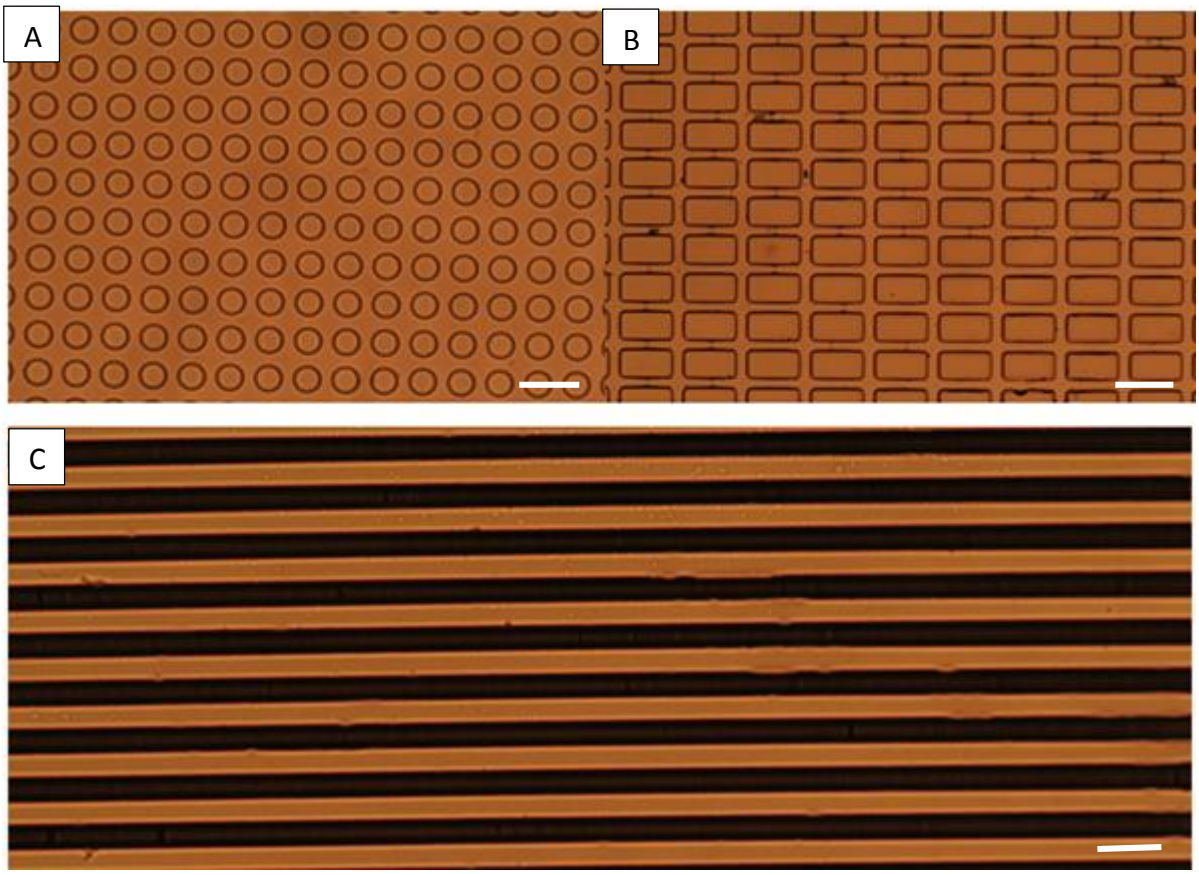

Figure 1.2: PDSM molds, made by **A)** cylindrical and **B)** rectangular holes, and **C)** stripes. The white line bar in the images is of 100 μm.

Optical images of the three PDMS imprinted structures, are shown in Figure 1.2. I was able to obtain the desired patterns.

1.2 Two-Photon Absorption

Direct laser writing (DLW) is a laser scanning fabrication technique allowing to maskless print structures into a photoresist, with a resolution depending solely on the output power and beam waist of the used laser beam [1-3]. When the optical absorption is governed by single photons processes, this technique allows for 3D patterning with resolutions down to typically few microns, in the same order of that given by the mask lithography. A huge improvement is achieved combining DLW with the two-photons absorption (TPA). In fact, exploiting the dependence of the TPA on the squared intensity and the presence of a threshold, features of hundreds nanometers, thus well below the diffraction limits can be created.

TPA is an optical process, theoretically predicted in 1930 by Maria Goeppert-Mayer [167], and then experimentally observed in 1961 by Kaiser and Garret [168]. As shown in Figure 1.3, a photon absorption excites a molecule from the ground energy level to a singlet excited energy level E_e, according to the process:

$$\Delta E = E_e - E_g = \hbar\omega_a \tag{1.1}$$

Where $\hbar$ is the reduced Planck constant, ω_a is the angular velocity of the absorbed photon.

The excited singlet level is typically unstable, therefore the system may lose energy and decay to a more stable intermediate energy level E_i, from which it may create a chemical bonding with other activated molecules, or it may release energy in a radiative (through an emitted photon which will have $\omega_e < \omega_a$), or non-radiative (local heating) way.

According to the Goeppert-Mayer's theory, the molecule may also be excited by the simultaneously absorption of two photons $\hbar\omega_k$ and $\hbar\omega_l$. This is a optical non-linear process involving the third order susceptibility, much smaller the main term responsible of the ordinary optics. Therefore, in order to observe TPA, a huge photon density is required [1-3], as in the case of a tightly focused laser beam. In general, TPA has to fulfil the condition:

$$\Delta E = \hbar\omega_a = \hbar\omega_k + \hbar\omega_l \tag{1.2}$$

In this case, the system is firstly excited to a virtual level E_v, whose lifetime $\Delta t \sim \hbar/\Delta E_k$ is typically in the order of 10^{-15} s, and then to the excited level E_e. If a single laser source is used, each photons has energy:

$$\hbar\omega_k = \frac{\hbar\omega_a}{2} = \frac{\Delta E}{2} \tag{1.3}$$

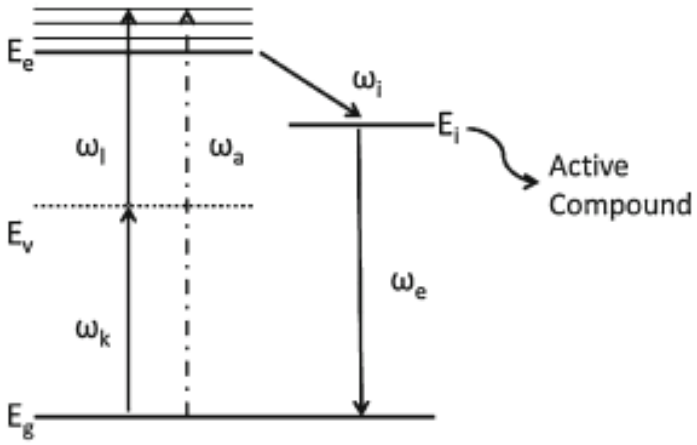

Figure 1.3 Energy level diagram for a molecule excited by a single photon (dotted line) or by two photons (straight line), from the ground level to an excited level. In both case, the compound may be activated or may release energy through radiative or non-radiative processes. [1]

The activation rate through TPA is strongly different in respect to the single photon absorption (SPA). For organic photo-resist, typical values of the SPA cross-section σ are in the order of 10^{-16} cm^2, while the TPA cross-section σ_2 is in the order of 10^{-50} cm^{4}s [1]. The SPA cross-section σ can be calculated according to Beer's law:

$$I(x) = I_0 e^{-\alpha c x} \tag{1.4}$$

Where: I is the laser intensity, $\alpha = \sigma N$ is the SPA absorption coefficient, N is the molecular number density, c is the molecular concentrations and x the path length. In the TPA case the eq. (1.4), becomes:

$$I(x) = \frac{I_0}{1 + \beta c x I_0} \tag{1.5}$$

In which $\beta = 10^{-3}\ (\sigma_2\, N_A\, c)/\hbar\omega$ is the TPA absorption coefficient, N_A is the Avogadro number, and σ_2 the TPA cross-section. If follows that σ_2 is a function of the square of the laser intensity [2].

1.2 Two-photon Polymerization

Through the TPA process, when an ultrafast near infrared (NIR) laser is focused on a UV-sensitive resin, polymerization is activated only in a very small volume inside the focus. This is the smallest polymerizable volume, usually called volume pixel (voxel) and defines the resolution of the photo-polymerization process [1-3].

Two-photon polymerization (TPP) presents two energy thresholds, as shown in Figure 1.4. The first one is the polymerization threshold, which depends on the laser intensity and the material cross-section σ_2. Only the portion of the Gaussian profile of the laser intensity that exceeds the threshold leads to local polymerization. Thus, the voxel dimensions strongly depend on the incident laser beam intensity. The second threshold is defined by the onset of the optical breakdown of the polymer: when the laser intensity is higher than this threshold, explosions can even occur and the resin is permanently damaged.

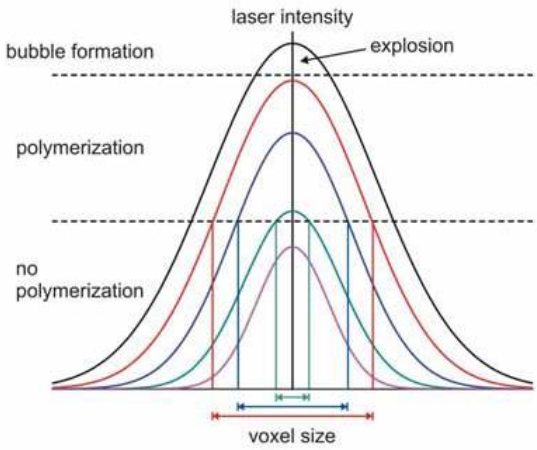

Figure 1.4: Laser intensity dependency of the voxel size. If the laser intensity is below the polymerization threshold no polymerization happens, else only the portion of the Gaussian beam higher than the threshold will lead to the voxel polymerization. Over the second threshold, the resist explodes and is permanently damaged [1].

Sweeping the laser beam into the photo-resist, is thus possible to create bi- and three-dimensional polymeric structures, whose resolution is given by the size of the voxel. A prediction of the diameter and length of a voxel is thus necessary to create refined 3D objects. The diameter d and the length l of the voxel are:

$$d(P,t) = r_{\omega_0}\sqrt{\ln\left(4\frac{P^2 t}{\nu t_L\left({r_{\omega_0}}^2\pi\cdot\hbar\omega\right)^2}\frac{\sigma_2}{\ln\left(\frac{\rho_0}{\rho_0-\rho_{th}}\right)}\right)} \tag{1.5}$$

$$l(P,t) = 2z_R\sqrt{\sqrt{\left(4\frac{P^2 t}{\nu t_L\left({r_{\omega_0}}^2\pi\cdot\hbar\omega\right)^2}\frac{\sigma_2}{\ln\left(\frac{\rho_0}{\rho_0-\rho_{th}}\right)}\right)}-1} \tag{1.6}$$

The voxel length and diameter depend then on the laser power P, the exposure time t and the TPA cross-section σ_2. The other terms are related to the materials and optical system used. $r_{\omega_0} = 0.61\ \lambda/N.A.$ is the beam waist, $z_R = \pi {r_{\omega_0}}^2/\lambda$ is the Rayleigh length, ν the pulsed laser repetition rate, t_L the single pulse width, $\hbar\omega$ the energy of the incident

photon, $\sigma_2^* = \sigma_2/ln[\rho_0/(\rho_0 - \rho_{th})]$ is the effective cross section for the TPA, ρ_0 and ρ_{th} are the initial density and the threshold density of radicals respectively.

1.4 TP-DLW

The TP-DLW system used presents a femtosecond Ti:Sapphire (λ = 780 nm) laser connected to an inverted microscope. The laser beam is focused on the sample through a 63x or 25x objective, with N.A. respectively of 1.4 and 1.1. 3D structures can be fabricated both through the glass, and by the diving the objective in the resist (Figure 1.5).

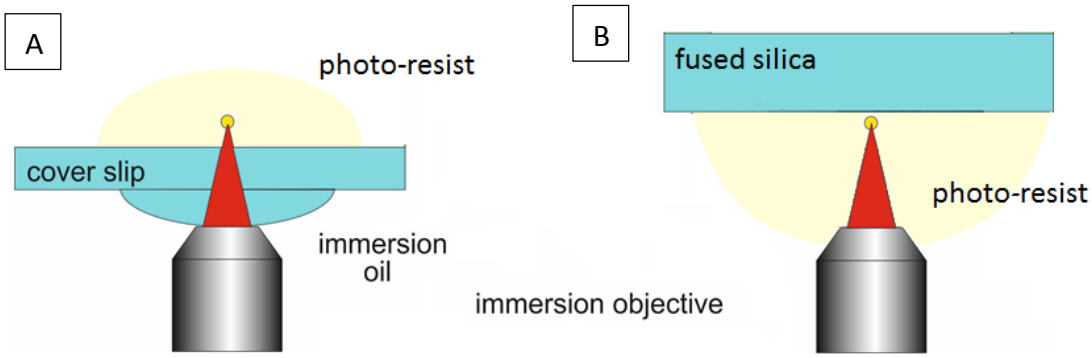

Figure 1.5 Scheme of the writing process **A)** through the glass, **B)** by immerging the objective inside the photo-resist.

During the printing process, the working distance of the objective (typically 350-400 μm) has to be taken in consideration when the TP-DLW is performed through the glass. Moreover, since the writing process occurs plane by plane, to create the highest parts of a structures, the laser beam has to go through the objects already created and is attenuated, generating smaller effective voxels.

By working with the objective immersed in the resin, it is possible to create 3D object with theoretically no vertical limits. However, fluid-dynamic effects may occur while moving the lens and affect the final result.

1.4.1 Modelling

To print a three-dimensional object, a 3D computer-aided design (CAD) software is preferable. In Figure 1.6 A is shown the example of the 3D model of the logo CNR Beyond-Nano Cosenza. In order to perform the printing, the model is sliced in layers (Figure 1.6 B), whose thickness has to be set accordingly to the voxel z-length, or they won't adhere each other.

Each plane is hatched in single segments (Figure 1.6 C), whose width has to be set accordingly to the voxel diameter.

It is than evident that a thorough study on the voxel dimensions in function of the laser intensity and exposure time has to be carried out for each used photo-resist.

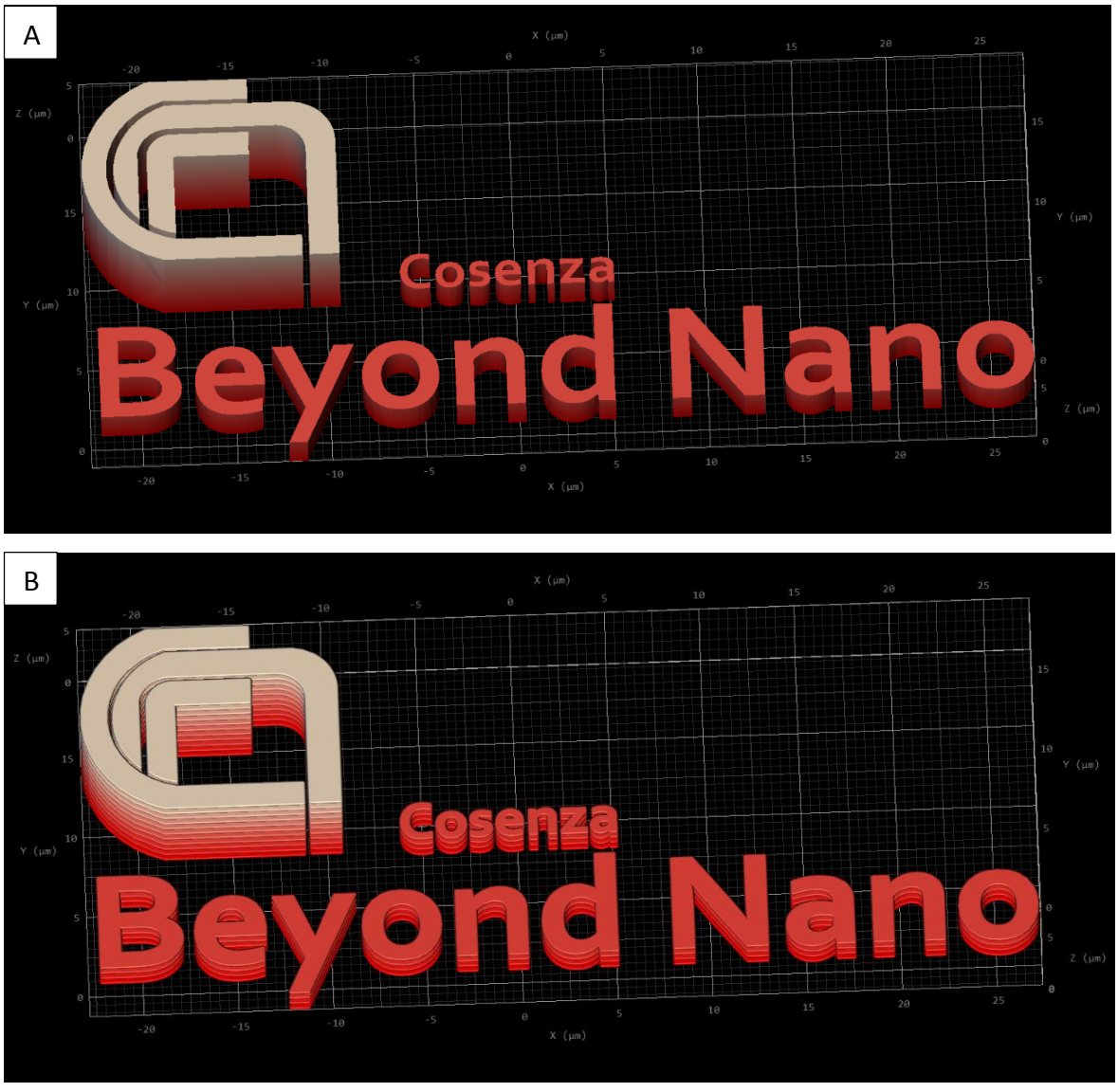

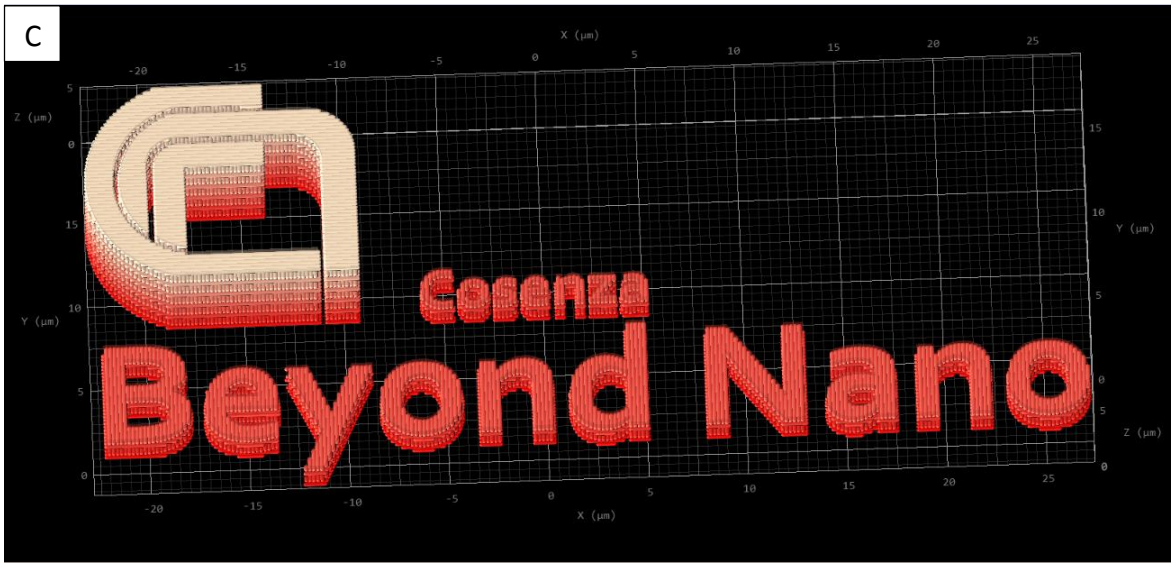

Figure 1.6 A) CAD model of the CNR Beyond Nano Cosenza logo, **B)** sliced in planes and **then C)** hatched in crossed lines.

1.4.2 Analyses.

Here is discussed the characterization of the voxel generated by diving the lens into the commercial photo-resist IP-Dip, whose refractive index is 1.52, matching that of the frontal lens. On the contrary, a refractive index mismatch between the photo-resist and the substrate is required to locate the interface, i.e. the z = 0 position. Therefore, a substrate of fused silica (refractive index: 1.46) was used.

In Figure 1.7 is shown the matrix of 1D gratings printed with the 63x, N.A. 1.4 objective, in order to characterize the voxel size.

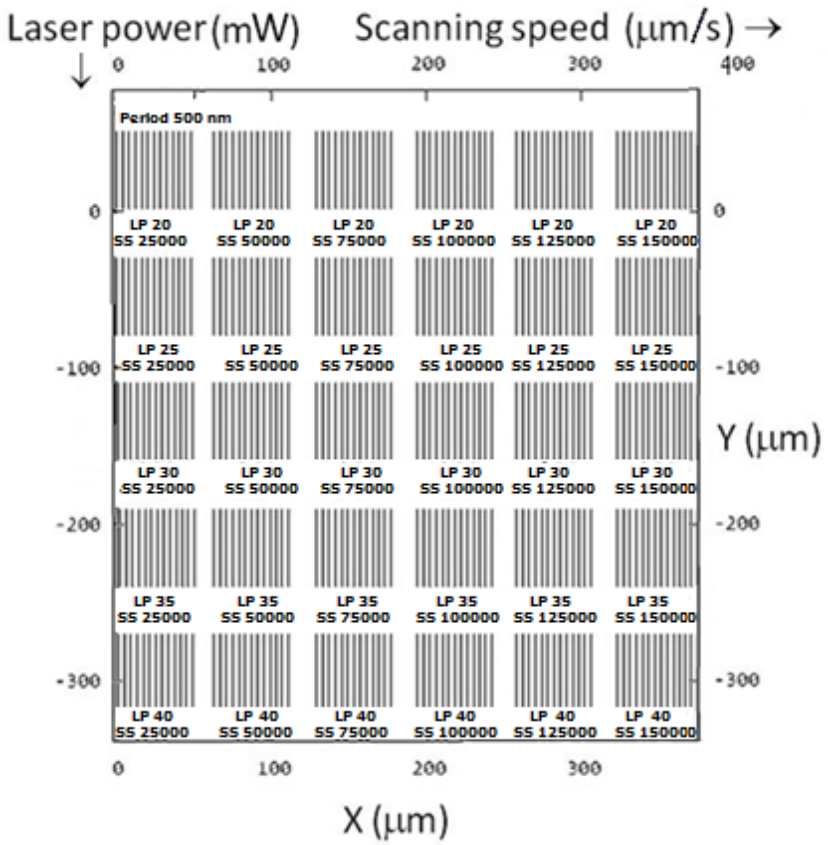

Figure 1.7 Scheme of the matrix of 50x50 μm^2 1D gratings printed. Each grating has period of 0.5 and µm was printed, using different values of laser power (20 - 40 mW, step 5 mW) and scan speed (2.5×10^4 - 1.5×10^5 µm/s, step 2.5×10^4 µm/s).

To remove all the non-exposed resist, after the printing process, the sample was developed through a bath in propylene glycol monomethyl ether acetate (PGMEA) for 25 minutes, and then in IPA for 5 minutes. When the sample dried, the gratings were analysed by means of scanning electron microscope (SEM) and atomic force microscope (AFM).

SEM is a well-known probing technique, which allows analysing objects, whose size is below the diffraction limits [169]. Briefly, the sample is probed with an electron beam. The electrons interact with the sample elastically (back-scattered electrons, BSEs) or lose their energy through multiple random scatterings, inside the interaction volume, which leads to the emission of secondary electrons (SEs) and X-ray radiation [169]. Different detectors may be used to collect the various signals, the BSEs provide information on the atomic number of the sample, the SEs on the topology, and the X-ray radiation on the atomic composition allowing the possibility to perform energy dispersive X-ray (EDX) analysis on the surface.

AFM allows to measure the three-dimensional profile of sub-micron objects. A tip, typically tall 5 μm and with a ending radius of 5 nm scan the object, reproducing its profile. The Wan der Vaals forces rule the interaction between the tip and the sample, thus the morphological analysis of any kind of solid surface is permitted [170].

An example of SEM and AFM imaging on a grating printed with laser power 20 mW and scan speed 7.5 x 10^4 μm is shown in Figure 1.8.

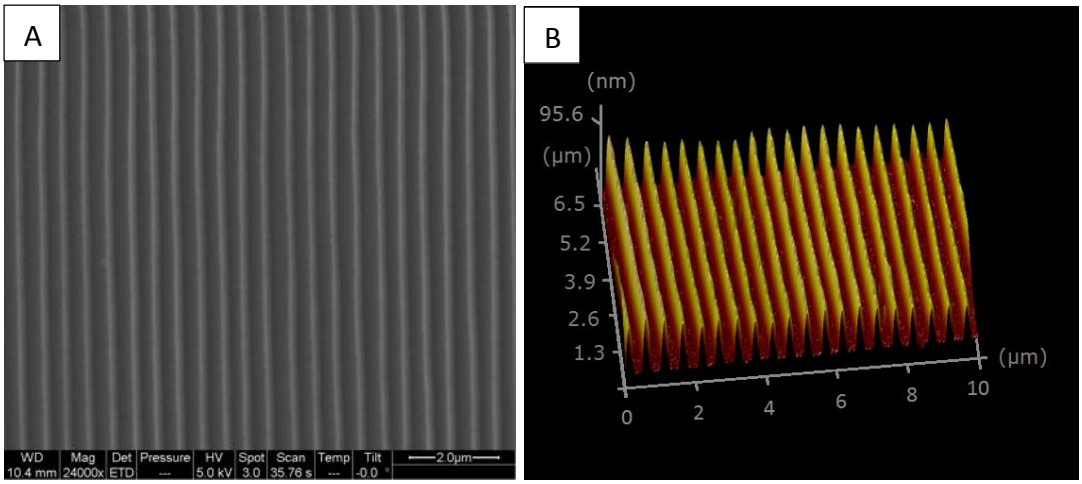

Figure 1.8: A) SEM image of a 1D grating created with laser power 20 mW and scan speed 75 x 10^4 μm/s. SEM allows to get best information on the spatial resolution, while AFM on the three-dimensional profile.

Combining the data obtained by SEM and AFM imaging, it is possible to characterize the voxel size of the photo-resist in function of the printing parameters.

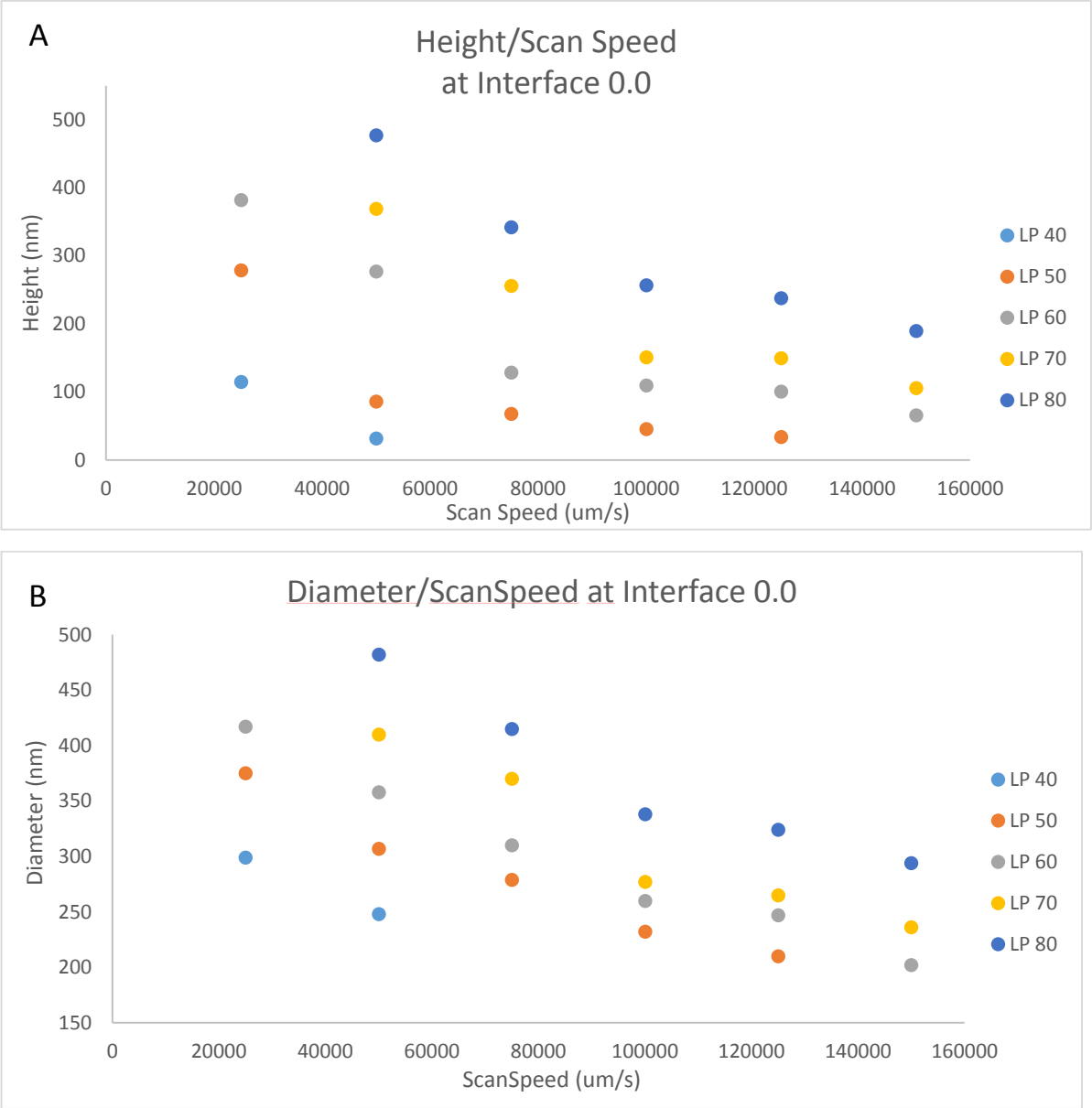

Figure 1.9 A) Length and **B)** Diameter of a voxel dependence on the scan speed of the laser beam during the writing process, measured for different laser power values.

In particular, according to Eq. (1.5) and Eq. (1.6), the effective cross-section of the photo-resist IP-Dip is $\sigma_2^* = (3{,}0 \pm 0{,}8)10^{-52} cm^4 s$. Moreover, I was able to define the polymerization and explosion thresholds, obtaining d = 200 nm and l = 80 nm as dimensions of the smallest polymerizable voxel and d = 480 nm and l = 960 nm for the largest one (Figure 1.9).

However, the AFM profile of the largest voxels does not reveals a Gaussian shape, in contrary to smaller ones. In Figure 1.10 A and B, the example of the voxels obtained by

printing two stripes at scan speed 7.5 x 10^4 µm/s and laser power respectively 20 mW and 40 mW are compared. Writing patterns with dense hatching, low velocities and high laser power values, leads to an enhancement of the local temperature, which can trigger the cross-linking of the monomers in the surrounding volume. As a consequence, adjacent segments appear as a bigger single stripe or a connected by a polymeric filamentation (Figure 1.10 C-D).

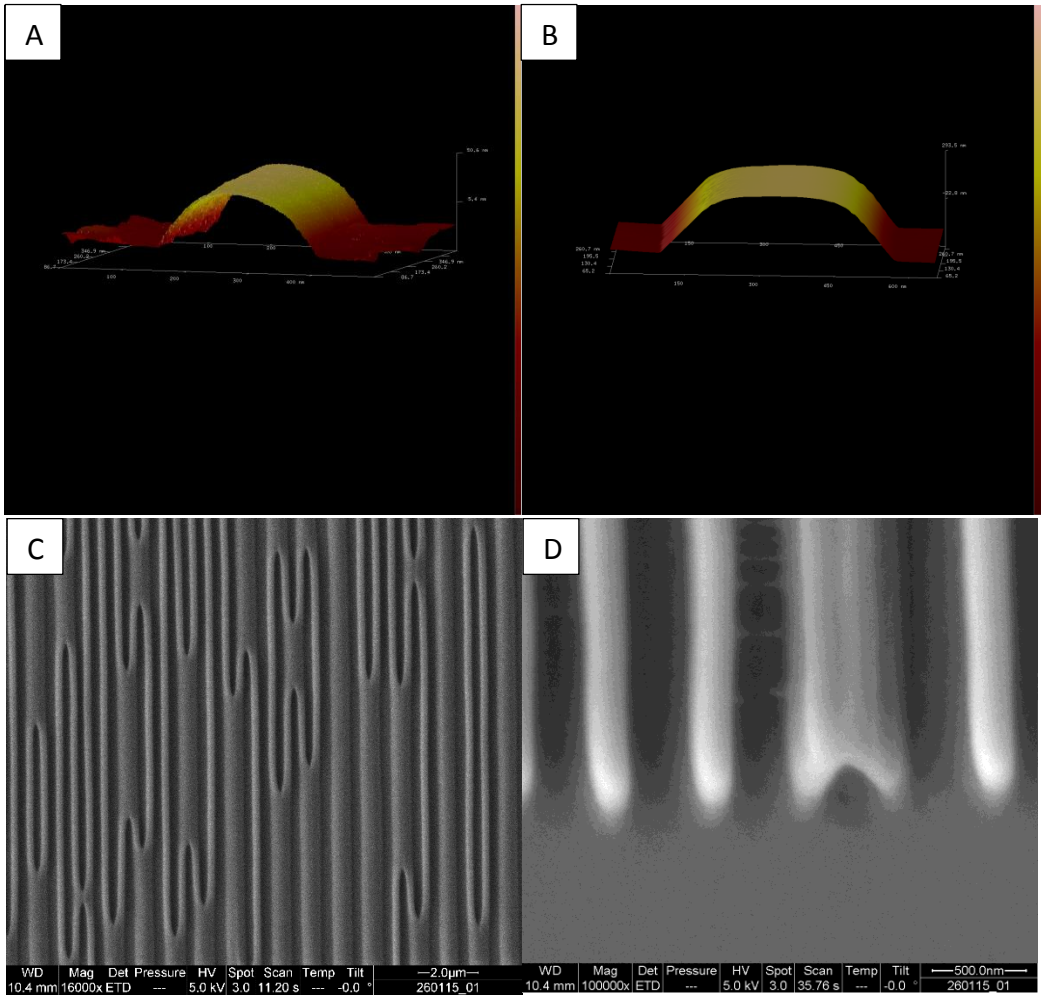

Figure 1.10 AFM profile of a single line of a 1D grating printed in IP-Dip @ 7.5x 10^4 µm/s and laser power **A)** 20 mW and **B)** 40 mW. **C)** SEM image of the latter gratings, with **D)** a bottom edge detail. Adjacent stripes written at high energy can be connected by a thin polymeric filamentation or two lines can generate a bigger one.

When one wants to print 3D microstructures has to take this effect in consideration: due to the linking between two different stripes, the final structure results more solid, but

the resolution worsens. Moreover, the temperature increases layer by layer and explosion may occur.

From this analysis, to write 3D solid object with high resolution in IP-Dip, I selected as best condition laser power 25 mW, scan speed 1.25 x10^5 µm/s, hatching 0.2 and slicing, 0.1.

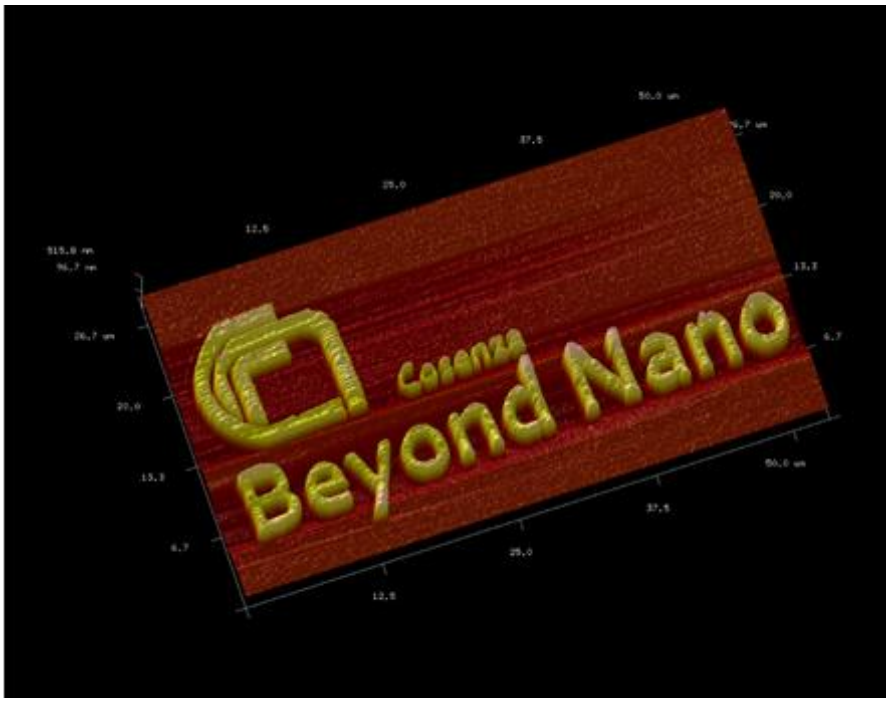

Figure 1.11 AFM imaging of the CNR Beyond-Nano Cosenza logo printed in IP-Dip, by selecting laser power 25 mW, scan speed 125000 µm/s, hatching 0.2 and slicing, 0.1. The logo is 50.0 µm x 21.0 µm x 0.5 µm, with features well below the diffraction limit.

E.g. I used these parameters to print the model in Figure 1.7. The AFM profile shows that the structure is (50.0 x 21.0 x 0.5) µm^3, with features inside the word 'Cosenza' in the order of 600 nm, and the thickness of each letter is 800 nm (Figure 1.11). The resolution of the logo is ~200 nm, well below the one obtainable through photolithography.

1.5 Meso-scale structures

Different challenges can be encountered while printing millimetric structures with nano- and micro-features. An example is given by the 3D microfluidic system (1 x 0.7 x 1 mm^3), in Figure 1.16. Even if it is a macro object, it presents micro channels and small features inside the tip. By using IP-Dip, a 63x objective, and the setting parameters indicated for micro-structures as the logo in Figure 1.12 no less than 8 days of printing were predicted.

Therefore, I used a 25x, N.A 1.1 objective, and the structure was printed in IP-S 780, a commercial photoresist that allows to obtain at best a resolution of 1 µm. After characterizing the photo-resist as in the last paragraph, the object was printed with laser power 30 mW @ scan speed 8 $x10^4$ µm/s, slicing 3 µm, hatching 1 µm. In this way, I was able to reduce the working time to 8 hours.

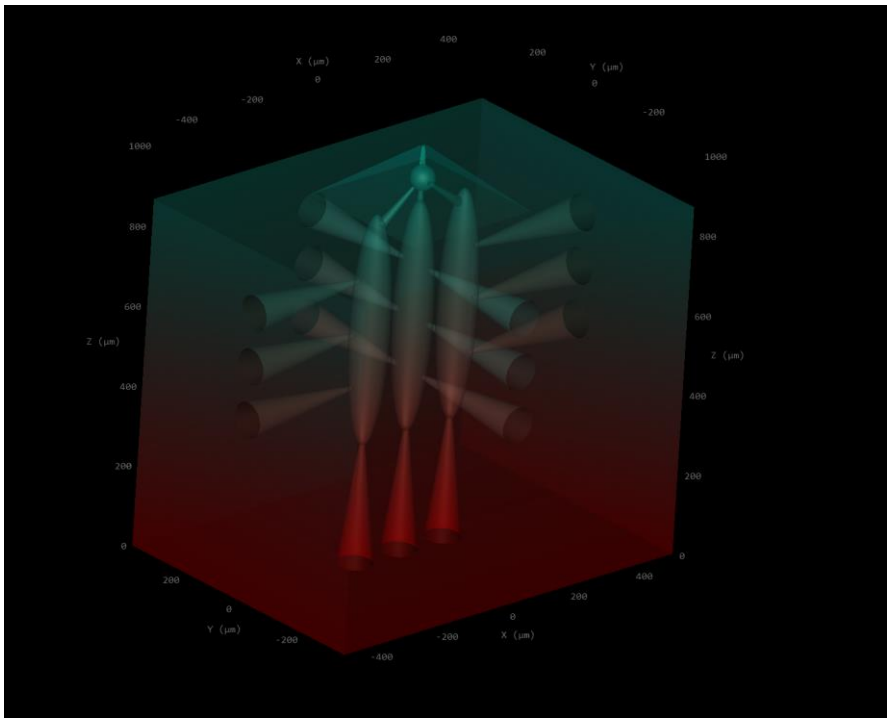

Figure 1.12 Three-dimensional (1 x 0.7 x 1 mm^3) micro-fluidic system: from each side and from the bottom, different micro-channels converge in three chambers. The three chambers are connected the a spherical hole, where fluxes may mix and flow towards an upper aperture.

1.5.1 Shell & Scaffold

To further speed up the printing process, I split out the model in the *shell & scaffold* mode. This technique allows to create a solid shell, containing inside the liquid monomer (Figure 1.17 A). To avoid the structure collapse, a tetrahedral scaffolds was printed inside (Figure 1.17 B). After the printing process, the object still contains the monomer inside, which can be single photon polymerized by using an UV source.

The tip of the structures, containing features as small as 10 μm, was completely fabricated by TP-DLW in order to minimize the distortion occurring during SPP, obtaining a resolution of 1 μm. Adopting this strategy allowed to reduce the fabrication time to 1.5 hours.

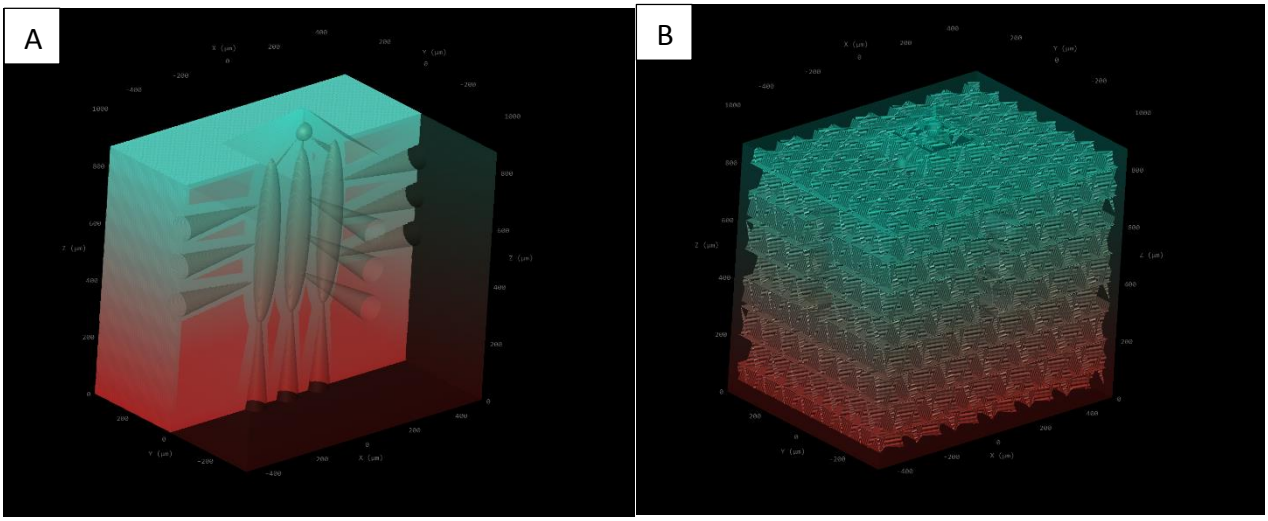

Figure 1.13 Simulation of the printing process. **A)** A compact shell is printed at the sides of the structure, **B)** while a tetrahedral scaffold is printed inside to reinforce it. The tip, with refined features, was printed line-by-line.

1.5.2 Developing issues

When creating microfluidic system, in order to avoid deformations and obstructions of the channels, one has to check that all the unpolymerized resin is removed from the channel during the development, before the final UV-curing.

The standard development protocol requires a bath in PGMEA of 25 minutes; however, that is an indicative time, tailored for convex objects, but it is not effective to develop an object featuring narrow channels. In this case, the developing process becomes a real challenge due to the difficulty to make the solvent flow in the channels. This is particularly true when the substrate obstructs the channels. In such a case, the development required two days, which caused swellings, deformations and cracks of the objects.

In order to overcome the issues, I defined a different protocol to develop microfluidic systems, described in the following.

Square pyramid trunks (base: 50 x 50 μm^2, period: 200 μm) were printed at the base of the object to support the microfluidic system and allow the solvent to flow between them and get inside the channels at the base.

Taking in account that the density of IP-S 780 is higher than that of the solvent, the sample was developed up-down for 15 minutes in PGMEA and then 5 minutes in IPA.

The sample was left to dry head up. In this way, possible droplets of organic photo-resist dip on the glass and may be removed by a second bath in PGMEA for 5 minutes, and 1 minute in IPA.

This technique allowed for the complete removal of the resin inside the channels, without any detectable damaging of the structure. However, a light swelling of the finest details turned out. In order to speed up further the developing process, I decided to create a suitable series of holes in the glass substrate, by using hydrofluoric acid, in correspondence of the channels openings. After the TP-DLW of the object, a 5 minutes bath in PGMEA is required to remove the majority of the un-polymerized resist; then the channels can be directly developed by pouring the solvent inside the holes. In this way, the development time is considerably shortened and, as a consequence, no swelling occurred.

After the development, I single-photon cured of the monomer inside the structure, by using a 365 nm led with output power of 3 Watt, for 10 minutes. UV-curing was performed in a chamber filled with nitrogen, to avoid quenching free-radicals with the present in air. After curing process, the structure obtained showed good compactness and well-refined features of the order of 10 μm.

1.6 Conclusions

In conclusion, nano- and micro-fabrication through SPA and TPA were performed. In particular, TP-DLW is a powerful technique to realize polymeric 3D objects with features down to 100 nm. To assess the resolution, a preliminary characterization of the photosensitive material in terms of voxel size vs. the laser intensity is mandatory.

The creation of mesoscales structures, with micro-features inside, can be a challenge, due to the issues encountered during the development process. In particular, the standard protocol is ineffective when one wants to develop micro-fluidic systems, due to the impossibility to directly flush the solvent inside the channels, when they are facing the glass substrate. This occurrence may happen when the object structure forces a given orientation on the substrate. Two different methods to overcome the issue were presented.

2 Micro-fabrication of 3D structures in Reactive Mesogens

The experiments shown in the previous chapter were aimed to improve the optical fabrication of polymeric three-dimensional objects with nanometric resolution. Bare nano-fabrication allowed to obtain great results in many technological fields, as described above. However, a great improvement in additive manufacturing has been obtained by combining TP-DLW with thermotropic liquid crystals (LCs).

Thermotropic LCs are states of matter, defined mesophases, whose mechanical properties are intermediate between those of a liquid and of a crystal. Between LCs, liquid crystalline elastomers (LCE) are particular relevant in the field of nanofabrication, since they can be polymerized thanks to one photon or multi-photons absorption. This grants the possibility to create 3D solid objects with the optical properties of LCs [171].

In this chapter, I show the results obtained on creation of structures made in nematic and cholesteric LCE, both by the technological and the physical point of view.

2.1 Liquid Crystals

While crystals exhibit highly ordered structures, molecules in fluid occupy random position, showing no kind of order. LCs present the typical fluidity of liquids, but they are composed by highly anisotropic molecules (mesogens), usually having the characteristic shape of rod-like or disk-like, which spontaneously tend to organize according specific structures and symmetries, at specific temperature [171].

Thanks to their internal order, LCs show extraordinary electric, magnetic and optical properties that have been highly investigated in the last decades, both by a scientific and a technological point of view. In fact, LCs have been employed in an ever-widening range of applications, such as optoelectronics [163, 172], micro-fluidics [173], optics [174], displays [175-176] and much more.

Thermotropic mesophases are determined by the degree and molecular arrangement of the LCs, which can usually be ascribed to three main phases: nematic, smectic and columnar or dischotic (so called because is typical of disk-like molecules) [171]. In particular, in nematic liquid crystals, the mesogen molecules do not have positional order, thus there is no correlation between their center of mass, but they present long range orientational order. The local orientation is described by the director vector **n**, a unit vector defining a vectorial field. The smectic and the columnar phase, vice versa, are also characterized by respectively 1D and 2D positional orders.

Among these main phases, it is important to consider the chiral (or cholesteric) nematic phase, in which the mesogens spontaneously twist in the axis perpendicular to the director.

In this chapter, I will put attention on the properties of nematic and chiral phase.

2.1.1 Nematic Liquid Crystals

As stated before, the difference between a nematic and an isotropic material is given by the anisotropic rod-like shape of the molecules, which tend to align along a common direction defining the director **n**. Due to thermal fluctuation, mesogens are usually skewed off the director and present orientation θ with respect to the director **n** [177].

Therefore order degree of the nematic is defined by the scalar order parameter S, according to which:

$$S = \frac{1}{2}\langle 3\cos^2\theta - 1\rangle \tag{2.1}$$

When S assumes the value 1, the molecules are perfectly oriented (crystals), vice versa, when it is equal to 0, molecules have no specific orientation and the system is isotropic (liquids). In LCs the order parameter is usually in the range of 0.3-0.9.

S strongly depends on temperature, which affects the ordering in nematic mesophase. In fact, variations of temperature increase the thermal fluctuation and can

induce a phase transition, changing considerably the symmetry of the mesophase. As a consequence, consistent changes in physical properties are observed, namely density, viscosity, and optics. To define the dependence of S on temperature T the Landau-de Gennes theory is used [178].

According to Landau formalism, the free energy volume density, near the transition point, can be described by the function [179]:

$$f(T) = f_0 + \frac{1}{2}a(T - T^*_{N-I})Q_{\alpha\beta}\,Q_{\beta\alpha} - \frac{1}{3}BQ_{\alpha\beta}\,Q_{\beta\gamma}\,Q_{\gamma\alpha} + \frac{1}{4}CQ_{\alpha\beta}\,Q_{\beta\gamma}\,Q_{\gamma\delta}\,Q_{\delta\alpha} + \cdots \quad (2.2)$$

Where T^*_{N-I} is the undercooling temperature, a, B and C are phenomenological material positive constants, which do not depend on temperature [180]. Q_{ij} are elements of the tensor order parameter, which describe all the symmetries of the phase and can be defined as [171]:

$$Q_{ij} = \frac{1}{2}S(3n_i n_j - \delta_{ij}) \quad (2.3)$$

Where n_i and n_j are the component of the director **n**, and δ_{ij} is the Kronecker delta. For a uniaxial nematic Q_{ij} eq. (2.3) becomes:

$$Q_{ij} = \frac{1}{2}S(n_i n_j - \frac{1}{3}\delta_{ij}) \quad (2.4)$$

Substituting this expression of Q_{ij} in equation (2.2), the energy volume density can be defined in function of S:

$$\Delta f(T) = f(T) - f_0 = \frac{1}{3}a(T - T^*_{N-I})S^2 - \frac{2}{27}BS^3 + \frac{1}{9}CS^4 + \cdots \quad (2.5)$$

Minimizing the function $\Delta f(T)$ with respect to S:

$$\frac{\partial f(T)}{\partial S} = 0 = a(T - T^*_{N-I})S - \frac{1}{3}BS^2 + \frac{2}{3}CS^3 + \cdots \tag{2.6}$$

The only possible solutions to equation (2.6) are [180]:

$$S_I = 0 \tag{2.7}$$

$$S_N = \frac{B}{4C}\left(1 + \sqrt{1 - \frac{24aC}{B^2}(T - T^*_{N-I})}\right) \quad \forall\, T < T_{N-I} \tag{2.8}$$

Where T_{N-I} is the temperature of transition from the nematic to the isotropic phase.

The first solution S_I describes the isotropic phase, the latter the dependence of S_N on temperature in the nematic phase. Thus, the order parameter decreases when the temperature is increased and drops to zero at for $T = T_{N-I}$ transition.

Transition temperature T_{N-I} and correspondent value of the scalar order parameter S_{N-I} are defined as [180]:

$$T_{N-I} = T^*_{N-I} + \frac{B^2}{27aC} \tag{2.9}$$

$$S_{N-I} = \frac{B}{3C} \tag{2.10}$$

The behavior of the order parameter in function of the temperature is shown in Figure 2.2 [181].

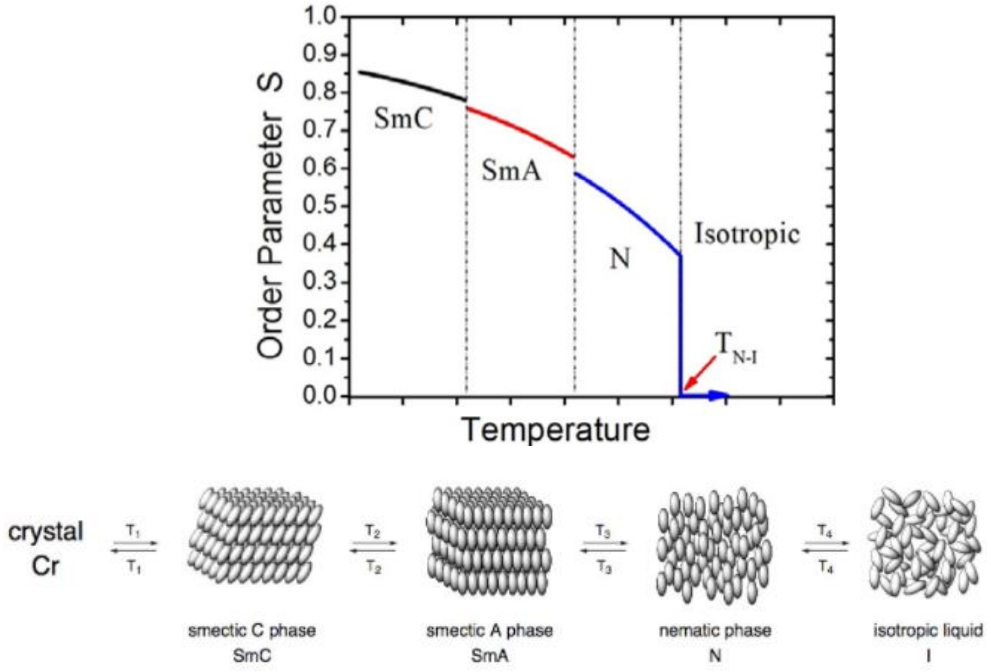

Figure 2.1 Scheme of the dependence of the order parameter in function of the temperature. In correspondence to $S \sim 0.6$ the transition between the smectics and the nematic phase happens. When the temperature is equal to T_{N-I} the order parameter drop to zero and the system shows isotropic behavior.

Due to their uniaxial symmetry, LCs shows different behavior (such as refractive index, dielectric permittivity, conductivity, magnetic susceptibility or viscosity) when are crossed by a polarized light beam, depending on the relative orientation of between **n** and the electric field of the polarized light beam. Particularly interesting are optical anisotropy, made manifest by the presence of ordinary n_0 and extraordinary n_e refractive index [171].

When the $\boldsymbol{k}$ vector of the incident light beam coincides with **n**, the electric vector propagates along n_0 (ordinary wave) and the material behaves as an isotropic medium. For all the remaining mutual orientations between **n** and $\boldsymbol{k}$ the material is birefringent, as the beam splits into an ordinary and an extraordinary wave, the latter propagating with n_e (Figure 2.3 A-B).

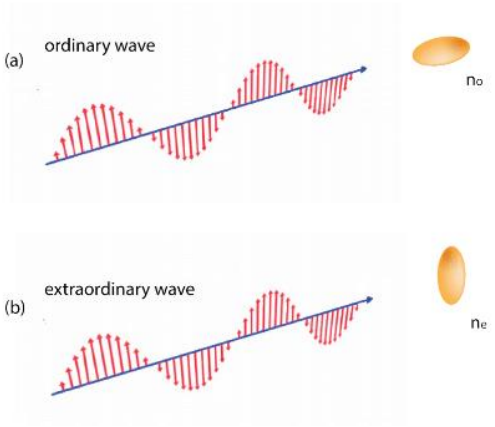

Figure 2.2 Light propagation in NLC occurs for the ordinary beam along n_0, B) for the extraordinary beam along n_e.

If the light hit the NLC with an angle ϕ with respect to the director, an effective extraordinary refractive index n_e^* is defined [182-183]:

$$n_e^* = \frac{n_e n_0}{\sqrt{n_e^2 \cos^2 \phi + n_0^2 \sin^2 \phi}} \tag{2.11}$$

The birefringence is then defined as:

$$\Delta n = n_e^* - n_0 \tag{2.12}$$

The propagation between of the ordinary and extraordinary waves through the sample occurs at different times, therefore the two waves emerge from the sample with a phase difference $\Delta\varphi$ depending on the thickness of the material d:

$$\Delta\varphi = \frac{2\pi}{\lambda}(\mathrm{n_e} - n_0)d \tag{2.13}$$

With λ being the wavelength associated to the propagating beam.

However, if the symmetry of the system changes, also the birefringence is subject to variation. In particular, when the temperature is such that the scalar order parameter $S = 0$,

the material is in the isotropic phase and no birefringence is observed [180-183]. In graph 2.4 is shown the dependence of the birefringence with respect to the temperature.

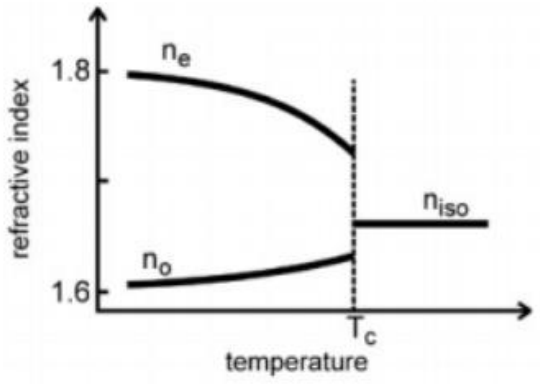

Figure 2.3: Refractive index dependence on temperature in NLCs.

2.1.2 Chiral liquid crystals

Both cholesteric and nematic present no correlation between the center of mass of the mesogens, but long range directional order which is defined by the director **n** [171]. However, while in nematics **n** is constant in space, in cholesteric liquid crystals (CLCs) it is subject to a spontaneous twist on the *x*-*y* plane, according to which:

$$n_x = \cos(qz + \phi) \tag{2.14}$$

$$n_y = \sin(qz + \phi) \tag{2.15}$$

$$n_z = 0 \tag{2.16}$$

Where ϕ is the phase angle and q is the chirality. According to the sign of q the twist is left-handed or right-handed. The twist of the director is periodic and describes an helix, whose pitch is defined as:

$$P = \frac{2\pi}{|q|} \tag{2.17}$$

When q is equal to 0 the pitch diverges and the LCs is in the nematic phase.

In NLCs, the cholesteric phase can be induced by adding a chiral dopant agent, which is able to induce the twist of the molecules. In this case, the pitch depends on the helical twisting power (HTP), measured in μm^{-1}, and the concentration c of the doping agent, therefore [184-186]:

$$P = \frac{1}{HTP \cdot c} \tag{2.18}$$

The lattice period $d = P/2$ is usually in the order of 100 nm, which confer to CLCs the peculiar property of selective reflection of optical wavelengths. Selective Bragg reflection happens when the pitch length and the wavelength of the impinging light are comparable [171, 187].

The electric field of the propagating light is described by Maxwell equation:

$$\nabla^2 \vec{E} - \nabla\left(\nabla \cdot \vec{E}\right) = \frac{\varepsilon_r}{c}\frac{\partial^2 \vec{E}}{\partial t^2} \tag{2.19}$$

Where c is the speed of light and ε_r is the tensor which describe the dielectric constant of the material. Considering, for example, a CLC with right-handed helix oriented along the **z** axis:

$$\varepsilon_r = \begin{pmatrix} \varepsilon_{||} & 0 \\ 0 & \varepsilon_{\perp} \end{pmatrix} \tag{2.20}$$

Describing the electric field as a plane wave $\vec{E} = \vec{E}_0(\hat{z})e^{i(kz-\omega t)}$, with $k = \frac{2\pi n}{\lambda_B}$ the wave vector and eq. (2.19) can be rewritten as:

$$\frac{d^2\vec{E}_0}{dz^2} + 2i\left(\frac{2\pi n}{\lambda_B}\right)\frac{d\vec{E}_0}{dz} + \left(\left(\frac{2\pi}{\lambda}\right)^2 \varepsilon_r - \left(\frac{2\pi n}{\lambda_B}\right)^2\right)\vec{E}_0 \tag{2.21}$$

Solutions of Eq. (2.21) are:

$$\left(\left(\frac{\lambda_B}{P}\right)^2 - \varepsilon_{||} + n^2\right) E_{||} = -2in\frac{\lambda_B}{P} E_{\perp} \tag{2.22}$$

$$\left(\left(\frac{\lambda_B}{P}\right)^2 - \varepsilon_{\perp} + n^2\right) E_{\perp} = -2in\frac{\lambda_B}{P} E_{||} \tag{2.23}$$

Solving this system, the eigenvalues in Eq. (2.22-23) are obtained:

$$n_{\pm}^2 = \frac{(\varepsilon_{||} + \varepsilon_{\perp})}{2} + \left(\frac{\lambda_B}{P}\right)^2 \pm \sqrt{(\varepsilon_{||} + \varepsilon_{\perp})^2 + 4\left(\frac{\lambda_B}{P}\right)^2 \frac{(\varepsilon_{||} + \varepsilon_{\perp})}{2}} \tag{2.24}$$

In Figure 2.4 is shown the behavior of $n_{\pm}^2$ in function of $\frac{\lambda_B}{P}$. In particular, if the light has the opposite handness of the helix is transmitted, otherwise it is reflected. In particular, the black line in Figure 2.4 B indicates the photonic band gap (PBG), correlated to the band of wavelengths that cannot propagate inside of the material.

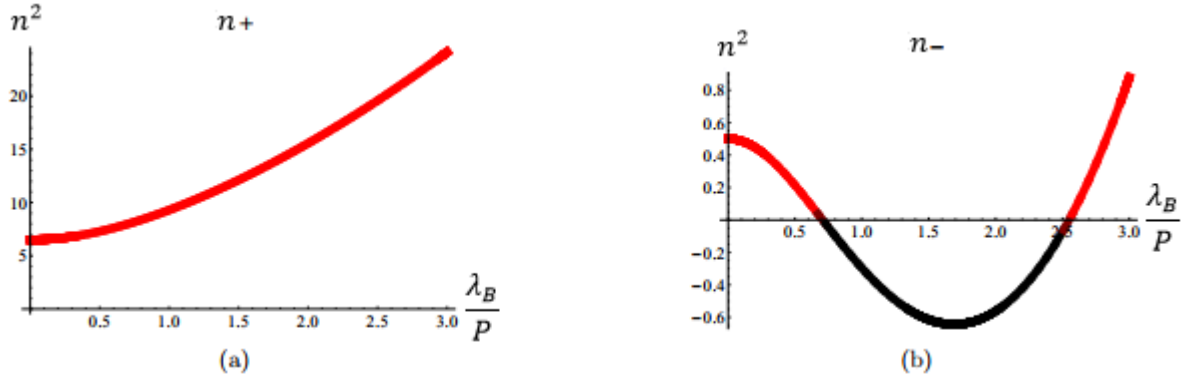

Figure 2.4: dependence of $n_{\pm}^2$ on $\frac{\lambda_B}{P}$. **A)** Polarized light with the perpendicular handness with respect to the helix is propagated, **B)** with opposite handness is reflected.

The limits of PBG can be calculated by putting eq. (2.24) equal to zero, which allow to obtain as result [171]:

(2.25)

$$\sqrt{\varepsilon_{\perp}} < \frac{\lambda_B}{P} < \sqrt{\varepsilon_{||}}$$

Considering $\sqrt{\varepsilon_{\perp}} = n_0$ and $\sqrt{\varepsilon_{||}} = n_e$, eq. (2.25) becomes:

$$Pn_0 < \lambda_B < Pn_e \tag{2.26}$$

Thus the width of the PBG is:

$$\Delta\lambda_B = P\Delta n \tag{2.27}$$

The central wavelength of the PBG is:

$$\lambda_B = \bar{n}P \tag{2.28}$$

Where $\bar{n}$ is the average refractive index.

When the incident light hits the sample at angle θ with respect to the chiral plane λ_B is described by the Bragg's law:

$$\lambda_B = 2\bar{n}d \sin\theta \tag{2.29}$$

In Figure 2.5 is shown a scheme summarizing the behavior of the Bragg reflection when a light beam is shined on a CLC, which generates a peak in the reflection spectrum, and thus a minimum in the transmission one [188].

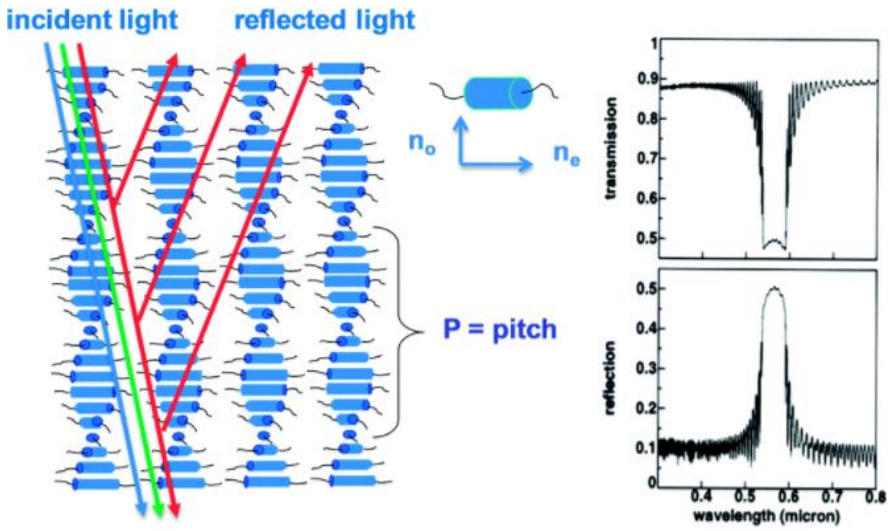

Figure 2.5: A) Selective Bragg reflection in a CLC, which lead to a square-shape **B)** hole in the transmission band and **C)** peak in the reflection band.

2.2 Microfabrication in Liquid Crystalline Polymer

Liquid crystalline polymer (LCP) is a polymer having molecular ordering typical of the liquid crystal (LC) state, thus showing anisotropic physical properties (i.e. birefringence, dichroism) unlike amorphous polymers. It incorporates anisotropic mesogenic moieties into the polymer main chain and/or as side chains, which have the tendency to orient their principal axis along the molecular director ($\hat{n}$). When coated on a aligning layer (rubbed of photoaligned polymeric thin films), the molecular director aligns accordingly, thus creating a uniform LC domain. Here a photopolymerizable reactive mesogen solution (RMs) has been used to microfabricate solid anisotropic structures made of LCP. The RMS (Licrivue RMs03-001C, by Merck) is a UV-curable mixture of LC molecules (30%) including acrylate-based photopolymerizable end-groups, dissolved in propylene glycol monomethyl ether acetate (PGMEA, 70%). The molecular structure of RMs03-001C is shown in Figure 2.6 [240]. In the LC (unpolymerized) state it exhibits nematic phase between 25 °C and 75 °C.

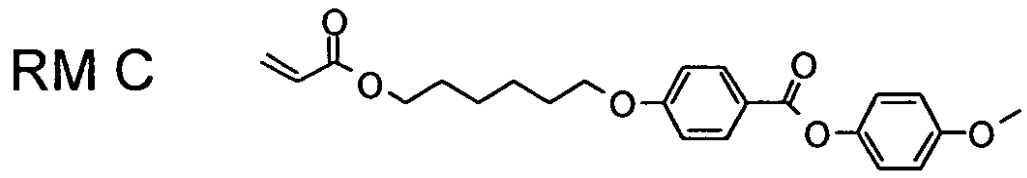

Figure 2.6: Molecular structures of the RMs C.

To correctly write inside a film of RMs03-001C, PGMEA has to be totally evaporated in a vacuum chamber ($0.3 \cdot 10^{-3}$ mbar at 50 °C for 24 hours), in order to avoid evaporation and bubble formation during the printing process, which can effectively damage the structures.

To align the RMs, a solution of 1% polyvinyl alcohol (PVA, Molecular weight: 13000-23000 g/mol, 98% hydrolysed) and 99% distilled water was spin-coated at 3600 rpm on a glass substrate. Polyvinyl alcohol was chosen thanks to its good mechanical properties and chemical stability. Moreover, it is soluble in water, which allow to separate the polymerized structures from the glass without damaging them.

The spin-coating process consists in spreading a coating material on a substrate, by rotating it at specific speeds per a given number of rounds per minute (rpm). After the spin-coating, the film was left to dry for 40 minutes at 105° and mechanically rubbed four times in antiparallel direction. Rubbing is made through a velvet roll. That is moved on the surface four times on the same direction while spinning, in order to create microgrooves (Figure 2.7) on the PVA film. The grooves induce a defined orientation of the PVA molecules, which is transmitted to the LC molecules anchored on the substrates; moreover, this kind of orientational order propagates in the bulk of the LC molecules via intermolecular forces [183].

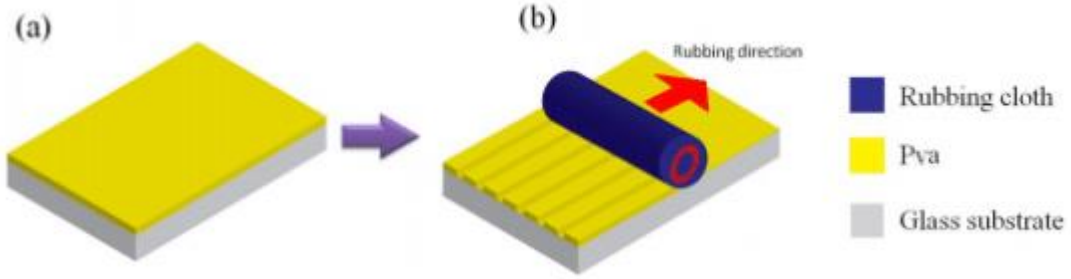

Figure 2.7: Rubbing process: **A)** A film of PVA is deposed on a glass substrate, **B)** the velvet roll create microgrooves in the polymer.

Nematic RMs was drop-casted on the PVA-coated substrate and left to rest for two hours. The 3D structures were written through the glass, on the rubbed surface, with linear polarization of the laser parallel to the rubbing direction.

After the TP-DLW, the samples were developed in PGMEA for 25' and left to dry in air. However, TP-DLW on RMs03-001C presented several critical points. First of all, the height of a single line is typically less than 100 nm, which is the resolution of the TP-DLW system used. Therefore, the voxel characterization cannot be performed by measuring the three-dimensional profile of 1D gratings. As a consequence, I printed 3D woodpiles made of ten crossed layers of 30 μm long stripes, having in-plane periodicity of 2 μm and vertical spacing of 400 nm, as shown in the AFM image in Figure 2.8 A. The woodpiles were printed at different values of laser power ranging from 5 to 30 mW, with step of 5 mW, and different values of scan speed ranging from 10^3 μm/s to 10^4 μm/s. Analysis were carried out by considering the AFM profiles of the nodes of the woodpile and described in function of the energy dose delivered in Figure 2.8 B.

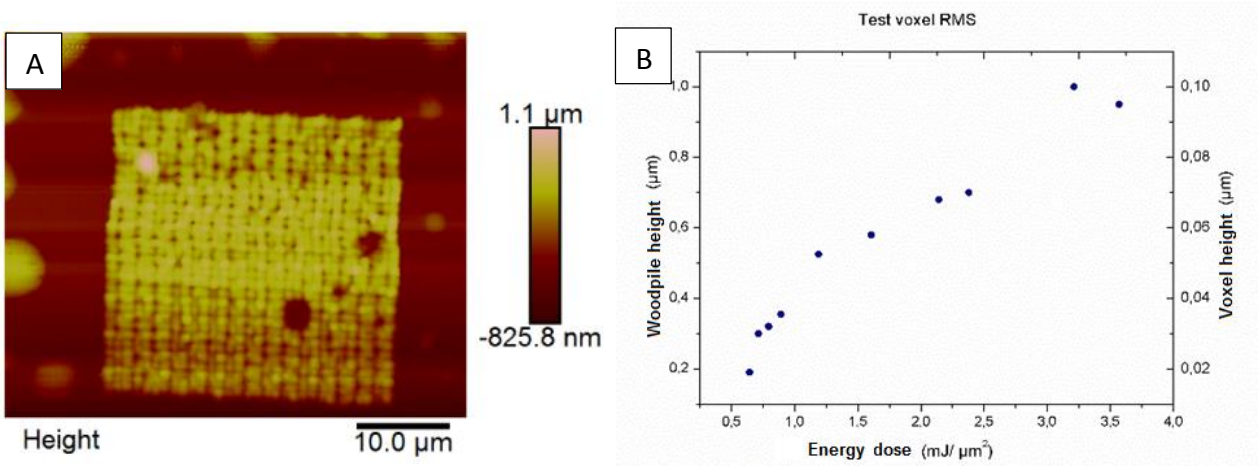

Figure 2.8: A) AFM image of a 30 x 30 x 1.3 μm^3 woodpile printed in RMS03-001C at laser power 20 mW @ Scan speed 4×10^3 μm/s. **B)** Analysis on the woodpile height and voxel height versus of the energy dose delivered.

Considering the height of the single voxel as 1/10 of the woodpile height, it seems that vertical resolution in the order of tens of nanometers is achievable by using RMs03-001C. However, in order to investigate the lateral proximity effect on contiguous lines I printed the 1D arrays of three parallel stripes showed in Figure 2.9 A. Each array is at progressively increasing distance each three lines (0.1 μm, 0.2 μm, 0.5 μm, 1 μm, 2 μm, 5 μm) at 20 mW @ 4×10^3 μm/s and the AFM analysis (Figure 2.9 B) on the grating showed that:

- stripes at distance 5 μm were not polymerized
- stripes at distance 2 μm are about 100 nm high
- stripes at distance 1 μm appear melted together creating a single line high 200 nm
- stripes at distance < 1 μm are melted all together in a single large block of polymer, with maximum height over 500 nm in correspondence of the stripes with distance 0.1 μm

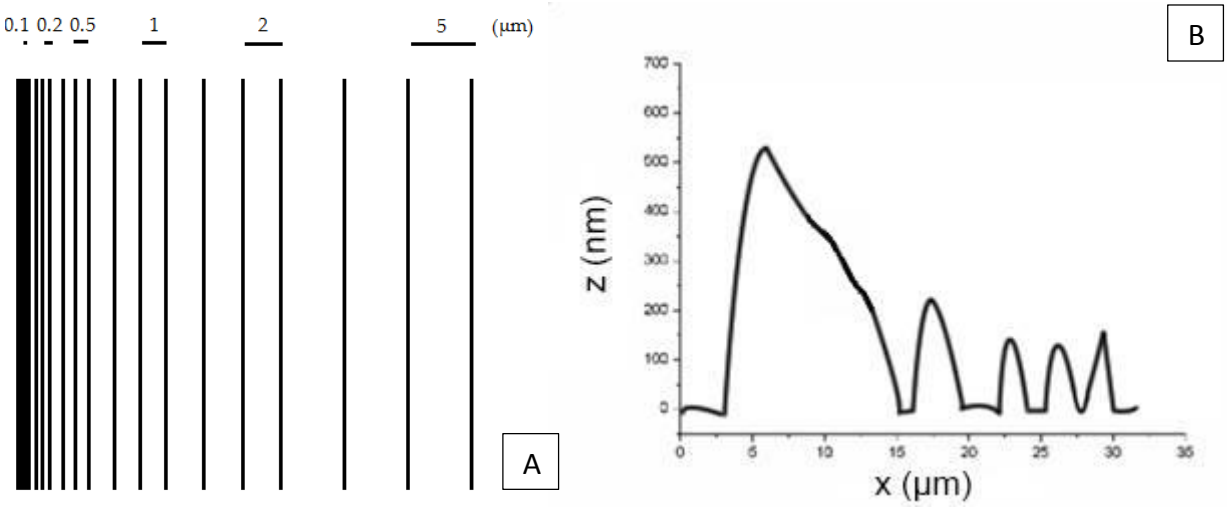

Figure 2.9: A) Scheme of grating made by single 50 μm at different changing each three lines with period ranging from 0.1 μm to 5 μm The periods between each three lines decreases. **B)** AFM profile of the gratings. The height of the stripes depends on the hatching due to thermal effects. No results are found for stripes with the largest period, while for the smallest the stripes are melted together.

I ascribe this result to the thermal diffusion occurring during TP-DLW. Photo-polymerization implies local heating of the resin, which trigger thermal polymerization of the area around the voxel and eventually bubbles formation. Therefore, considering the height of a single voxel as a fraction of multilayer structure, is an incorrect approximation, since the height of the voxel is very likely higher for each plane, due to accumulative heating. Consequently no statistical analysis can be carried out on structures made on RMs03-001C without controlling thermal effects.

Moreover, a negative consequence of this result is that no structure higher than 2 μm can be correctly created, since accumulated heating leads to bubble formation, and therefore expansion, explosion and permanently damaging of the structure.

In Figure 2.10 two cylinders from CADs having 15 μm diameter, 2 μm (A) and 8 μm (B) height, have been printed at energy dose of 0.7 mJ/μm^2. While dimensions in the first case (A) were respected, the second structure is severely deformed showing holes due to bubble explosion, maximum height of 6 μm and diameter around 25 μm.

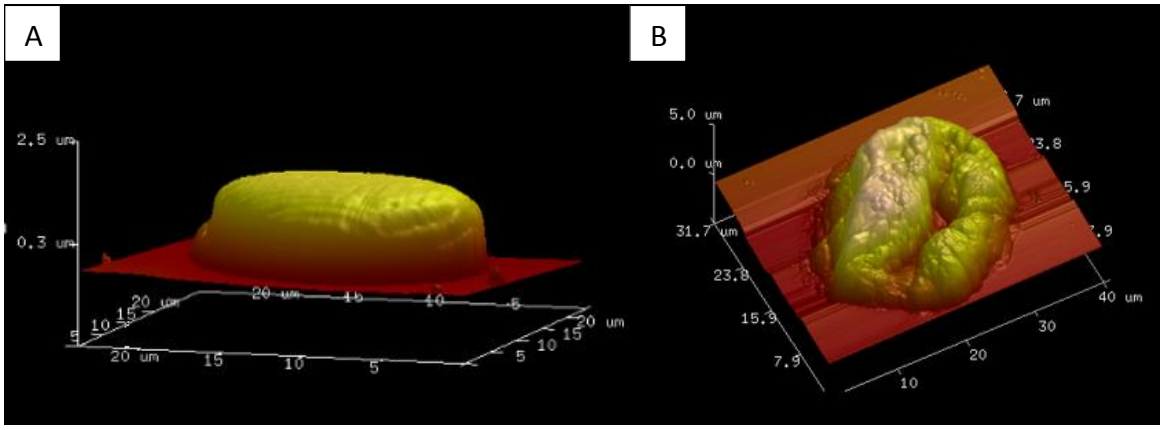

Figure 2.10: AFM profile of two cylinders created with energy dose of 0.7 mJ/ μm^2, with nominal diameter of 15 μm, and nominal height of **A)** 2 μm and **B)** 8 μm.

2.2.1 Birefringence analysis.

In order to overcome the limitation described above a photo-initiator, Irgacure 2100 (Phenylbis(2,4,6-trimethylbenzoyl)-phosphine oxide), whose molecular structures is shown

in Figure 2.11 A [244], was added to the solvent-free RMS, 3% by weight, and the mixture stirred for 1 hour at 60 °C.

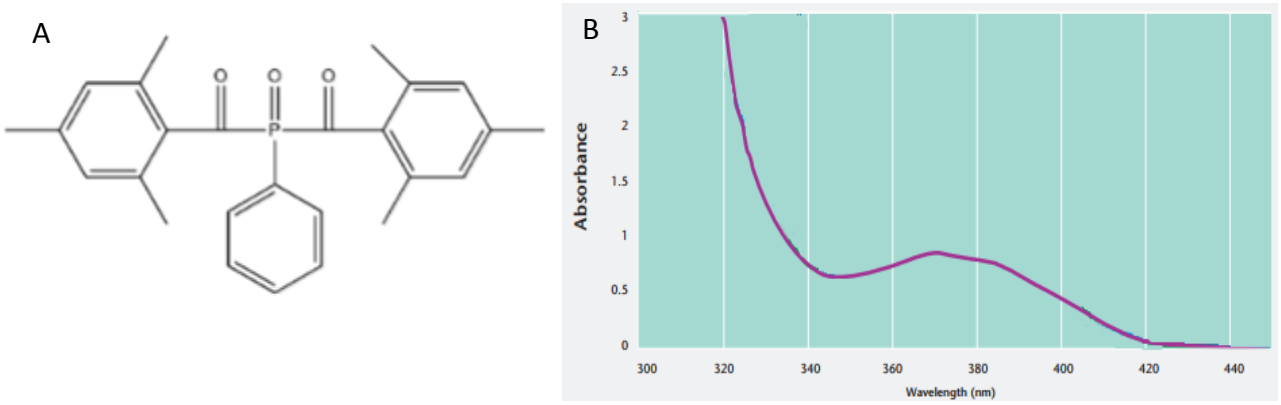

Figure 2.11: A) Molecular structures of Irgacure 2100 (Ciba Speciality Chemicals, Switzerland). **B)** Absorbance spectrum of Irgacure 2100

The photo-initiator, whose absorbance has a peak at ~375 nm (Figure 2.11 B), is used to increase the TPA cross-section of the RMS and to aid cross-linking between molecules. In fact, it consented to create solid structures of desirable height. Again, I started from the CAD model of a cylinder with diameter of 15 μm and height of 8 μm, which is sliced in layers separated by 0.4 μm, and each plane hatched in lines with a period of 0.3 μm (Figure 2.12 A). To obtain compact structures, I cross-hatched consecutives slices. This model was reproduced, using different values of laser power, ranging from 5 to 25 mW, and scan speed ranging from 2×10^3 μm/s to 1×10^4 μm/s, as shown in Figure 2.12 B.

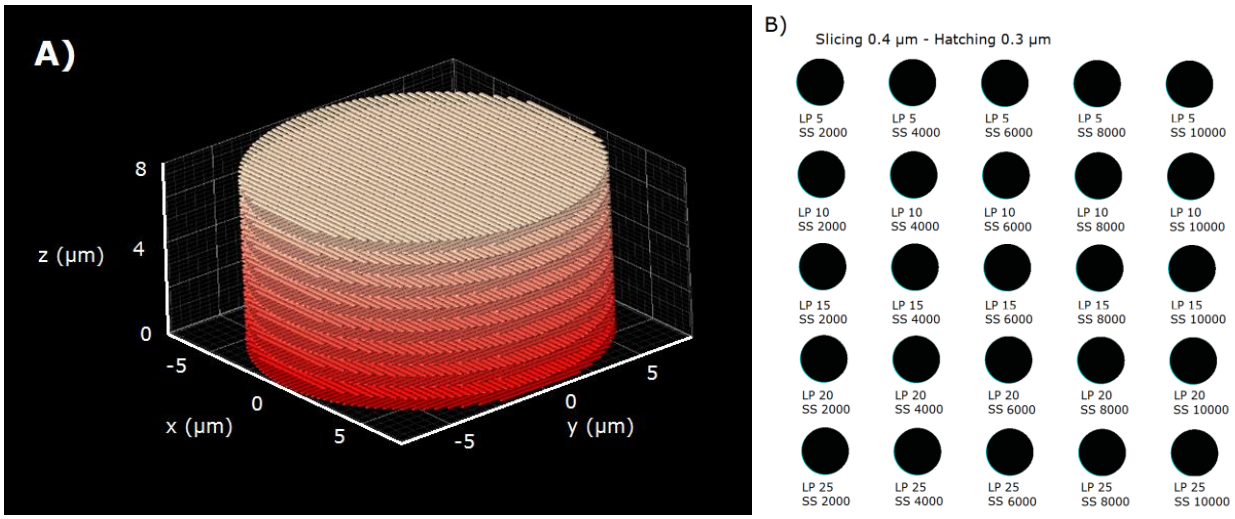

Figure 2.12: A) CAD model of a cylinder having diameter of 15 µm, height 8 µm, slicing of 0.4 µm and hatching of 0.3 µm. **B)** Scheme of the spatial organization of RMs cylinders. The laser power (LP) increases from top to down with steps of 5 mW, while the scan speed (SS) increases from left to right with steps of 2×10^3 µm/s.

The width and height of the single stripes, realized by scanning the laser focus through the sample, strictly depend on the energy dose delivered [1-3]. Therefore, the structures have different degree of polymerization and compactness.

As shown by the profilometry measurements in Figure 2.13 A, at high value of laser power, the single stripes have larger dimensions than the ones predicted in the model, which leads to over-exposition and the explosion of the cylinders. At low energy dose, the cylinders have a low degree of compactness and shrink during the development process, when all the un-polymerized material is removed. Due to the shrinking, the structures are smaller and lose their cylindrical shape.

Defining the density of energy delivered as the product between the laser power and the exposure time, on the surface of the beam spot, I estimate that high quality of TP-DLW fabrication is obtainable at energy doses between 5 and 25 µJ/µm^2, the threshold of polymerization and explosion, respectively. The three-dimensional shape of the structures was analysed via atomic force microscopy (AFM). Figure 2.13 shows the AFM image of a cylinder written at 15 mW and 4000 µm/s, whose diameter (15.0 ± 0.1) µm and height (7.8 ±

0.1) µm match those of the CAD model. The roughness of the top surface, about 200 nm, is due to the hatching of the uppermost layer.

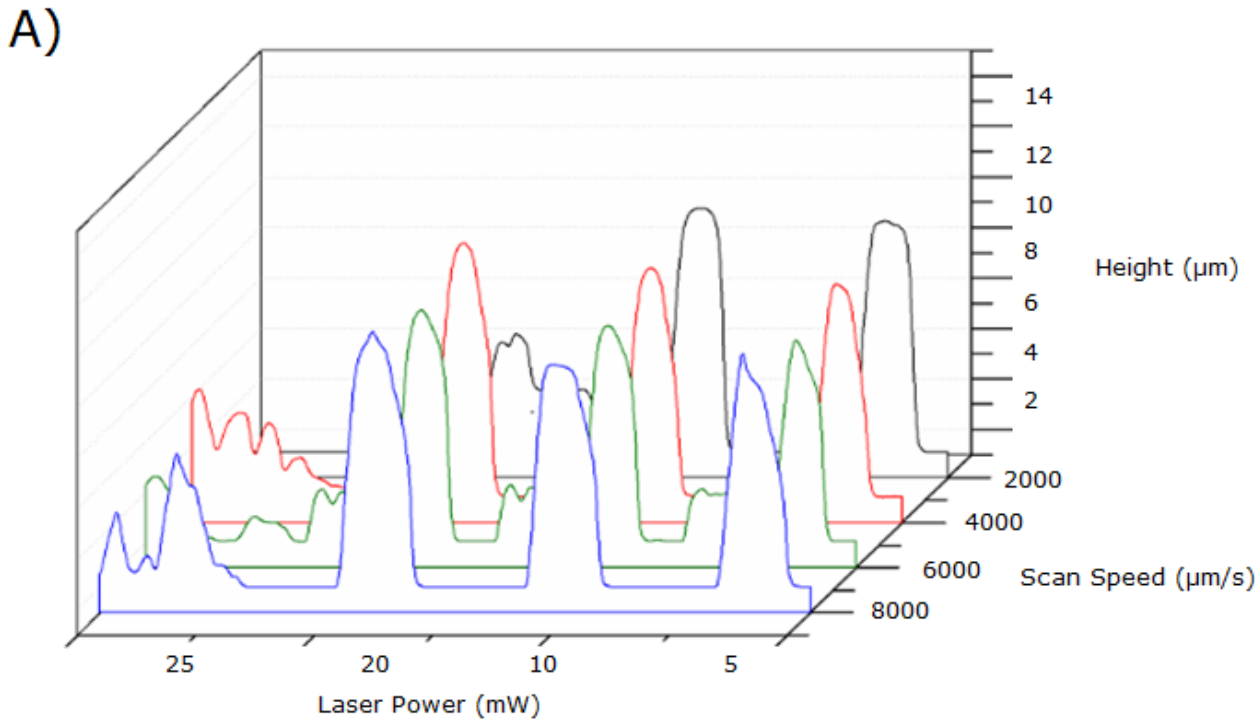

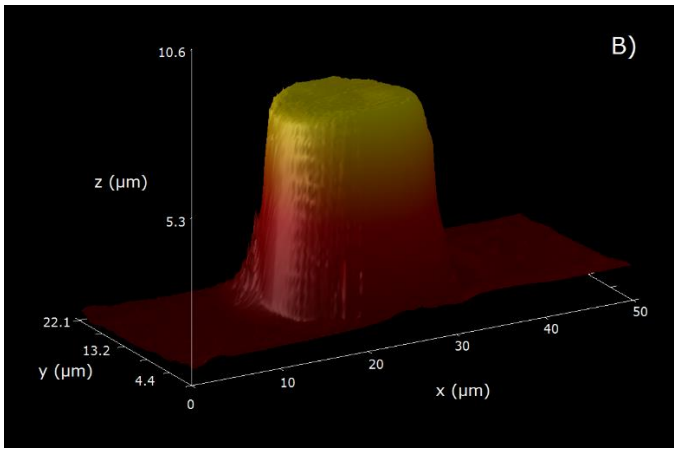

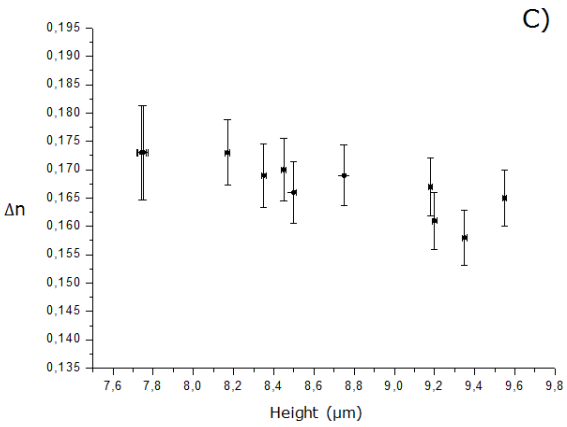

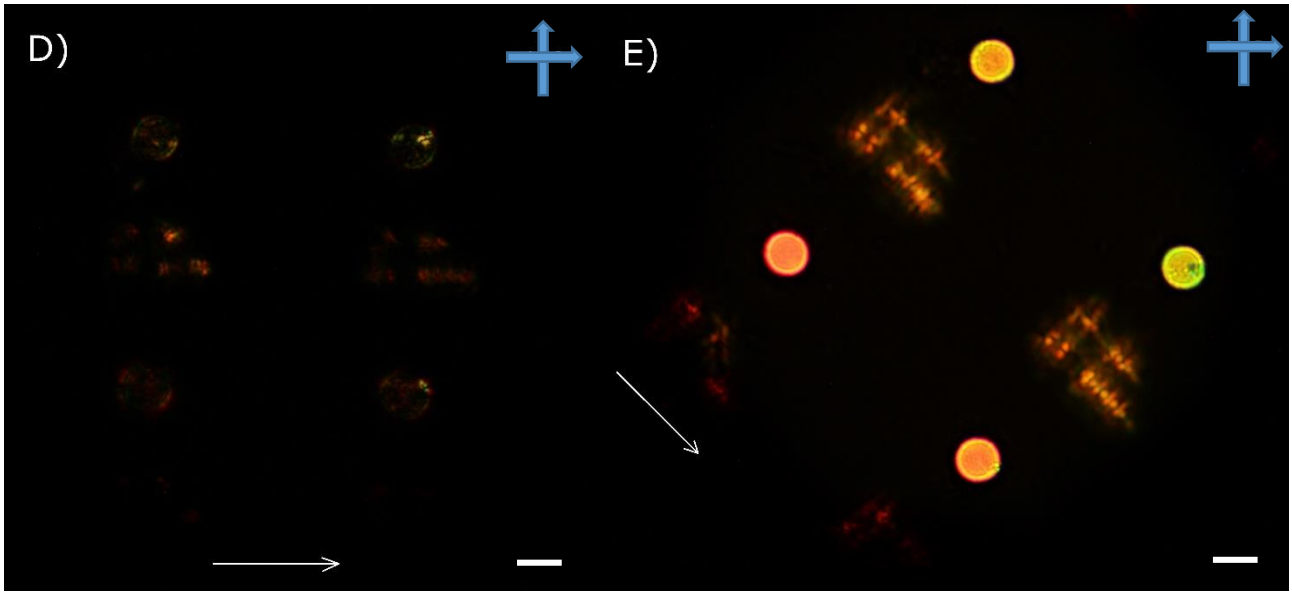

Figure 2.13: A) Profilometry measurements of the nematic RMS cylinders. On the x-axis we reported the laser power, on the y-axis the scan speed, on the z-axis the height of the structures. **B)** AFM image of a cylinder written at 15 mW @ 4000 μm/s. The hatching of the lines determines the roughness of the surface. **C)** The birefringence Δn of the cylinders versus height. **D)** Optical image taken between crossed polarizers of cylinders created at different values of laser power and scan speed. The rubbing direction is parallel to the polarizer and **E)** at 45°, showing the birefringence of the structures. The difference between the colours depends on the different heights of the cylinders. The white vector under the cylinders indicates the rubbing direction. Line bar in figure D) and E) is of 15 μm.

When micro-fabricating LCP structures, one of the most desirable goals is to preserve the liquid crystalline order and the alignment of the RMS and, consequently, their optical properties (i.e. birefringence and optical axis) after the 2P-DLW process. A first easy evidence of this is obtained by looking at the cylinders with a polarizing optical microscope between crossed polarizer-analyser. The Figure 2.13 D and E report the microscope pictures of four cylinders at 50X magnification with the rubbing direction oriented at 0° and 45°, respectively, with respect to the polarizer.

The fact that the cylinders appear dark at 0° and bright at 45° proves that i) the photo-polymerized microstructures are birefringent and ii) their optical axis is oriented along the rubbing direction as one would expect for the calamitic nematic LC. Moreover, considering

that the cylinders are photo-polymerized with two values of laser power and scan speed, the different colours of Figure 2.13 E (from green-yellow to orange) can be explained in term of different voxel heights, thus optical phase retardations ($\propto h\Delta n/\lambda$). Using a Berek tilting compensator, we could quantitatively determine the retardation for each cylinder and, provided that their heights h have been independently measured, we can derive the birefringence Δn (Figure 2.13 B). I have found very similar values for all the cylinders (Δn 0.19 ± 0.03), which are on the higher side of the nominal Δn for RMs03-001C (0.155 ± 0.005), considered for a 2 μm aligned film polymerized with unpolarized UV-light.

This result demonstrates the possibility to create three-dimensional solid objects showing optical properties typical of liquid crystals and features well below the diffraction limit. As such, we realized a matrix of cylinders having a 2 μm thick shell and a tetrahedral grating scaffold printed inside, at different values of laser power and scan speed. By profilometry and AFM analysis, we verified that the new set of structures preserved the outer cylindrical shape and dimensions. Moreover, the optical images in transmission mode (Figure 2.14 A) show the tetrahedral grating inscribed in the cylinder and its diffractive nature. Between crossed polarizers (Figure 2.14 B), is observed their birefringence, at 45° with respect to the rubbing (bright position).

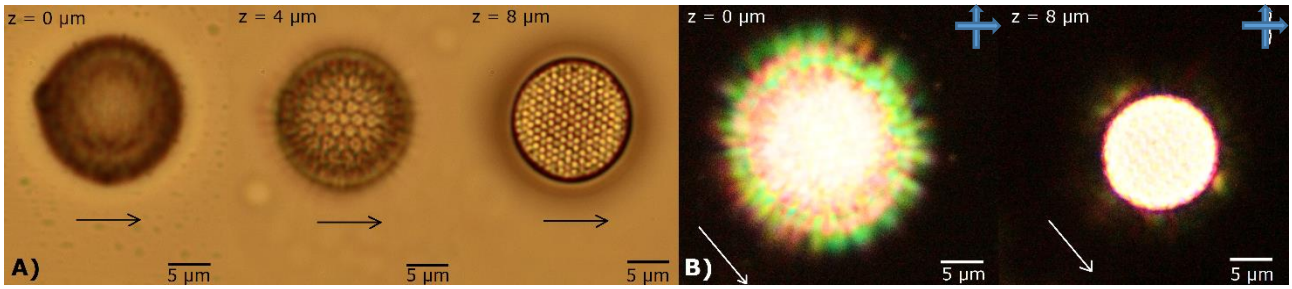

Figure 2.14: Cylinder of 15x15x8 μm^3, with 2 μm shell thick and tetrahedral scaffold, observed in transmission mode: **A)** at different focus position, **B)** between crossed polarizers. The cylinder is created at 20 mW and 4000 μm/s, the diameter of each scaffold is 600 nm, which allows the diffraction of light.

2.2.2 TP-DLW effects on birefringence

The analysis on the birefringence of the microstructures suggests that TP-DLW process interferes with the order parameter of the RMS, since the actual Δn is higher than the nominal one. In other words, during the printing process the laser beam confers an enhanced order to the molecules involved in the photo-polymerization, which could be caused by the linear polarization of laser (parallel to the rubbing) and/or the hatching direction (i.e. the direction of the single lines).

The following experiments have been performed with the aim of discerning the physical phenomenon involved in enhanced birefringence. Considering that the optical axis of the RMs depends on the rubbing direction, I printed different cylinders (laser power 17 mW @ scan speeds 4000-10000 μm/s, step 2000 μm/s) at different angles between the rubbing and the polarization of the laser beam, from 0° to 90° (step 30°) still keeping the single lines parallel to the rubbing direction. However, all the structures exhibit comparable birefringence values, therefore the role of the light polarization has been ruled out.

Vice versa, interesting results were found by changing the angle between the rubbing and the hatching direction. In order to avoid the effect of the superimposed slices, a single layer was written, with lines at four different angles with respect to the rubbing direction (0°, 30°, 60°, 90°). Four arrays of these circles were printed at the same laser power value 17 mW and scan speeds ranging from 4000 μm/s to 10000 μm/s, at step of 2000 μm/s. In figure 2.15 A is shown the scheme of the matrix. Five of these matrices were printed, which differ by the distances between the hatching lines, from 200 nm to 1 μm, with step of 200 nm.

In figure 2.15 B-E, the matrix of circles having hatching 200 nm and 400 nm are shown between crossed polarizers, at 0° (dark, B and D) and 45° (bright, C and E) with respect to the rubbing direction. At the smaller hatch=200 nm, independently of the hatching direction, the circles have the same brightness at 45° (Figure 2.15 C). The latter decreases versus the scan speed, mainly because the height of the voxel reduces at lower energy dose. However, at higher hatch = 400nm the brightness at 45° (Figure 2.15 E) changes even for the circles printed at the same scan speed, decreasing versus the angle between the hatching and the rubbing direction.

Indeed, the structures hatched with lines parallel (0°) to the rubbing direction appear brighter than the ones hatched at 30°, as well as at 60°, with the ones hatched at 90° being the dimmest. Through AFM analysis, I verified that the height of the structures do not depend on the hatching angle. Being the height of the lines constant, this evidence supports that the birefringence diminishes by increasing the hatching angle with respect to the rubbing direction up to 90°. Nevertheless, the optical axis of all these structures remains always parallel to the rubbing direction.

On the other hand, the circles hatched at 600 nm, besides being overall dimmer than previous ones, present a different behaviour. When rubbing direction is parallel to the polarizer (Figure 2.15 F) the circles whose stripes were written at 30° and 60° appear brighter than those at 0° and 90°. The opposite occurs when the sample is rotated with the rubbing direction at 45° with respect to the polarizer (Figure 2.15 G). These evidences suggest that, at higher hatching values, the optical axis of the structures deviates from the rubbing direction and is influenced by the hatching lines.

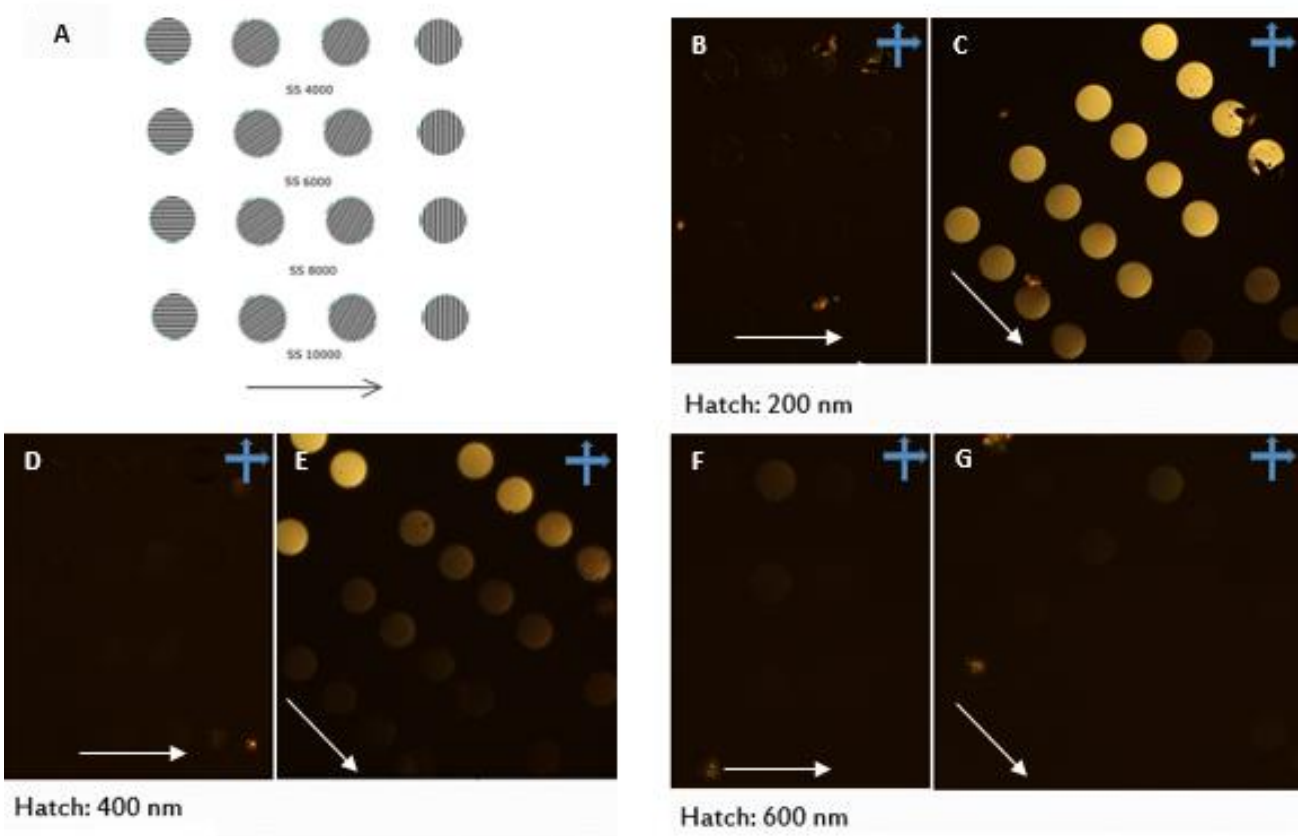

Figure 2.15: Optical images between crossed polarizers at 0 and 45° of arrays of 1D circular gratings written at laser power 17 mW @ scan speed ranging from 4000 μm/s, to 10000 μm/s. Each arrays is composed by gratings made of segments parallel to the rubbing direction, or inclined at 30°, 60°, 90°. **A)** Scheme of each matrix printed; the vector in the bottom indicating the rubbing direction. Matrices were printed @ hatching of **B-C)** 200 nm, D**-E)** 400 nm, which present homogeneous birefringence, and F**-G)** 600 nm. At 600 nm of hatching, dark e bright condition are not the same for each gratings, with 0° being the brighter condition for the grating printed at 30° with the respect to the rubbing direction; 45° the brighter condition for the gratings printed parallel to the rubbing direction.

AFM analysis demonstrates that these phenomena can be ascribed to the effect discussed in paragraph 1.6.2, in which the morphological profile of overexposed 1D gratings was shown. In brief, overexposure of a photo-resist leads to local heating which triggers cross-linking between the surrounding monomers, thus their polymerization. I performed AFM on the circles created at laser power 17 mW @ scan speed 4000 μm/s. Details of the gratings obtained at hatching 400 nm and 800 nm are shown in Figure 2.16. Hatching a structure each 400 nm (Figure 2.16 A) induces local polymerization, between the stripes, thus the formation of a uniform compact disk from which the stripes emerge. Hatching higher than 600 nm, instead, creates single well-defined stripes (Figure 2.16 B).

Quantitative results for gratings created with hatching 400 nm and 800 nm are shown in Table 2.1. Gratings created @ hatching 400 nm are high 270-400 nm, with the smaller being the one whose stripes are perpendicular to the rubbing direction. All the gratings are compensated at 135° and shows birefringence of ~ 0.2. Gratings with hatching of 800 nm, instead, are considerable smaller, with their height of 140-150 nm and show different angles of compensation: 135° for the grating parallel and perpendicular to the rubbing direction, and 175° for the ones created at 30° and 60° in respect to the rubbing direction. Moreover, the grater the angle between rubbing and writing directions, the smaller the birefringence Δn of this second set of structures.

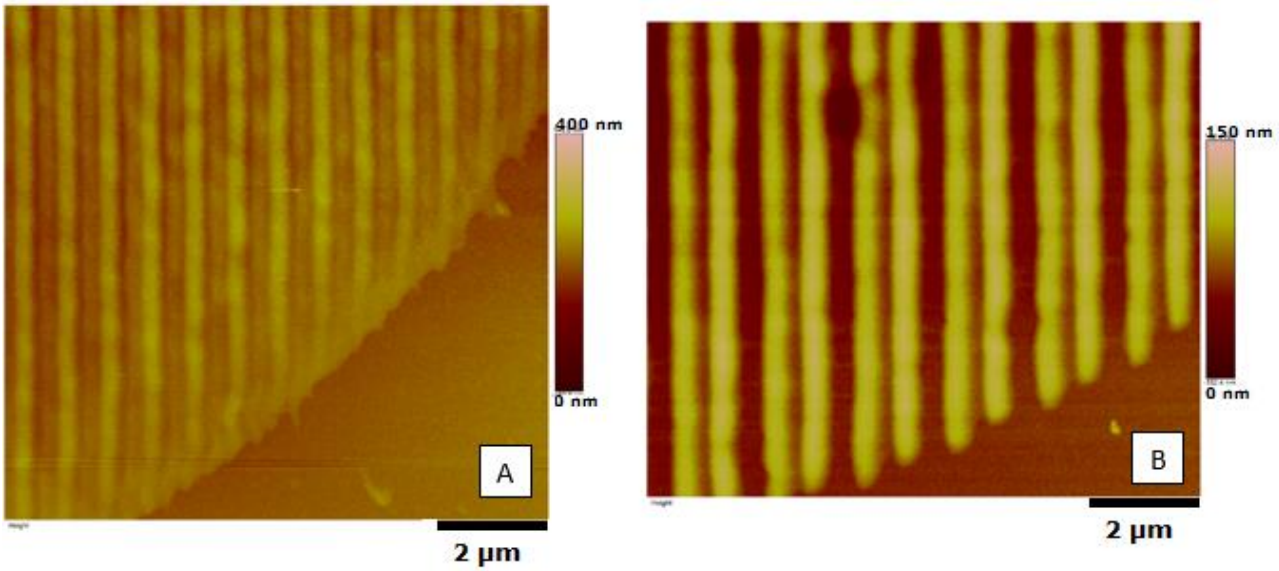

Figure 2.16: AFM profile of an edge of 1D gratings written at 17 mW @ scan speed 4000 µm/s, and hatching of **A)** 400 nm and **B)** 800 nm. While in the latter case a grating is obtained, the former is a compact structure with no effective separation between single segments.

Rubbing direction: 0°						
Hatching (µm)	Scan Speed (µm/s)	Writing direction (°)	Dark condition (°)	Compensation angle (°)	Heigth (nm)	Δn
0,4	4000	0	0 – 90	135	380	0,211
		30	0 – 90	135	400	0,200
		60	0 – 90	135	350	0,206
		90	0 – 90	135	270	0,207
0,8	4000	0	2 – 92	137	145	0,207
		30	35 – 125	170	145	0,234
		60	45 – 135	180	148	0,020
		90	-2 – 88	133	142	0,000

Table 2.1 Analysis on two different arrays of gratings with hatching 400 nm and 800 nm, written at laser power 17 mW @ scan speed 4000 µm/s. Gratings at hatching of 400 nm show identical behaviours; the ones at hatching of 800 nm are smaller, compensated at different angles and the birefringence of gratings written at 60° or more, with respect to the rubbing direction, is suppressed.

This characterization was mandatory to define the behaviour of RMS during TP-DLW. In fact, according to the chosen hatching, the created structures can be either compact or woodpile-like. In the first case, writing direction does not interfere with the internal structure of the LC, imposed by the aligning surface. In fact, as specified in the first chapter, TPA is a non-linear optical process whose duration is in the order of 10^{-15} s, responsible of the excitation of the RMS and the local heating.

After the photo-absorption, the molecules link together reproducing the CAD model and then relax. When all the volume of the model is involved in this process, molecular cross-links follow the internal order and the final structure shows an optical axis depending on the rubbing direction. Vice versa, in single stripes the strong anisotropy of the excited volume favours cross-links along the stripes, competing with the alignment imposed by the rubbing direction. Consequently, single layer gratings created with stripes perpendicular to the rubbing direction @ hatching larger than 600 nm do not present birefringence.

Summarizing, the birefringence of objects created by TP-DLW in RMS can be tuned by proper choice of hatching distance and orientation with respect to the rubbing direction. Moreover, it is important to stress that since writing direction can induce an internal order on the cross-links, objects created with isotropic photo-resist can shows birefringence. To verify this point, I created, in IP-Dip, IP-L 780 and IP-S, being all of them isotropic photo-resists, 3D pairs cylinders (diameter: 50 μm, height: 12 μm) made only by verticals stripes or by alternating layers of horizontal and verticals stripes @ different hatching values (from 200 nm to 1000 nm, at step of 200 nm). In Figure 2.17 are shown the optical images between crossed polarizers of the pairs printed with hatching of 400 nm (Figure 2.17 A-B) and hatching of 800 nm (Figure 2.17 C-D). As expected, no birefringence is observed for hatching of 400 nm, but for hatching at 800 nm. In fact, both the cylinders created with hatching of 800 nm reveal four extinction positions starting from 0° and the brightest shifted at 45°, even if by using only vertical stripes (along the y-axis), the cylinder on the left collapsed towards the centre.

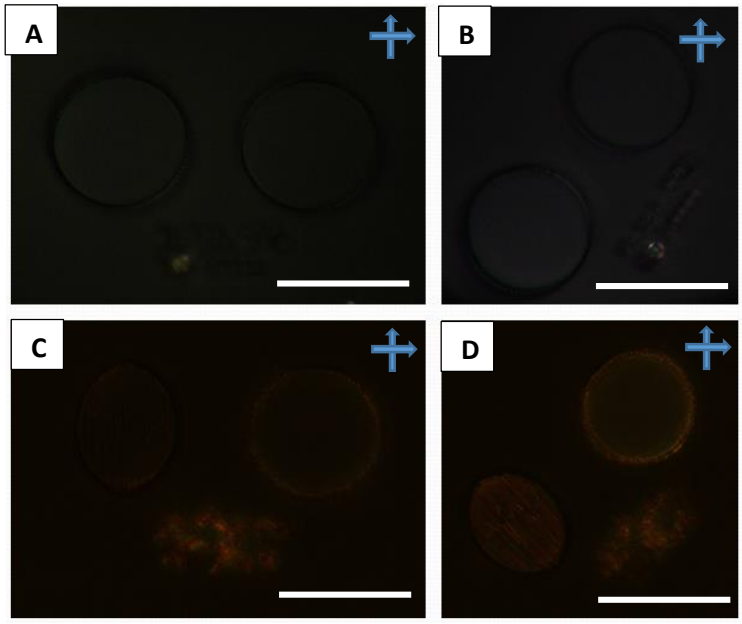

Figure 2.17: Optical images between crossed polarizers of cylinders of 50 μm of diameter and 12 μm high created with IP-L, an isotropic photo-resist. The pairs cylinders are made of vertical segments (on the left) or by alternate layers of vertical and horizontal stripes (on the right). Those created at hatching 400 nm, show no birefringence, when observed at **A)** 0° or **B)** 45°. Vice versa, cylinders created at 800 nm present internal order and show dark condition at **C)** 0° and brighter condition at **D)** 45°. The line bar in the images is of 50 μm.

This analysis, hence, allowed to identify a limit value for the hatching above which, during TP-DLW the alignment imposed by the rubbing is in competition with that imposed by the laser sweep. To maintain the optical properties of a RMS is then mandatory that 3D objects are printed with hatching and slice of maximum 400 nm, in order to avoid the rearrangement of the mesogens.

2.2.3 Photoluminescence in RMs 3D structures doped with dyes

The experiments shown in the previous paragraphs were aimed at elucidating the influence of the TP-DLW on the internal order of the RMs, thus to ensure no variation on the molecular structure during the printing process. This kind of analysis was mandatory if one wants to adapt the properties of LCs to additive manufacturing. Some authors [77-81], in fact, have shown possible applications on different technological fields of solid structures

made in liquid crystalline elastomers (LCE), due to the response of the LCE to the impinging light. In particular, they showed that additive manufacturing of LCE can be adapted to improve micro-robotics. However, until now, scientists did not focused on the possibility to opportunely dope the LCE with the purpose to confer other unique properties to a 3D solid object.

Therefore, I investigated the behaviour of RMs when doped both with dyes and with chiral agents. Dyes have been added with the aim to confer to the solid object photoluminescence in a selected wavelength range; while chiral agents, introducing a cholesteric arrangement in the molecular order of the RMs, pave the way for the realization of 3D structures capable to selectively reflect the incident light.

Combining both properties in a solid object, TP-DWL would allow to realize mirrorless micro-laser of any desired shape and nanometric resolution, since the fluorescent dye in a chiral structure acts like as active medium in a resonant cavity.

In this paragraph, are shown results obtained on additive manufacturing on nematic RMs doped by different dyes, namely: Nile Red (Figure 2.18 A), Rhodamine B (Figure 2.18 B) and Pyrromethene 567, whose extinction coefficient for both single and two-photon absorption at the laser wavelength is low.

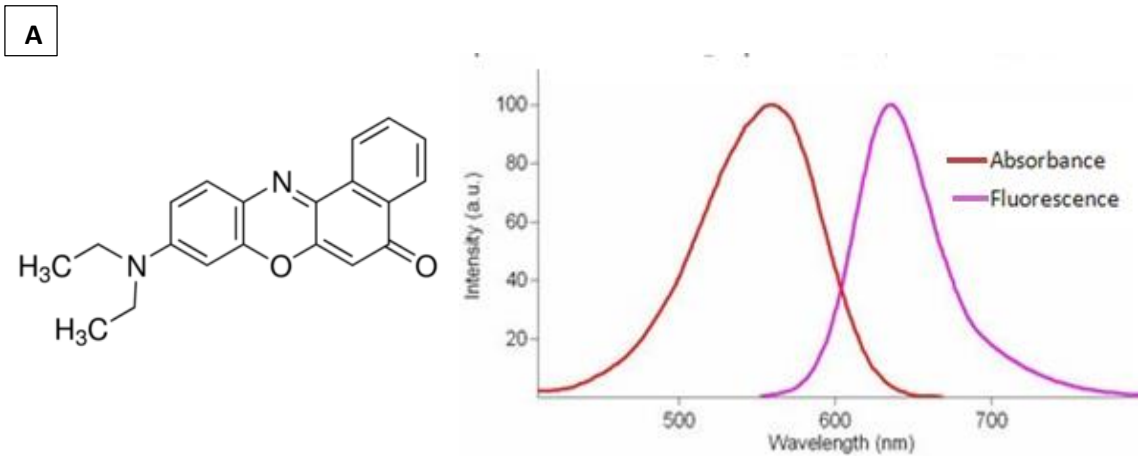

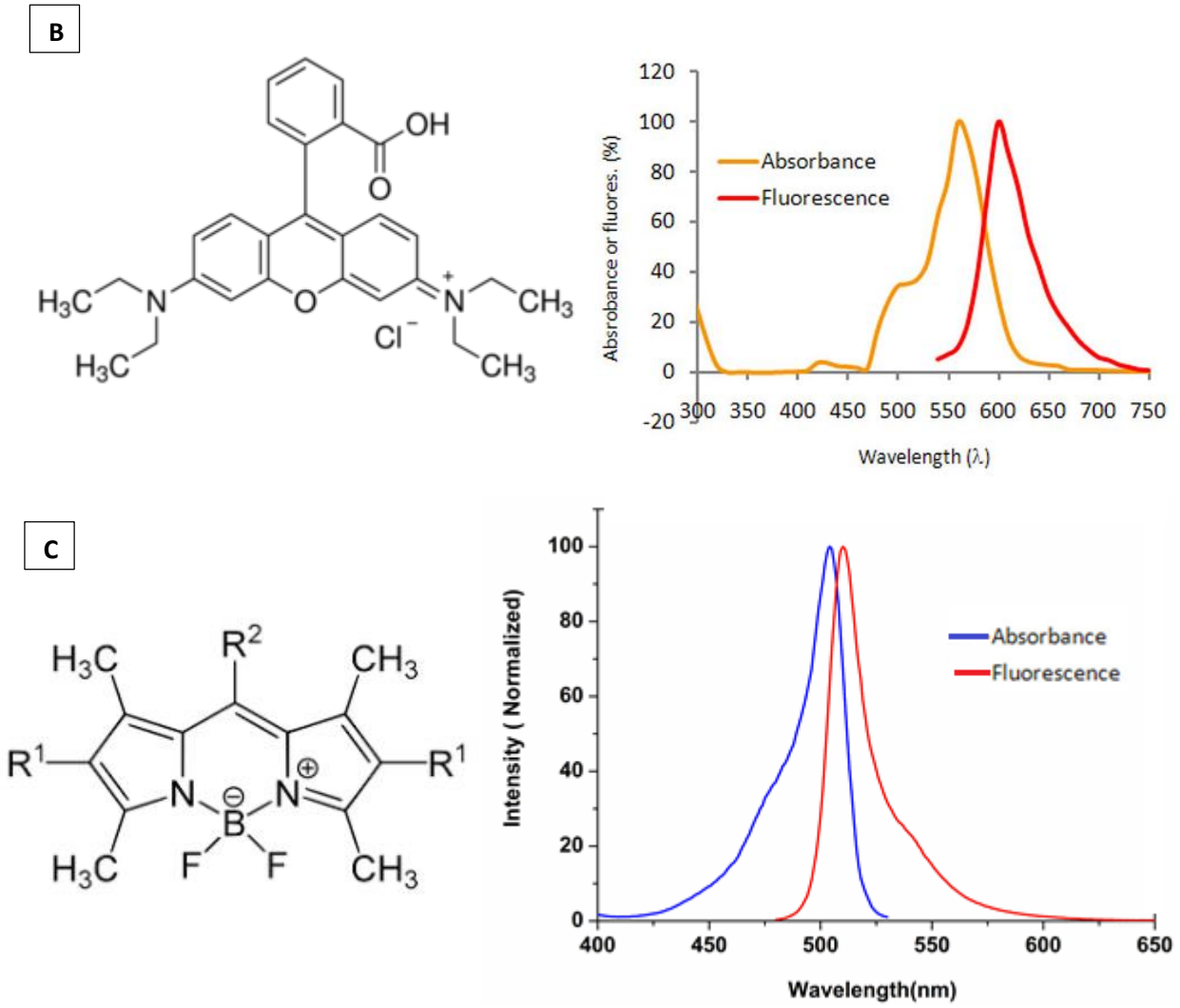

Figure 2.18: Molecular structures and absorbance/fluorescence spectra of **A)** Red Nile, **B)** Rhodamine B, **C)** Pyrromethene 567.

Here, I want to check if dyes withstand the TP-DLW process, remaining in the polymerized RMS matrix without bleaching or being expelled during the cross-linking of RMs molecules.

Therefore, I printed for each mixture a matrix of cylinders (of diameter 50 μm and height 8 μm) at laser power 10-25 mW (step 5 mW) @ scan speed 4 x 10^3 -8 x 10^3 μm/s (step 2 x 10^3 μm/s). The CAD model of the cylinder was sliced each 400 nm, and each layer was hatched with a period of 300 nm, in order to avoid unwanted rearranging of the molecular alignment due to the writing direction. In Figure 2.19 A the optical images of the matrix printed in the mixture doped with nile red are shown.

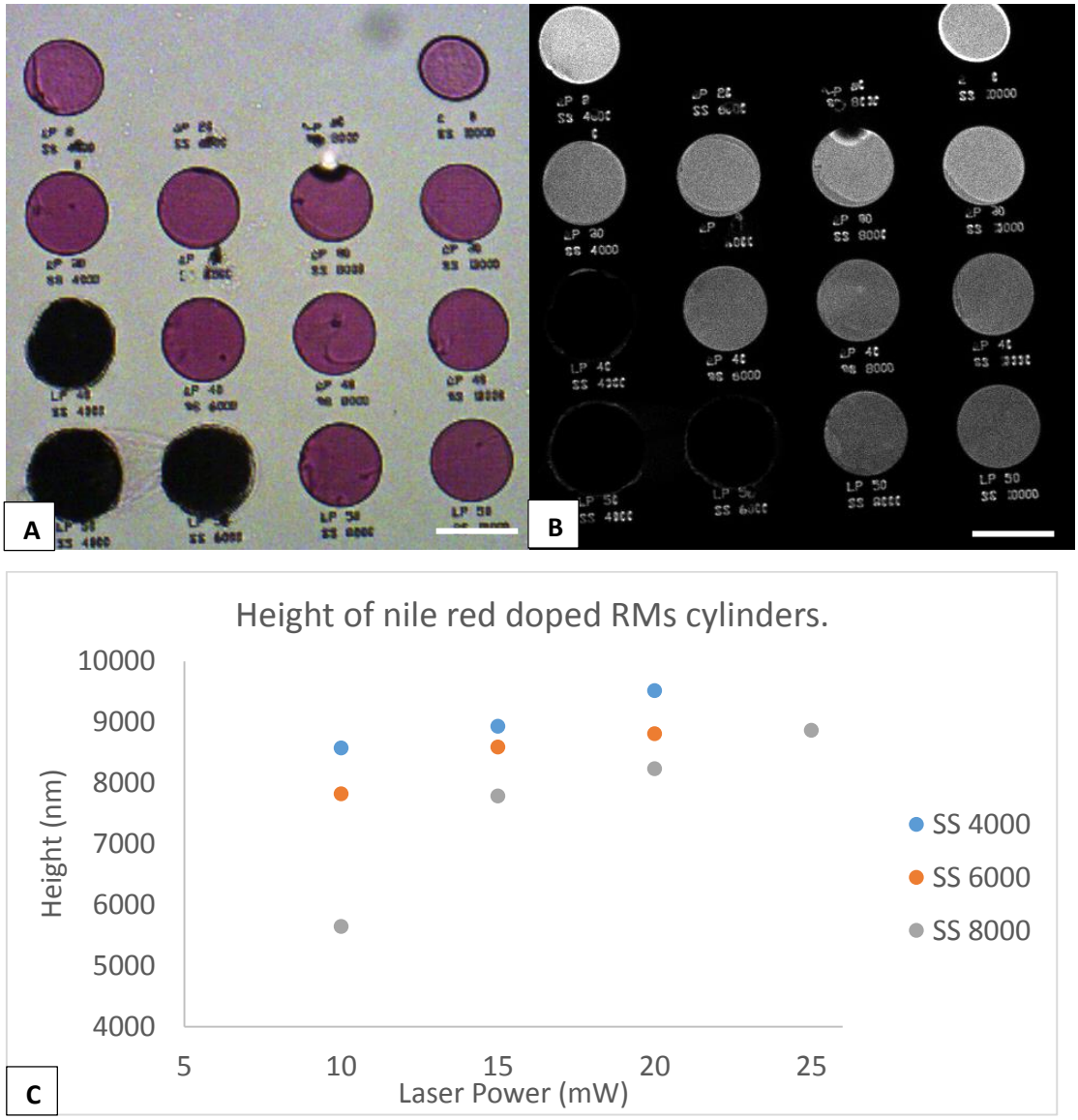

Figure 2.19: Cylinders of nominal diameter 50 µm and height 8 µm, printed at laser power 10-25 mW (step 5 mW) @ ScanSpeed 4 x 10^3 -8 x 10^3 µm/s (step 2 x 10^3 µm/s) printed in RMs01-003 C doped with 5% of nile red. The matrix was analysed through **A)** optical microscopy and **B)** confocal microscopy. The line bar in the two images is of 50 µm. **C)** Cylinders height was measured by means of AFM. No consistent differences in height or shapes is revealed between these cylinders and those un-doped.

AFM and profilometry measurements on the cylinders were performed in order to verify that the presence of dye inside the RMS does not affect the printing quality. No significant difference was observed both for the height and the shape for any dye considered.

Further analysis was performed in order to investigate the fluorescence of the structures, through confocal microscopy (Figure 2.19 B). This technique allows to investigate the luminescence of samples: a laser beam is connected to the microscope and used to excite the samples. Excited molecules of the sample, relax through radiative processes and therefore emit photons of lower energy, thus higher wavelength. An opportune filter is used to cut the excitation light, in order to collect only the radiation emitted by the sample on the detector. Varying the focal plane, it is possible to collect the fluorescence emitted by the sample at different *z*-heights, therefore a 3D reconstruction of the object is obtained.

The cylinders were excited with the 488 nm wavelength of an Argon laser. In Table 2.2 are exposed the fluorescence emission band collected by the different matrices.

Dye	Fluorescence band (nm)
Nile Red	580-625
Pyrromethene 56	550-590
Rhodamine B	565-600

Table 2.2 Emitted fluorescence collected by the cylinders created in RMs doped with different dyes.

The confocal image of the matrices (in Figure 2.19 B is shown the one written in RMs doped with nile red) reveals that TP-DLW in doped material allows to obtain fluorescent structures. However, I observed that the higher the energy dose the lower is intensity of the fluorescence. I ascribe this effect to the local heating generated during TP-DLW of the RMs: increasing the delivered energy dose, the sample reaches higher temperatures, which can degrade the dyes molecules, resulting in a darkening of the structures, as revealed by the cylinder at highest energy in Figure 2.19 A.

It is thus demonstrated that through TP-DLW, it is possible to create 3D objects which maintain both the fluorescence of the dye, and the optical properties of the nematic liquid crystal. Figure 2.20 shows the cylinder printed at 15 mW and 4000 μm/s in the mixture doped with nile red. The optical image of the cylinder reveals uniform pink colour (Figure

2.20 A), thanks to the dye. By confocal microscopy, I observed maximum fluorescence emission at (660 ± 40) nm (Figure 2.20 B). Between crossed polarizers (Figure 2.20 C-D), the cylinder reveals its birefringence, in accordance to the results obtained for the pure nematic structures (Figure 2.5).

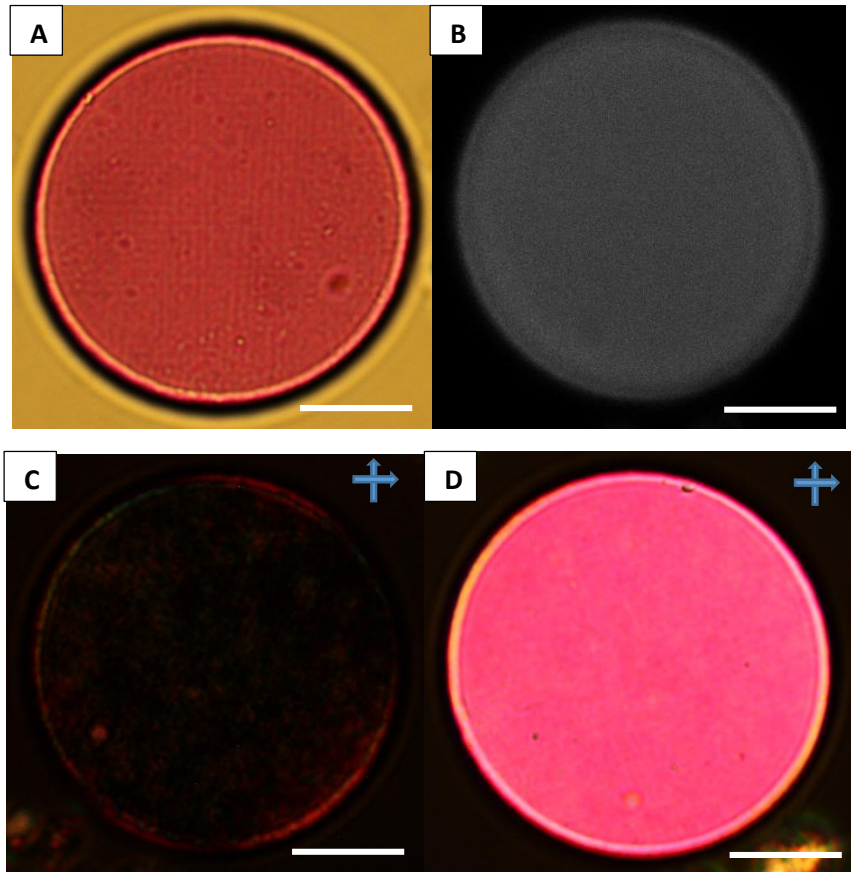

Figure 2.20: 3D cylinder created by doping the RMs with nile red dye, printed at laser power 15 mW and scan speed 4000 μm/s, observed with a 50x objective **A)** through an optical microscope; **B)** confocal microscope, the cylinder is excited with a 488nm laser and shows fluorescence at 620-690 nm; and between crossed polarizers **C)** at 45° respect the rubbing direction, **D)** parallel to the rubbing direction. The line bar in the images is of 15 μm.

It can be concluded, that TP-DLW in dye-doped anisotropic photo-resist preserves both the properties of the photo-luminescent dye and that of the reactive mesogens, provided that the energy dose delivered is not too high. In fact, while higher energy doses favour the fabrication of more compact structures, they may degrade the dye.

2.3 3D Chiral structures

In this paragraph I report the experiments and analysis performed on the 3D fabrication in photopolymerizable cholesteric liquid crystals (CLCs), namely chiral doped nematic RMS. As stated above, doping a nematic LCs with a chiral agent induces a twist in the molecular orientation in the plane perpendicular to the director **n**. This confers peculiar optical properties to the material, as the Bragg's selective reflection of wavelengths comparable with the optical periodicity, corresponding to one half the cholesteric pitch, p.

In order to realize technologically relevant micro-structures, it is mandatory to analyse the effects of TP-DLW on the CLC structure of the chiral doped RMS. In fact, in the homogenously aligned nematic phase I have demonstrated that, when hatching and slicing are larger than voxel sizes, the hatching direction interferes with the pre-aligned RMS affecting both the birefringence and the local optical axis, through the order parameter and the director orientation. One can reasonably expect that similar behaviour happens also in case of TP-DLW in CLC. Therefore, I printed the 3D structures selecting opportune slicing and hatching, in order to maintain the internal order of the CLC.

However, I observed that the pitch of the CLC helix in the photopolymerized structures depends on the energy dose delivered. This experimental finding is a remarkable result, because it implements a never explored feature of TP-DLW, that is the possibility to locally tune the photonic band gap of a 3D object of any shape, with sub-micrometric resolution. In particular, I created a 4D quick response (QR) code, a data storage code usually composed by 69x69 pixels. With respect to standard QR code, the one I created features also height and colour codes, thus two additional degrees of freedom. This property can be exploited in innovative labelling and for a new generation of anti-counterfeiting solutions.

2.3.1 Effects of SPA on chiral RMs

RMs was opportunely doped with a chiral agent (S811, Merck), whose chiral structures is shown in Figure 2.21, and the photo-initiator (Irgacure 2100, 3% in volume).

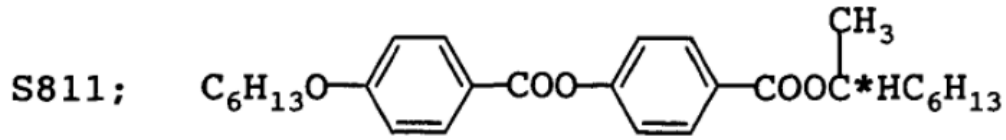

Figure 2.21: Molecular structure of the chiral agent S811.

In order to align the cholesteric reactive mesogen (CRMs) with the CLC helical axis perpendicular to the substrates, it was infiltrated inside cells, made by two standard coverslips (22 x 22 x 0.13 mm^3) treated as indicated in paragraph 2.2, with rubbed PVA film in parallel geometry and separated by polyester spacers 12 μm thick.

According to the concentration of the chiral agent (5%, 6% and 7% in volume), three CLC with different pitches, thus three different reflection bands, were investigated. The first analysis was aimed at verifying that the polymerization process of the material does not affect its liquid crystalline order. Therefore, spectrophotometer measurements were performed on the microstructures after exposure to a UV source (365 nm) for 1 hour, which lead to the total polymerization of the material due to SPA.

Spectra were collected by using the fiber-optic spectrophotometer AvaSpec 2048, connected to a microscope. The light, emitted by a halogen lamp (emission spectra ranging from 300nm to 900 nm), invests the sample and is collected through the fiber and then diffracted, before it arrives on the detector. The Lambert-Beer law defines the fractions of light absorbed or transmitted:

$$T = \frac{I}{I_0} = e^{-\tau} = 10^{-A}$$

Where T is the trasmittance, I_0 and I the light intensity of the source and transmitted by the sample, τ is the optical depth, which depends on thickness and the extinction coefficient of the sample, A is the absorbance.

In Figure 2.22, the transmission spectra of the three mixtures are shown before (coloured line) and after (gray line) UV-induced photo-polymerization, respectively of A) 5%, B) 6% and C) 7% of S811. Increasing the concentration of chiral dopant agent, the pitch decreases, which leads to a blue-shift for the selective reflection (from 820 nm to 630 nm). For all the cases, the UV photo-polymerization induces a further blue-shift, of the order of 10 nm, due to shrinking.

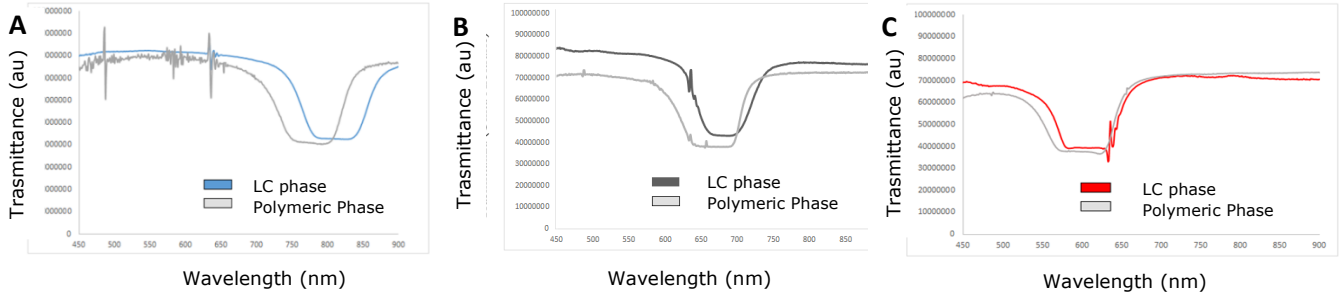

Figure 2.22: Transmission spectra before and after UV photo-polymerization of RMs doped with **A)** 5%, **B)** 6%, **C)** 7% of S811.

2.3.2 Effects of TPA on chiral RMs

From the spectra collected on the three mixtures before and after UV photo-polymerization, I calculated the pitches of the cholesteric reactive mesogens (CRMs), from the selective reflection, obtaining values of 510 nm, 423 nm and 380 nm, for the 5%, 6% and 7% mixtures, respectively. Considering these results, I sliced the CAD model of the cylinders each 400 nm, in order to approximately match the CLC pitches. Matrices of cylinders (diameter: 50 μm, height: 8 μm), were created through TP-DLW in the three cells, containing the three mixtures, at laser power 17.5 mW and scan speed 4000 μm/s.

After the TP-DLW, the cells were mechanically opened and the glasses were soaked in PGMEA for 25 minutes in order to remove the unpolymerized RMS. The samples were

left to dry for 30 minutes, at controlled temperature (23 °C) and humidity (42%) condition. On the dried samples, I analysed the photonic band gaps (PBG) through optical microscope, in reflection mode (Figure 2.23 B-D) and through a spectrometer. In Figure 2.23 A the spectra of the light reflected by the three cylinders are shown, with central wavelength at 630 nm, 520 nm and 460 nm, respectively.

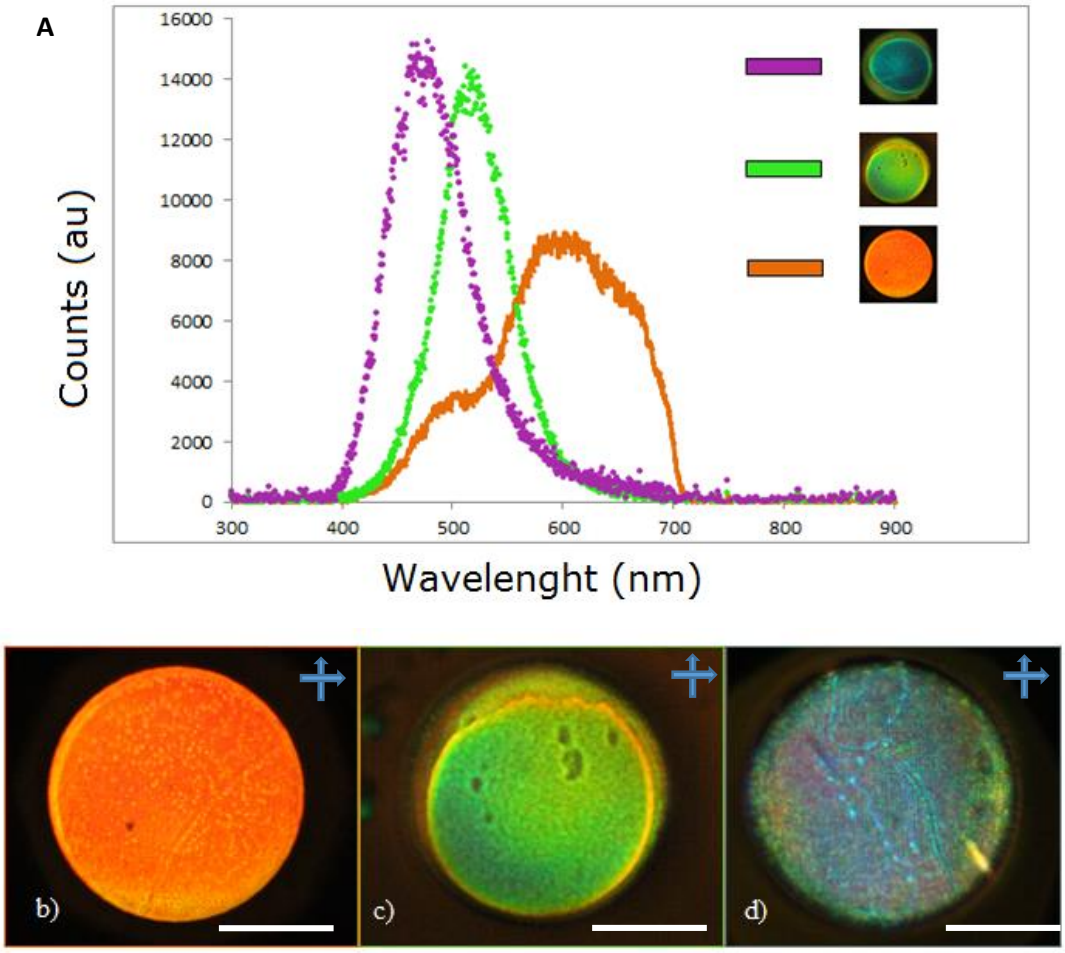

Figure 2.23: A) Reflection spectra of 50x50x8 μm^3 cylinders, sliced at steps of 0.4 μm and hatched each 0.3 μm, at laser power 17.5 mW and scan speed 4000 μm/s. The cylinders were created in RMS doped with 5% (orange line), 6% (green line), 7% (purple line) of chiral dopant agent S811. Optical images, taken with a 100x objective in reflection mode, of the cylinders created at the **B)** 5%, **C)** 6% and **D)** 7%, of S811. The line bar in the images is of 20 μm.

The spectra demonstrate that TP-DLW process does affect the optical properties of CRMs, since a blue-shift is registered for all the three samples, which is even larger than

the one yielded by UV polymerization. From AFM and profilometer images, it was verified that the objects created preserved cylindrical shape and that their sizes are in accordance with the CAD model.

I ascribe the blue-shift to a partial polymerization of the CRMs. As previously observed, a low degree of compactness leads to a partial polymerization of the 3D objects, which shrink after the development. CLCs are characterized by internal helical structure, whose period determines the PBG [171, 187]. To preserve their optical properties in the polymeric structure, or to keep the blue-shift at minimum value (i.e. the one achieved by UV polymerization), the whole CRMs bulk must be fully polymerized. This implies that the voxel depth has to be equal to (or larger than) the slicing, which here is comparable to the helical pitch (i.e. 400nm).

At low values of energy dose, the thickness of the single voxel is reduced, therefore the helix of the CRMs is only partially polymerized and the residual material is expelled during the development. This results in a "truncation" of the effective pitch and, as a consequence, a blue shift of the PBG. A scheme of the process is shown in Figure 2.24.

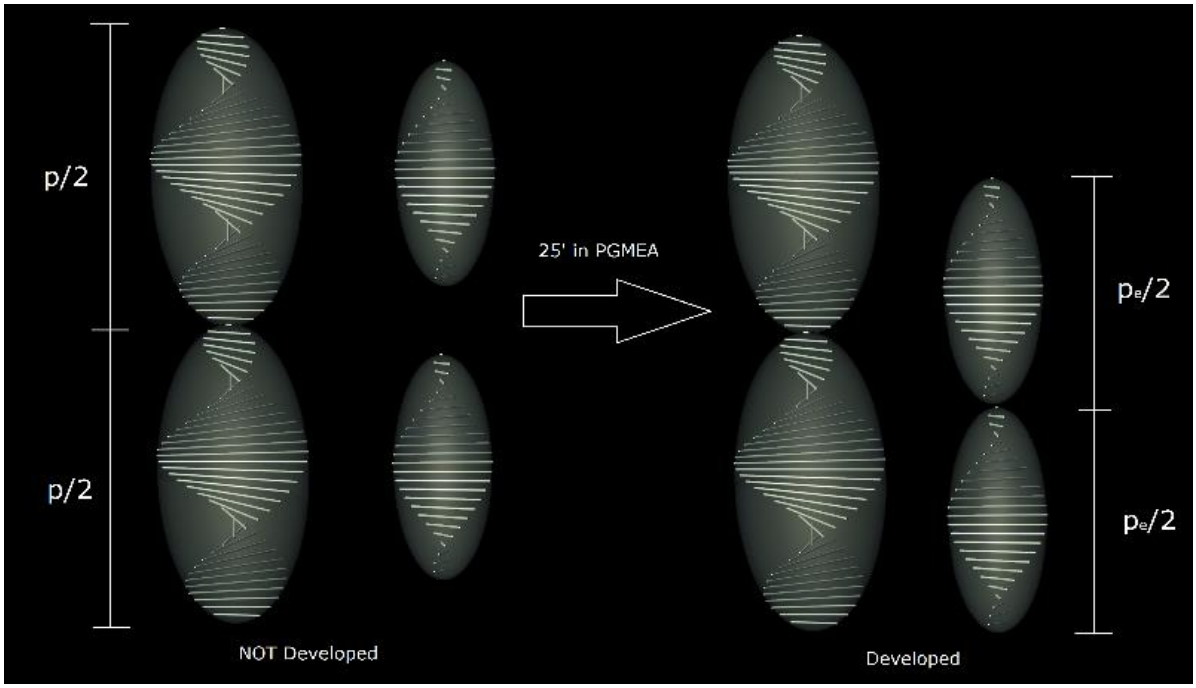

Figure 2.24: Scheme of the "truncation" of the pitch of the chiral helix, during TP-DLW of CRMs. If the voxel length is comparable to half of the pitch (p/2) all the helix is polymerized and

the blue-shift is minimized. Vice versa, if the voxel length is considerably smaller than p/2, after the development in PGMEA, all the un-polymerized material and thus a portion of the helix is removed. As a result, the structures shrink and the effective pitch is truncated, which leads to a blue-shift in the PBG.

To verify this phenomenology, the developing process of a cylinder, printed in a mixture of RMs doped with the 5% of s811, was observed by means of optical microscope, between crossed polarizers (Figure 2.25). A 20X objective was used.

Before the development, no consistent difference between the selective reflection of the polymerized and un-polymerized material is observed (Figure 2.25 A).

After the development, the solvent is still inside of the structures and the cylinder reflects selectively at ~650 nm (Figure 2.25 B). After 30 minutes, the blue-shift observed is of 20 nm (Figure 2.25 D), thus no relevant difference is evident when the sample is still wet.

When the drying process starts, all the non-exposed materials inside the cylinders is removed from the structure and the structure shrinks rapidly generating a consist blue-shift of the PBG (Figure 2.25 E).

During the shrinking the "effective" pitch changes dynamically until the structure is not completely compact. After 24 hours the selective reflection of the cylinder had a maximum at 490 nm, with a blue shift of 160 nm.

When a sample printed in CRMs is completely dry, the PBG is stable: no variations in the selective reflection of the cylinder was observed after six months, or by changing the temperature conditions (from 4° C to 90° C).

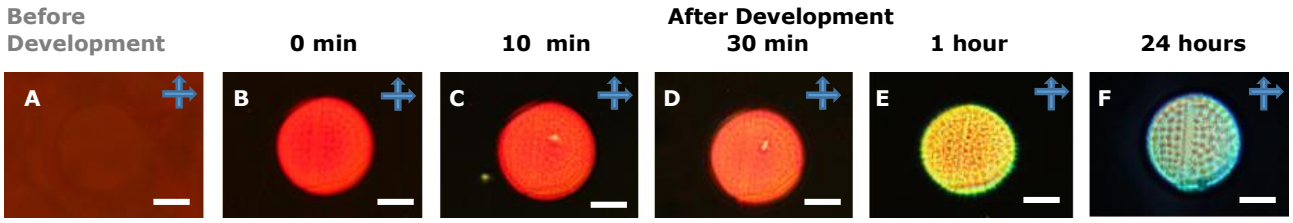

Figure 2.25: Development of a cylinder of (diameter: 50 µm, nominal height: 8 µm, effective height: 6.4 µm). The cylinder was printed with laser power 15 mW @ 8 x 10^3 µm/s. **A)** After the printing, no difference in the selective reflection between the polymerized and the un-polymerized

photoresist is observed. **B)** After the development, the selective reflection of the cylinder is of 650 nm. **C)** After 10 minutes, no variation is observed. **D)** After 30 minutes the blue-shift is of 20 nm. The sample is still wet. **E)** After 1 hour the sample starts to dry and the pitch changes. The selective reflection is of 580 nm. **F)** After 24 hours the shrinking process is complete and the definitive selective reflection of the cylinder is of 490 nm. The line bar in the images is 20 μm.

From the results obtained, it is evident that a smart way to obtain different PBG is to modulate the "effective" pitch by tuning the energy dose delivered during TP-DLW. Thanks to its longer pitch and spontaneous selective reflectance in the NIR, by using a mixture of RMs doped with 5% of S811 one can micro-fabricate objects reflecting all the wavelengths of the visible spectrum.

In Figure 2.26 is shown the example of a matrix of cylinders printed by using different values of laser power and scan speed. Each cylinder shows different PBG, in particular they reflect selectively the light from blue to orange, as the energy dose is increased.

This result is totally in accordance with the model described in figure 2.24 for the TP-DLW of CRMs.

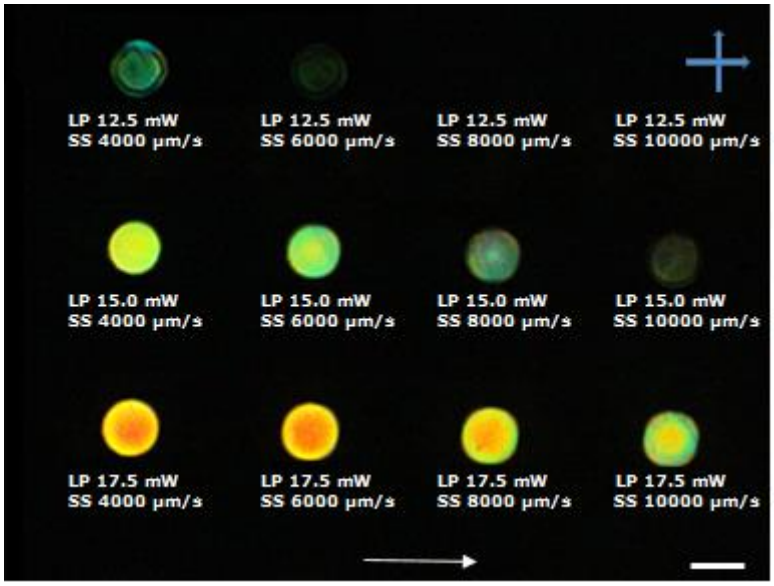

Figure 2.26: Matrix of cylinders (diameter: 50 μm; nominal height: 8 μm) at different value of laser power 12.5-17.5 mW (step 5 mW) @ scan speed 4 x 10^3 -1 x 10^4 μm/s (step 2 x 10^3 μm/s). . The

optical image, taken between crossed polarizers in reflection mode, shows a blue-shift by decreasing the energy dose. The white vector indicates the rubbing direction. The line bar in the image is 50 μm.

In order to establish the dependence of the blue-shift on the printing parameters, a statistical analysis was performed. I printed two arrays of cylinders:

- for the first one, I fixed the scan speed (4×10^3 μm/s) and tuned the laser power from 14.0 to 18.0 mW.
- For the second one, I fixed the laser power (17.5 mW) and tuned the scan speed from 4×10^3 μm/s to 1.2×10^4 μm/s, step 1×10^3 μm/s.

In Table 2.3, quantitative results are shown. The PBG of the cylinders, whose emission spectra is shown in Figure 2.27 A and C, had maximum wavelength ranging from 570 nm to 470 nm, and bandwidth of 90-150 nm. It is relevant to underline that the bandwidth narrows by increasing the energy dose (i.e. high values of laser power, or low values of scan speed). Thus, higher polymerization degrees generates sharper PBGs.

In Figure 2.27 B and D the dependence of the PBG on the printing parameter are shown.

Cylinders written @ Scan Speed 4×10^3 μm/s			Cylinders written @ Laser Power 17.5 mW		
Laser Power (mW)	Wavelength (nm)	Band width (nm)	ScanSpeed (μm/s)	Wavelength(nm)	Band width (nm)
14.0	500	90	4000	580	90
14.5	510	120	5000	550	100
15.0	520	100	6000	540	120
15.5	540	90	7000	535	110
16.0	545	90	8000	520	120
16.5	540	130	9000	510	130
17.0	545	130	10000	515	120
17.5	555	140	11000	490	120
18.0	560	150	12000	470	120

Table 2.3: Wavelength and band width of the emission spectra collected by two arrays of cylinders (diameter: 50 μm; nominal height: 8 μm) printed @ scan speed 4×10^3 μm/s and laser power 14-18 mW, and @ scan speed 17.5 mW

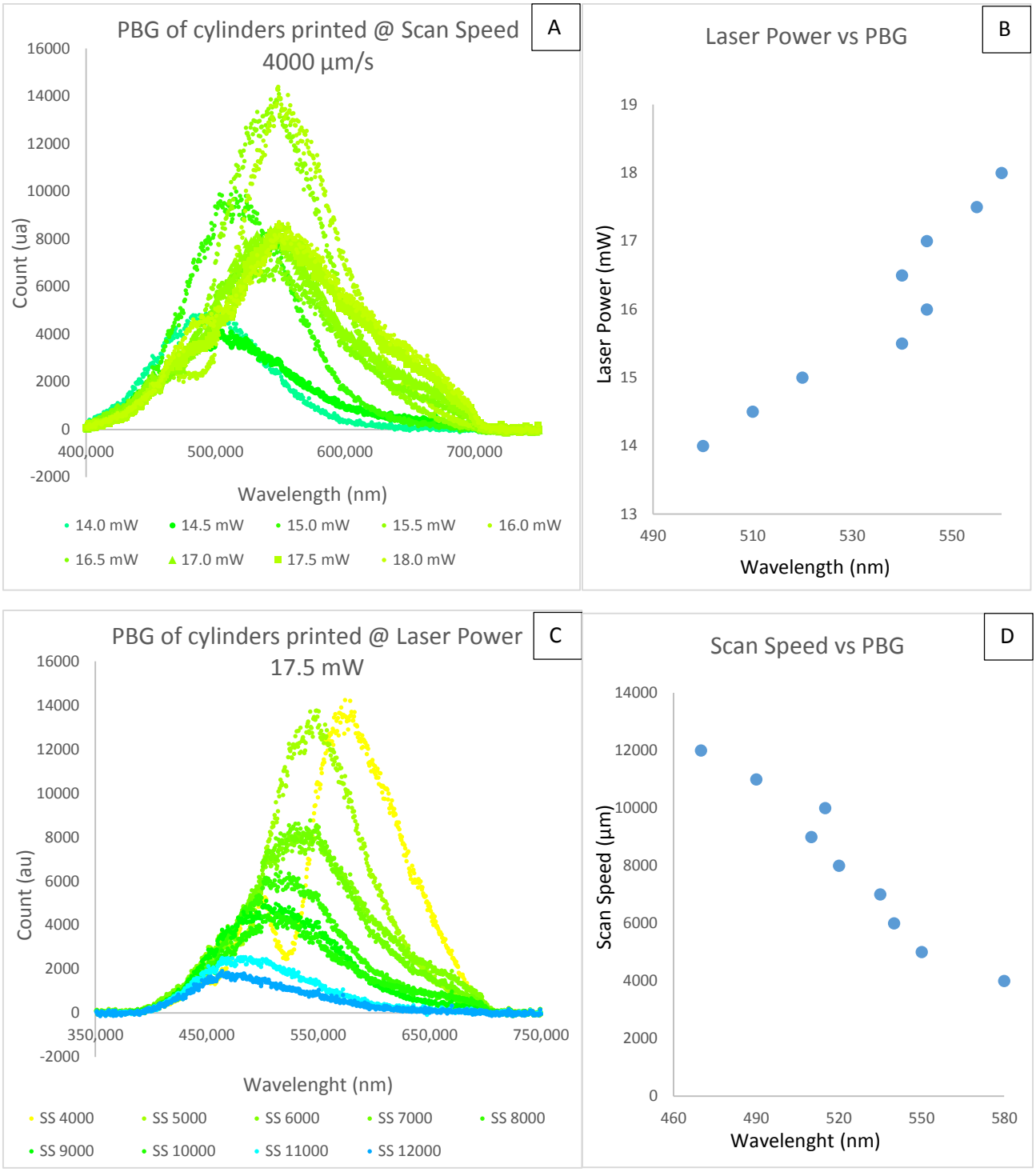

Figure 2.27: **A)** Emission spectra obtained on the array of cylinders created @ scan speed 4 x 10^3 µm/s and laser power changes from 14.0 to 18.0 (step 0.5) mW. **B)** Dependence of the PBG on the laser power. **C)** Emission spectra obtained on the array of cylinders created @ laser power 17.5 mW and scan speed ranging from 4 x 10^3 µm/s to 1.2 x 10^4 µm/s (step 1 x 10^3 µm/s). **D)** Dependence of the PBG on the scan speed. The cylinders were created in RMs03-001C, doped with 3% of Irgacure 2001 and 5% of S811. The colours in the graphs are related to the maximum wavelength of each spectra.

The analyses performed allow tuning the selective reflection of the printed objects, as a function of the delivered energy dose. By changing the energy dose during the fabrication process, one can obtain a 3D "multi-coloured" micro-object.

This result is extremely interesting under a technological point of view, since it leads to the possibility to create new highly sophisticated anti-counterfeiting and data storage systems. At this purpose, I considered the technology behind a quick responsive (QR) code, which is a bi-dimensional bar code made by 29 x 29 pixels. TP-DLW of a QR code in isotropic photo-resist allows to add a third dimension to the system, thus to fabricate a 3D QR code, with a resolution down to 100 nm.

However, fabricating the QR code in CRMs, by using different energy values, allows the addition of a "colour-code" to the QR. The 3D micro-object obtained can be considered a four-dimensional (4D) barcode, hardly falsifiable and that can contain a larger amount of data in less than 100x100 μm^2.

In Figure 2.28 A is shown the model of QR that I printed. From this image, I generated a CAD model of size (100x100x4) μm^3, and printed it in the mixture of RMs doped with 5% of S811. I used laser power 14 mW @ scan speed ranging from 3.5 x 10^3 μm/s to 7.5 x 10^3 μm/s, in order to tune the height and polymerization degree of different pixels.

As a consequence, the AFM imaging of the QR (Figure 2.28 B) reveals that different features have height ranging from 3.2 μm to 4.0 μm, with resolution of 0.2 μm, thus different polymerization degree. Therefore, the optical image of the 4D-QR (Figure 2.28 C-D) reveals that the PBG of the pixels is tuned from 490 nm (smallest pixels) to 600 nm (highest pixels). Four different PBGs are clearly distinguished.

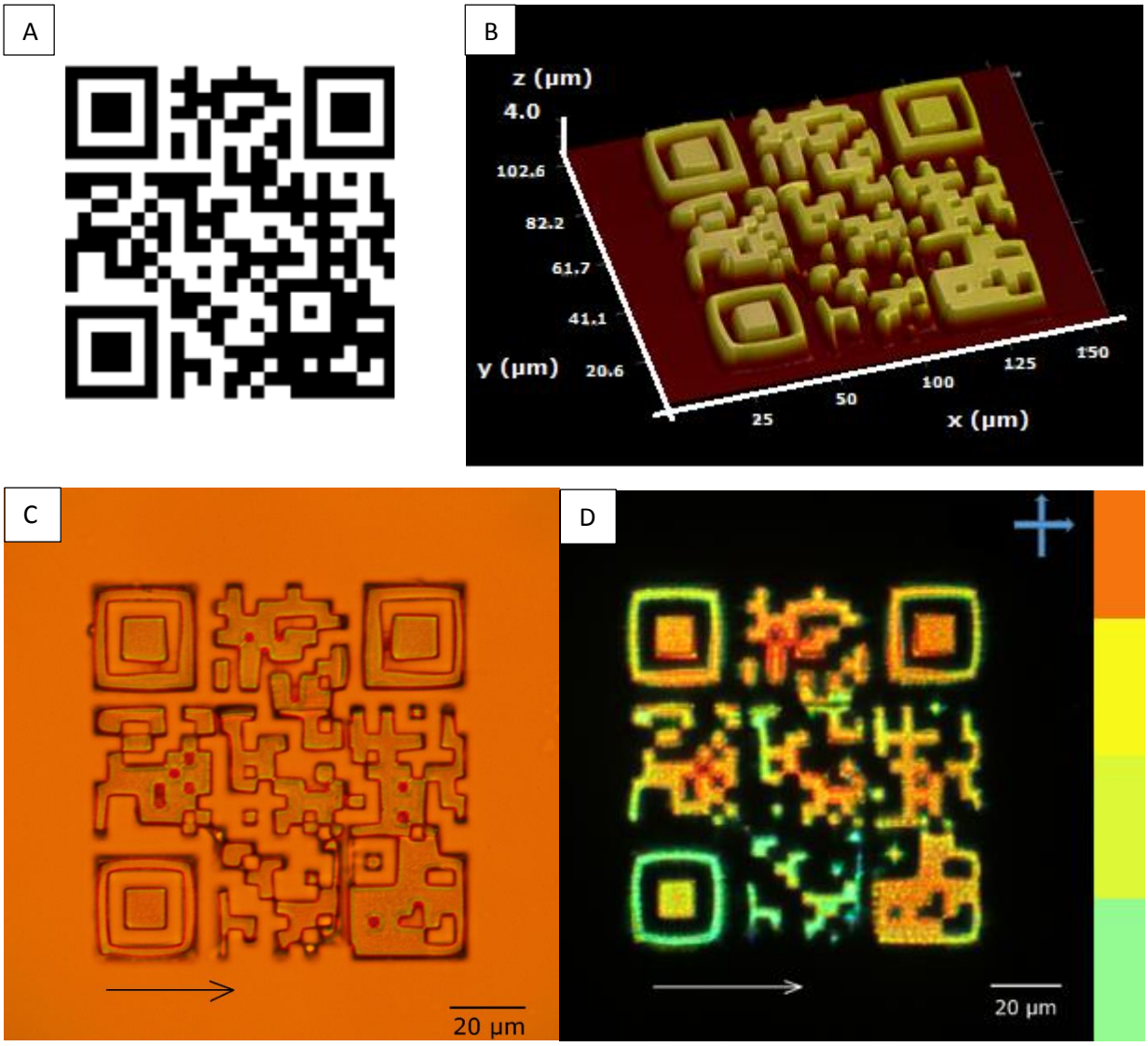

Figure 2.12: A) Model of the bi-dimensional QR code. The model was split in 500 nm layers and hatched with 300 nm thick lines and printed in a solution of RMs doped with 5% of S811 at 14 mW @ scan speed ranging from 3.5 x 10^3 µm/s to 7.5 x 10^3 µm/s. **B)** AFM image of the micro-fabricated QR code. Due to the different values of scan speed used, the height of the different areas differs of few hundred nanometers. **C)** Optical image, in transmission mode, of the 3D QR code. **D)** In reflection mode, between crossed polarizers, the chiral structures the selective reflection of different colours, according to the scan speed used to create each part of the code, thus revealing a colour code.

In conclusion, I demonstrated the possibility to micro-fabricate 3D chiral structures, by additive manufacturing in CRMs. Tuning the energy dose delivered during TP-DLW, the helical internal structure of the CRMs can be fully or partially polymerized. In the latter

case, during the development of the sample, all the un-polymerized parts of the helix are removed: as a consequence the structure shrinks and the PBG is blue-shifted.

This result indicates that TP-DLW can be used to tune the selective reflection of 3D objects created in CRMs. Thus, multi-colour micro- and nano-fabrication is achieved, paving the way to new technologic fields. E.g. I micro-fabricated a new anti-counterfeiting system: by printing a QR code, with different energy dose. In result, it presented features with different heights and reflection bands.

I implemented, in this way, a four-dimensional barcode, whose chiral optical properties can guarantee a colour fingerprint, impossible to replicate with other techniques.

3 Optical control of metal nanoparticles created by photo-reduction of metal precursors through TP-DLW

3.1 Two-photon photo-reduction (TPPR) of metal precursors in polymeric matrix

In the previous sections, I discussed about the physical processes behind the additive manufacturing through TP-DLW with the aim to optimize the whole process. As stated in the introduction, combining TP-DLW with advanced materials, smart 3D objects with intriguing mechanical and optical properties can be created. In the last decade, a number of authors investigated the possibility to include metallic details in polymeric structures or even to create completely metallic structures, paving the way for the realisation of metallic/polymeric nano-composites with this technique. TP-DLW can be employed to directly print patterns rich in noble metal nanoparticles, in polymeric matrices containing a photo-sensitive metal precursor [128, 190]. However, beyond the bare photo-chemistry, the physical processes governing the nanoparticles growth and aggregation remained unconsidered until now. Some authors were able to get control on size, shape and density of photo-created NPs by adding surfactants to the solution, to inhibit the apparently random growth of NPs, but a physical modelling is still missing [113, 129-132].

I performed a series of experiments to elucidate the physics involved in TPPR. I tested different metal precursors to work with TP-DLW, namely: silver nitrate ($AgNO_3$), copper chloride ($CuCl_2$), nickel(II) chloride ($NiCl_2$) and tetrachloroauric acid ($HAuCl_4$). However, the analyses showed in the following concern only the gold precursor, on which I put my attention due to the extensive fields of applications in which GNPs are required.

Tetrachloroauric acid ($HAuCl_4$) is the most common precursor used to optically synthetize gold nanoparticles. In fact, gold in tetrachloroauric acid can be photo-reduced by ultraviolet irradiation [189] and thus by two-photons absorption of infrared light [128]. The photo-reduction reaction [189] is briefly described below.

$$(Au^{3+}Cl_4)^- + h\nu \rightarrow (Au^{3+}Cl_4^-)^* \quad (3.1)$$

$$(Au^{3+}Cl_4^-)^* \rightarrow (Au^{2+}Cl_3^- \ldots Cl) \quad (3.2)$$

$$(Au^{3+}Cl_3^- \ldots Cl) \rightarrow (Au^{2+}Cl_3)^- + Cl \quad (3.3)$$

$$2(Au^{2+}Cl_3)^- \rightarrow (Au^{3+}Cl_4)^- + (Au^{+}Cl_2)^- \quad (3.4)$$

$$(Au^{+}Cl_2)^- + h\nu \rightarrow Au^0 + Cl^- + Cl^0 \quad (3.5)$$

$$nAu^0 \rightarrow (Au^0)_n \quad (3.6)$$

In the first step (3.1), the single or double photon absorption leads to the activation of the tetrachloroauric ions. As for the organic photoresist, the excited molecule may lose its energy through radiative (fluorescence) or non-radiative (local heating) processes, thus relaxing to more stable states (3.2-3.4).

The photo-reduction of $(Au^{+}Cl_2)^-$ (3.5) has been estimated to occur slower than the photo-reduction of $(Au^{+}Cl_4)^-$ [190]. However this process, involving electronic transitions, is several orders of magnitude faster than the laser pulse duration (typically 10^{-15} s vs 10^{-3} s); $(Au^{+}Cl_2)^-$ ions reiterate the TPA process and the Au^+ is photo-reduced in Au^0. TP-DLW of tetrachloroauric acid allows then the nucleation of seeds of gold, inside to the virtual voxel, which I define as the fraction volume of the laser focus figure in which the TPA threshold is reached. The seeds grow through autocatalytic reduction of the surrounding ions [241] and a gold nanoparticle (GNP) is created (3.6). It is important to stress that while the nucleation occurs typically in 10^{-13} s, the growth of gold nanoparticles is extremely slower, as it depends on diffusive phenomena. In fact, gold seeds diffuse and aggregate to generate larger nanoparticles. A second source of growth is obviously given by the chloroauric ions which diffuse from the solution surrounding the nanoparticle and are reduced on its surface by autocatalysis [189, 241]. The first process is ruled by the available seeds and is much slower than the latter. Moreover, the seeds are created only inside to the virtual voxel, a volume negligible with respect to the volume of the system. Therefore, the growth for auto-aggregation of the seeds is forcedly very limited. On the contrary, the number of ions available in the system can be considered unlimited with respect to the number of seeds.

For this reason, it appears logical try to manage and exploit the ionic diffusion in order to get a control on the growth process of GNPs created through TP-DLW.

Samples were prepared as follows: a solution (7.35 mM) of tetrachloroauric acid tetrahydrate ($HAuCl_4 \cdot 3H_2O$) and (18.06 mM) of polyvinyl alcohol (PVA, molecular weight: 13.000–23.000 g/mol), in Milli-Q water (18.2 MΩ cm) was prepared. In this system PVA acts as a passive polymeric matrix to trap the GNPs created, thus limiting their uncontrolled diffusion. I chose PVA because it is water soluble, it is not absorbing under UV or IR irradiation (black curve in Figure 3.1), it can be heated up to 230°C without damages.

The mixture presents an absorption peak centred at 400 nm and practically no absorbance is registered above 500 nm (blue line in Figure 3.1). Therefore, it is compatible with the TP-DLW system used.

Samples were prepared under the laboratory conditions, at controlled temperature (22 ± 1 °C) and humidity (45% RH), by drop-casting 50 μL of gold solution on a coverslip, corresponding to 70 mg. The drop is left to dry over 1 hour and half, until only 0.4 mg of solution are left on the glass substrate. At this point, the film composition is: 42% in weight of tetrachloroauric acid, 5.5% of PVA and 52.5% of deionized water. The obtained film thickness, measured by the AFM profile of a scratch, is in the order of 1.5 μm.

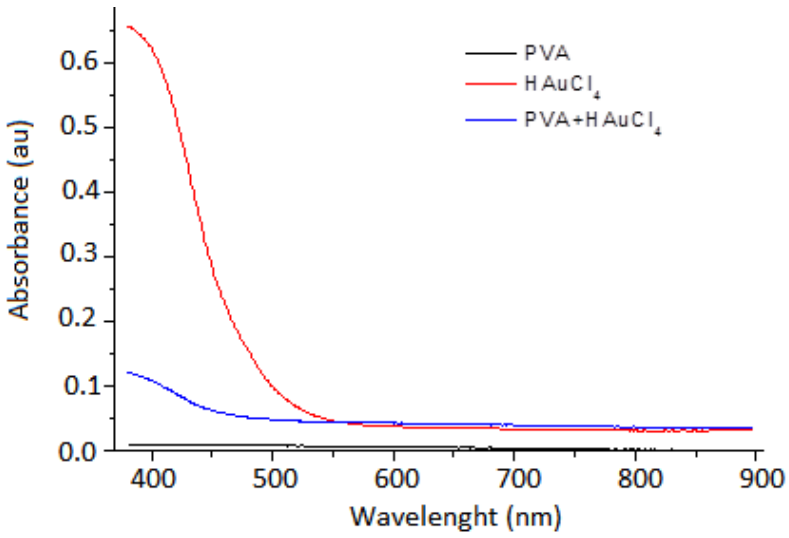

Figure 3.1: Absorption spectra of dried films of: gold-doped PVA (blue line), $HAuCl_4$ (red line) and PVA (black line). The absorption band, confirms the sensitivity of gold-doped PVA to the 2P absorption process induced by the 780 nm laser beam, due to the gold ions.

Because of the TPA, as in the case of organic photo-resist, the photo-reduction process happens on a very thin surface layer, whose thickness is defined by one half of the virtual voxel, close to the glass substrate. Swiping the laser on the surface results in the creation of stripes of GNPs, allowing to *draw* patterns made by segments rich in gold nanoparticles.

However, as discussed in the previous paragraph, for organic photo-resist, a control on the geometrical features of the single segment is mandatory to obtain high-quality additive manufacturing.

3.2 Voxel characterization of two-photon photo-reduced gold nanoparticles (GNPs)

The aim of my experiments was to analyse and improve the direct laser writing of structures made of noble metal nanoparticles. Recent studies have focused their attention on the possibility to combine organic photoresist and aqueous solutions of metal precursors, with the aim to nanofabricate bi-composite structures [192-193]. The possibility to create in the same time three-dimensional polymeric objects rich in gold nanoparticles allows to create photo-excitable smart templates, which show the collective response of the GNPs when opportunely irradiated.

To obtain simultaneously photo-polymerization of an organic photoresist and photo-reduction of a metal precursor, at least their TPA cross-sections must be comparable [1-3]. Therefore, the first experiments series was devoted to estimate the TPA cross-section of chloroauric ions. To this purpose, it was mandatory to establish the dependency of the virtual voxel size on the energy dose delivered. Therefore, I printed 1D gratings made of 30 μm long segments with a period of 3 μm, covering a surface of 30x30 μm^2, using different values of the laser power (from 2.5 mW to 22.5 mW) and of the scan speed (from 10 μm/s to 8000 μm/s).

The width and the characteristics of each segment were investigated by SEM analyses. Figure 3.2 show the SEM images of a sample obtained with 22.5 mW laser power @ 90 μm/s scan speed, showing the onset of sub-micrometer sized particles inside the exposed areas, embedded in the PVA matrix.

$Au^{(0)}$ nanoparticles were formed inside the scanned segments, by direct photo-reduction of $AuCl_4^-$, according to the mechanism reported in Ref. [189]. An additional reduction mechanism is governed by the thermal effects occurring at temperatures higher than 60 °C, present in our system because of the local heating induced by the laser [1-3], as will be discussed in the following paragraph.

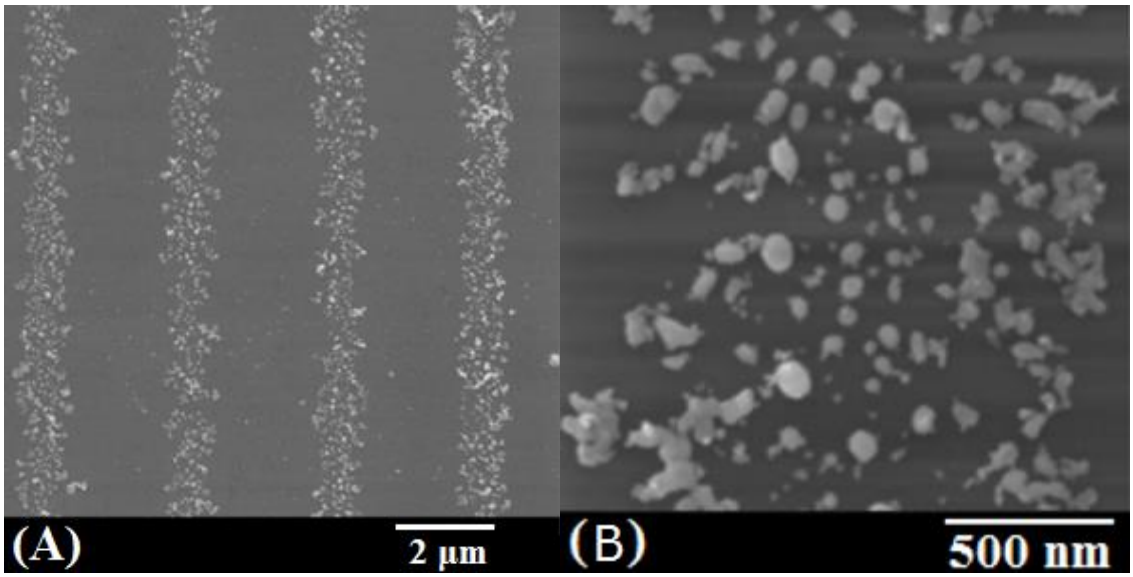

Figure 3.2: SEM image of **A**) a 2-P reduced grating (22.5 mW @ 90 μm/s) of GNPs in the PVA matrix; **B**) a single stripe of a grating rich with GNPs.

The nature of the nanoparticles is revealed by the optical absorption spectrum (Figure 3.3 A), exhibiting the typical gold LSPR absorption band centred at 570 nm. The broadening of the LSPR peak is due to the size dispersion of the GNPs: the diameter of the created nanoparticles, depending on the exposure time and the laser power, varies over two order of magnitude with the largest in the order of 100 nm. Further confirmation is obtained by the back-scattering SEM imaging and by Energy Dispersion X-Ray (EDX) spectra (Figure 3.3 B-C), performed on the unexposed gold-doped PVA film and on the created segments,

showing an important growth of the gold peak in the latter case. Quantitative comparison of the atomic percentages is reported in Table 1.

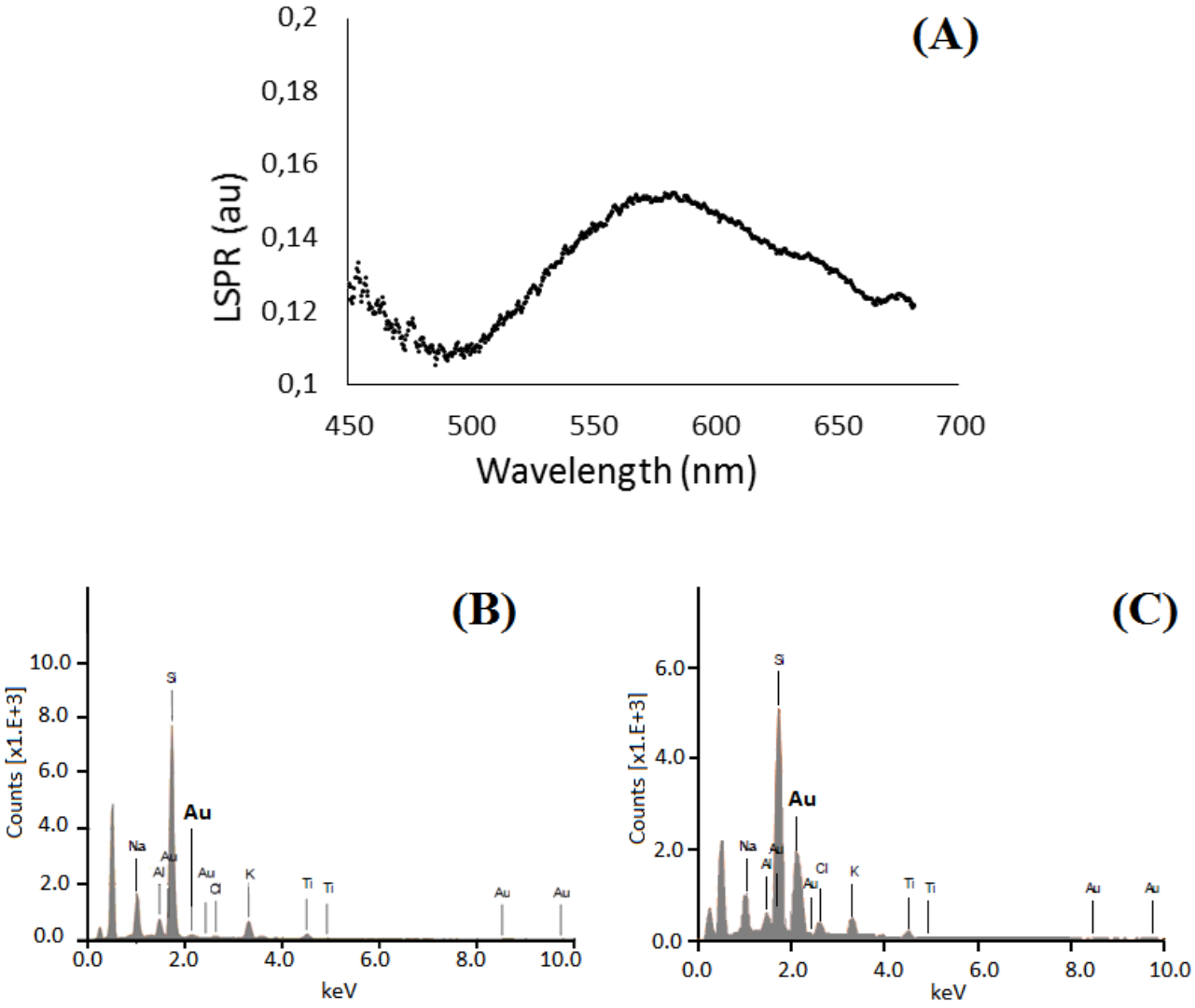

Figure 3.3: A) Absorption spectrum performed on the gratings showing the typical localized surface plasmon resonance of gold NPs at @570nm. EDX spectra on the resist before **B)** and upon **C)** the exposure to the laser beam. The enhancement of the elemental Au peak for the exposed resist demonstrates the nature of the nanoparticles.

Element	Atomic Percentage (%)	
	Unexposed resist	**Exposed resist**
Na	10.45	10.78
Al	5.69	3.44
Si	62.22	51.98
Cl	6.26	5.67
K	8.78	7.55
Ti	4.10	4.14
Au	**2.51**	**16.43**
Total	100.00	100.00

Table 3.1: Atomic percentages of: the glass substrate, the unexposed resist and the created stripes of nanoparticles. The huge presence of gold upon the exposure demonstrates the GNPs creation.

The width of the GNPs segments, as expected because of the TPA threshold, depends on the intensity and hence on the power of the irradiating laser beam, larger the power larger the voxel width (Figure 3.4 A).

Analysis of the power/time dependence of the voxel size allows to derive important parameters involved in the process, namely the laser effective beam waist and the TPA cross-section. To get this goal, the experimental data are compared with the theoretical predictions on the voxel size, discussed in the first chapter.

The diameter of the voxel generated by the TPA depends on the laser power P and on the exposure time t, according to the law described in equation (1.5). It is important to stress that this model holds for bare photo-sensitive polymers and during TPPR doesn't occurs any polymerization. Therefore, the physical meaning of parameters ρ is different from that exposed in equation 1.5. In particular, the term $ln[\rho_0/(\rho_0 - \rho_{th})]$ expressing the polymerization probability, in this case should account for different physical quantities as f.i. the seeds density. As a consequence, I consider only the effective TPA cross-section, $\sigma_2^* = \sigma_2/ln[\rho_0/(\rho_0 - \rho_{th})]$, where ρ_0 and ρ_{th} have to be considered in the sense exposed above.

Therefore eq. (1.5) reads:

$$d(P,t) = r_{\omega_0}\sqrt{\ln\left(4\frac{P^2 t}{\nu t_L\left(r_{\omega_0}{}^2\pi\cdot\hbar\omega\right)^2}\sigma_2^*\right)} \tag{3.1}$$

The measured values for the width of the stripes vs. laser power are then fitted with Eq. 3.1, in the form $f(x) = A\sqrt{\ln(Bx^2/A^4)}$, where:

$A = r_{\omega_0}$

$B = \frac{4}{\nu t_L(\pi\cdot\hbar\omega)^2}\,\sigma_2^* t$ where t is expressed by the ratio between $2r_{\omega_0}$ and the scanning speed.

$x = P$.

The constants A and B are the fit parameters. In Figure 3.4 A the measured width for stripes written @250 μm/s Vs. the laser power are compared with the best fit of Eq. 3.1. Due to the irregular shape of the segments, the experimental data reported are an average value of the measured width. The SEM images were analysed with the software ImageJ, which allows to analyse the area occupied by the stripe of GNPs and to extrapolate the average size and the standard deviation [238].

From the fit of Figure 3.4, I evaluate the beam waist as r_{ω_0} = (780 ± 70) nm, which corresponds to the asymptotic value of the voxel width when *P* or *t* become very large. From the obtained value of the B parameter, I got the effective cross section σ_2^* = (3.9 ± 0.5) 10^{-51} cm^4s, comparable to those reported for photo-sensitive polymers [1]. This parameter characterizes the "sensitivity" of the material and should be taken into account if hybrid systems are considered in the case one aims to embed GNPs in polymeric 3D structures.

I analysed the NPs diameter as a function of the exposure time, at fixed values of the laser power. In Figure 3.4 B are reported the measured segments width data obtained @17.5 mW and the best fit of Eq. 2, from which I got identical values for σ_2^* = (3.5 ± 0.7) 10^{-51} cm^4 s and r_{ω_0} = (740 ± 60) nm.

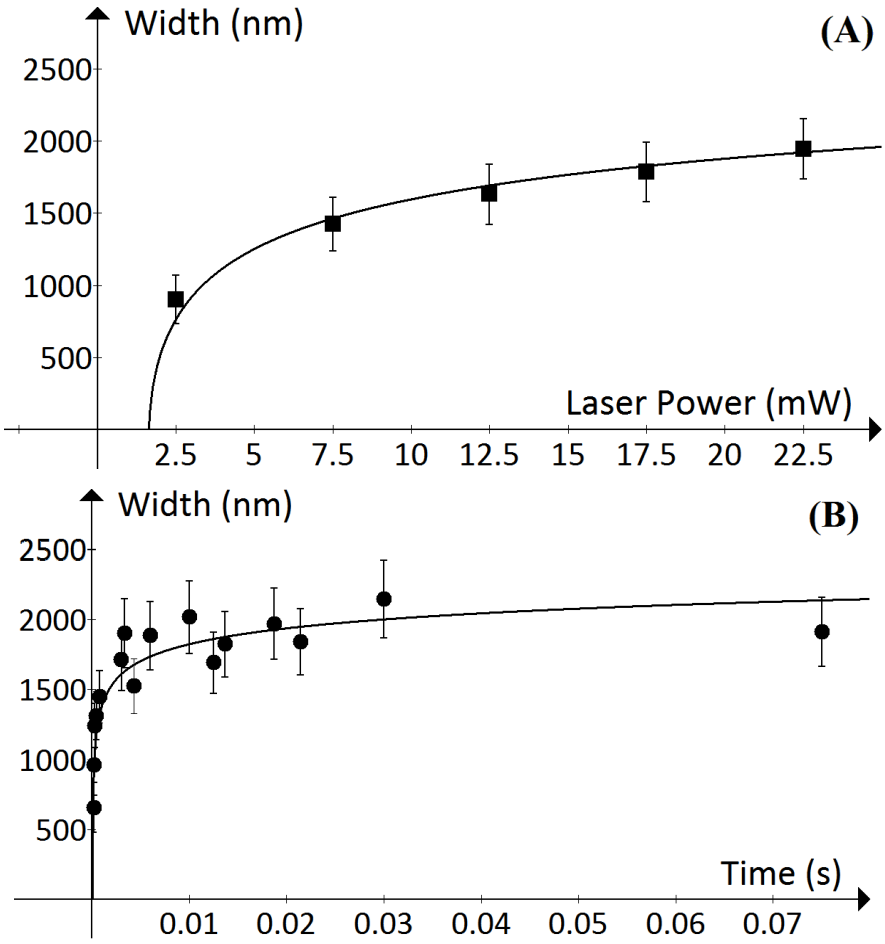

Figure 3.4: Dependency of the width of the stripes on **A)** on the laser power at a fixed scan velocity 250 μm/s and **B)** on the exposure time at a fixed value of laser power of 17.5 mW. Dots are the experimental data and the solid line is the best fit of Eq. 4.2.

3.3 Density and size analysis on the GNPs created during TP-DLW

Analysis on the voxel obtained by TP-DLW were performed in the PVA that is unwanted to get SEM and AFM imaging with an adequate quality. Therefore, to study the density and sizes the sample has been developed in distilled water for 20 minutes and left to dry at room temperature over a few hours. SEM imaging reveals that after the development step the PVA was completely removed and the gratings were made by the solely gold nanoparticles sticking on the glass substrate (Figure 3.5 A). A basic statistical analysis of the NPs size and density, based on the SEM images, was performed. By analysing

several gratings created at fixed laser power and different scan speed values, I estimated that the density of GNPs ranges from 90 μm^{-2} to 360 μm^{-2}, increasing with the exposure time, as one would expect.

The results of this analysis are summarized in the histogram of Figure 3.6 B, showing that the growth of GNPs with a diameter of about 10 nm is highly favourite (at the used laser power) when the exposure time increases. Nevertheless SEM images show as well that a number of overgrown GNPs (> 50 nm) is present.

I qualitatively explain this result considering that the $AuCl_4^-$ ions are evenly distributed in the PVA matrix, but one can expect the presence of localized density peaks. In fact, as shown in the SEM image in Figure 3.5, which displays a matrix of GNPs 1D gratings (laser power 2.5-22.5 @ scan speed 50-80 μm/s), precipitates of tetrachloroauric acid can be present in the system. Even if very small and not visible, they are actually a very large source of gold ions and therefore they affect locally the ions density. If a given seed is very close to a such Au-ions extra source, the growth can be very fast.

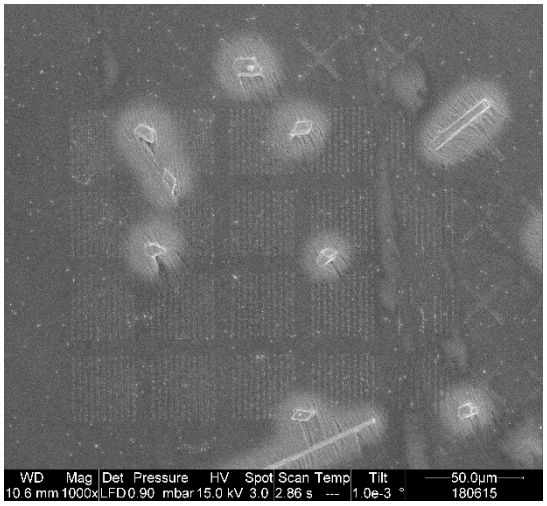

Figure 3.5: Metal precursor precipitates in correspondence of the printed structures.

Very likely, this mechanism is at the origin of overgrown GNPs (larger than 50 nm), always visible in my samples for any writing power and speed. Otherwise, the nanoparticles size is in the range from 10 nm to 50 nm. The created GNPs size is finally ruled by the growth

process depending on the chloroauric ions density and on their mobility inside the PVA matrix.

Above 50 nm, no changings in GNPs density are observed for the different scan speeds I used, indicating that the scan speed does not influence their creation. On the contrary, at longer exposure times the presence of smaller nanoparticles, further than the larger ones, is observed. This result indicates that the local peaks of density define zones where the ionic concentration is higher and hence with higher probability of seeding. In these zones the higher ionic and seeds concentration feeds the growth of the larger NPS at a higher rate [241]. Slower scan speeds are effective in activating seeds in the lower concentration zones, where smaller nanoparticles are grown thanks to the "normal" ionic diffusion. Therefore, the average diameter of the GNPs varies from 40 nm obtained at the highest scan speed, to 17 nm obtained at the lowest. It is important to highlight that in this analysis the average diameter is calculated considering the whole GNPs size distribution, and the shift in the value of the average is due to the increasing in the number of small nanoparticles, as demonstrated by SEM images of the gratings (Figure 5C-E).

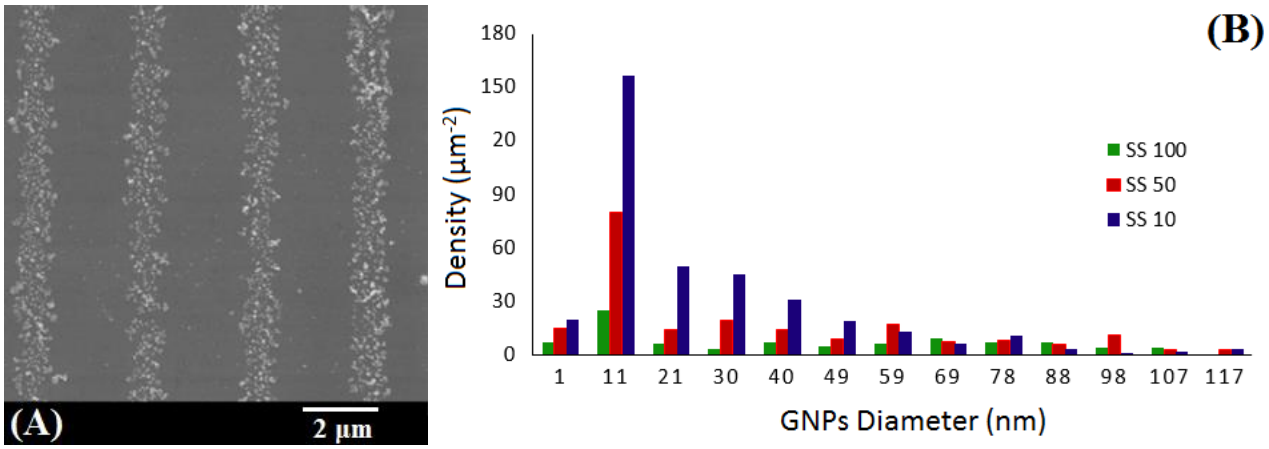

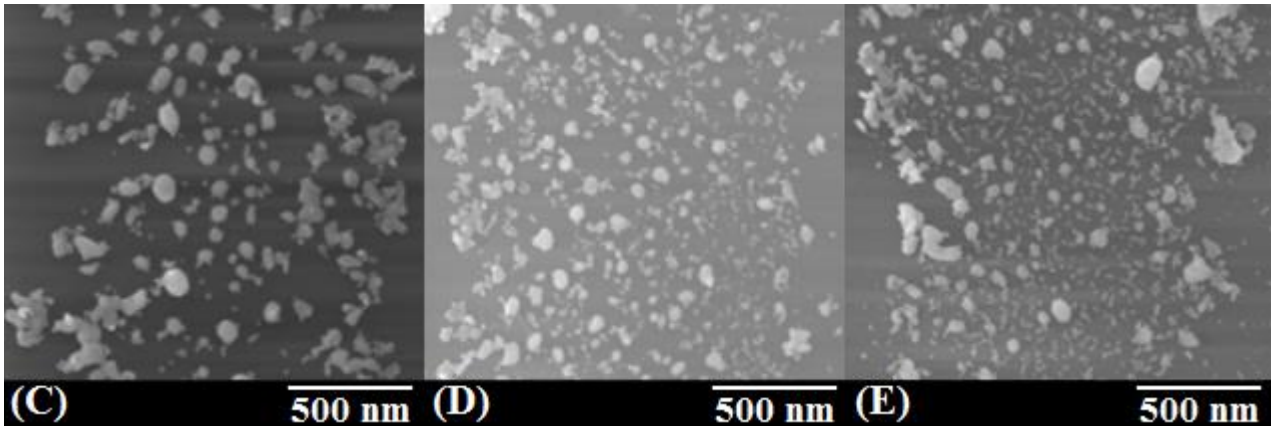

Figure 3.6: A) SEM image of a grating (2.5 mW @ 100 μm/s) of gold nanoparticles free on the glass, after the water development process. **B)** Histogram of the density of nanoparticles in function of their diameter, for gratings printed at 100 μm/s **(C)**, 50 μm/s **(D)** and 10 μm/s **(E)**, at a laser power of 12.5 mW. SEM images **C-E**, of stripes for each gratings, show the rising number of GNPs about 10 nm at the decreasing of the scan speed.

3.4 Diffusive and thermal effects overview

Given that the growth of GNPs is ruled by the chloroauric ions Fickian diffusion, I focused my attention on the possibility to discriminate and to control the diffusive effects. Let us analyze what happens during a single laser shot. Firstly, let us suppose that all the gold ions inside of the virtual voxel are photo-reduced. Further photo-reductions must involve the ions diffusing from the unexposed volume, preventing any feeding to the internal seeds by ionic autocatalysis. But the seeds created at the voxel boundary surface can grow during the exposure because of the ionic diffusion. As a consequence, GNPs of different sizes are created.

To improve the control on the growth of GNPs, one can think to deliver the energy dose in multiple shots. This method should allow the chloroauric ions to diffuse in the virtual voxel during the time between consecutive shots, restoring the initial condition of the system. Thus, tuning the waiting time between each shot, one can monitor the concentration of gold ions photo-reduced by each fraction of energy, and get a finer control on the density and size of the nanoparticles created.

Therefore, through Fick's model of diffusion, it is possible to estimate the time dependence of the gold ions concentration inside the virtual voxel.

3.4.1 Diffusive effects

The dynamics of the chloroauric ions diffusion respond to the second Fick's law:

$$\frac{dc(x,y,z,t)}{dt} = D_{ion}\nabla^2 c(x,y,z,t) \tag{3.2}$$

Where D_{ion} is the ion diffusivity, c is the ions concentration. Because of the symmetry of my system, I chose a polar reference frame. Moreover I assume that c does not depend on polar and azimuthal angles. Therefore, Eq. (3.2) can be rewritten as:

$$\frac{dc(r,t)}{dt} = D\frac{d^2c(r,t)}{dr^2} \tag{3.3}$$

This is a second order differential equation, that can be solved by considering the boundary conditions: at time $t = 0$, for $r > R$ concentration is $c = c_0$, for $r < R$ concentration is $c = 0$, with R as the virtual voxel. Therefore, a possible solution for equation (3.3) is [194-195]:

$$c(r,t) = c_0\left(1 - \mathrm{erf}\left(\frac{r}{4D_{ion}t}\right)\right) \tag{3.4}$$

Where:

$$D_{ion} = \mu_{ion}K_BT = \frac{K_BT}{6\pi R_{ion}\eta} \tag{3.5}$$

In Eq. (3.5), μ_{ion} is the ion mobility, K_B is the Boltzmann constant, T is the room temperature (300 K), R_i is the radius of the ion considered, and η is the viscosity of the medium.

The radius of the tetrachloroauric acid triidrate molecule was calculated as $R_{ion} = \sqrt[3]{\frac{3m_{ion}}{4\pi\rho_{ion}}} = 3.4\ 10^{-10}m$, being the mass of the ion $m_{ion} = 6.5\ 10^{-25}kg$ and the ion density $\rho_{ion} = 3.9\ 10^{3}kg/m^{3}$ at room temperature.

To define the viscosity, it was considered that the polymeric matrix I'm printing in is composed by 1 part of PVA and 10 part of distilled H_2O, thus $\eta = 8.6\ 10^{-3}kg/ms$.

Equation (3.4) is plotted in Figure 3.7.

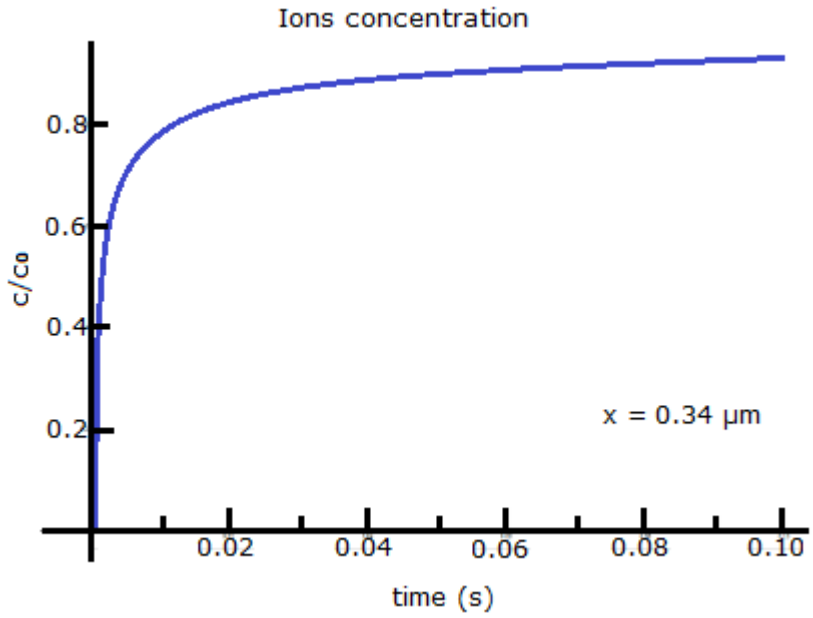

Figure 3.7: Time dependence of the chloroauric ions concentration inside the virtual voxel after the laser exposure (Eq 3.4). To refill the voxel spot are required a few hundreds ms.

From this plot it can be seen that, shooting a single point in the polymeric matrix, the volume of the virtual voxel is refilled by the ions in a time in the order of 10^{-2}-10^{-1}s.

In order to verify the theoretical prediction, I have delivered the energy dose through multiple shots. In fact, if one consider a single exposure of 100 ms a continuous migration of ions occurs from the outside to the voxel area. However, the incoming ions are two-

photons photo-reduced by the laser beam as soon as they enter the exposed area, therefore, no other photo-reduction occurs inside the virtual voxel.

In Figure 3.8 A is shown a spot created at 25 mW @ 1 shot of 100 ms. The agglomerate is composed by poly-dispersed GNPs, mainly distributed on the border. In correspondence of the virtual voxel, at the centre, is presents an area of diameter 600 nm, where the density of GNPs has a minimum and contains only few GNPs of ~30 nm. The growth of the GNPs occurs outside the virtual voxel.

Vice versa, if the energy dose is delivered through multiple shots, in the time interval between consecutive shots, the chloroauric ions in the surrounding volume diffuse toward the centre of the virtual voxel and then can be photo-reduced by the following laser shot. This allows to create dense cluster of less poly-dispersed GNPs. In Figure 3.8 B, is shown a cluster of GNPs obtained by delivering 100 shots of 1 ms @ 1 mW. Even, if the energy dose is much lower than before (Figure 3.8 A) a denser cluster occupies the virtual voxel.

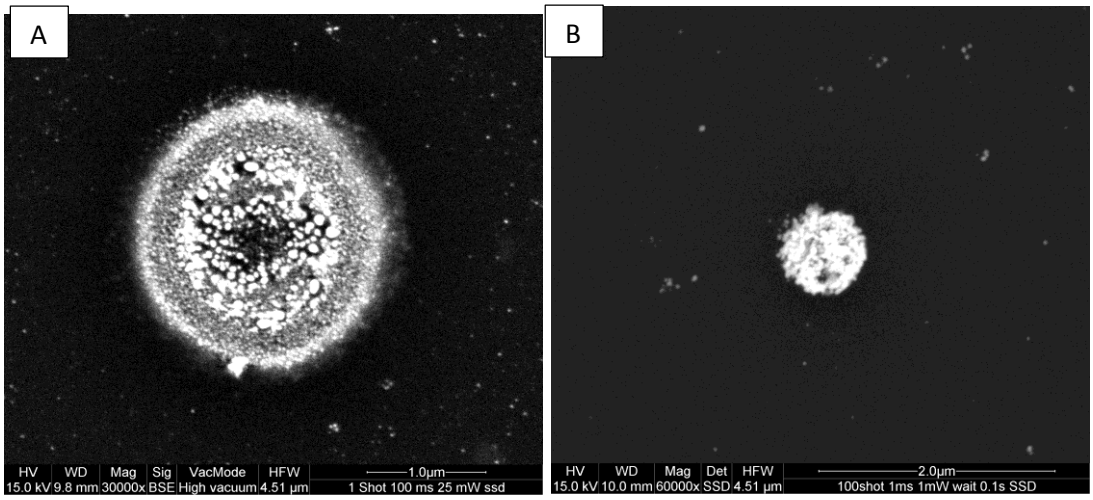

Figure 3.8: Back-Scattering SEM imaging of spots created by delivering **A)** 25 mW @ 1 shot of 100 ms and **B)** 1 mW @ 100 shots of 1 ms, with waiting time 100 ms. SEM imaging in back-scattering mode emphasize the gold nanoparticles density. Thus, the brightness of the spot created by multiple shots @ waiting time 0.1 implies it is denser than the others, indicating blasting effects occur at longer waiting time.

This result allows to elucidate the physics involved in the phenomenon. Seeding is a very fast process, since photo-reduction of the chloroauric ions occurs in the typical time of

electronic transition [189].Vice versa, the growth of the GNPs is much slower and depends on the time of diffusion of the chloroauric ions.

During the exposure of a single shots in the order of 10^{-3}-10^{-1} s, as in my case, all the ions inside of the virtual voxel are reduced. It is important to stress again that the ions diffusing during the exposure cannot enter inside of the volume of the virtual voxel, so they are either photo-reduced at the side of the virtual voxel or reduced by the nanoparticles due to auto-catalytic process and contribute to their growth. Either way, the poly-dispersity of the GNPs inside of the spot is increased.

Delivering the energy dose through 100 shots, instead, allows to increase of the same factor the seeds density, compared to the case of a single shot. As a consequence, the spot obtained is denser, and poly-dispersity is reduced.

The waiting time between consecutive shots plays a key role, since the longer the waiting time the higher the percentage of ions which refill the virtual voxel, till saturation. To observe the effects of the waiting time, I repeated the printing in Figure 3.8 B at different waiting times between consecutive shots, ranging from 0.001 s to 10 s.

It is to be noted that with a single shots of 100 ms, no ordered pattern of GNPs aggregates was found on the sample. When the energy dose was delivered through 100 shots, instead, I was not able to recognize on the substrates any cluster for waiting times of 0.001 s and 0.01 s, however, for waiting time larger than 0.1 s aggregates of GNPs were revealed (Figure 3.8-9).

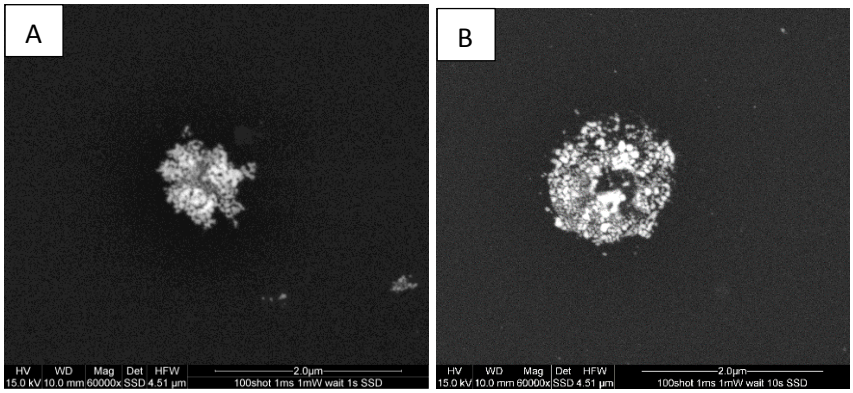

Figure 3.9 Back-Scattering SEM images of spots created at laser power 1 mW @ 100 shots of 1 ms of exposure time, with waiting times of **A)** 1 s, **B)** 10 s.

In Figure 3.9 are shown the SEM images of the GNPs aggregates obtained for waiting time of 1 s and 10 s. The spot shown in Figure 3.8 B, created with a waiting time of 0.1 s is a dense cluster of diameter ~800 nm, comparable to the laser beam waist, and made of GNPs of ~30 nm.

However, when the wait time is longer than 0.1 s, I observe the onset of new regime. In fact, at 1 s of waiting time, a larger spot is obtained, but is appears less dense and shattered. This becomes more evident by increasing the waiting time and @ 10 s (Figure 3.9 B) the spot presents again a ring shape. This behaviour will be discussed in the next paragraph.

In conclusion, delivering the energy dose through multiple shots allows to control the ions density involved in TP-DLW. Compact aggregates of GNPs with resolution up to few hundreds nanometer can be obtained. Thus, multi-shots printing turns out to be an effective technique to improve additive manufacturing of GNPs based structures, providing that the system is finely tuned.

3.4.2 Water diffusion

The behaviour observed for waiting time > 0.1 s suggests that some other effects have to be considered. In fact, a series of experiments demonstrated that when the waiting time is 1 s or larger, a blasting wave originating in the laser focus takes place, strongly affecting the resulting GNPs spot geometry.

As it will be demonstrated, the water diffusion inside the polymeric matrix is responsible of this effect. While more GNPs are created through the photo-reduction of the ions inside the virtual voxel, an increasing of the local temperature has to be expected as well. In fact, as indicated in paragraph 3.1, TPA leads to electronic transitions inside of the involved molecules, which relax also through non-radiative energy emission, namely heat.

Heating causes the rapid evaporation of water inside the voxel, pushing around the surrounding liquid. As a consequence, a local dehydration of the polymer occurs. At long

waiting times, namely larger than 1 s, the expulsed water refill the virtual voxel and therefore each shot concurs with a thermal shock-wave, ejecting GNPs to the outside.

This phenomenology has been confirmed by a series of experiments. I 3D-printed a series of cylindrical-like barriers of different shapes in a photo-sensitive polymer (IP-L 780) (Figure 3.10 A), with the aim to observe the effect of the blasting over more sturdy structures.

50 μL of a mixture made by 10.0% in volume of isinglass, 89.8% of Milli-Q water (18.2 MΩ cm) and 0.2% of HAuCl4 were drop-casted upon the glass substrate. Isinglass is an organic hydro-gel, typically used as food thickener. I used isinglass in this experiment because its low cross-linking degree and low viscosity allow to water to diffuse faster than in PVA.

Spots of gold nanoparticles were printed inside of the different cylinders, with laser power of 30 mW @ overall exposure time of 100 ms, both in a single shot and in 100 shots of 1 ms, with waiting times ranging from 0.001 s to 10 s.

In Figure 3.10 is shown the analysis performed on the sample, by means of laser scanning confocal microscopy. I observe that after even a single shot, the structures are deformed. In case of multiple shots the effect increases with the waiting time. I ascribe this effect to the pressure wave that is generated by the thermal shock.

For longer waiting time, the effects of water "jets" are more evident and lead to the total destruction of the barriers and deformations in the hydrogel.

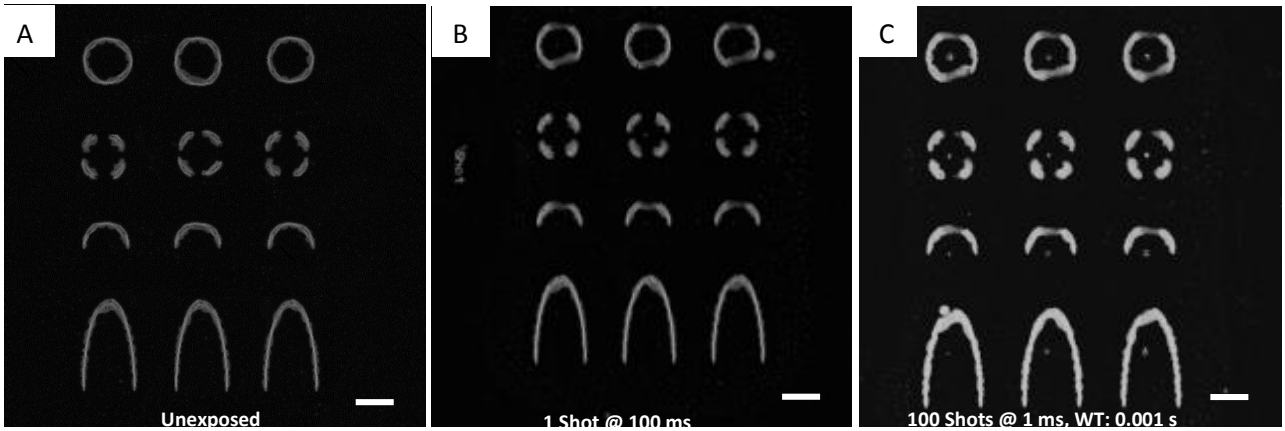

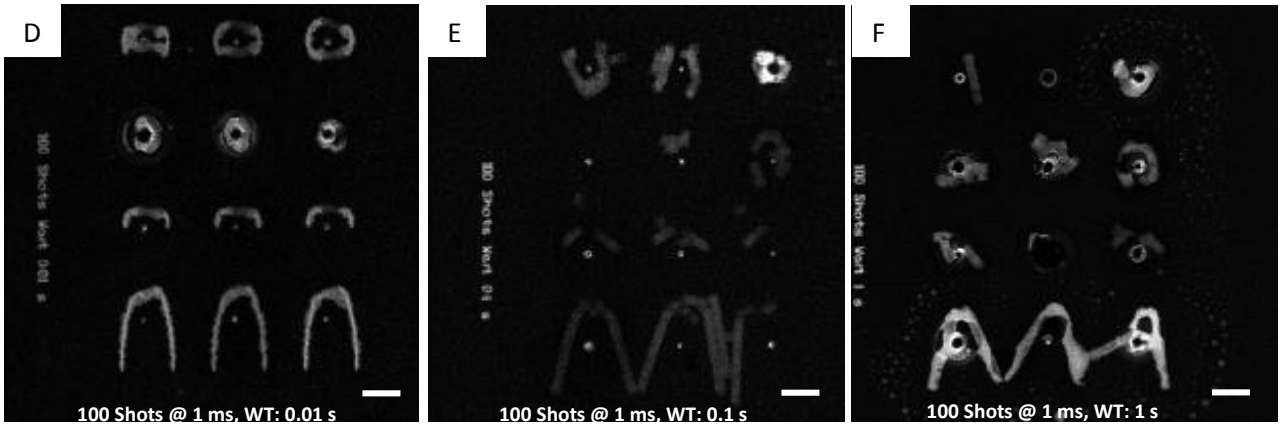

Figure 3.10: **A)** Confocal microscopy imaging of a matrix of 4 x 3 barriers of cylinders-like shapes (diameter 20 μm, height 5 μm) created in IP-L 780. The first array of cylinders does not allow water diffusion from outside, while the others have respectively four and one channels to permit the flow. An organic hydrogel doped with $HAuCL_4$ was drop-casted inside of them. Spots of GNPs were printed at laser power 30 mW @ **B)** 1 shots of 100 ms or 100 shots of 1 ms with waiting time of **C)** 0.001 s, **D)** 0.01 s, **E)** 0.1 s and **F)** 1 s. The line bar in the photo is of 20 μm.

From this experiment, it can be concluded that excessive waiting time allows to the system to go back to its initial concentration both of ions and water. Thus, consecutive shots may lead at the same time to the reduction of new GNPs and to further local evaporation that generates a thermal shock-wave, which transfers a momentum to the surrounding material, may it be the polymer or the GNPs. This results in a blast of the cluster of GNPs (Figure 3.9) and in the permanent damaging of the polymeric matrix (Figure 3.10).

To verify this interpretation, I studied water diffusion in PVA according to the Fick's law, taking in account that dehydration happens in correspondence of the spot volume. Thus, water concentration at the initial time is $c_w(r, 0) = c_{w_0}$ for $r > r_{spot}$, and $c_w(x, 0) = 0$ for $r \leq r_{spot}$, where r_{spot} is the radius of the spot of GNPs measured through SEM and AFM measurements.

Taking in account, for example, the spot size obtained at laser power 25 mW @ 100 shots of 1 ms, with waiting 10 s (Figure 3.11 A), on a sample prepared as in paragraph 3.2, the concentration profile obtained is plotted in Figure 3.11 C.

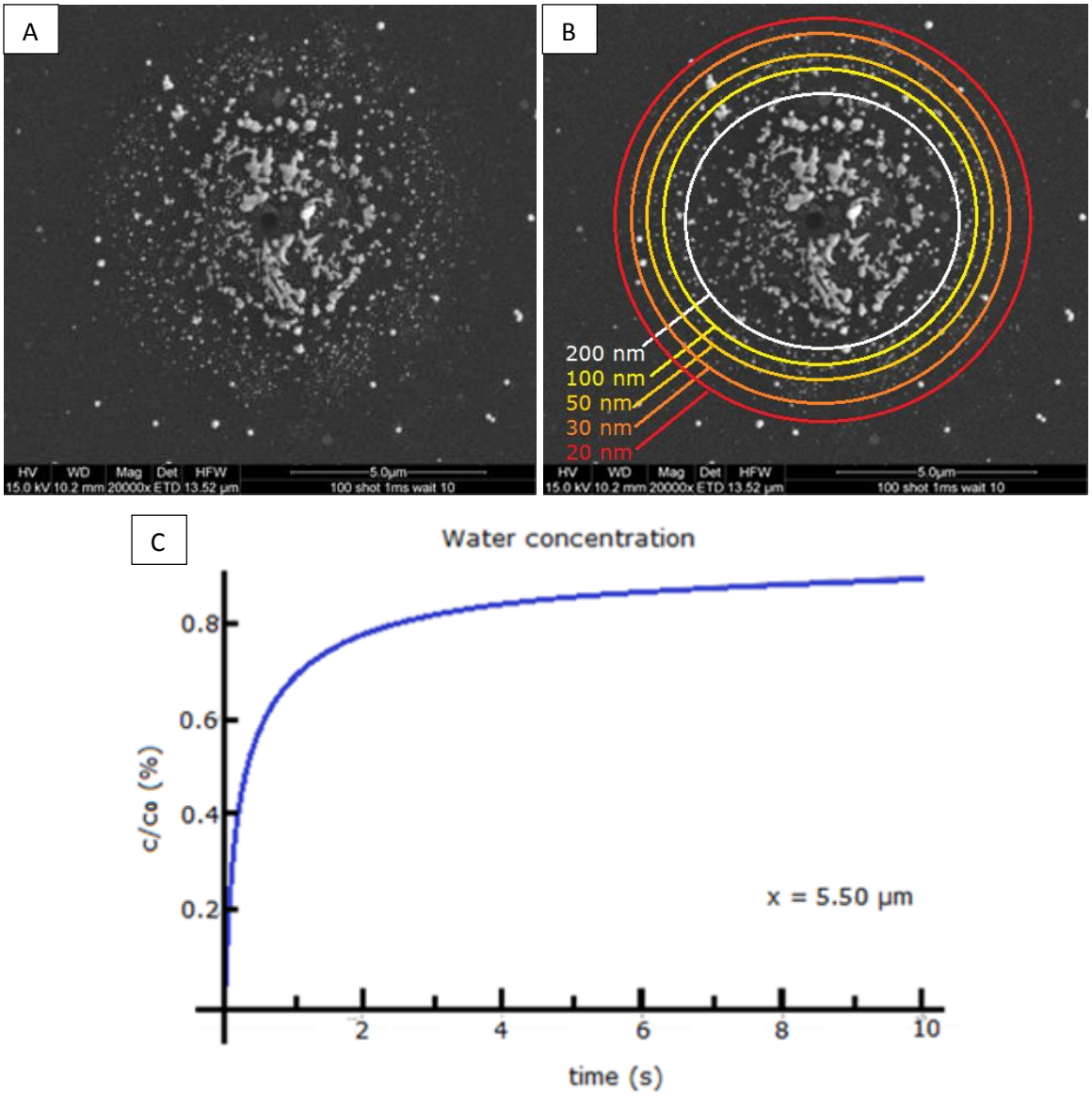

Figure 3.11: A) SEM image of a spot of GNPs created in PVA at laser power 25 mW @ 100 shots of 1 ms with waiting time of 10 s. A spot of radius 5.5 µm is obtained, Gold nanoparticles are expulsed from the centre toward the outside, with the smaller ones farther away. **B)** The radial position at which different nanoparticles stop is indicated in function of their size. The largest GNPs (radius: 100 nm) are ejected at 4 µm from the centre, the smallest ones at 5.5 µm. **C)** Water concentration profile Vs time.

As shown in Figure 3.11 B, around the spot created, there is an *annulus* made by the gold nanoparticles ejected from the centre by the thermal shock-waves. The largest

nanoparticles (radius 100 nm) land near the centre (at a distance of 4 μm); the smallest (radius 10 nm) farther away from the centre (at a distance of 5.5 μm).

This result seems coherent with the hydrodynamic model, according to which GNPs running in a fluid are subjects to viscous forces which stop their motion.

The plot for water diffusion (Figure 3.11 C) shows that water refills the spot area in about 10 s, therefore each shot is responsible of a shock-wave, whose energy depends on the intensity of the laser beam and on the ionic concentration. The shock-wave runs over the GNP and transfer to it a momentum $q = m_P v_0$, where $m_P = \frac{4}{3}\pi\rho_{Au} r_P^3$ is the mass of the gold nanoparticle; v_0 is the NP's initial speed just after the blasting wave stroke; ρ_{Au} is the gold density and r_P is the radius of the spherical GNP.

After the collision, the GNP is ejected in the direction of the shock-wave propagation, and its motion is stopped by the viscous forces.

According to the fluid-dynamics, the system regime is described by the Reynolds number:

$$Re = \frac{2 r_P v(t) \rho}{\eta} \tag{3.6}$$

Where $v(t)$ is the velocity of the GNP and ρ is the density of the fluid. The Reynolds number is dimensionless and allows to characterize the regime involved in the GNP motion. Three regime can be predicted [196]:

- **Turbulent regime**, describes the fluid-dynamics of the system for $Re \geq 10^6$. However, according to the Eq. (3.6) turbulent regime would present in my case for velocity $v \gg v_{sound}$, where $v_{sound}$is the velocity of the sound in the aqueous solution. Since, the GNPs ejected cannot reach supersonic speeds, the turbulent regime cannot be used to describe my system.
- **Laminar regime**, is the second regime in which $Re \geq 1$ and the velocity is $v(x) = v_l(x),\ \forall\ 0 \leq x \leq x_t$, with x_t being the position at which the regime

transition occurs. The viscous force opposed to the motion, in this regime, is defined as:

$$F_l(x,t) = \frac{1}{2} c_r \rho S v_l^2(x,t) \tag{3.7}$$

Where c_r is the aerodynamic coefficient that takes in account the shape of the particles and is equal to 0.5 for a sphere. S the cross-sectional area of the gold nanoparticle.

- **Stokes' regime**, which describe the system when $Re < 1$ and the velocity is $v(x) = v_s(x), \forall\, x_t < x < x_d$. x_d defines the position at which the velocity is comparable to the Brownian diffusion. The transition from the laminar to the Stokes' regime occurs when $Re \sim 1$, $x = x_t$ and $v_l(x_t) = v_s(x_t)$ [196]. In Stokes' regime the viscous force is:

$$F_s(x) = -6\pi r_s \eta v_s(x) \tag{3.8}$$

Where r_s is the radius of the GNP.

The nanoparticles travelling close to the surface, stop on the substrate at distance x_d with respect to the centre of the spot. Measuring this position by means of SEM and AFM, should be possible to estimate the initial velocity of the particles, thus the momentum transferred by the shockwave.

To do this, it has to be considered that the velocity in the laminar regime is:

$$v_l(t) = v_0 - a_l(t)\, t \tag{3.9}$$

Where $a_l(t) = F_l/m_P$ is the acceleration of the GNP due to viscosity.

Using Eq. (3.7), Eq. (3.9) can be rewritten as:

$$v_l(t) = v_0 - \alpha v_l^2(t)\, t \tag{3.10}$$

Where $\alpha = \frac{1}{2m_P} c_r \rho S$ denotes all the constant parameters. The solution of eq. (3.10) is:

$$v_l(t) = -\frac{1 + \sqrt{1 + 4\alpha v_0 t}}{2\alpha t} \tag{3.11}$$

No information on the duration of the motion can be experimentally be acquired. Therefore, in order to define the velocity as a function of the position, I calculated the function $x_l(t)$ by integration of (3.11) with respect to the time:

$$x_l(t) = \int v_l(t)\, dt = \frac{1}{2\alpha} \int \frac{-1 + \sqrt{1 + 4\alpha v_0 t}}{t} dt = \frac{\sqrt{1 + 4\alpha v_0 t} - \ln\left(\sqrt{1 + 4\alpha v_0 t} + 1\right)}{\alpha} + x_0 \tag{3.12}$$

I want to get rid of the parameter t from Eq. (3.11), therefore the Eq (3.12) has to be inverted. In order to do this, the equation is approximated at the second order by considering the Taylor's serie: $\ln(s + 1) \sim s - \frac{s^2}{2}$, thus:

$$x_l(t) = \frac{\sqrt{1 + 4\alpha v_0 t} - \sqrt{1 + 4\alpha v_0 t} + (1 + 4\alpha v_0 t)/2}{\alpha} + x_0 = \frac{(1 + 4\alpha v_0 t)}{2\alpha} + x_0 \tag{3.13}$$

Considering the initial condition: $x_l(t = 0) = 0$, I obtain $x_0 = -1/2\alpha$. Then:

$$x_l(t) = 2v_0 t \tag{3.14}$$

Substituting eq. (3.14) in the expression of velocity (3.11), it is possible to calculate the velocity as a function of the position in the region $0 \leq x \leq x_t$:

$$v_l(x) = v_0 \frac{\sqrt{2\alpha x + 1} - 1}{\alpha x} \tag{3.15}$$

The velocity $v_l(x)$ of the gold nanoparticles decreases according the eq. (3.15) until the transition from the laminar to the Stokes' regime, defined by Reynolds number $Re \leq 1$.

In this region, according to Stokes' law, viscous force $F_s(t)$ is:

$$F_s(t) = -\beta v_s(t) \tag{3.16}$$

Where $\beta = \frac{6\pi\eta r_P}{m_P}$ is a constant parameter.

In analogy with the case of laminar regime, the velocity in the Stokes' regime is defined as:

$$v_s(t) = v_{s_0} - \beta v_s(t)\, t \tag{3.17}$$

It is important to point out that v_{s_0} refers to the intercept of the function which describes the velocity in the Stokes' regime, thus would correspond to $v_s(x = 0)$. This value doesn't have any physical meaning, since the Stokes' regime holds for $x_t < x < x_d$.

The solution of Eq. (3.17) is:

$$v_s(t) = \frac{v_{s_0}}{\beta t + 1} \tag{3.18}$$

$x_s(t)$ is calculated integrating Eq. (3.18):

$$x_s(t) = \int v_s(t)\, dt = v_{s_0} \int \frac{1}{\beta t + 1} dt = v_{s_0} \frac{\ln(|\beta t + 1|)}{\beta} + x_{s0} \tag{3.19}$$

From the boundary condition $x_s(t = 0) = 0$, it turns out $x_{s0} = 0$. Therefore eq. (3.19) is rewritten as:

$$e^{\frac{x\beta}{v_{s_0}}} = \beta t + 1 \tag{3.20}$$

Substituting eq. (3.21) in eq. (3.19), the velocity in the Stokes' regime is:

$$v_s(x) = v_{s_0} e^{-\frac{x\beta}{v_{s_0}}} \tag{3.21}$$

Equation (3.22) expresses how the velocity $v_s(x)$ of the gold nanoparticles decreases.

If we look at the $v_s(x)$ we see that converges to zero asymptotically when x becomes large (Eq. 3.22). Therefore, we have to consider some other term in the energy balance, "truncating" the motion in correspondence of the positionx_d, in the order of the measured radii. When the velocity of the GNP is comparable to the particles diffusion, thus $v(x) = v_d(x), \forall\, x \geq x_d$, the system becomes unpredictable and cannot be described in terms of Stokes' regime anymore. Instead, the particle assumes Brownian motion.

According to the energy conservation law:

$$m_P v_d^2(x) = KT \tag{3.22}$$

Where K is the Boltzmann constant, T is the room temperature of 300 K.

Considering the GNP mass as $m_P = \frac{4}{3}\pi r_P^3 \rho_{Au}$, where $\rho_{Au} = 1.9\ 10^4 kg/m^3$ is the density of gold, it is possible to calculate the diffusion velocity v_d, for a given r_s.

As stated before, x_d is measured experimentally and its value depends on the nanoparticle size. v_d is calculated from equation (3.22).

This allows us to calculate the value of v_{s_0} from eq. (3.21), since $v_s(x_d)$ is known. It is important to stress once more that v_{s_0} does not have any physical meaning, but is necessary to properly define eq. (3.21). Moreover, from the condition $Re = 1$ it is possible to calculate the velocity of the nanoparticle in correspondence of the coordinate x_c, (Eq. 3.6). x_c is the coordinate where the changing in the hydro-dynamical regime occurs; in this position $v_l(x_t) = v_s(x_t)$. Under these conditions, x_t is calculated from eq. (3.21). Substituting this value in eq. (3.15) the initial velocity v_0, which is the actual initial velocity of the GNP, can be calculated.

In Figure 3.12 is represented the velocity profile Vs. the distance of gold nanoparticles of different size, from r_P 10 nm to 100 nm. At $x = 0$, the GNP velocity is maximum and depends on the momentum transferred by the blasting wave. In blue is indicated the laminar region, in which the GNP velocity decreases according to Eq. (3.16). At position x_t,

the transition from laminar to Stokes' regime occurs and the velocity decreases according to Eq. (3.21).

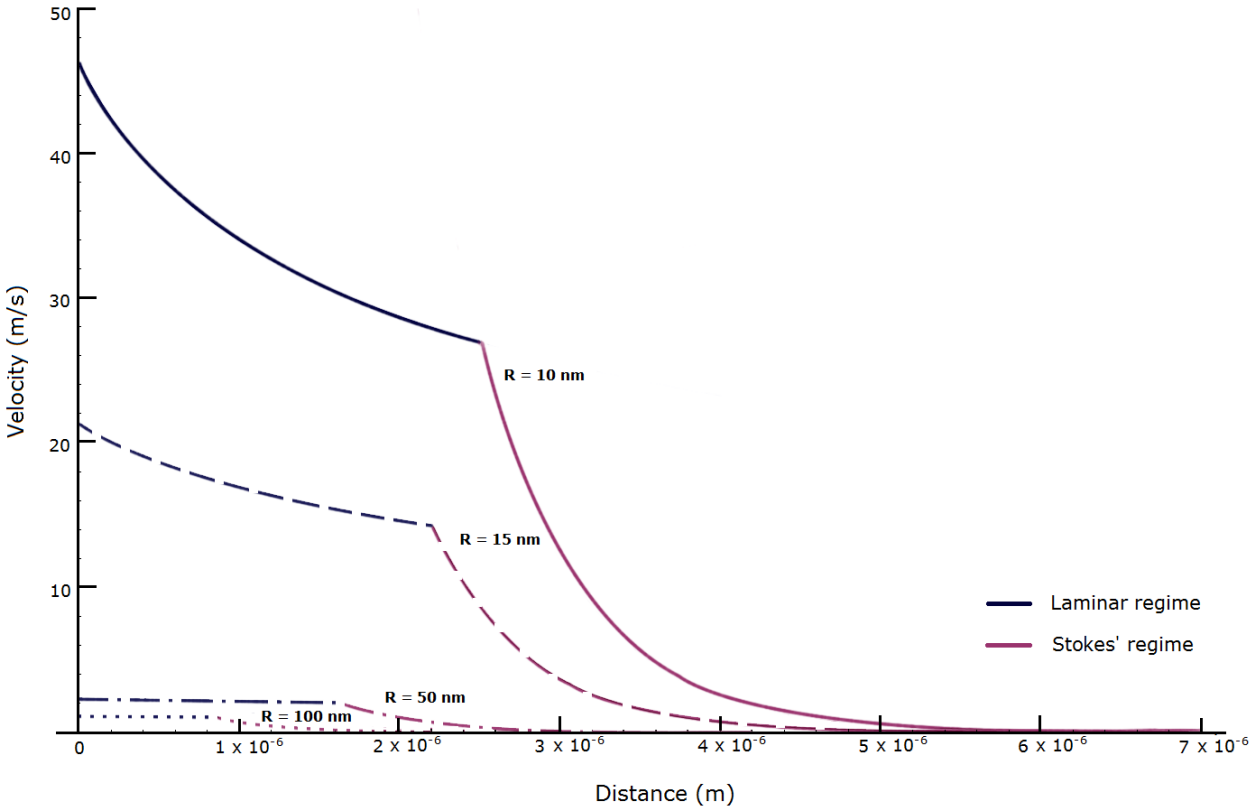

Figure 3.12: Velocity profile in function of the distance of gold nanoparticles of different sizes that are ejected from the centre of the voxel to the outside. After the blast, GNPs follows the laminar regime (in blue) when the velocity of the GNP decrease to get Re = 1, a changing in the regime is observed and the velocity is described according to the Stokes' law (in violet), until the velocity becomes comparable to the Brownian diffusion velocity of the GNP.

The velocity profile is in accordance with the hydrodynamic model. In fact, as can be observed in figure 3.12 v_0 strongly depends on the size of the NPs. However, from the model, it turns out that the energetic balance between the initial NP kinetic energy doesn't equals the work of the viscous forces, calculated as the integral of F(x) in eq. (3.23), as it results considerably larger than the kinetic term.

$$W = \int_0^{x_t} F_l(x)dx + \int_{x_t}^{x_d} F_s(x)dx \tag{3.23}$$

This result suggests that the motion of the GNPs occurs more likely inside of a solid matrix instead that in a fluid, and other mechanisms of interaction between the GNPs and the polymeric matrix have to be considered to properly describe the NPs dynamics. This result also suggests that the blasting wave propagates faster that the ejected NPs. However, the different experiments exposed above (Figure 3.6-10) demonstrate the role of ionic diffusion in accordance to the Fickian model. Thus, chloroauric ions diffuse inside of an aqueous solution. A possible conclusion is that the blasting wave does not completely dries the PVA layer.

Ionic diffusion occurs the presence at least of a molecular water layer, around the PVA molecules, in which the ions can diffuse. However, this content of water is not enough to allow the gold nanoparticles to run inside of the PVA according to the hydrodynamic model.

Therefore, due to TPA, water generates a thermal-shockwave, which transfer a momentum to the particles running over it; therefore the NP motion occurs in an almost dried polymeric matrix, in which it cannot diffuse. On the other hand, the polymer is not completely dried, since ionic Fickian diffusion is observed.

In about ten seconds, as observed in the experiments (see Figure 3.8-9) the water diffusion restores the initial condition inside of the spot, and another shock-wave is generated. However, it has to be underlined that the blast of the GNPs cluster does not occurs immediately, but is due to cumulative thermal shock-waves.

To verify this point, I prepared a sample as in paragraph 3.2 and printed single GNPs spots delivering the same energy dose through different numbers of shots. In figure, 3.X are shown the spots printed with laser power 7 mW @ 1 shot of 100 ms (Figure 3.13 A), @ 2 shots of 50 ms (Figure 3.13 B), @ 5 shots of 20 ms (Figure 3.13 C) and @ 10 shots of 10 ms (Figure 3.13 D). The waiting time between each shot is in the order of 10 s.

Analysing the different cases, it appears that, as expected, one single shot leads to the formation of a carpet of gold nanoparticles on the substrate. Two shots generates a denser cluster of GNPs with respect to the first case, indicating that more GNPs have been created

inside of the virtual voxel, thanks to ionic diffusion. No blasting effects are observed till now.

Some effects of blasting are visible only after the fifth shot: the cluster at the centre of the spot starts to crumble, the average diameter is reduced from 2.2 μm to 1.9 μm, and some GNPs cover the surrounding area. A full blast occurs after the tenth shot. In fact, in the SEM image in Figure 3.13 D it can be observed how the cluster of GNPs is the smallest; in the insert, instead, the annulus of GNPs ejected from the virtual voxel is recognizable.

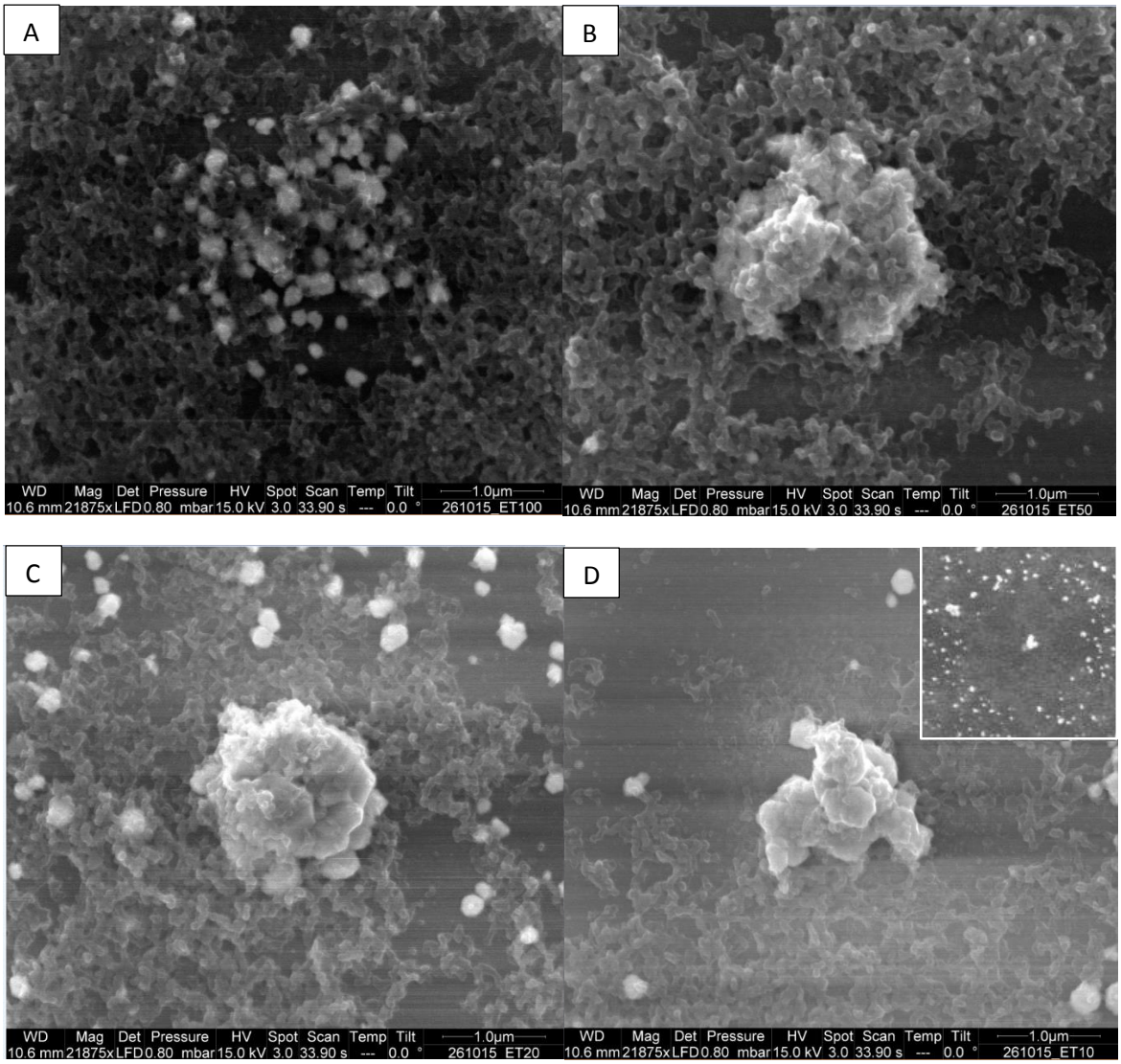

Figure 3.13: SEM images of spot of GNPs printed at 7 mW **A)** @ 1 shot of 100 ms, **B)** @ 2 shots of 50 ms, **C)** @ 5 shots of 20 ms, **D)** @ 10 shots of 10 ms. Delivering the energy in multiple shots allow to grow the cluster of GNPs inside of the virtual voxel, untile the blasting, generated by multiple thermal shock-wave, takes place. In the inset the same spot is shown at a different scale. The size of the inset is of 10 x 10 μm^2.

In conclusion, during multi-shot printing, water diffusion can be controlled by tuning the waiting time between consecutive shots and the viscosity of the polymeric matrix hosting the gold nanoparticles. Enough long waiting times allow the complete rehydration of all the volume involved, thus each shot generates a new thermal shock-wave.

Cumulative thermal shock-waves are responsible of the shattering of the GNPs cluster created by TP-DLW and an annulus of GNPs around the spot is found. The shock-waves transfer a momentum to the GNPs and runs over them. Therefore, the GNPs run in a dry polymer in which the water content is not enough to describe the motion of the GNPs with the hydrodynamical model, but enough to allow the Fickian ionic diffusion.

Moreover, in order to obtain denser cluster of GNPs and minimize the blast effects, one can tune the number of shots by which the energy dose is delivered,

3.4.3 Blast effects in water solutions.

The result observed in the previous paragraphs allows to improve the quality of TP-DLW of GNPs by controlling the density of the nanoparticles inside of a pattern designed in a polymeric matrix. However, it is interesting to observe that the radius of the spot obtained by a single laser shot in Figure 3.13 A is of 1.2 μm, considerably larger than the laser beam waist, that is estimated as [198] $\omega_0 = 0.61\lambda/N.A. = 340\,nm$. It has to be considered that a degradation of the laser beam occurs at the interface, due to the refractive index mismatch between the glass substrate and the mixture of water, PVA and HAuCl4; however, it is not enough to explain the actual dimension observed for the voxel.

According to the model presented in paragraph 3.4.2 and the experimental results showed till now, thermal shock-waves are generated during the printing, since TPA of chloroauric ions causes local heating of the involved zone. This phenomenon is at the base

of the blasting effects observed and it is never completely avoidable, even if it can be minimized by tuning the laser power, waiting time and the number of shots.

To verify this point, in last analysis, I analysed the effects of the blast in a mixture without PVA. In fact, all the experiments presented were performed into a polymeric matrix, in order to trap the GNPs created in the virtual voxel and generate pattern recognizable even after the development. However, the hosting polymer obviously interferes with the mobility of the particles involved. Its presence, in fact, increases the viscosity of the material, braking the motion of the NPs and obstructing the blast effects. Moreover, different polymers lead to completely different results.

Cao et al. [132] in their work showed single spots of silver nanoparticles printed in different polymeric matrices by exposing a metal precursor for 800 ms @ 1.3 mW. Delivering the same energy dose, they obtained aggregates of NPs of diameter ranging from ~0.5 μm to ~1.5 μm, depending on the chain length of the molecules of the polymer used. In particular, for shorter chain lengths and the lower viscosity, bigger spots of gold nanoparticles are obtained, since the ion diffusion is favoured. Their result is in accordance with the analysis presented in paragraph 3.4.2.

In order to maximize the process efficiency, one could think to avoid the polymeric matrix and use only water solution of the metal precursor. However, the nanoparticles created are free to diffuse inside the droplet; this process is favoured by the hydrophilic character of "solvent", substrate and GNPs. I have confirmed this experimentally, since no recognizable structure was found on the substrates. Thus, in order to get the possibility to "trap" them on the substrate and analyse their behaviour after the development, the created NPs should have a good affinity for the substrate and a poor one for the solvent. This can be obtained f.i. by silanization of both the glass surface and the created NPs. Other authors have already demonstrated that adding surfactants in an aqueous solution of metal precursor it is possible to create metal structure sticking to the surface. [129, 131]

Instead of adding surfactants to the mixture, I've silanized some coverslips (22 x 22 x 0.13 mm^3) with a molecular film of dimethyloctadecyl[3(trimethoxysilyl)propyl]

ammonium chloride (DMOAP), a surfactant whose chemical structure is shown in Figure 3.14.

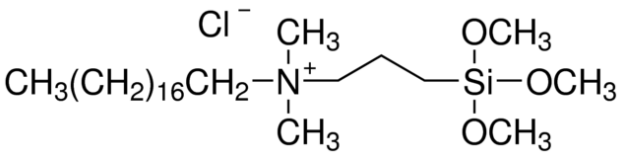

Figure 3.14: DMOAP molecular structure.

The film was deposed by dip-coating of the glass substrates in a solution made as 0.9% in volume ultrapure water and 99.0% IPA, in which was added 0.1% of DMOAP. After the dipping, a baking step of 45 minutes at 120 °C ensured a covalent bonding between the polar head of DMOAP and the glass surface. In this way, DMOAP on the substrate exposes the hydrophobic chain toward the solution, making hydrophobic the interface. After that, some of the substrates were rinsed in deionized water, in order to remove the possible excess of unbounded DMOAP from the surface, whereas the remaining ones don't.

I drop-casted 50 μL of water doped with (7.35 mM) $HAuCl_4$, and on each of them I printed a matrix of 5 x 5 spots by exposing for an overall time of 100 ms (delivered through 1 shot or 100 shots of 1 ms, with waiting times ranging from 0.001 s to 10 s) @ 5 mW laser power.

On the substrates rinsed after the dipping, no recognizable printed patterns were found after the development, due to the hydrophilic nature of the GNPs created. However, on the substrates not rinsed after the baking step, GNPs close to the substrate can collect unbounded molecules of DMOAP from the substrate, which bind with their polar head to the gold surface. Vice versa, the nanoparticles created in the bulk have a lower probability to collect DMOAP molecules so they do not "stick" on the hydrophobic substrate and are free to diffuse in the water film.

Under these conditions the GNPs near the surface, ejected by the blast, have a hydropathic affinity with the substrate and are subject to an increased surface viscosity due to the interaction between the hydrophobic chains of the surfactant on the NP surface and

on the glass. Therefore, the motion of the particles is braked and stopped by the surfactant-induced friction [199], and they are trapped on the coverslip even after the removal of the PVA film by the development step.

Comparing the SEM images of the spot created by delivering the energy dose through a single shot (Figure 3.15 A) of 100 ms, or 100 shots of 1 ms with waiting time of 0.001s (Figure 3.15 B) and 0.1 (Figure 3.15 C), no consistent difference is revealed in the diameter, whereas the NPs density increases at longer waiting time. In all the cases, I obtained a ring of gold nanoparticles with diameter of 800 nm, made by mono-dispersed GNPs of (30 ± 10) nm. This is an indication that exceeding DMOAP on the substrate was enough to cover and trap only few GNPs. In the virtual voxel, however the effect of DMOAP is not observed.

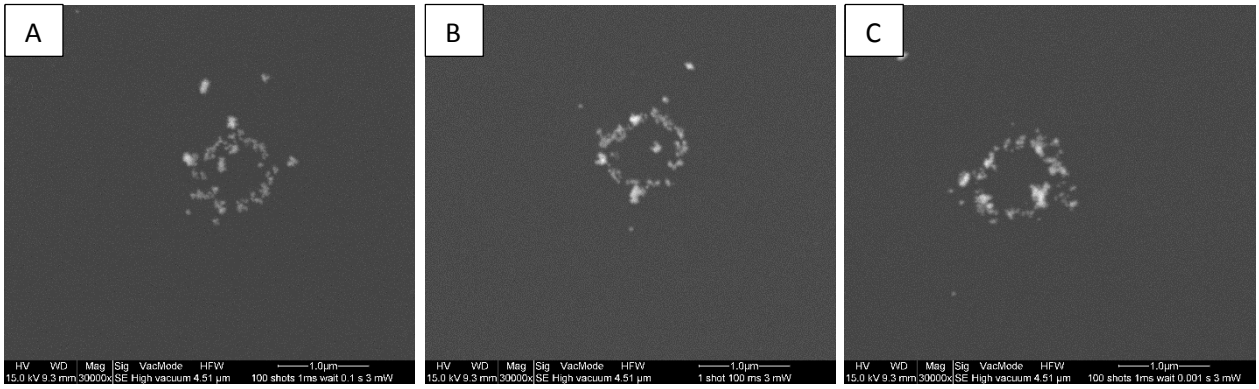

Figure 3.15: SEM images of a spot printed at laser power 3 mW **A)** @ 1 shot of 100 ms; **B)** @ 100 shots of 1 ms with waiting time 0.001 s; **C)** @ 100 shots of 1 ms with waiting time 0.1 s.

It is important to underline that the surfactant does not bond with the GNPs during their photo-reduction, since is ablated by the local heating [114]. Therefore, the GNPs that sticks on the surface are the ones ejected from the voxel after the exposure, which collect DMOAP molecule from the surface. These GNPs can grow until the until their surface isn't totally covered by the surfactant molecules, then their growth is inhibited [129, 131] and low polydispersity is observed. These phenomena are observed in case of both single and multiple shots. Thus, blasting effects are no completely avoidable and are observed even after the first single shot.

Thanks to the presence of PVA, in the other experiments (Figure 3.6-10, 13), the GNPs were trapped also inside to the virtual voxel and it was possible to carry out analyses on them. Moreover, the diameter observed for the ring printed in the water solution with a single 100 ms shot (Figure 3.15 A), is much smaller than that obtained in PVA at quite the same laser power (Figure 3.13 A), due to the high surface viscosity induced by the surfactant.

Summarizing, the possibility to write GNPs directly in water was demonstrated. This allowed to point out the role of polymeric matrices in the growth of agglomerates of gold nanoparticles, because of the underlying diffusive phenomena. In fact, as demonstrated by the experiments shown in this paragraph, the diameter of the cluster of GNPs obtained by TP-DLW depends on the blast that ejects GNPs from the virtual voxel and the viscosity of the surface. Using a substrate covered with a molecular film of surfactant, the surface viscosity is increased and the diameter of the spot is reduced. Moreover, since the surfactant inhibits the growth of GNPs low polydispersity is obtained.

3.4.4 Thermal effects

The characterization carried out until now allowed to get a complete picture on the diffusive phenomena involved during TP-DLW of single points. However, blasting effects are evident not only when exposing isolated points, but are also evident while printing patterns rich in GNPs. In fact, creating stripes, in polymeric matrices by using high values of energy dose, a shock-wave is generated during the printing process, and consequently GNPs are ejected from the scanned trajectory. Thus, on the top of the PVA film, GNPs appears to define the outline of the stripes, while, after development, multiple segments can be observed (Figure 3.16 C-D). This effect is not observed while printing patterns at low values of energy, in which local heating and thus the blasting wave effects are reduced (Figure 3.16 A-B), as discussed in paragraph 3.4.2.

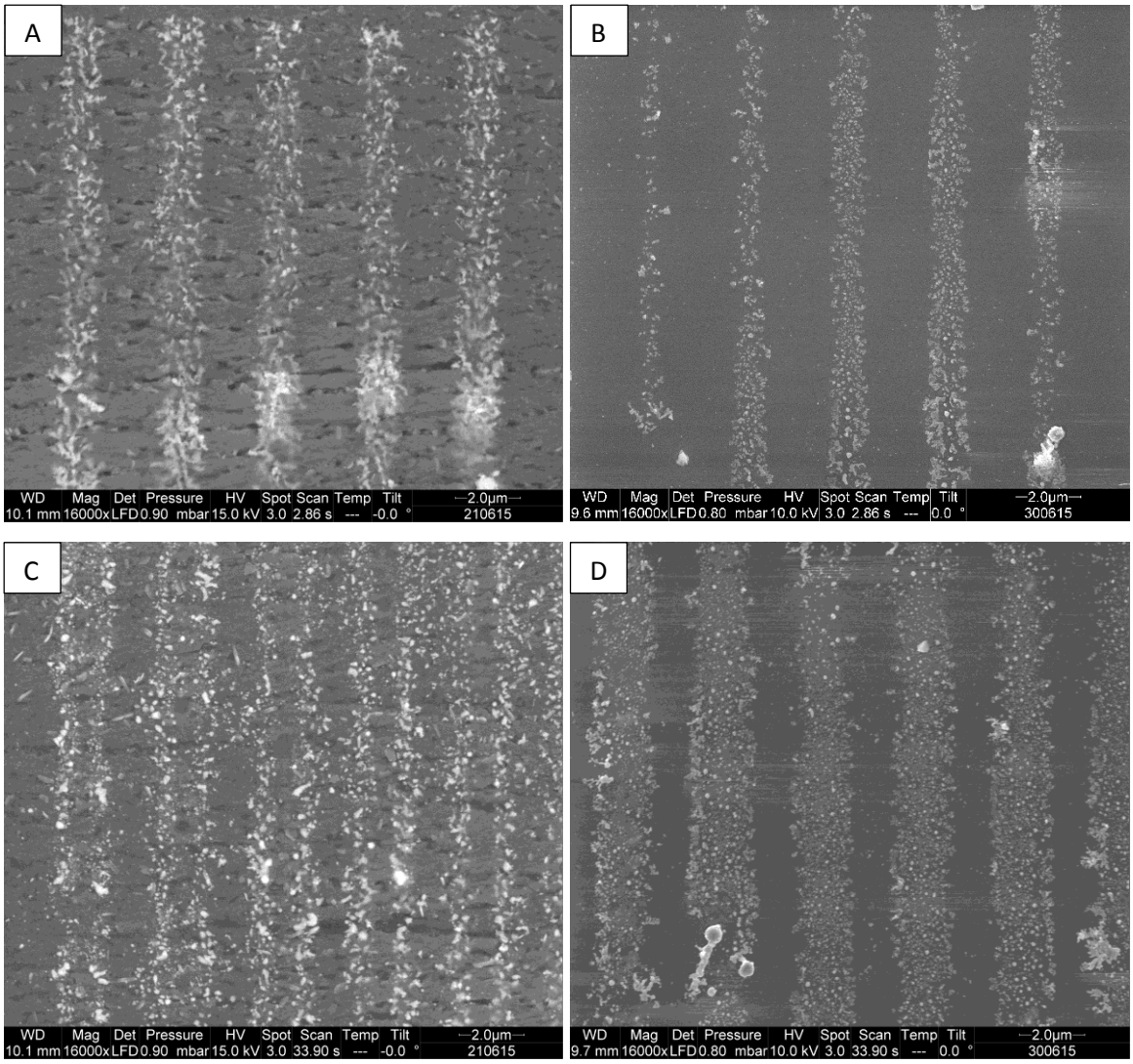

Figure 3.16: SEM images 1D gratings printed at scan speed 80 μm/s @ laser power 2.5 mW **A)** before and **B)** after development; and @ laser power 22.5 **C)** before and **D)** development. While the grating written at low laser power appears made by lines rich in GNPs both before and after the development, at high laser power gold nanoparticles at the top surface of PVA define the outline of the stripes, due to the ejection from the centre.

Therefore, two different results can be reached during TP-DLW of a metal precursor: either nanoparticles grow inside the focus figure and generate a compact structure, or a *twin stripes*, resulting from the ejection of GNPs from the centre toward the sides, will be obtained. sides. The difference between the two situations is relevant while creating 3D structures by using metal precursor in PVA, as in my case, or in combination with other photo-resists: blasting effects continuously change the boundary conditions, lead to

uncontrolled ablations, and generates an actual voxel larger than the predicted one, preventing the realization of three-dimensional structures.

In order to elucidate the dependence of the blasting on the delivered energy dose, I printed spots made by 100 shots of duration 1 ms, and waiting time between consecutive shots of 10 s, @ laser power ranging from 1 mW to 25 mW. In Figure 3.17 is shown the SEM images.

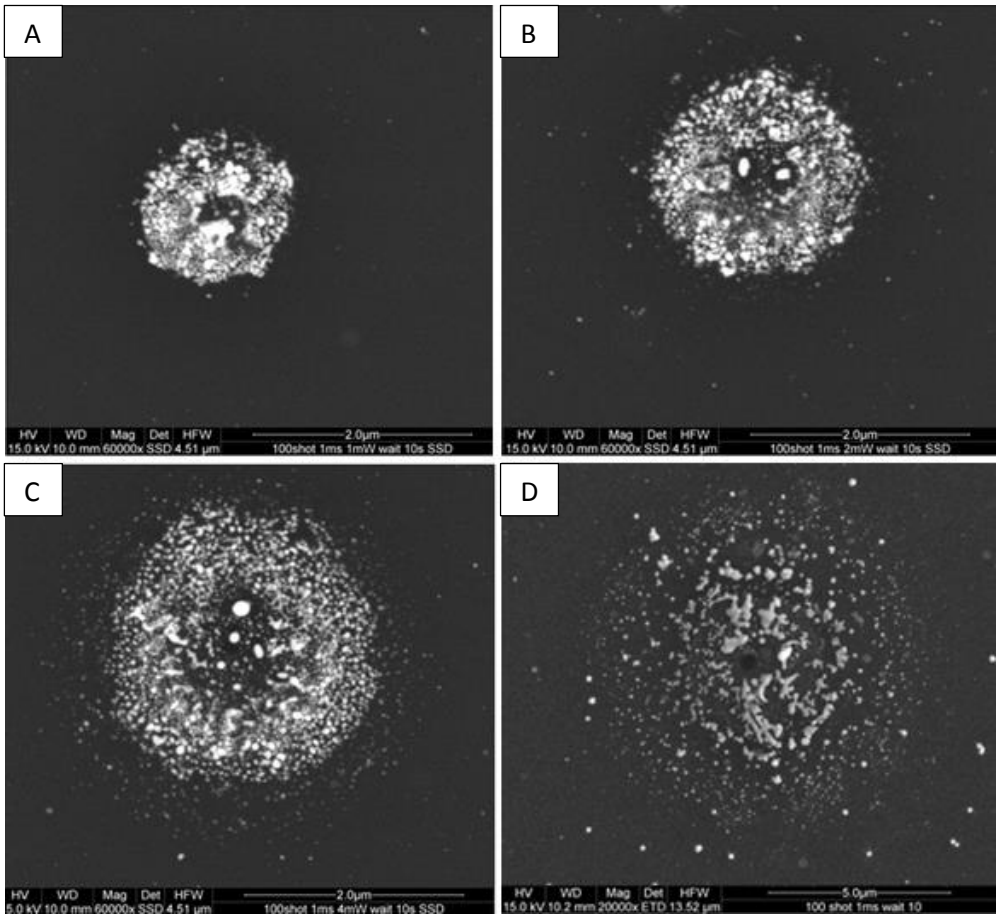

Figure 3.17: Spots of GNPs created by delivering energy through 100 shots of 1ms, with waiting time between each shot of 10 s. Laser Power used to obtain the spots are of **A)** 1 mW, **B)** 2 mW, **C)** 5 mW, **D)** 10 mW. The diameters of the GNPs aggregates range from 1.6 μm to 9.8 μm. A ring of ejected GNPs is observable in the spots written at higher laser power.

The higher the laser power, the higher the probability of TPA, which leads both to denser spots of GNPs created and to higher local temperature. As a consequence, the diameter of the spots created changes drastically from 1.6 μm to 9.8 μm, two orders of

magnitude larger than the diameter of the virtual voxel (680 nm). It is then clear that, in order to obtain GNPs dense, high-resolution structures, laser power has to be set accordingly, i.e. as low as possible, in order to reduce the local heating generating the blast.

Moreover, a temperature higher than 60° triggers the thermal reduction of chloroauric ions [242-243], resulting in the creation of GNPs in the heated surrounding area, affecting the resolution and increasing the dispersity.

All these effects are evident in the spot created at the highest laser power in Figure 3.17 C-D. The spot obtained has diameter 9.8 μm, at the centre of which a hole in the glass substrate is observable, confirmed by AFM analysis, as shown in Figure 3.18, indicating that the laser power was so high to generate a blast capable to hatch the substrate. The hole has a diameter of 480 nm, comparable with the laser beam waist, deepness of 30 nm and presents few nanoparticles inside.

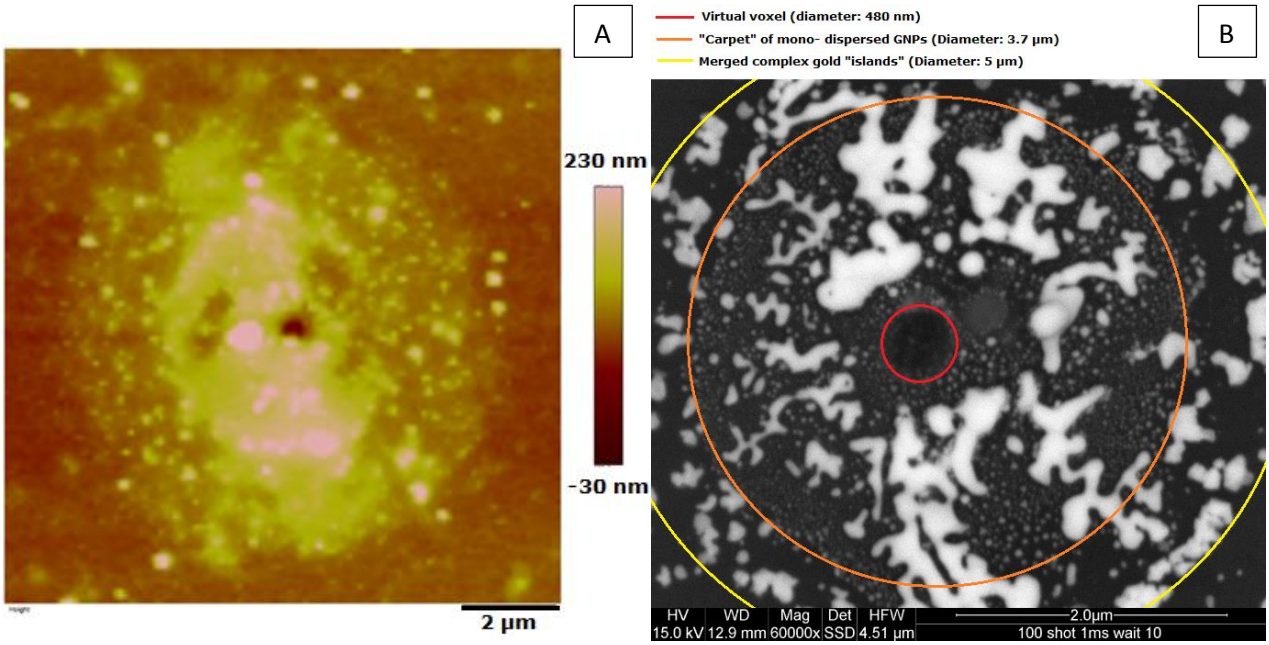

Figure 3.18: A) AFM image of the spot created with 100 shots of 1 ms, waiting time 10 s, with out-power of 25 mW, showed in Figure 3.17 D. The glass substrate presents a hole of 30 nm depth at the centre of the spot. **B)** SEM image of the centre of the spot. In red is evidenced the hole in the glass in correspondence of the virtual voxel (diameter of 480 nm). In orange the area occupied by mono-dispersed gold nanoparticles (diameter 3.7 μm). In yellow the area occupied by gold merged structures (diameter 3.7 μm).

As can be observed in Figure 3.18 B. inside of the spot, different μm areas are revealed:

- The hole generated by the blast in correspondence to the virtual voxel;
- a carpet of ~30 nm GNPs which occupy a diameter of 3.7 at the centre of the spot;
- larger complex gold structures that lay upon the carpet of GNPs and occupy a diameter of 5 μm;
- The annulus described in Figure 3.11.

According to the literature [200], when GNPs are heated at temperature above 200 °C, they merge together to generate larger complex structures. Thus, the GNPs polydispersity becomes uncontrollable when high temperatures are reached.

Moreover, if one wants to print bi-composite structure, using mixtures containing metal precursors and organic photo-resist, has to consider that many resins cannot be heated at temperature larger than 200 °C, since the resin may either decompose and be permanently damaged, or spontaneous uncontrolled polymerization is triggered.

For these reasons, it is extremely relevant to estimate the temperature reached during TPPR. To probe temperature, thermocouples or thermo-cameras are usually employed. However, due to the small dimensions of the area considered and the short life-time of the phenomena, these instruments are unsuitable during TP-DLW of gold nanoparticles.

In order to have a quick mapping of the temperature reached during the TP-DLW, I made a series of experiments of TP-DLW using a chip of thermographic paper (that is commonly used to print the cash tickets) as matrix for the chloroauric solution. Thermographic paper works in combination with thermal printer: the print pins are heated and pressed on the paper surface, which is covered by a film of triarylmethane phthalide, a colourless dye in crystalline form, darkening during the solid-liquid phase transition. A sensitizer and a stabilizer are added to the mixture, to stabilize the threshold temperature of coloration around 100 °C, to stabilize the melted phase and to prevent the dye crystallization when the temperature decreases [201].

To characterize the thermal paper, I wetted different chips with deionized water, and heated single points directly on the wetted thermo-sensitive surface of the paper, by using a heated tip controlled by a thermocouple. The actual tip temperature value was read by means of a thermo-graphic camera.

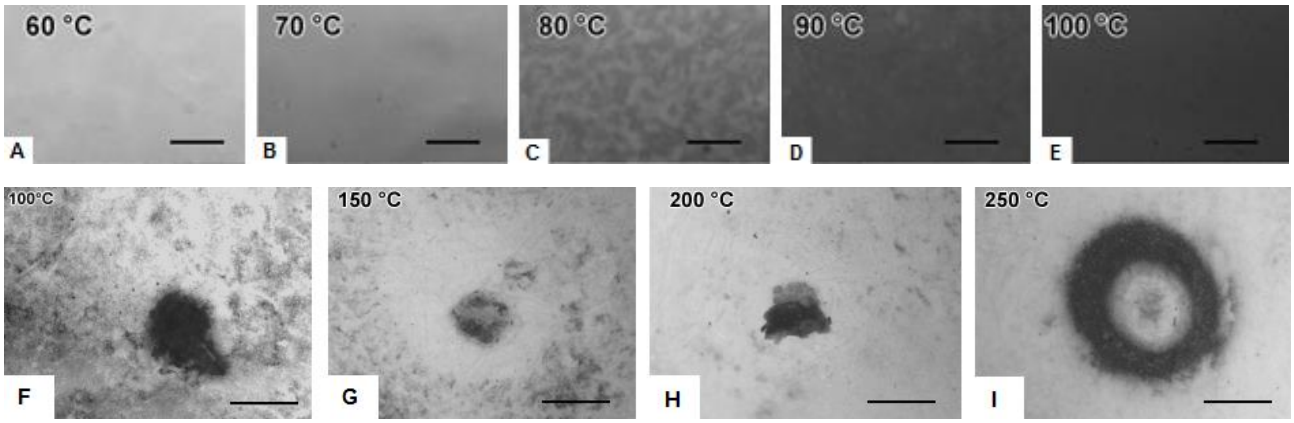

Figure 3.19 Optical images taken in reflection mode, of thermo-graphic paper heated by a tip. **A-E)** The paper darkens when heated at temperatures ranging from 60 °C to 100 °C, due to the phase transition of the dye. The line bar in the inserts is of 30 μm. No darker results has been obtained over 100 °C, **F-I)** however the dye darkens in specific patterns in function of temperature. At 100 °C a black spot, whose dimension is comparable with the diameter of the heated tip, is surrounded by a grey area, due to thermal diffusion on the water film during the printing. Increasing the temperature, evaporation lead to an expulsion of the dye, and therefore a white area can be seen around the spot. After 250 °C, an internal white area and a black ring surround a grey spot, whose dimension. Temperature has to be considered equal to or larger than 250 °C inside the black ring. In this second set of image, the line is of 1.5 mm.

In Figure 3.19, are shown the different shades and patterns of grey in which the thermo-chromatic paper turns. No darkening is revealed below 60 °C, it starts to darkens around 70 °C and it becomes black when the temperature is equal to or larger than 100 °C (Figure 3.19 A-E). For temperature higher than 100°C, no darker shades are achieved, however specific patterns were observed.

In fact, as shown in Figure 3.19 F-H, between 100 °C and 200 °C, a single black spot of the dimension of the tip is formed. Around the spot a white area is revealed. Increasing

the temperature up to 250 °C or above, the pattern observed is made of a dark spot surrounded by a white area and a black ring.

I wetted a square of 1 x 1 cm^2 of thermo-graphic paper with a water solution of tetrachloroauric acid, free of PVA, as in paragraph 3.4.3. The sample was sandwiched between two 22 x 22 x 0.13 mm^3 coverslip, to obtain a flat interface. I printed two 5 x 5 matrices of single points in an area of 200 x 200 μm^2, with a single shot of 100 ms @ 25 mW in one sample, and 100 shots of 1 ms @25 mW and wait time 10 s between each shot, in the other. Analysis on the thermo-graphic paper was performed by means of optical microscope working in reflection mode, with a 5x and a 20x objectives. The obtained patterns have been compared with those obtained in the characterization step.

Figure 3.20 A shows that delivering the energy dose by a single shot (25 mW @ 100 ms), temperature reached is around 100 °C, with a dark spot of 10 μm as diameter. At the centre of the black point, it can be recognized the yellow spot of GNPs of diameter 2 μm thanks to the scattering of the light from the clusters of gold nanoparticles. When the energy dose is instead delivered by means of 100 shots @ 1 ms with waiting time of 10 s (Figure 3.20 B) the temperature is increased up to around 250 °C, since the pattern obtained for the shots is similar to that obtained in the last inset in Figure 3.20 B. In Figure 3.20 C, I have also compared the dimensions of the pattern obtained on the thermo-graphic paper, with the spot of GNPs written in the polymeric matrix and analysed in Figure 3.20 F. The diameter spot of GNPs corresponds to dark internal area of the pattern, thus all the spot reached a temperature larger than 250 °C.

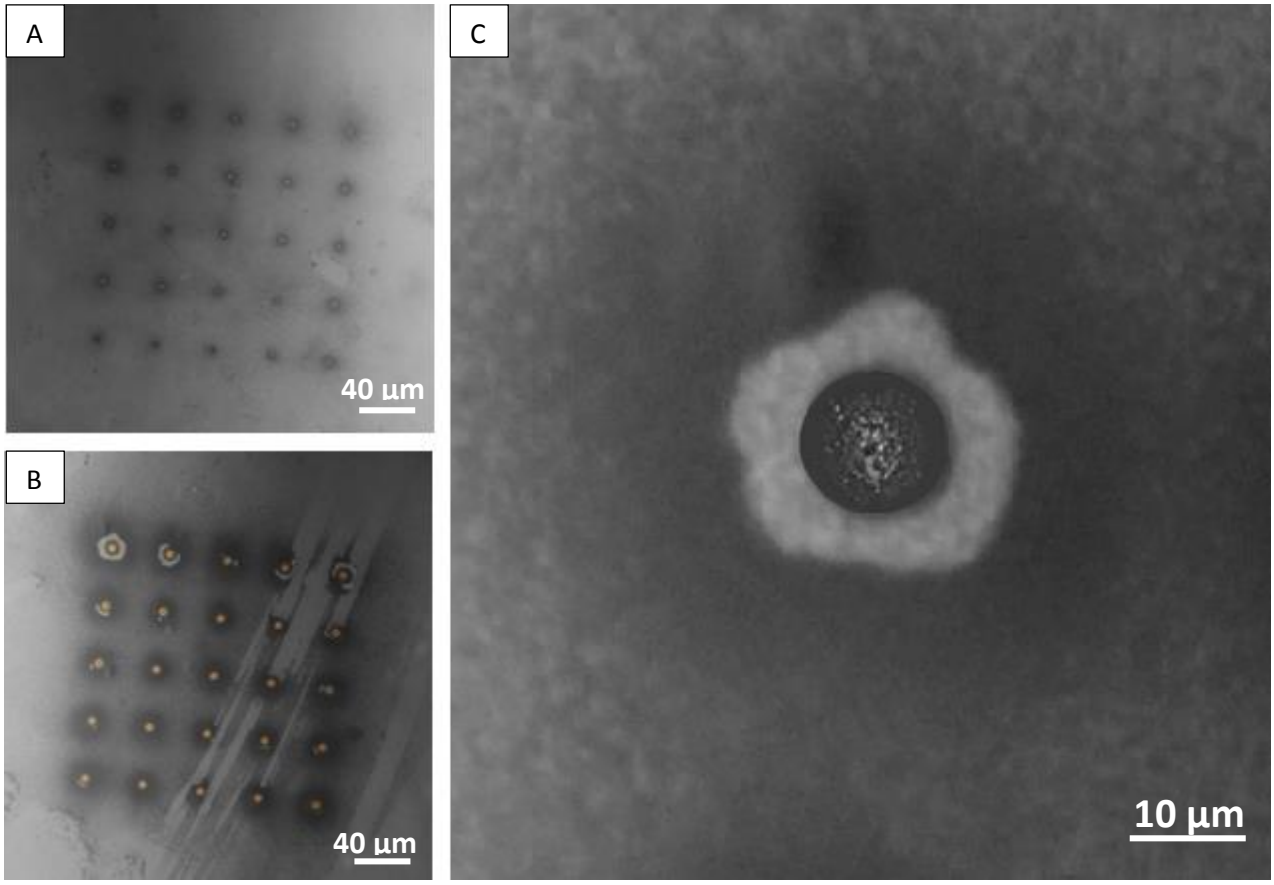

0Figure 3.20: Matrix of points written at 25 mW laser power by exposure of **A)** a single shot of 100 ms **B)** 100 shots of 1 ms, with 10 s of waiting time. **C)** Comparison between the first point of the second matrix created on the thermo-graphic paper and the spot observed by SEM imaging, created in the same laser condition.

I want to stress that this has to be considered mostly as a qualitative result, however according to my best knowledge, this is the first successful attempt of a direct temperature measurement and mapping with an adequate resolution, during TPPR of metal precursor. Moreover, this method allows to demonstrate that the temperature reached while printing at high laser power is such to trigger uncontrolled growth of GNPs due to thermal effects and to justify the presence of fused structures of GNPs, in accordance with Ref. [200].

In conclusion, from my work it appears clear that diffusive effects during TP-DLW of metal precursors are not negligible and strongly interfere with resolution of the system. In the realization of 3D structures made of metallic nanoparticles, blasts have absolutely to be avoided, therefore different effects have to be taken in account.

First of all, it has been shown that delivering the energy dose through multiple exposures can consistently improve the final result, provided to wait between each shot a time long enough to allow to the ionic diffusion to refill the exposed area. However, in order to minimize blasting effects, the number of shots at which deliver the energy dose and the hosting matrix has to be opportunely selected.

Moreover, thermal effects can be a hindrance in the realization of high-resolution pattern of GNPs, thus have to be controlled by means of ions concentration and laser power. Lastly, a new method to measure and map the temperatures reached during TPPR has been carried out.

3.5 Control of the ions diffusion through electric fields

My studies on the physical phenomena involved in TP-DLW of GNPs. demonstrated the key-role played by the ionic and water diffusions. In particular, to get structures of GNPs with high density and resolution it is mandatory to minimize the heating. To do this, low concentrations of precursor are favourable. However, at the same time, ionic diffusion has to be controlled in order to get denser aggregates of GNPs.

Here, I propose a different approach with respect to that used in the previous experiments, or in literature. Applying an electric field to the system, the local ionic concentration can be tuned, making the seeding and the growth of GNPs controlled.

To this purpose, I created an electrolytic cell made by a standard coverslip (22 x 22 x 0.13 mm^3) and a ticker glass plate (20 x 18 x 1 mm^3). Their surfaces were sputtered with a thin film of ~20 nm of indium tin oxide (ITO). Two stripes of copper, thick 100 μm, were put between the two electrodes and alternatively insulated on a side by a Mylar film of 10 μm, to avoid direct charging transfers and short circuits between the electrodes. An epoxy resin was used to seal the cell and to insulate its sides. Is thus possible to obtain a vertical electric field by applying a voltage to the ITO electrodes (Figure 3.21).

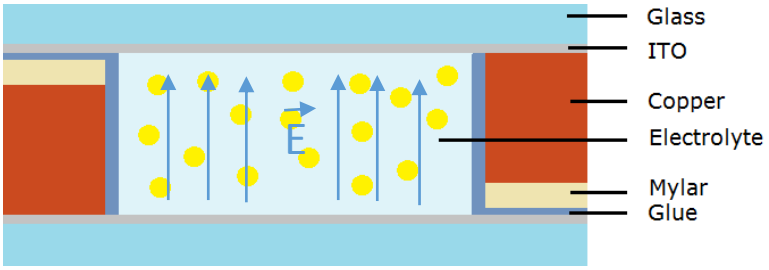

Figure 3.21: Scheme of the electrolytic cell built. Two coverslip were coated with an ITO film. Two copper stripes were used to connect the electrodes to a DC source. A thin Mylar film was used to insulate the electrodes. An epoxy resin was used to seal the cell.

The cell was filled with an aqueous solution made of deionized water and 0.73 mM in $HAuCl_4$, one tenth of the concentration used before. No PVA or other polymers were added to the solution.

The chloroauric ion $AuCl_4^-$ is present in water as a solvated ion, thus it is surrounded by water molecules, with the positive dipole facing it. Ions near the surfaces are adsorbed upon them in order to neutralize their charge density. Thus an electric double layer is generated. When a voltage is applied, more ions are involved in the EDL in order to shield the electric field [202]. Solvated ions in the volume are not affected, providing that their concentration is high enough.

In this way, one can use an adequate potential difference, well below the reduction potential of $AuCl4^-$, in combination with low concentration, to move the ions on an electrode. This process should allow to select the number of ions involved in the photo-reduction, minimizing the thermal effects. Moreover, tuning the potential, after the exposure, diffusion of the chloroauric ions is controlled, thus an homogeneous growth of the GNPs can be reached.

To describe the system, Stern-Gorahem model is used [202]. When a potential is applied in an electrolytic cell, three region can be distinguished:

- **Inner Helmholtz plane (IHP)**, layer made by ions absorbed on the surface, which have partially or completely lost the solvated shell. Its thickness is equal to the ion radius.

- **Outer Helmholtz plane (OHP)**, a second layer generated by solvated, non-adsorbed ions, which approach the electrode only up the IHP and interacts with the surface through long-range electrostatic forces. Its thickness is equal to the solvated ion radius. IHP and OHP together forms the compact layer, or Stern layer.
- **Diffusive layer** or mobile layer, assumed the Maxwell-Boltzmann statistic, the solvated diffuse ions near the surface are subjected to electrical and thermal fields and their charge distribution depends on the distance from the electrode.

The thickness of the EDL $1/\chi$, namely the Debye's length, depends on the ion concentrations:

$$\frac{1}{\chi} = \sqrt{\frac{\varepsilon KT}{8\pi e^2 \sum_i c_i^0 Z_i}} \tag{3.24}$$

Where ε is the dielectric constant of the solution, c_i^0 is the concentration of a specie of ion inside of the electrolytic cell and Z_i is its charge.

The charge distribution is a function of the distance between the solvated ions and the electrode, and can be estimated thanks to the Debye-Hückel approximation.

$$Q = -\frac{\varepsilon}{4\pi}\frac{d^2\psi(z)}{dz^2} \tag{3.25}$$

Where $\psi(z)$ is the electrical potential, which decrease linearly in the Stern layer, but as $\psi(z) = \psi_0 e^{-\chi z}$ in the diffusive one (Figure 3.22 B). At distance larger than the Debye length $\psi(z)$ is equal to zero.

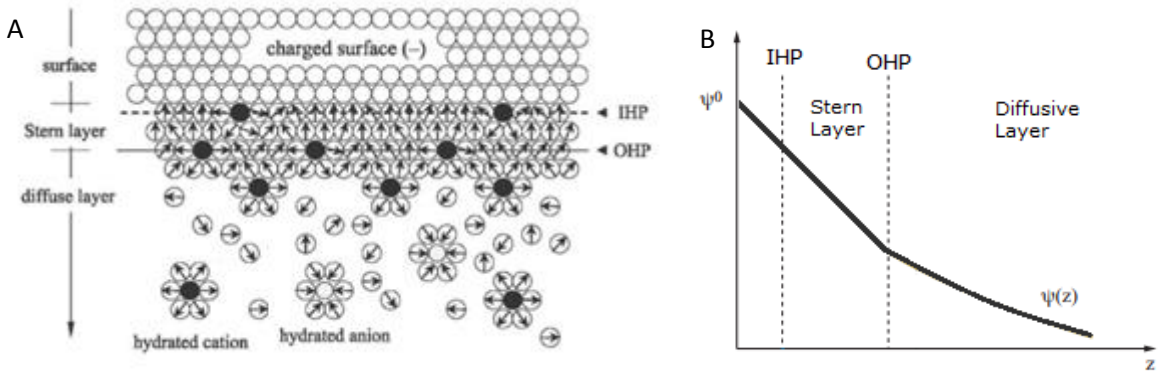

Figure 3.22: A) Scheme of the Double layer: adsorbed and solvated ions generate respectively the inner and outer Helmholtz plane in correspondence of the electrode, thus the Stern compact layer, over which diffusive solvated ions form the diffusive layer. **B)** Electric potential in correspondence to the Stern and Diffusive layers.

According to the model exposed, a double layer of $AuCl_4^-$ ions is generated on the positive electrode when the potential difference is applied, while a double layer of the counterion is on the negative electrode. Hence, by printing on the surface of the two electrodes, different results are expected, provided that low concentrations are used.

In fact, it is important to underling that the Debye's length is usually in the order of 1 nm, while the virtual voxel depth is two order of magnitude larger. Since the ions in the virtual voxel, beyond the Debye length, are not affected by the electric field, their diffusion cannot be controlled in this way. Thus, printing on both the electrodes of an electrolytic cell, containing high ionic concentration, the same result is obtained as in the case of zero E field, but in correspondence of the Debye length. Vice versa, if the concentration is low enough so that all the available ions are involved in the EDL, printing on the positive electrode should allow the gold seeding of the solvated chloroauric ions of the EDL, while no results are expected on the negative one.

However, according to the literature [203], even in case of very low concentration, both a positive and a negative electrical potential can be used to efficiently obtain the electrodeposition of GNPs. Gotti et al., in fact, showed electrodeposition of GNPs on glassy carbon electrodes by applying both a voltage of +0.7 V and -0.3 V. In the former case, they obtained low density of GNPs of diameter 90 nm, in the latter the deposition of GNPs of 10

nm of density two order of magnitude higher than the one obtained with a positive potential. Moreover, they show that increasing the duration of the electrodeposition, no interesting result is observed for the negative potential, while at +0.7 V the density of GNPs is reduced, and their dimension is increased of one order of magnitude, suggesting the aggregation of the GNPs.

Their work demonstrated that two different photo-reducible species of ions are involved during the electrodeposition. According to eq. (3.1-6), the specie to be reduced to obtain the gold reduction is $AuCl_2^-$, which is generated during the photo-exposure. However, according to their work, a positive ion (Au^+) is present in the mixture to grant the electrodeposition of GNPs on the negative electrode.

To verify their results, I applied 1 V to my system showed in Figure 3.21 for 40 minutes and measured the results by means of AFM. As shown in Figure 3.23, on the negative electrode a uniform layer of mono-dispersed GNPs with diameter ~90 nm was created, while on the positive electrodes larger agglomerates were obtained. EDX measurements were performed to verify the golden nature of the objects.

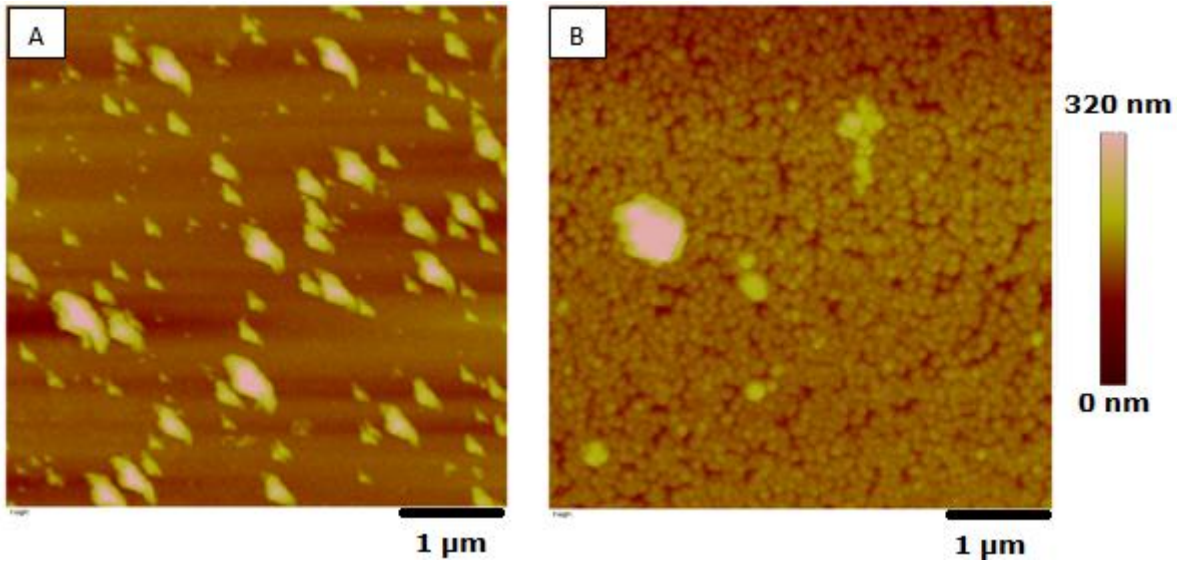

Figure 3.23: AFM imaging on the **A)** positive and **B)** negative ITO electrode after electrodeposition of GNPs by applying a potential difference of 1 V for 40 minutes.

This effect can be explained assuming the presence of ions Au^+ in the solution, thus an instability in the $AuCl_4^-$ specie, which lead to the formation of a double layer of Au^+ on the negative electrode. To verify this hypothesis, I applied a potential difference of ±50 mV, well below the reduction potentials, and printed lines of GNPs on both the electrodes. SEM imaging was performed on samples written using laser power 25 mW @ scan speed from 10^2 μm/s to 10^5 μm/s on the electrode @ -50 mV (Figure 3.24 A-H) and @ +50 mV (Figure 3.24 I-P).

The biggest differences observed on the samples in Figure 3.24 do not depend on the voltage applied: increasing the scan speed, the exposure time is reduced, therefore thermal and diffusive effect, as seen in the previous paragraph, are reduced as well. In function of the exposure times blasting effects and strong concentration gradients can occur, which lead to the formation of large aggregates of GNPs (up to 10 μm). The creation of these clusters, hence, has to be ascribed to the interplay between ions mobility and the exposure time.

While high local ions concentrations lead to the creation of GNPs aggregates, elsewhere a segment of low density of mono-dispersed GNPs of diameter (30 ± 5) nm is obtained, after the laser sweep (Figure 3.24 B, J). The highest the scan speed, the smaller the number of cluster obtained, thus the higher the density of the nanoparticles in the segment. In fact, @ scan speed 100.000 μm/s, no micro-cluster are created, therefore the lines of GNPs are made of high density GNPs, which aggregates together in nano-cluster, paving the way to realization of continuous stripes of GNPs through this technique.

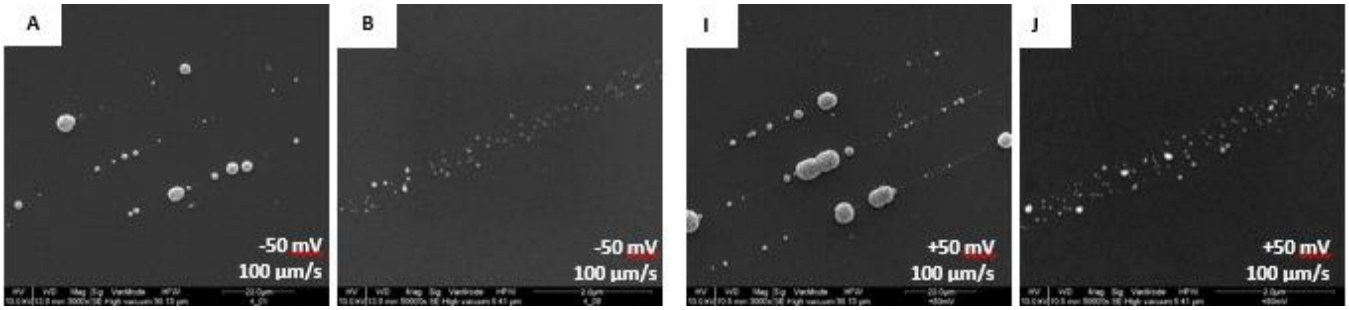

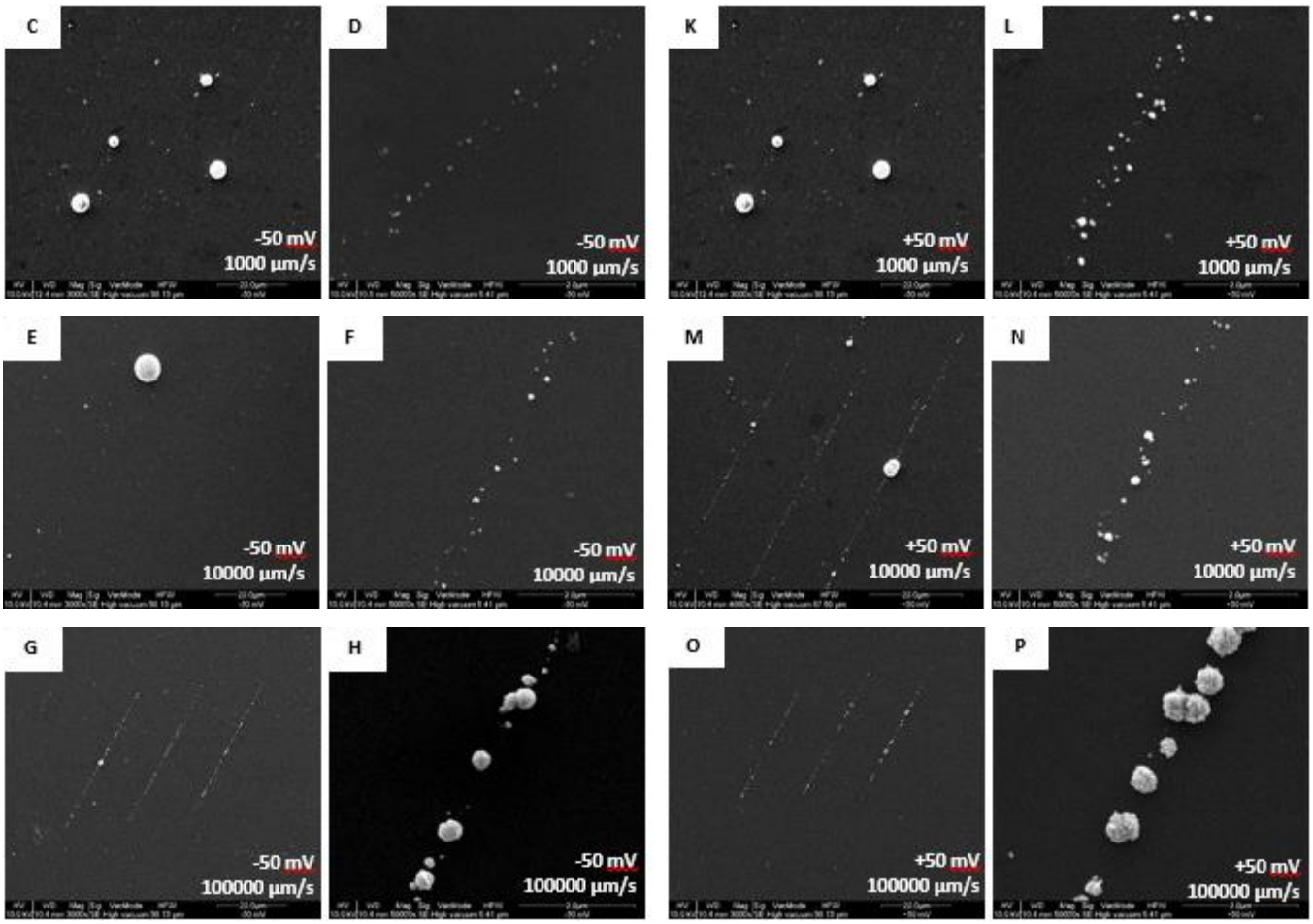

Figure 3.24 SEM images of lines written at laser power 25 mW @ **A-B)** 100 µm/s; **C-D)** 1000 µm/s; **E-F)** 10000 µm/s; **G-H)** 100.000 µm/s on the electrode at -50 mV, and @ **I-J)** 100 µm/s; **K-L)** 1000 µm/s; **M-N)** 10000 µm/s; **O-P)** 100.000 µm/s on the electrode at +50 mV.

One of the most relevant results observed is the possibility to stick GNPs on the glass surface, without using any polymeric matrix, but writing inside of the double layer. Moreover, thanks to the low ions concentration, local heating is reduced and the blast effects negligible. In fact, the diameter of all the obtained lines is equal or lower than the beam waist, from 300 to 600 nm.

This result is obtained both for the positive and the negative electrode, however the lines created on the positive electrode present generally higher density, which indicates that the $AuCl_4^-$ ions involved in the TP-DLW process are more than the Au^+ ions, as expected.

However, the most interesting phenomenon observed is connected to the time of growth of the GNPs in the segments. In Figure 3.25 are shown the optical images of stripes

created on the negative electrode at laser power 25 mW @ scan speed 2000 μm/s, taken through the camera connected to the oil-immersed 63x objective of the system. Patterns of GNPs appear in black on the camera and, printing on the positive electrode, the lines appeared immediately afterwards the laser swept. Vice versa, Figure 3.19 A shows the laser sweeping the third line and no trace of the first two lines is observed. After 1 minutes and 30 seconds at -50 mV three gray segments can be recognized on the substrates, which darken after 4 minutes (Figure 3.25 B-C). Then, the intensity of the voltage was increased up to -100 mV, and darker lines are obtained after 40 s, and they become black after 4 minutes. (Figure 3.25 D-E).

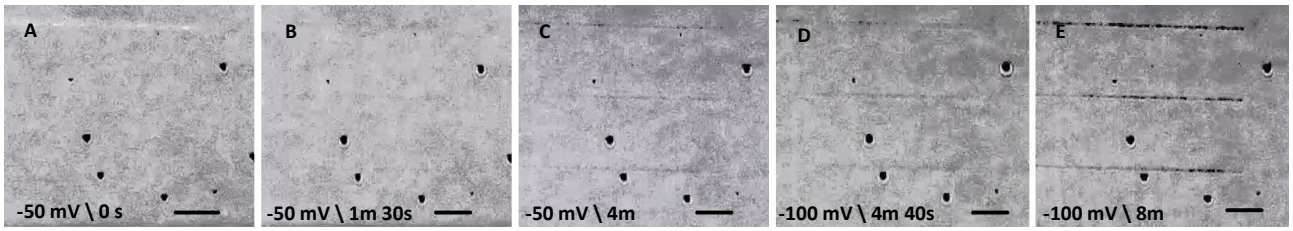

Figure 3.25: Optical images obtained through a camera connected to a 63x objective of the **A)** Direct laser writing process of three lines of GNPs in an electrolytic cell, written at laser power 25 mW @ scan speed 2000 μm/s, while a voltage of -50 mV was applied. The lines are written from the bottom to the top, so no line appear after the laser swept. After the printing, the sample was observed after **B)** 1 min and 30 s and **C)** 4 min. The potential different was increased at -100 mV and the sample was recorded after **D)** 40 s, **E)** 4 min. The scale in the image is 10 μm.

I ascribe this result on the lower density of Au^{+} ions present in the solution. Therefore, the laser sweep creates some seeds of gold Au^{0}, not visible. However, after the photo-reduction, the seeds absorbed on the negative electrode act as a sharp tip, on which the electric field is magnified (Figure 3.26). As a consequence, the local electric field focuses the Au^{+} ions coming from the bulk. When the gold ions Au^{+} come to the surface of the gold seeds, they are reduced by autocatalysis, and the growth process starts [241]. Increasing the voltage more ions are involved in the process and bigger nanoparticles are obtained in a shorter time.

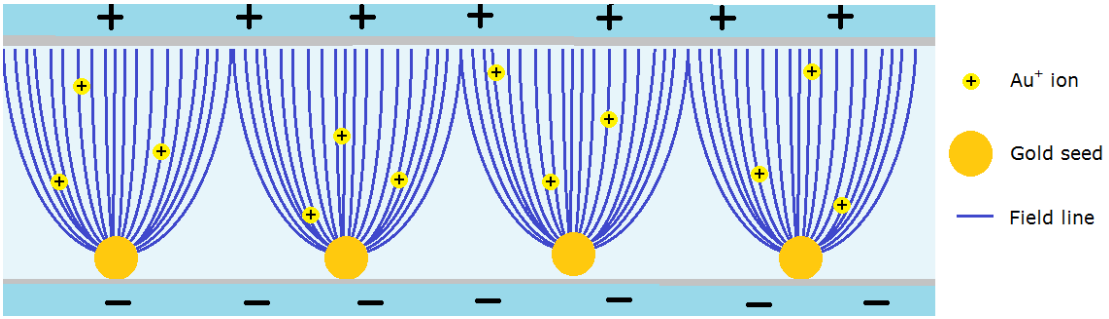

Figure 3.26: Electric field in correspondence of the gold seeds. Thanks to their size, they act as sharp tip and focus the Au^{+} ions coming from the bulk. Thanks to autocatalysis, the ions are reduced on the surface of the seed and the growth process starts.

This result demonstrates that in controlling the size of GNPs three elements play a key role: low concentration, to minimize thermal effects; the amplitude of the applied voltage that allows to control the local ionic concentration and diffusion; the time of diffusion of the ions from an electrode to the other one which could last even few minutes.

In conclusion, the physics involved in the TPPR of a gold precursor was investigated. In particular, I pointed out the role of concentration and thermal diffusion, during the exposure and demonstrated how the different phenomena have been discriminated in order to get a control on resolution, size and poly-dispersity of the GNPs patterns created. To do this, TP-DLW with an electrophoretic control of the local ionic concentration appeared to be a most promising method to optically nano-fabricate GNPs structures.

4 TP-DLW of gold nanoparticles for thermo-plasmonics and detecting applications

In last chapter, I showed how to obtain better control of micro-fabrication of structures made in GNPs. Thanks to the exotic properties that gold manifests at the nanoscale, in the last decade, GNPs have been employed in a wide field of applications, such as sensing [85], diagnostic [89], drug delivery [90], cancer therapy [91-92], imaging [93-94] and much more.

The technological interest in GNPs is due to their interaction with light. Light with wavelength λ and penetration depth δ much larger than the size of a metal nanoparticle can entirely probe the electron cloud of the NP, putting into oscillation the electrical charges of matter (conduction electrons and protons) [204].

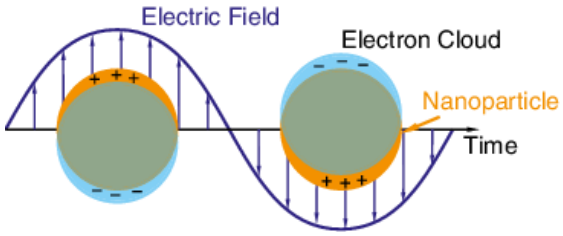

Figure 4.1: The electric field that runs over the nanoparticles put in oscillation the Au electron cloud, which acts as a dipolar oscillator.

The system can be described as a dipolar oscillator characterized by a resonance frequency called Localized Surface Plasmon Resonance (LSPR). The electrons oscillate in phase, creating an electric field opposed to the excitation field, which results in a restoring force. However, this oscillation is partially dumped, through the emission of a secondary radiation (light scattering) and creation of heat.

As it will discussed below, these effects can be exploited respectively to detect biological molecules or to induce controlled local heating of the surrounding material with nanometric resolution (thermo-plasmonics).

In this chapter, is briefly exposed the interaction between GNPs and light; then, some possible smart-applications for patterns of GNPs created through TP-DLW are shown.

4.1 Localized Surface Plasmon Resonance

When light impinges on a noble NP distorts its electric cloud. In terms of metal polarizability the distortion can be described as [96, 205]:

$$\alpha(\lambda) = 3\varepsilon_m(\lambda)V_P \frac{\varepsilon(\lambda) - \varepsilon_m(\lambda)}{\varepsilon(\lambda) + \chi\varepsilon_m(\lambda)} \tag{4.1}$$

Where $\varepsilon = Re[\varepsilon(\lambda)] + i\, Im[\varepsilon(\lambda)]$ and ε_m are respectively the dielectric constant of the nanoparticle and of the surrounding material; V_P is the volume of the nanoparticle and χ is a geometrical parameter equal to $\chi = 2$ for a sphere.

From equation (4.1), the absorption cross-section σ_{abs} can be obtained [95,206]:

$$\sigma_{abs} = \frac{18\pi\sqrt[3]{\varepsilon_m^2(\lambda)}}{\lambda} V_P \frac{Im[\varepsilon(\lambda)]}{\big(Re[\varepsilon(\lambda)] + 2\,\varepsilon_m(\lambda)\big)^2 + Im[\varepsilon(\lambda)]^2} \tag{4.2}$$

From this equation it appears evident that the plasmon resonance is strictly correlated to the volume of the nanoparticles and its dielectric constant. Moreover, σ_{Ext} is maximized for:

$$Re[\varepsilon(\lambda)] \sim -\chi\, \varepsilon_m(\lambda) \tag{4.3}$$

Eq. (4.3) indicates that changing the shape or the dielectric constant of the surrounding material, the frequency of the LSPR is tuned. When the condition in eq. (4.3) is verified, the enhancement of the internal electric field E_i is obtained and the resonance occurs.

It is important to underline that in condition of quasi-static approximation (NP diameter $d_P \ll \lambda$) the absorption and extinction cross-section are comparable:

$$\sigma_{Ext} = \sigma_{abs} + \sigma_s \sim \sigma_{abs} \tag{4.4}$$

In this approximation, in fact, the field inside the sphere can be considered uniform and the surface charge distribution generate a single dipole. Otherwise, for larger NP ($d_P \sim \lambda$) a multipolar configuration is to be considered and the extinction cross-section depends also on a term of scattering, described in equation (4.5) [206]:

$$\sigma_s = \frac{24\pi\varepsilon_m^2(\lambda)}{\lambda^4} V_P^2 \left(\frac{Re[\varepsilon(\lambda)] - \varepsilon_m(\lambda)}{Re[\varepsilon(\lambda)] + 2\,\varepsilon_m(\lambda)} \right)^2 \tag{4.5}$$

In Figure 4.2 the contribution of σ_s and σ_{abs} to the extinction cross-section is revealed.

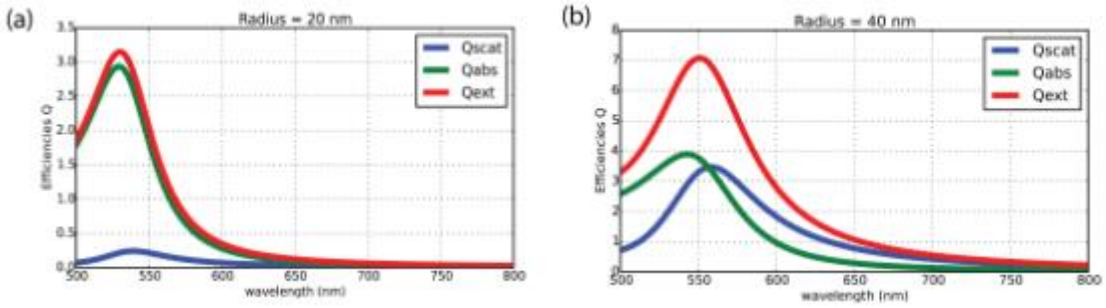

Figure 4.2: Extinction spectra for a GNP of radius **A)** 20 nm and **B)** 40 nm. For smaller nanoparticles, the extinction spectrum is approximable to the absorption one. For larger nanoparticles, scattering plays a no-negligible role.

The plasmon resonance has a maximum in the visible or NIR range of the spectrum for gold nanoparticles, and its extinction cross-section is usually much larger than the NPs geometrical size, or that of conventional dyes. [207]

Moreover, noble NPs behave as nanolenses and, when the LSPR is excited, the dipole radiates a near-field electro-magnetic wave, whose amplitude can be enhanced by a factor up to 10, and rapidly falls off with distance. This effect overcomes the typical resolution limit of far-field optics, allowing light localization on nanometric or subnanometric scale [87]. Since the LSPR of a GNPs depends on the dielectric constant of the surrounding

material ε_m, even a small changing in the medium leads to a shift in the extintion spectra of the GNP. Thus, noble NPs are great candidates for sensing of chemical and biological molecules, because of their intrinsic sensitivity.

4.2 SERS enhancement scattering from TP-photo-reduced arrays of GNPs

A powerful analytical technique for detection of chemical and biological active molecules adsorbed on rough metallic surfaces or on metallic nanoparticles is given by Surface-Enhanced Raman Scattering (SERS).

Briefly, Raman spectroscopy is a non-disruptive technique based on the inelastic scattering of light. Inelastic scattered light is shifted in energy from the laser frequency due to interactions between the incident electromagnetic waves and the vibrational energy levels of the molecules in the sample [208].

The electrodynamic enhancement of the local electric field due to LSPR of noble nanoparticles is one of the most powerful mechanism to obtain enhancement of the Raman signal [209-210]. The most favourable conditions for LSPR enhancement are met on specific "hot spots" of the surface, which are usually associated with nanoscale metallic tips [211-212] (tip hot spots) or the gap between two closely spaced metallic nanoparticles, the so called "gap hot spots" [213-214]. Much of the efforts in SERS research in recent years have been focused on fabrication of artificial plasmonic structures in order to maximize the electrodynamic enhancement, as well as to accurately tune the SPR in a desired spectral range [215].

Other authors have already showed how TP-DLW of gold and silver NPs can be employed as SERS substrates. I put instead attention on how the enhancement factor of the signal can be improved as a function of the energy dose delivered to write the structures. Here are reported some preliminary results.

The sample was prepared according to the procedure showed in chapter 3.2. On it, a batch of 50 gold 1D arrays was produced by 2-PDLW, with the laser power in the range 2.5-

22.5 mW @ scanning speed from 10 to 100 μm/s with a step of 10 μm/s. The period of the parallel gold stripes within a single array was 4 μm.

Raman spectra were recorded on a LabRAM micro-Raman spectrometer with a He-Ne laser excitation at 632.8 nm. The laser beam was focused onto the glass surface through microscope equipped with ×50 objective onto a spot of typical diameter of 5 μm, as shown in Figure 4.3. Reference Raman spectra were taken from the substrate and the gold stripes prior to any SERS measurements. After that Raman spectra were recorded with the sample immersed in a 10^{-5} M water solution of rhodamine-6G. Subsequently, the sample was washed in ethanol and exposed to a technical grade xylene (mixture of ortho-, meta-, and para- isomers) for 5 minutes, then washed again in ethanol, and finally the Raman spectra were investigated for detection of trace amounts of xylene.

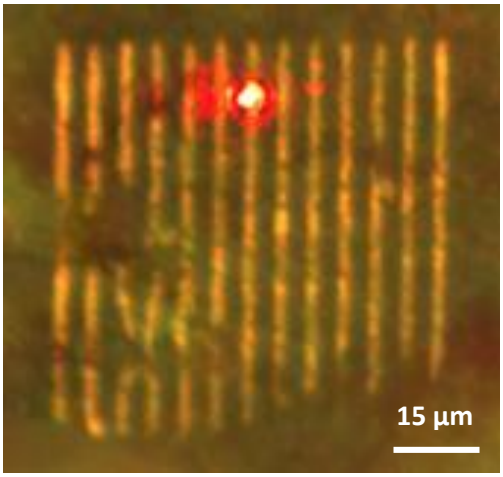

Figure 4.3. Gold stripes as seen under optical microscope. The laser focus on the sample is also visible as a bright spot

The reference spectrum, taken from the bulk of concentrated 10^{-3} M R6G solution, is shown in Figure 4.4 A. A typical spectrum taken in correspondence of a GNPs strip, when the glass substrate was immersed in a 10^{-5} M R6G solution, is shown in figure 4.4 B. The Raman lines of R6G significantly widen in the vicinity of gold stripes and increase in intensity. When the integrated intensity of the Raman bands is normalized to the R6G concentration, as described in [216], the SERS enhancement factor (EF) accounts for $\approx 10^4$ on average for the array written @22.5 mW/10 μm/s during the 2-PDLW process.

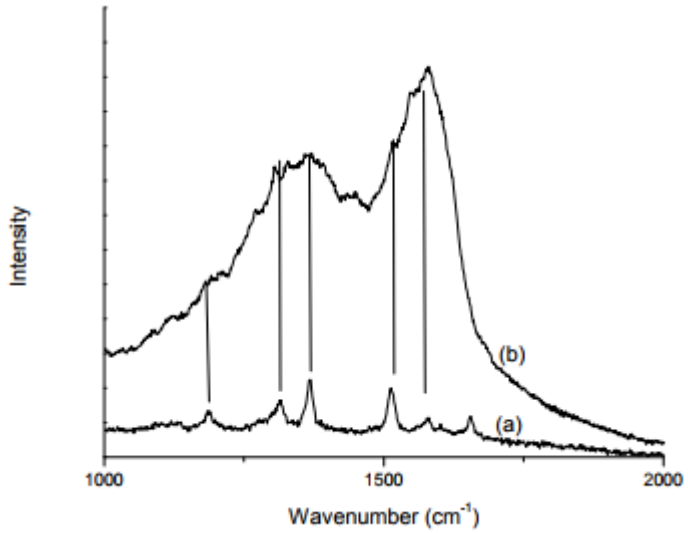

Figure 4.4: A) A reference spectrum of a bulk 10^{-3} M R6G water solution. B) Raman spectrum taken from a gold strip immersed in a 10^{-5} M R6G water solution. The intensity scale is the same for the two spectra.

Although a significant EF was evidenced for R6G, the quality of the SERS spectra is far from being satisfactory due to the poor resolution of the spectral features. This fact could be explained by the strong enhancement of the wide photoluminescence (PL) background, which masks to a large extent the Raman signal. The physical origin of the PL enhancement is essentially the same as that of SERS, a SPR amplification of the local electric field around the metals surface [217]. According to [217], the PL background hampers the SERS signal at distances from the surface exceeding ≈ 10 nm. Thus, it can be draw the conclusion that the R6G water solution does not penetrate effectively into the gaps between the gold nanoparticles, probably due to the large surface tension of water. Therefore, it would be instructive to test the SERS properties of our samples against organic solvents, which typically have about three times smaller surface tension than water.

Xylene ($C_6H_5(CH_3)_2$), a common organic solvent in many industrial applications, was chosen as a test substance. The toxicological hazard of xylene is well documented, which imposes specific regulations on its content in the common-life products [218]. Therefore, it

could be of a definite practical interest to develop analytical methods for detection of trace amounts of xylene.

Figure 4.5 A shows a reference Raman spectrum of xylene, while spectra in Figure 4.5 B-E were recorded on gold stripes after exposure of the sample in xylene, as described in section 2. The Raman spectrum of bulk xylene overlays a wide PL background, which makes the Raman lines poorly resolvable. It is noteworthy that the spectrum in Figure 4.5 A is expanded by a factor of 5 10^3 in order that its characteristic Raman features fit of the spectra Figure 4.5 B-E.

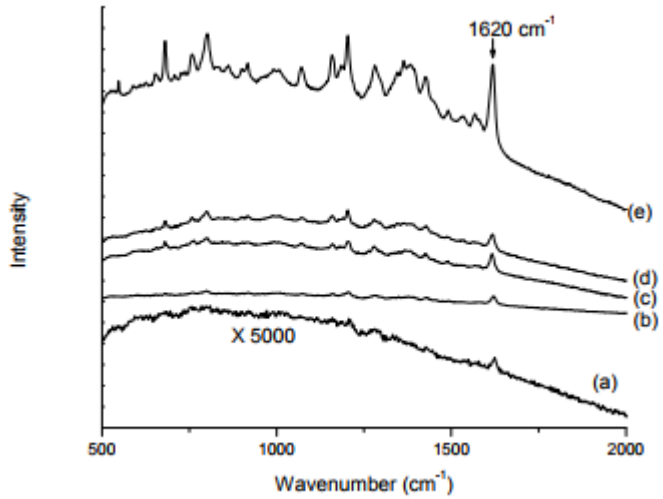

Figure 4.5 A) Reference spectrum from bulk xylene; SERS spectra recorded on gold stripes written at a laser power of 22.5 mW and a scanning speed of **B)** 100, **C)** 70, **D)** 40, **E)** 10 μm/s respectively.

Therefore, the spectra presented in Figure 4.5 evidence for a large SERS enhancement of xylene Raman features on the gold stripes. The PL backgrounds enhances as well, but to a much lesser extent than the Raman spectrum. According to [217] this fact implies close proximity between xylene molecules and the gold nanoparticles.

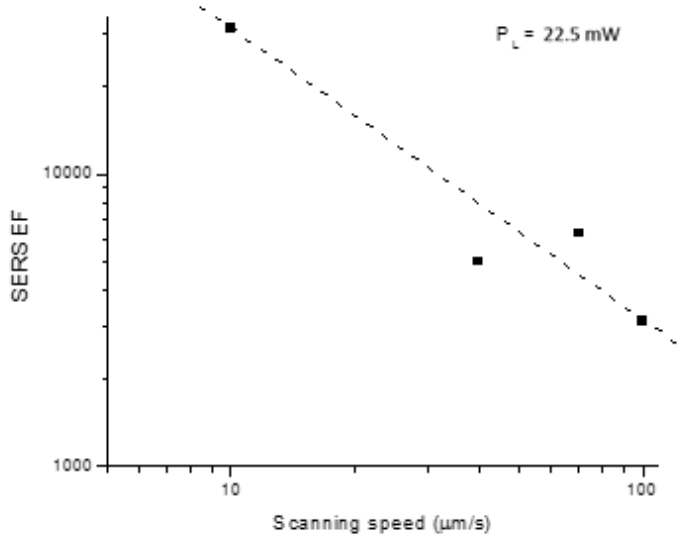

Figure 4.6. A log-log plot of the estimated SERS EF for the xylene line at 1620 cm^{-1} versus scanning speed, at a constant laser writing power of 22.5 mW.

The SERS EF estimated for the strongest xylene line at 1620 cm^{-1} (see figure 4.5) correlates with the scanning speed (SS) in the process of laser writing, as shown in figure 4.6. The same order of magnitude EF have been estimated also for the other Raman lines present in the spectrum. Roughly, the SERS EF scales as 1/SS, i.e. in a proportion to the deposited laser energy per unit length. As discussed in chapter 3, the surface density of GNPs increases at smaller scanning speeds. Thus, my data correlate the SERS EF to the GNP density, which corroborates the assumption for formation of gap hot spots upon closer GNP packing.

4.3 Thermo-Plasmonics

In this paragraph, it will be discussed another important effect correlated to the surface plasmon resonance: thermo-plasmonics. When the LSPR is excited in a GNP, the absorbed light induces an unavoidable damping of the LSPR and generates a non-equilibrium electron distribution that decays via electron-electron collisions. [219] The hot

electron gas equilibrates with lattice phonons, which transfer the generated energy to the surrounding medium, resulting in a local temperature increase.

The temperature increasing ΔT for a spherical nanoparticle depends on its absorption cross-section and size, and the thermal conductivity κ of the environment [220]:

$$\Delta T = \frac{\sigma_{abs} I}{4\pi\kappa r_P} \tag{4.6}$$

Where I is the irradiance of the laser beam r_P and the radius of the GNP.

Although this photo-induced heating is considered as a generally unwanted side effect for optical applications, the potential to exploit nano-localized heat is largely recognized for different kinds of applications such as plasmon assisted nano-chemistry [221-222], photothermal imaging [223-224], nano-surgery [225], plasmonic photothermal delivery [226-228] photothermal cancer therapy [229-232].

A number of recent theoretical and experimental works give insights into temperature changes around GNPs [233-234]. Therefore, TP-DLW of gold nanoparticles represent a potential strong way to create thermo-smart platform, since dimension and density of GNPs can be optically controlled and therefore the local temperature tuned.

4.3.1 Photo-thermal effects on randomly distributed gold nanoparticles

Before working on structure of GNPs photo-reduced through TP-DLW, I collaborated on the experimental analysis on the photo-thermal effects obtained on randomly distributed GNPs, both to master the technique and later to observe difference obtained on sample created through TP-DLW. Experiments on monolayers of random GNPs have been performed with two different values of surface density. GNPs were functionalized on glass substrates by following the Turkevich method [235], according to which a strong oxidizing agent (Piranha solution) is used to obtain a positively charged surface. The growing processes of GNPs, from gold seeds attached on the glass substrate, is

performed by dipping the substrate into a Au^{3+}/NH_2OH solution at room temperature (Figure 4.7 A).

The electrostatic interaction between the negative charged GNPs and the functionalized surface enable to obtain a strong adhesion. The procedure was repeated twice by changing the functionalization time from 50 minutes to 1 hour and 45 minutes (Figure 4.7 B), in order to obtain two samples with two different values of GNPs surface density; it is worth to stress that the obtained samples were characterized by the presence of GNPs on both sides of the substrate (Figure 4.7 C). A spectral analysis shows the typical LSPR absorption of spherical NPs in the green region of the spectrum, centred at 515 nm for both the samples; after removing the NPs from one side of the two substrates (Figure 4.7 D), a decrease of approximately 50% in the resonance peak occurs as expected (Figure 4.8). Scanning Electron Microscopy (SEM) and Atomic Force Microscopy (AFM) images reported in Figure 4.7 F-G reveal well-dispersed GNPs randomly distributed on the entire surface of both samples. Average size, polidispersity and surface density of NPs have been evaluated by means of a statistical analysis performed by means of a Java-based software (ImageJ).

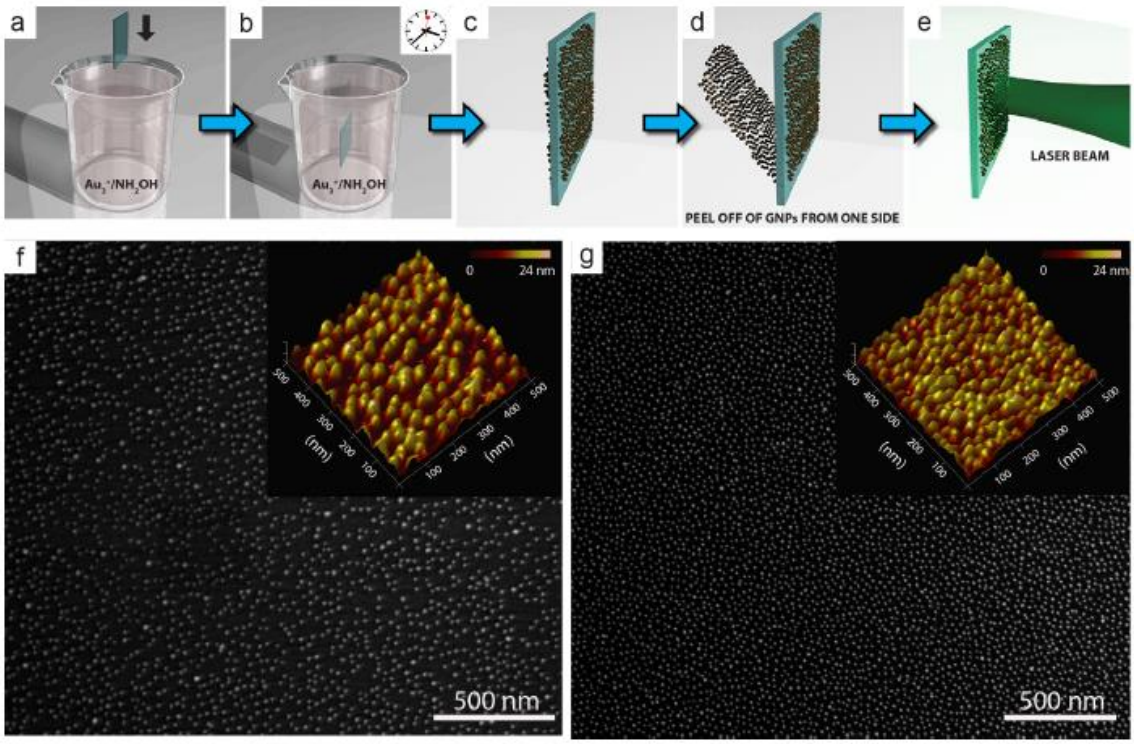

Figure 4.7: Sketch of the samples preparation and probing: **A)** samples were immersed in a Au^{3+}/NH_2OH solution, B**)** for two specific time depending on the selected surface density; C**)** samples were characterized by the presence of NPs on both sides; D**)** NPs are removed from one side and **E)** then the photo-heating is induced by means of a green beam laser. SEM images of GNPs distributed on glass substrates with two different values of surface density: **F)** sample 1, surface density of 355 μm−2 and **G)** sample 2, with surface density of 701 μm−2. Insets are the 3D view AFM images of the same samples.

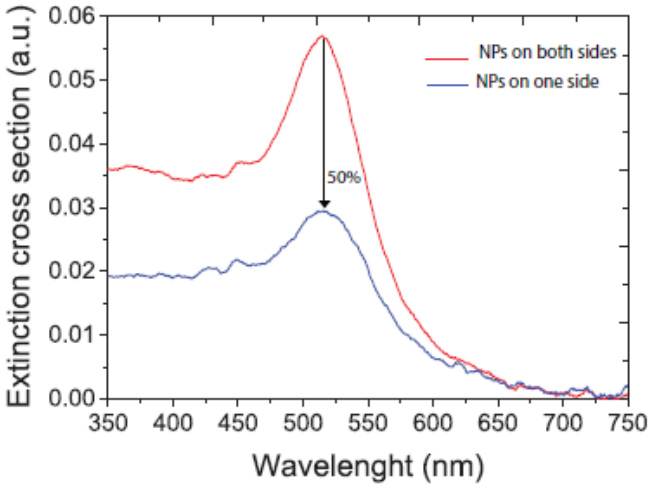

Figure 4.8: The sample obtained by dipping the glass substrate in the solution of NPs is characterized by the presence of NPs on both sides (red curve). A spectral analysis shows the typical absorption of spherical NPs in the green region of the spectrum. Spectra acquired before and after removing the NPs from one side of the glass substrate are quite different: As expected, after removing the NPs from one side, absorption of the sample (blue curve) decreases noticeably.

	Polidispersity (%)	Average diameter (nm)	Surface density (μm^{-2})
Sample 1	18.78	20.4	355
Sample 2	6.02	19.6	701

Table 4.1: Polidispersity, average diameter and surface density of the GNPs in Sample 1 and Sample 2.

In Table 4.1 are reported the data obtained by the morphologic analyses on Sample 1 (S1) and Sample 2 (S2). The AFM images (insets of Figure 4.7 F-G) shows an average height of NPs of approximately (20 ± 3) nm.

S1 and S2 were illuminated by a continuous green laser at λ = 532nm (Figure 4.7 E), with a spot size of 0.21 cm^2. Measurements are made at power intervals of 50 mW in the range 10 − 250mW, corresponding to intensity variations from 0.05 to 1.19W/cm^2. A thermo-graphic analysis has been performed at a small angle with the pump beam (that impinges perpendicularly to the sample) by using a thermo camera (E40 by FLIR) characterized by a sensitivity of 0.07 °C and a spatial resolution of 2.72 mrad. Thermal images for S1 and S2 are reported in Figure 4.9. Figures 4.9 A-F related to sample S1 represent the thermo-graphic analysis for six different values of excitation intensity, whereas Figure 4.9 H-O refer to S2. Both set of images present hot-spots, related to the photoinduced heat generated by the GNPs, in resonance with the external laser excitation. For both samples, the scale of the thermo camera WAS properly set in order to appreciate temperature changes in the range of values 19.9–26.9 °C. By monitoring temperature values of the central pixel of each hot-spot, corresponding to the highest temperature value, it is possible to plot the temperature variation $\Delta T = T - T_0$ as a function of the impinging intensity (see Figure 4.9 G for S1 and Figure 4.9 P for S2); a linear increase is observed in both samples.

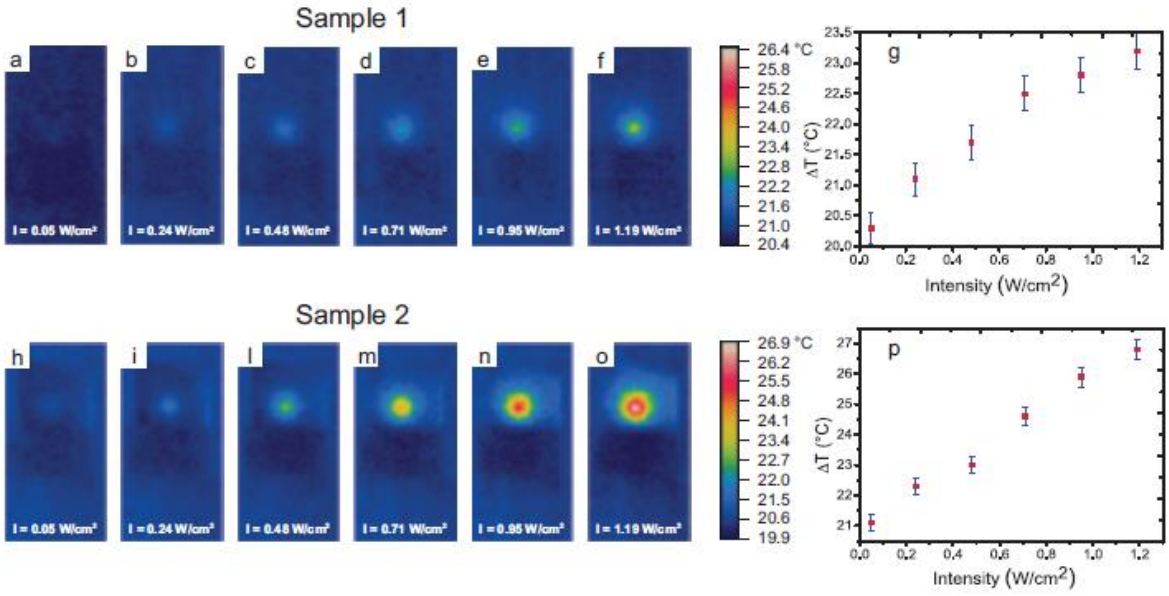

Figure 4.9: Thermographic images of **A-I)** sample 1 and **H-O)** sample 2, for different values of the pump beam intensity. **G)** and **P)** show the dependence of ΔT on the impinging intensity, respectively for the sample 1 and 2.

The measured temperature variation for S1 is (3.0 ± 0.4) °C, while for S2 it is (6.0 ± 0.4) °C. It is important to stress here that the surface density of S1 is about half of S2, resulting in a linear increase of ΔT as a function of the density of GNPs. Same values of ΔT were detected by monitoring different areas of the same sample. In order to verify the stability of GNPs on the substrate, samples have been tested with high incident intensity, generating a ΔT of about 40 °C. Morphological analysis shows that the distribution of the GNPs is not affected by this procedure.

A further investigation was related to the possibility of controlling ΔT by changing the refractive index of the GNPs surrounding medium. A polymer (PAAD-22 synthesized by BeamCo) was spin-coated onto sample S1 at 1000 rpm for 30 s. The thickness of the deposited polymer layer is evaluated by means of an AFM analysis, resulting approximately (20 ± 3) nm. The obtained sample is labelled as S3. A UV-VIS spectrum analysis of S3 shows a red-shift of about 12 nm of the peak wavelength and an increase of the overall extinction value of the LPR of about 78% (Figure 4.10).

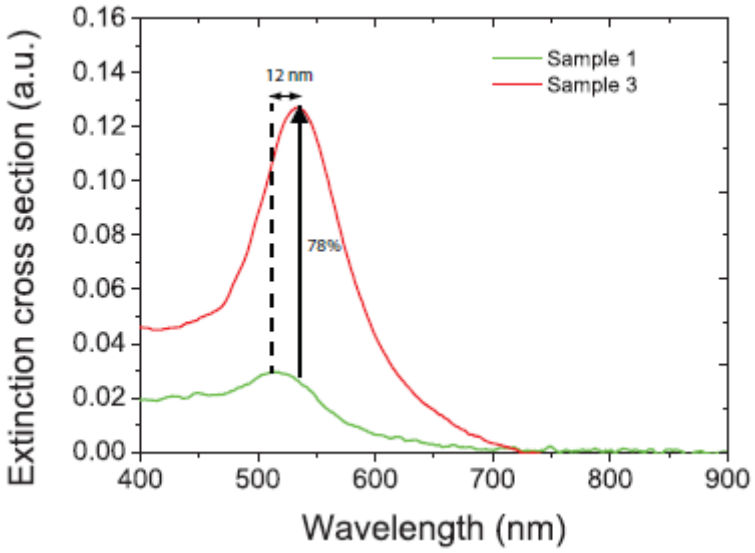

Figure 4.10: UV-VIS spectrum analysis of S3 respect to S1 shows a red-shift of about 12nm of the peak wavelength and an increase of the overall extinction value of the LPR of about 78%.

Thermal-images for S3 related to the same six excitation intensities used for S1 and S2 are reported in Figure 4.11 A-F, where scale is set in the range 20.5 °C ÷ 35.5 °C, in order to

include also the highest temperature variation measured in this case; once again, results confirm a linear dependence of ΔT on the excitation intensity (Figure 4.11 G), but with a different slope. The increase of the refractive index of the host material surrounding GNPs, with the same surface density considered in S1 (355μm^{-2}), causes a higher photo-induced heat, corresponding to ΔT values of about 15 ± 0.4 ◦C.

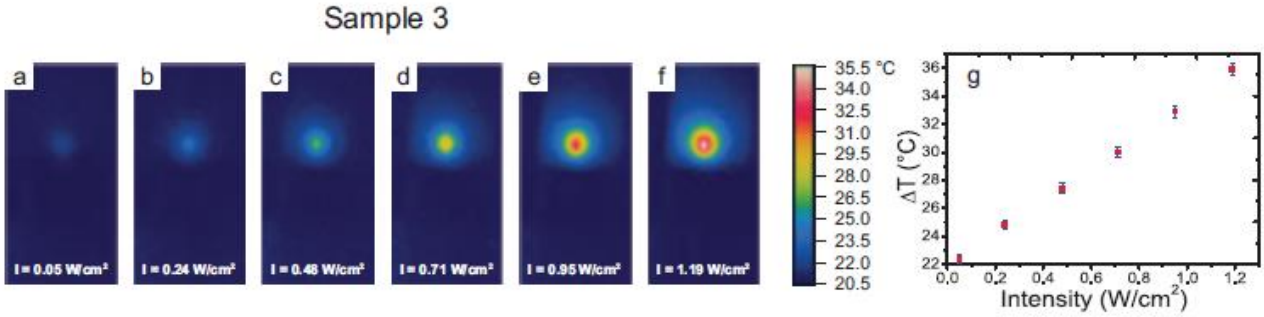

Figure 4.11: Thermographic images for different values of intensity of the pump beam for sample 3, with a polymer as surrounding medium.

The experimental results have been interpreted by an innovative theoretical model based on the Olbers paradox [236]. This model is well known in astrophysics and describes the sky brightness taking in account each star, even the most distant, gives an equal contribution. In a similar way, Dr. Luigia Pezzi et al. [237] describe the temperature variations of the samples, taking in account the contribution of all the GNPs, even the farther away from the focus of the irradiating laser beam. According to this model, the temperature variation of the sample ΔT has to be estimated as the sum of all the single ΔT_i associated to each GNPs.

$$\Delta T = \sum_i \Delta T_i = \sum_i \frac{c(\lambda) I(\boldsymbol{r_i})}{|\boldsymbol{r} - \boldsymbol{r_i}|} \tag{4.7}$$

Where is a parameter $c(\lambda)$ which provides the photo-heating effectiveness of the system [237], $I(\boldsymbol{r_i})$ is the light intensity in correspondence of the GNPs in position i, $|\boldsymbol{r} - \boldsymbol{r_i}|$ is the distance between the positions of the $\boldsymbol{r}$ on which the analysis is performed, and that $\boldsymbol{r_i}$ of the GNP.

4.3.2 Photo-thermal effects on 1D gratings of gold nanoparticles

Similar analyses as those showed above were performed on surface of 1 mm^2 1D gratings of mono-dimensional GNPs, direct laser written in dried films of PVA and $HAuCl_4$, according to the receipt discussed in the previous chapter, in paragraph 3.2. The samples were developed in H_2O to remove all the unexposed material, leaving only the stripes of GNPs stick to the glass substrate.

The width of each GNPs stripe, obtained by using a laser power of 25 mW and a scanning speed of 200 μm/s, is of the order of 1.5 μm. Then, I designed four gratings with different periods in order to control the number of GNPs that are excited at the same time by the resonant radiation; in particular the periodicity between the stripes was of: 0.5 μm, 2 μm, 10 μm and 100 μm. The four samples were firstly analyzed by means of an optical microscope and then by AFM.

Optical images were acquired through a 50X and 100X objective, between crossed polarizers, which allow evidencing the macroscopic response of gold nanoparticles and identifying the different gratings, due to scattering effects (Figure 4.12). The sample with period 0.5 μm, in Figure 4.12 A, appears like a dense square of GNPs, which does not show any pattern inside. On the other hand, the grating structure is well evident in the samples with the other designed periods, thus I obtained stripes rich in GNPs, spaced from 0.5 μm (Figure 4.12 A) to 100 μm (Figure 4.12 D) .

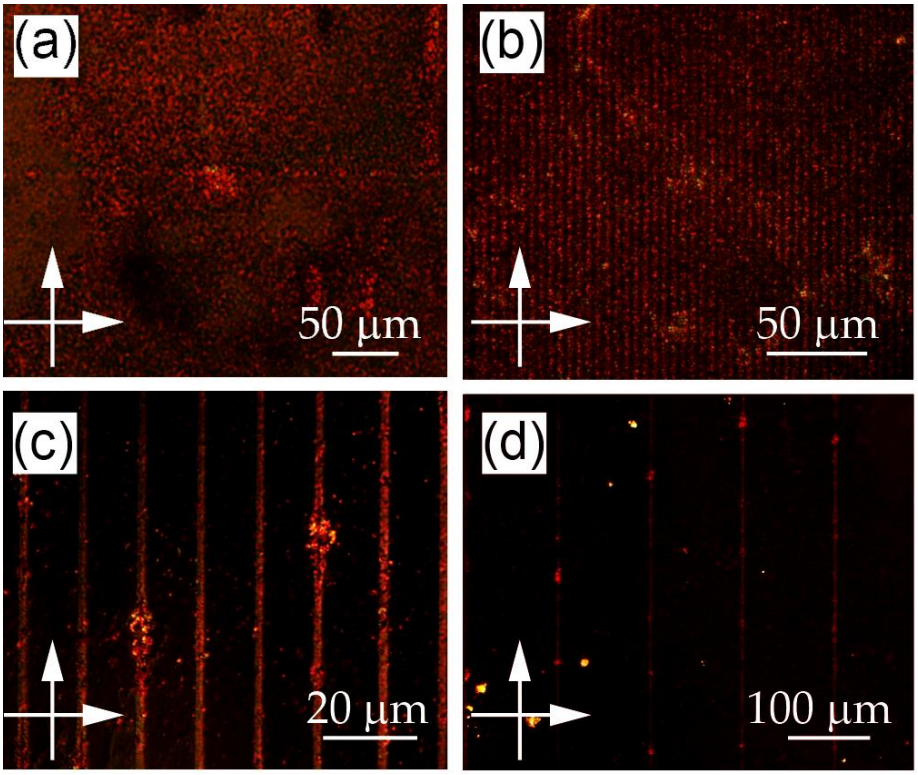

Figure 4.12: Microscope optical images, acquired between crossed polarizers, of the GNPs gratings with period of **A)** 0.5 μm, **B)** 2 μm, **C)** 10 μm, **D)** 100 μm.

AFM images (Figure 4.12 A-D) confirm the obtained arrangement of GNPs in vertical stripes, showing that the diameter of nanoparticles, depending on the local concentration of gold precursor and the energy dose delivered by the laser, varies over two order of magnitude, with the largest value of the order of 100 nm. However, for all the samples I observe an average height of approximately 40 nm, measured from the AFM observation.

It is worth noting that the GNPs with diameter of the order of 100 nm are due to a higher local concentration of gold ions, therefore this effect is less visible in the stripes from 0.5 μm to 2 μm where the highest concentration of gold ions has been photo-reduced in the first path of the writing beam. This leads to a consequent creation of smaller GNPs, characterized by a lower polydispersity.

In order to estimate the average size of the GNPs, a testing sample with only one stripe has been prepared, obtained with the same energy dose used for the fabrications of the other samples. Scanning Electron Microscopy analysis was performed on this sample characterized by a length of 1 mm and a width of 1.5 μm (Figure 4.13 E). By using the same

energy dose stripe characterized by the same number and dispersion of GNPs can be obtained. By means of Image-J software [238] I counted and determined the size distribution of the GNPs in this stripe, obtaining a density value of 90 μm^{-2}. This value was used to calculate the density of the GNPs in each sample.

The statistical analysis confirms that all the samples exhibit an average NP diameter of approximately 40 nm. Moreover, they present a surface density of 1.8 10^8 mm^{-2}, 4.5 10^7 mm^{-2}, 9 10^6 mm^{-2} and 9 10^5 mm^{-2}, respectively for the samples with grating periods of 0.5 μm, 2 μm, 10 μm and 100 μm.

During the direct laser writing, the two photons absorption induces a local heating of the photo-resist, which leads to the thermal photo-reduction of the metallic precursor in the area surrounding the stripes and the creation of random GNPs between them. These random nanoparticles are observed in all the four samples and present a density of 0.5 10^5 mm^{-2}, which does not affect the total density of the samples nor give a consistent macroscopic contribute.

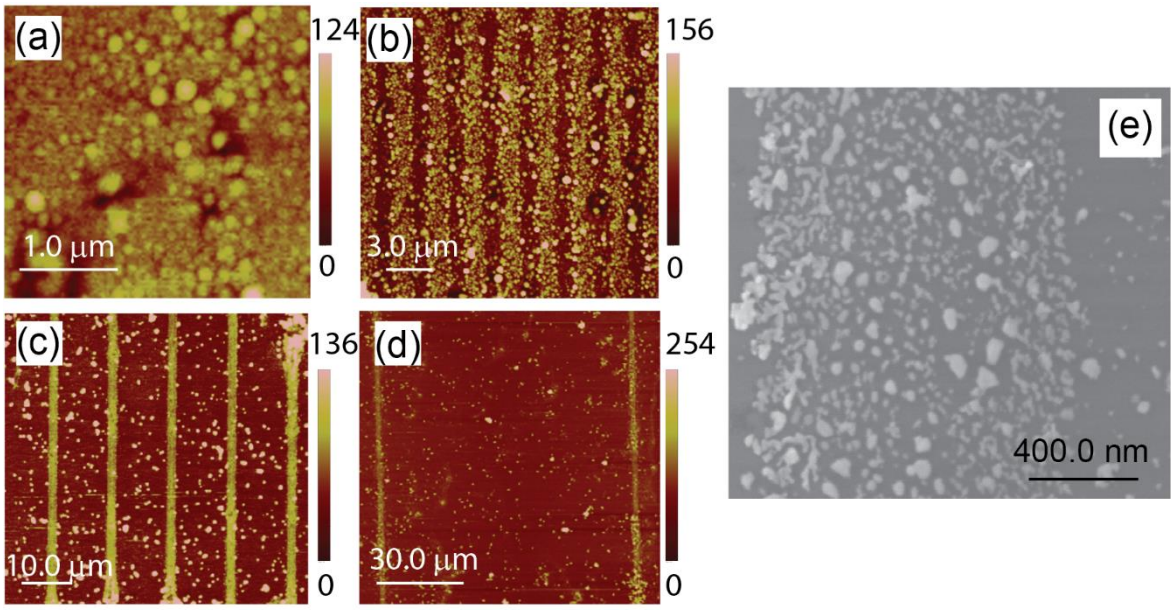

Figure 4.13: Atomic Force Microscopy images of GNPs with period of **A)** 0.5 μm, **B)** 2 μm, **C)** 10 μm, **D)** 100 μm. **E)** SEM image of GNPs distributed in one stripe.

The absorbance spectra (Figure 4.14 A), obtained by probing the sample with unpolarised white light (wavelength in the range 400 – 900 nm) at normal incidence, exhibit the typical gold LSPR absorption band centred at 560 nm for the GNPs grating with period of 0.5 μm, 575 nm for the GNPs grating with period of 2 μm, 587 nm for the GNPs grating with period of 10 μm, while, in the case of the grating with period of 100 μm the plasmonic band cannot be appreciate. The broadening of the LSPR peak is due to the size dispersion of GNPs, revealing that the highly density of smaller nanoparticles in the samples with 0.5 μm and 2 μm period, leads to a blue-shift in the spectrum resonance [239].

Thermal analysis was carried out by illuminating the samples orthogonally with a continuous green laser at λ = 532 nm, with a beam diameter of (2.25 ± 0.22) mm. Measurements are made at power intervals of 50 mW in the range 50 – 550 mW, corresponding to intensity variations from 1.26 to 13.84 W/cm^2. The photo-induced temperature variation has been monitored by using a thermo-camera (E40 by FLIR) characterized by a sensitivity of 0.07 °C and a spatial resolution of 2.72 mrad. The camera control-parameters have been appropriately set to consider both environment and materials properties (room temperature, level of humidity in the room, emissivity of the material). By detecting the highest temperature value T, corresponding to the central pixel of each hot-spot shown in the thermographic images, it is possible to plot the characteristic temperature variation $\Delta T \equiv T - T_0$ as a function of the impinging power density (Figure 4.14 B, here T_0 is the room temperature). A linear increase is observed in all the samples.

The measured temperature variations result of 55.1 ± 0.3°C, 40.0 ± 0.3°C, 13.9 ± 0.3°C, and 6.2 ± 0.3°C, respectively for the samples with 0.5 μm, 2 μm, 10 μm and 100 μm grating period.

Same values of ΔT were detected by monitoring different areas of the same sample. Morphological analysis carried out after the thermal test show that the distribution of the NPs is not affected by the laser exposure. According to experimental measurements the temperature variations ΔT strongly depends on two parameters: i) the GNPs surface density and ii) the intensity of the pump beam.

By increasing the power density of the pump beam, *T* increases linearly until gets to saturation, while, variations in the GNPs stripes pitch results a change in the P-T curve slope.

By following the fabrication protocol described in this work, one can easily control the photo-induced temperature variations by acting on the number and the distance between the GNPs stripes. It represents a really fast and simple way to obtain integrable-on chip photo-thermal active areas.

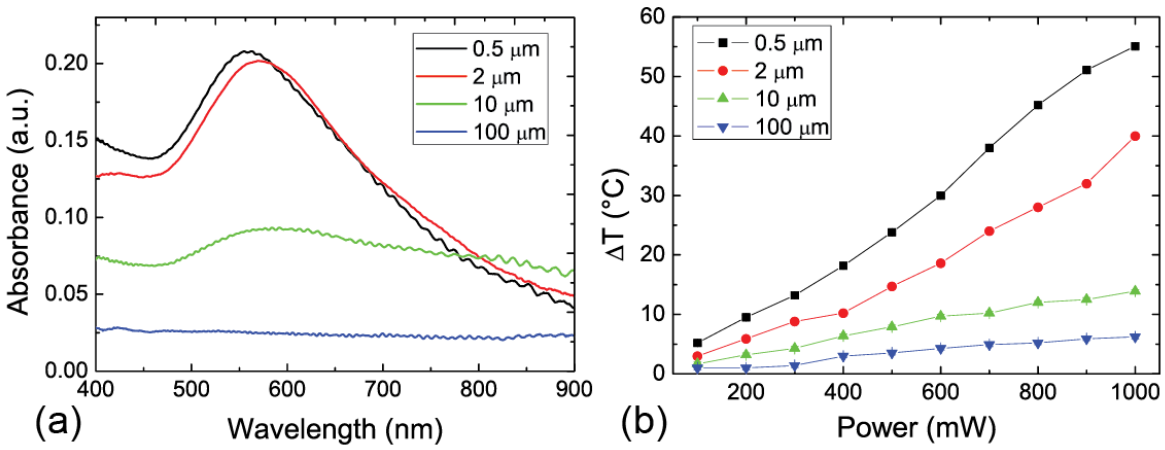

Figure 4.14: A) Spectral response of the GNPs substrate. **B)** Temperature variations of the GNPs layer for different values of the pump beam laser.

In conclusion, a characterization of the photo-induced heat delivered by GNPs arranged in stripes onto a solid flat substrate has been carried out. The samples were obtained by means of a Direct Laser Writing technique based on a Two-photon photo-reduction process, used on a PVA matrix doped with $HAuCl_4$.

I created four 1D-gratings of 1 mm^2 rich in gold nanoparticles, with different periods of: 0.5 μm, 2 μm, 10 μm and 100 μm. The morphologic characterization was carried out through AFM and SEM imaging, which allowed for measuring the density of GNPs in the four samples. Irradiating the gratings with a continuous green laser at different power values, I was able to induce a consistent temperature variation from 6.2 ± 0.3°C to 55.1 ± 0.3°C.

These results demonstrated that by controlling the stripes pitch in the obtained 1D gratings of GNPs, one can control the number of GNPs excited at the same time and the resulting macroscopic temperature variations, paving the way to a wide range of applications, in many fields, as: sensing platforms, solar energy harvesting and thermo-catalysis.

Acknowledgment

Additive manufacturing through photo-lithography and two-photons direct laser writing, and most of the characterization techniques showed in this work (atomic force microscopy, scanning electron microscopy, confocal microscopy, optical imaging, spectrophotometry) were performed at Beyond Nano Cosenza – CNR User Facility.

Samples preparation made in RMs01-003 C, showed in chapter 2, was performed with the support of Dr. Alfredo Mazzulla, prof. Gabriella Cipparrone and Alfredo Pane.

The gold precursor used to print pattern of gold nanoparticles, as in chapter 3 and 4, was prepared with the support of Dr. Loredana Ricciardi, prof. M. La Deda, Franco Cofone and Alfredo Pane.

SEM imaging was performed thanks to the technical support of Giovanni Desiderio and Mariano Davoli.

SERS spectra were collected in collaboration with professor V.G. Ivanov of the Department of Physics of University of Sofia and professor E.S. Vlackov of the Bulgarian Academy of Science.

Thermo-analysis on the samples was performed in collaboration with Dr. Giovanna Palermo.

Samples S1, S2, S3, in chapter 4, of gold nanoparticles stuck on a glass substrates starting from a colloidal solution, were prepared by Dr. Ugo Cataldi.

Conclusions

In this thesis, I elucidated the physical processes in single and multiple photons additive manufacturing of 3D nanostructures made of different materials, i.e. organic isotropic and anisotropic photoresists, and metallic precursors.

For each photoresist used, I performed the voxel characterization, in order to define the best resolution obtainable. In particular, I verified the dependence of the voxel size on the printing parameters, and defined their effective cross-section.

Moreover, I defined the best protocol, to fabricate microfluidic systems and elements of millimetric size, with micro- and nano-features, inside the channel. To reduce the printing time, TPA was exploited to create a shell, an internal structural scaffold and eventual microscopic details of the object, and SPA to polymerize its bulk. However, the standard development process is unsuitable to microfluidic systems, due to the difficulty to make the solvent flow in the channels, in particular if the substrate obstructs the channels opening.

To solve this issue, I created a sacrificial matrix of pyramid trunks at the bottom of the microfluidic systems to support the object and allow the solvent to flow between them and get inside the channels at the base. In this way, it was possible to develop the sample through a bath up-down for 15 minutes in the solvent. Leaving the sample to dry head up, remaining droplets of organic photo-resist dipped on the substrate and were removed by a second bath in the solvent for 5 minutes.

A faster possible way to develop correctly a microfluidic system consists in creating a suitable pattern of holes in the substrate, in correspondence of the channels opening, in order to pour the solvent inside of the channel directly.

Interesting achievements were obtained by combining TP-DLW with an anisotropic photoresist, which allowed the fabrication of 3D solid structures, maintaining the optical properties of liquid crystals, in combination with the mechanical properties of polymers. To create 3D objects in liquid crystalline elastomers, I used a photopolymerizable reactive mesogen solution (RMs), aligned on a rubbed PVA film. Analyses on 1D and 3D gratings

created in RMs, showed the necessity to add a photo-initiator to the solution in order to enhance the TPA cross-section of the mixture.

In this way, it was possible to create three-dimensional solid objects showing optical properties typical of liquid crystals and features well below the diffraction limit. However, I demonstrated that the birefringence of the objects created by TP-DLW in RMS can be tuned by a proper choice of hatching distance and orientation with respect to the rubbing direction. Moreover, since writing direction can induce an internal order on the cross-links, objects created with isotropic photo-resist can shows birefringence. To maintain the optical properties of the photo-resist is then mandatory that 3D objects are printed with hatching and slice of maximum 400 nm, in order to avoid the rearrangement of the mesogens.

Moreover, I showed that by adding fluorescent dyes to the RMs, it is possible to create structures which maintain both the fluorescence of the dye, and the optical properties of the nematic liquid crystal. However, high energy dose can results in the damaging of the dye.

More interesting were the results obtained by doping the RMs with a chiral agent, which confer a helical order to the molecules. As result, a chiral LC reflects selectively the wavelength and the polarization of the impinging light. TP-DLW in CRMs resulted in the micro-fabrication of chiral 3D objects. I observed that the single photon polymerization induces a blue-shift of the photonic band gap. The PBG blue-shift is enhanced during TP-DLW, and can be tuned in function of the energy dose delivered.

In fact, to preserve their optical properties in the polymeric structure and keep the blue-shift at a minimum value, the whole CRMs bulk must be fully polymerized. This implies that the voxel depth has to be equal to (or larger than) the slicing, which here is comparable to the helical pitch.

At low values of energy dose, the thickness of the single voxel is reduced; therefore, the helix of the CRMs is only partially polymerized and the residual material is expelled during the development. This results in a "truncation" of the effective pitch and, as a consequence, a blue shift of the PBG.

This result indicates that TP-DLW can be used to tune the selective reflection of 3D objects created in CRMs. Thus, multi-colour micro- and nano-fabrication is achieved, paving

the way to new technologic fields. E.g. I micro-fabricated a new anti-counterfeiting system: by printing a QR code, with different energy dose. In result, it presented features with different heights and reflection bands.

I implemented, in this way, a four-dimensional barcode, whose chiral optical properties can guarantee a colour fingerprint, impossible to replicate with other techniques.

Last, but not least, I studied the physical processes that occur during TP-DLW in polymeric matrices doped with a gold precursor. I observed that sweeping the laser inside the matrix, a stripe rich in gold nanoparticles is obtained. The stripe width increases with the laser power and the exposure time, showing a behaviour similar to the photo-polymerization.

I have also analysed the influence of the exposure time over the nano-particles size distribution and density and showed that by suitably adjusting the exposure time it is possible to maximize the occurrence of a given diameter. In particular, I observed no changings in density, for GNPs with diameter > 50 nm, for the different scan speeds I used, indicating that the scan speed does not influence their creation. On the contrary, at longer exposure times, I observed the presence of smaller nanoparticles, further than the larger ones. This result indicates that the local peaks of density define zones where the ionic concentration is higher and hence with higher probability of seeding and faster growing. In these zones the higher ionic and seeds concentration feeds the growth of the larger NPS at a higher rate. Slower scan speeds are effective in activating seeds in the lower concentration zones, where smaller nanoparticles are grown thanks to the "normal" ionic diffusion.

Therefore, the ion diffusion plays a key-role in the creation of the GNPs aggregates during TP-DLW. To improve the control on the growth of GNPs, I delivered the energy dose in multiple shots. This method allows the chloroauric ions to diffuse in the virtual voxel during the time between consecutive shots, restoring the initial condition of the system. Tuning the waiting time between each shot, it is possible to monitor the concentration of gold ions photo-reduced by each fraction of energy, and get a finer control on the density and size of the nanoparticles created. As a consequence, it is possible to obtain denser aggregates of GNPs, with reduced polydispersity.

However, I observed that when the waiting time between consecutive shots is 1 s or larger, a blasting wave originating in the laser focus takes place, strongly affecting the resulting GNPs spot geometry. The photo-reduction of the ions inside the virtual voxel leads to the increasing of the local temperature. Heating causes the rapid evaporation of water inside the voxel, pushing around the surrounding liquid. As a consequence, a local dehydration of the polymer occurs. At waiting times larger than 1 s, the expulsed water refill the virtual voxel and therefore each shot concurs with a thermal shock-wave, which transfer a momentum to the particles. This effect is due to the cumulative thermal shockwaves, obtained when the energy dose is delivered through multiple shots.

However, I observed that the hydrodynamic model fails in describing the motion of the ejected GNPs. This result suggests that the blasting wave runs over and propagates faster that the ejected GNPs, that move in the dry polymeric matrix; thus, I can conclude that the ionic diffusion occurs even in presence of at least of a molecular water layer, around the PVA molecules, in which the ions can diffuse.

Blasting effects are never completely avoidable. To verify this point, I implemented a new technique to create GNPs directly in a water solution of $HAuCl_4$ only: the substrate was silanized with a surfactant (DMOAP) film. On the substrate rinsed with water, no nanoparticle was found on the surface after the printing process, due to the hydrophilic nature of gold. When the substrate is not rinsed at the end of the process, few unbound surfactants molecules are left on the substrate. The surfactant molecules in the virtual voxel are damaged by the local heating, thus no GNP is found at the centre of the spot, due to the hydrophilic nature of gold and the particle diffusion in water. The GNPs observed are the ones ejected from the voxel after the exposure, which collect the unbound DMOAP molecules from the surface. The result is an increasing in the surface viscosity, as the surfactant-enhanced friction drags the GNPs and make them stick on the surfaces. These GNPs can grow until their surface is not totally covered by the surfactant molecules, then their growth is inhibited leading to the observed low polydispersity. These phenomena are observed in case of both single and multiple shots. Thus, blasting effects are no completely avoidable and are observed even after the first single shot.

Moreover, the higher the energy dose delivered, the larger the blast effects observed. Thus, I attempted to directly evaluate the temperature distribution in the area of interest, as a function of the energy delivered, by printing on thermo-graphic paper, wetted with an aqueous solution of tetrachloroauric acid. According to my best knowledge, it is the very first experiment that allowed for a temperature mapping at the nanoscale, and whose results are consistent with theoretical predictions present in the literature.

The different analyses performed allowed to point out that, in order to get best control on the GNPs photo-reduction, thermal effects have to be reduced, while a fine control on the ionic concentration is required. To this purpose, I prepared electrolytic cells made of Glass plated coated with ITO transparent electrodes, in which I infiltrated a very diluted solution of HAuCl4 in water, and printed stripes of GNPs at an energy dose sufficient to activate the seeding process of TP-photo-reduced gold ions. Because of the low ionic density, the growing process of GNPs is inhibited.

Growing of gold nanoparticles was then performed by applying an electric potential difference between the two electrodes, well below the electro-chemical reduction threshold, in order to increase the ionic concentration close to the boundary surfaces. I verified the presence of two ionic species involved in the reduction process ($AuCl_4^-$ and Au^+). The electric field allows controlling the surface density of the ionic species of interest, both for the seeding and the growth phases. Regarding the last, I consider that in proximity of a gold seed a tip effect is obtained, "driving" the gold ions toward the seed rather than the ITO electrode, where they are reduced through auto-catalytic processes. Analyses on the stripes confirmed a voxel size comparable to the laser beam waist, and that the gold nanoparticles TP-photo-reduced are mono-dispersed, demonstrating that the proposed electrophoretic method is effective in controlling the local ionic concentration and hence the GNPs density ad size.

Finally, I investigated the possibility to use TP-DLW of metal precursor to realize smart platform rich in GNPs suitable to different application. In particular, I created detecting substrates for Surface-Enhanced Raman Spectroscopy (SERS). The Raman spectra were recorded from samples immersed in a solution of rhodamine-6G (R6G), as well as,

after exposure of the samples in xylene. SERS enhancement factors of up to ~10^4 were obtained for both rhodamine-6G and xylene.

Great interest was due to the thermo-plasmonic effects typical of the GNPs. To this purpose, I studied the photo-thermal effects obtained on randomly distributed GNPs, both to master the technique and later to observe difference obtained on sample created through TP-DLW. Therefore, I created 1D gratings of GNPs on which I was able to induce a consistent temperature variation from 6.2 ± 0.3°C to 55.1 ± 0.3°C, by irradiating them with a continuous green laser at different power values.

In conclusion, I tried to go more inside into the physics involved in two-photon optical lithography, both for organic resists and more in particular for inorganic metallic precursors, delivering the key for managing these effects, with the aim to get a finer control of this fascinating nano-fabrication technique.

List of Figures

cylinder is created at 20 mW and 4000 μm/s, the diameter of each scaffold is 600 nm, which allows the diffraction of light. 055

Figure 2.15: Optical images between crossed polarizers at 0 and 45° of arrays of 1D circular gratings written at laser power 17 mW @ scan speed ranging from 4000 μm/s, to 10000 μm/s. Each arrays is composed by gratings made of segments parallel to the rubbing direction, or inclined at 30°, 60°, 90°. **A)** Scheme of each matrix printed; the vector in the bottom indicating the rubbing direction. Matrices were printed @ hatching of **B-C)** 200 nm, D**-E)** 400 nm, which present homogeneous birefringence, and F**-G)** 600 nm. At 600 nm of hatching, dark e bright condition are not the same for each gratings, with 0° being the brighter condition for the grating printed at 30° with the respect to the rubbing direction; 45° the brighter condition for the gratings printed parallel to the rubbing direction.

058

Figure 2.16: AFM profile of an edge of 1D gratings written at 17 mW @ scan speed 4000 μm/s, and hatching of **A)** 400 nm and **B)** 800 nm. While in the latter case a grating is obtained, the former is a compact structure with no effective separation between single segments. 059

Figure 2.17: Optical images between crossed polarizers of cylinders of 50 μm of diameter and high 12 μm created with IP-L, an isotropic photo-resist. The pairs cylinders are made of vertical segments (on the left) or by alternate layers of vertical and horizontal stripes (on the right). Those created at hatching 400 nm, show no birefringence, when observed at **A)** 0° or **B)** 45°. Vice versa, cylinders created at 800 nm present internal order and show dark condition at **C)** 0° and brighter condition at **D)** 45°. The line bar in the images is of 50 μm. 060

Figure 2.18: Molecular structures and absorbance/fluorescence spectra of **A)** Red Nile, **B)** Rhodamine B, **C)** Pyrromethene 567. 063

Figure 2.19: Cylinders of nominal diameter 50 μm and height 8 μm, printed at laser power 10-25 mW (step 5 mW) @ ScanSpeed 4 x 10^3 -8 x 10^3 μm/s (step 2 x 10^3 μm/s) printed in RMs01-003 C doped with 5% of nile red. The matrix was analysed through **A)** optical microscopy and **B)** confocal microscopy. The line bar in the two images is of 50 μm. **C)** Cylinders height was measured by means of AFM. No consistent differences in height or shapes is revealed between these cylinders and those un-doped. 064

over 100 °C, **F-I)** however the dye darkens in specific patterns in function of temperature. At 100 °C a black spot, whose dimension is comparable with the diameter of the heated tip, is surrounded by a grey area, due to thermal diffusion on the water film during the printing. Increasing the temperature, evaporation lead to an expulsion of the dye, and therefore a white area can be seen around the spot. After 250 °C, an internal white area and a black ring surround a grey spot, whose dimension. Temperature has to be considered equal to or larger than 250 °C inside the black ring. In this second set of image, the line is of 1.5 mm. 117

Figure 3.20: Matrix of points written at 25 mW laser power by exposure of **A)** a single shot of 100 ms **B)** 100 shots of 1 ms, with 10 s of waiting time. **C)** Comparison between the first point of the second matrix created on the thermo-graphic paper and the spot observed by SEM imaging, created in the same laser condition. 119

Figure 3.21: Scheme of the electrolytic cell built. Two coverslip were coated with an ITO film. Two copper stripes were used to connect the electrodes to a DC source. A thin Mylar film was used to insulate the electrodes. An epoxy resin was used to seal the cell. 121

Figure 3.22: A) Scheme of the Double layer: adsorbed and solvated ions generate respectively the inner and outer Helmholtz plane in correspondence of the electrode, thus the Stern compact layer, over which diffusive solvated ions form the diffusive layer. **B)** Electric potential in correspondence to the Stern and Diffusive layers. 123

Figure 3.23: AFM imaging on the **A)** positive and **B)** negative ITO electrode after electrodeposition of GNPs by applying a potential difference of 1 V for 40 minutes. 124

Figure 3.24 SEM images of *lines written at laser power 25 mW @ **A-B)** 100 μm/s; **C-D)** 1000 μm/s; **E-F)** 10000 μm/s; **G-H)** 100.000 μm/s on the electrode at -50 mV, and @ **I-J)** 100 μm/s; **K-L)** 1000 μm/s; **M-N)** 10000 μm/s; **O-P)** 100.000 μm/s on the electrode at +50 mV. 126

Figure 3.25: Optical images obtained through a camera connected to a 63x objective of the **A)** Direct laser writing process of three lines of GNPs in an electrolytic cell, written at laser power 25 mW @ scan speed 2000 μm/s, while a voltage of -50 mV was applied. The lines are written from the bottom to the top, so no line appear after the laser swept. After the printing, the sample was observed after **B)** 1 min and 30 s and **C)** 4 min. The potential different was increased at -100 mV and the sample was recorded after **D)** 40 s, **E)** 4 min. The scale in the image is 10 μm.

References

[1] S. Engelhardt, “Direct Laser Writing,” in Laser Technology in Biomimetics, V. Schmidt, and M. R. Belegratis, eds., 13–56 (Springer-Verlag, Berlin/Heidelberg, 2013).

[2] G. V. Freymann et al., Three-Dimensional Nanostructures for Photonics, Adv. Funct. Mater. 2010 , 20 , 1038.

[3] M. Roehrig, M. Thiel, M. Worgull, et al., “3D Direct Laser Writing of Nano- and Microstructured Hierarchical Gecko-Mimicking Surfaces,” Small 8(19), 3009–3015 (2012).

[4] Mack, Chris. Fundamental principles of optical lithography: the science of microfabrication. John Wiley & Sons, 2008.

[5] Rötting, O., et al. "Polymer microfabrication technologies." Microsystem Technologies 8.1 (2002): 32-36.

[6] Becker, Holger, and Ulf Heim. "Hot embossing as a method for the fabrication of polymer high aspect ratio structures." Sensors and Actuators A: Physical 83.1 (2000): 130-135.

[7] Becker, Holger, and Claudia Gärtner. "Polymer microfabrication methods for microfluidic analytical applications." Electrophoresis21.1 (2000): 12-26.

[8] Lu, Y., and S. C. Chen. "Micro and nano-fabrication of biodegradable polymers for drug delivery." Advanced drug delivery reviews 56.11 (2004): 1621-1633.

[9] Thompson, Larry F. "An introduction to lithography." 1983. 1-13.

[10] Vieu, C., et al. "Electron beam lithography: resolution limits and applications." Applied Surface Science 164.1 (2000): 111-117.

[11] Tseng, Ampere A., et al. "Electron beam lithography in nanoscale fabrication: recent development." IEEE Transactions on Electronics Packaging Manufacturing 26.2 (2003): 141-149.

[12] Pease, R. F. W. "Electron beam lithography." Contemporary Physics 22.3 (1981): 265-290.

[13] Jacobs, Paul Francis. Rapid prototyping & manufacturing: fundamentals of stereolithography. Society of Manufacturing Engineers, 1992.

[14] Jacobs, Paul F. Stereolithography and other RP&M technologies: from rapid prototyping to rapid tooling. Society of Manufacturing Engineers, 1995.

[15] Hull, Charles W. "Apparatus for production of three-dimensional objects by stereolithography." U.S. Patent No. 4,575,330. 11 Mar. 1986.

[16] Melchels, Ferry PW, Jan Feijen, and Dirk W. Grijpma. "A review on stereolithography and its applications in biomedical engineering." Biomaterials 31.24 (2010): 6121-6130.

[17] Sun, Hong-Bo, and Satoshi Kawata. "Two-photon laser precision microfabrication and its applications to micro-nano devices and systems." Journal of lightwave technology 21.3 (2003): 624.

[18] Serbin, J., et al. "Femtosecond laser-induced two-photon polymerization of inorganic–organic hybrid materials for applications in photonics." Optics letters 28.5 (2003): 301-303.

[19] Cumpston, Brian H., et al. "Two-photon polymerization initiators for three-dimensional optical data storage and microfabrication." Nature 398.6722 (1999): 51-54.

[20] Deubel, Markus, et al. "Direct laser writing of three-dimensional photonic-crystal templates for telecommunications." Nature materials 3.7 (2004): 444-447.

[21] Seet, Kock Khuen, et al. "Three-Dimensional Spiral-Architecture Photonic Crystals Obtained By Direct Laser Writing." Advanced Materials 17.5 (2005): 541-545.

[22] Wong, Sean, et al. "Direct Laser Writing of Three-Dimensional Photonic Crystals with a Complete Photonic Bandgap in Chalcogenide Glasses." Advanced Materials 18.3 (2006): 265-269.

[23] Rill, Michael S., et al. "Photonic metamaterials by direct laser writing and silver chemical vapour deposition." Nature materials7.7 (2008): 543-546.

[24] Gansel, Justyna K., et al. "Gold helix photonic metamaterial as broadband circular polarizer." Science 325.5947 (2009): 1513-1515.

[25] Deubel, Markus, et al. "Direct laser writing of three-dimensional photonic-crystal templates for telecommunications." Nature materials 3.7 (2004): 444-447.

[26] Engstrom, Daniel S., et al. "Additive nanomanufacturing–a review." Journal of Materials Research 29.17 (2014): 1792-1816.

[27] Franklin, Daniel, et al. "Polarization-independent actively tunable colour generation on imprinted plasmonic surfaces." Nature communications 6 (2015).

[28] Gissibl, Timo, et al. "Two-photon direct laser writing of ultracompact multi-lens objectives." Nature Photonics 10.8 (2016): 554-560.

[29] Stone, Adam, et al. "Direct laser-writing of ferroelectric single-crystal waveguide architectures in glass for 3D integrated optics." Scientific reports 5 (2015).

[30] Staude, I., et al. "Waveguides in three-dimensional photonic-bandgap materials by direct laser writing and silicon double inversion." Optics letters 36.1 (2011): 67-69.

[31] Kadic, Muamer, et al. "On the practicability of pentamode mechanical metamaterials." Applied Physics Letters 100.19 (2012): 191901.

[32] Bückmann, Tiemo, et al. "Tailored 3D mechanical metamaterials made by dip-in direct-laser-writing optical lithography." Advanced Materials 24.20 (2012): 2710-2714.

[33] Bückmann, T., et al. "An elasto-mechanical unfeelability cloak made of pentamode metamaterials." Nature communications 5 (2014): 4130.

[34] Danilevicius, Paulius, et al. "Micro-structured polymer scaffolds fabricated by direct laser writing for tissue engineering." Journal of biomedical optics 17.8 (2012): 0814051-0814057.

[35] Melissinaki, Vasileia, et al. "Direct laser writing of 3D scaffolds for neural tissue engineering applications." Biofabrication 3.4 (2011): 045005.

[36] Klein, Franziska, et al. "Two-component polymer scaffolds for controlled three-dimensional cell culture." Advanced materials23.11 (2011): 1341-1345.

[37] Greiner, Alexandra M., Benjamin Richter, and Martin Bastmeyer. "Micro-engineered 3D scaffolds for cell culture studies." Macromolecular bioscience 12.10 (2012): 1301-1314.

[38] Malinauskas, Mangirdas, et al. "3D microporous scaffolds manufactured via combination of fused filament fabrication and direct laser writing ablation." Micromachines 5.4 (2014): 839-858.

[39] Selimis, Alexandros, Vladimir Mironov, and Maria Farsari. "Direct laser writing: Principles and materials for scaffold 3D printing." Microelectronic Engineering 132 (2015): 83-89.

[40] Ho, Chee Meng Benjamin, et al. "3D printed microfluidics for biological applications." Lab on a Chip 15.18 (2015): 3627-3637.

[41] Kim, Sangwon, et al. "Fabrication and characterization of magnetic microrobots for three-dimensional cell culture and targeted transportation." Advanced Materials 25.41 (2013): 5863-5868.

[42] Vaezi, Mohammad, Hermann Seitz, and Shoufeng Yang. "A review on 3D micro-additive manufacturing technologies." The International Journal of Advanced Manufacturing Technology67.5-8 (2013): 1721-1754.

[43] Waheed, Sidra, et al. "3D printed microfluidic devices: enablers and barriers." Lab on a Chip 16.11 (2016): 1993-2013.

[44] Mayer, Frederik, et al. "3D Fluorescence-Based Security Features by 3D Laser Lithography." Advanced Materials Technologies 2.11 (2017).

[45] Seet, Kock Khuen, et al. "Three-Dimensional Spiral-Architecture Photonic Crystals Obtained By Direct Laser Writing." Advanced Materials 17.5 (2005): 541-545.

[46] Chen, Hui, et al. "Direct laser writing of microtunnels and reservoirs on nanocomposite materials." Advanced Materials18.21 (2006): 2876-2879.

[47] Au, Thi Huong, et al. "Direct Laser Writing of Magneto-Photonic Sub-Microstructures for Prospective Applications in Biomedical Engineering." Nanomaterials 7.5 (2017): 105.

[48] Ivanova, Olga, Christopher Williams, and Thomas Campbell. "Additive manufacturing (AM) and nanotechnology: promises and challenges." Rapid Prototyping Journal 19.5 (2013): 353-364.

[49] Alessandri, Ivano, and Laura E. Depero. "Laser-induced modification of polymeric beads coated with gold nanoparticles." Nanotechnology 19.30 (2008): 305301.

[50] Zheren, Du, et al. "3D micro-concrete hybrid structures fabricated by femtosecond laser two-photon polymerization for biomedical and photonic applications." Industrial Technology (ICIT), 2016 IEEE International Conference on. IEEE, 2016.

[51] Radke, André, et al. "Three-dimensional bichiral plasmonic crystals fabricated by direct laser writing and electroless silver plating." Advanced Materials 23.27 (2011): 3018-3021.

[52] Juodkazis, Saulius, et al. "Two-photon lithography of nanorods in SU-8 photoresist." Nanotechnology 16.6 (2005): 846.

[53] Zeng, Hao, et al. "High-resolution 3D direct laser writing for liquid-crystalline elastomer microstructures." Advanced materials26.15 (2014): 2319-2322.

[54] Flatae, Assegid Mengistu, et al. "Optically controlled elastic microcavities." Light: Science & Applications 4.4 (2015): e282.

[55] Wei, Renbo, et al. "Nematic liquid crystalline elastomer grating and microwire fabricated by micro-molding in capillaries." Macromolecular rapid communications 34.4 (2013): 330-334.

[56] G. Gu et al., “Transparent organic light emitting devices,” Appl. Phys. Lett. 68, 2606–2608 (1996).

[57] Yoon T. et al., “Liquid Crystal Light Shutters for Simultaneous Control of Haze and Transmittance”, Proc. SPIE 9769, Emerging Liquid Crystal Technologies XI, 97690W (March 7, 2016);

[58] Bueno J.M., Polarimetry using liquid-crystal variable retarders: theory and calibration, Opt. A: Pure Appl. Opt. 2 (2000) 216–222

[59] Finkelmann H. et al, Tunable Mirrorless Lasing in Cholesteric Liquid Crystalline Elastomers Adv. Mater. 2001, 13, No. 14, July 18

[60] Deubel, M et al, Direct laser writing of three-dimensional photonic-crystal templates for telecommunications. Nature materials, 3(7), 444-447 (2004)..

[61] LM Blinov et al., Mirrorless lasing from nematic liquid crystals in the plane waveguide geometry without refractive index or gain modulation, Applied physics letters 89 (3), 031114

[62] Coles, H. J. & Morris, S. M. Liquid-crystal lasers. Nature Photon. 4, 676–685 (2010).

[63] Muth, Joseph T., et al. "Embedded 3D printing of strain sensors within highly stretchable elastomers." Advanced Materials 26.36 (2014): 6307-6312.

[64] Ruiz, Ulises, et al. "Liquid crystal microlens arrays recorded by polarization holography." Applied optics 54.11 (2015): 3303-3307.

[65] Jiang, Hongrui, Chensha Li, and Xuezhen Huang. "Actuators based on liquid crystalline elastomer materials." Nanoscale 5.12 (2013): 5225-5240.

[66] Ohm, Christian, Martin Brehmer, and Rudolf Zentel. "Liquid crystalline elastomers as actuators and sensors." Advanced Materials 22.31 (2010): 3366-3387.

[67] Yu, Yanlei, and Tomiki Ikeda. "Soft actuators based on liquid-crystalline elastomers." Angewandte Chemie International Edition 45.33 (2006): 5416-5418.

[68] H. Yang, A. Buguin, et al. "Micron-sized main-chain liquid crystalline elastomer actuators with ultralarge amplitude contractions", J. Am. Chem. Soc. 131 (2009) 15000–15004.

[69] J. Naciri, A. Srinivasan, H. Jeon, N. Nikolov, P. Keller, B.R. Ratna, "Nematic elastomer fiber actuator", Macromolecules 36 (2003) 8499–8505.

[70] Cipparrone, Gabriella, et al. "Chiral Self-Assembled Solid Microspheres: A Novel Multifunctional Microphotonic Device." Advanced Materials 23.48 (2011): 5773-5778.

[71] Donato, M. G., et al. "Polarization-dependent optomechanics mediated by chiral microresonators." Nature communications 5 (2014): 3656.

[72] Hernández, R. J., et al. "Cholesteric solid spherical microparticles: chiral optomechanics and microphotonics." Liquid Crystals Reviews 4.1 (2016): 59-79.

[73] Cipparrone, Gabriella, et al. "Chiral Self-Assembled Solid Microspheres: A Novel Multifunctional Microphotonic Device." Advanced Materials 23.48 (2011): 5773-5778.

[74] Hernández, R. J., et al. "Cholesteric solid spherical microparticles: chiral optomechanics and microphotonics." Liquid Crystals Reviews 4.1 (2016): 59-79.

[75] Uchida, Yoshiaki, Yoichi Takanishi, and Jun Yamamoto. "Controlled fabrication and photonic structure of cholesteric liquid crystalline shells." Advanced Materials 25.23 (2013): 3234-3237.

[76] Humar, M., and I. Muševič. "3D microlasers from self-assembled cholesteric liquid-crystal microdroplets." Optics express 18.26 (2010): 26995-27003.

[77] Sungur, Emel, et al. "External stimulus driven variable-step grating in a nematic elastomer." Optics express 15.11 (2007): 6784-6789.

[78] Zeng et al, High-Resolution 3D Direct Laser Writing for Liquid-Crystalline Elastomer Microstructures, Adv. Mater. 2014, 26, 2319–2322

[79] Zeng et al, Alignment engineering in liquid crystalline elastomers: Free-form microstructures with multiple functionalities, Applied Physics Letters 106, 111902 (2015)

[80] Nocentini, S., et al. "Towards liquid crystalline elastomer optically tunable photonic microstructures." SPIE Nanoscience+ Engineering. International Society for Optics and Photonics, 2016.

[81] Zeng, Hao, et al. "Light-Fueled Microscopic Walkers." Advanced Materials 27.26 (2015): 3883-3887.

[82] Jain, Prashant K., et al. "Review of some interesting surface plasmon resonance-enhanced properties of noble metal nanoparticles and their applications to biosystems." Plasmonics2.3 (2007): 107-118.

[83] Moores, Audrey, and Frederic Goettmann. "The plasmon band in noble metal nanoparticles: an introduction to theory and applications." New Journal of Chemistry 30.8 (2006): 1121-1132.

[84] Kelly, K. Lance, et al. "The optical properties of metal nanoparticles: the influence of size, shape, and dielectric environment." (2003): 668-677.

[85] Zeng, Shuwen, et al. "A review on functionalized gold nanoparticles for biosensing applications." Plasmonics 6.3 (2011): 491.

[86] Ghosh, Partha, et al. "Gold nanoparticles in delivery applications." Advanced drug delivery reviews 60.11 (2008): 1307-1315.

[87] Amendola et al “Surface plasmon resonance in gold nanoparticles: a review” J. Phys. Condens. Matte., 29 (2017), p. 203002.

[88] Rai, Mahendra, Alka Yadav, and Aniket Gade. "Silver nanoparticles as a new generation of antimicrobials." Biotechnology advances 27.1 (2009): 76-83.

[89] Boisselier, Elodie, and Didier Astruc. "Gold nanoparticles in nanomedicine: preparations, imaging, diagnostics, therapies and toxicity." Chemical society reviews 38.6 (2009): 1759-1782.

[90] Ghosh, Partha, et al. "Gold nanoparticles in delivery applications." Advanced drug delivery reviews 60.11 (2008): 1307-1315.

[91] Paciotti, Giulio F., et al. "Colloidal gold: a novel nanoparticle vector for tumor directed drug delivery." Drug delivery 11.3 (2004): 169-183.

[92] Jain, S., D. G. Hirst, and J. M. O'sullivan. "Gold nanoparticles as novel agents for cancer therapy." The British journal of radiology85.1010 (2012): 101-113.

[93] Jain, Prashant K., et al. "Calculated absorption and scattering properties of gold nanoparticles of different size, shape, and composition: applications in biological imaging and biomedicine." J. Phys. Chem. B 110.14 (2006): 7238-7248.

[94] Murphy, Catherine J., et al. "Gold nanoparticles in biology: beyond toxicity to cellular imaging." Accounts of chemical research 41.12 (2008): 1721-1730.

[95] Maier S A 2007 Plasmonics: Fundamentals and Applications (Springer).

[96] Kreibig U and Vollmer M 1995 Optical Properties of Metal Clusters (Berlin: Springer).

[97] Haes A J, Haynes C L, McFarland A D, Schatz G C, Van Duyne R P and Zou S 2005 MRS Bull. 30 368–75

[98] Xia Y and Halas N J 2005 MRS Bull. 30 338–48

[99] Saha K, Agasti S S, Kim C, Li X and Rotello V M 2012 Chem. Rev. 112 2739–79

[100] Di Fabrizio E, Schlücker S, Wenger J, Regmi R, Rigneault H, Calafiore G, West M, Cabrini S, Fleischer M and Van Hulst N F 2012 J. Opt. 18 063003

[101] B. Kaehr, N. Ertaş, R. Nielson, R. Allen, R. T. Hill, M. Plenert, and J. B. Shear, Anal. Chem. 78, 3198 (2006).

[102] J. Li, B. Jia, G. Zhou, and M. Gu, Opt. Express 14, 10740 (2006).

[103] Y. L. Zhang, Q. D. Chen, H. Xia, and H. B. Sun, Nano Today 5, 435 (2010).

[104] E. B. Kley, Microelectronic Eng. 34, 261 (1997).

[105] F. Korte, J. Serbin, J. Koch, A. Egbert, C. Fallnich, A. Ostendorf, and B. N. Chichkov, Appl. Phys. A 77, 229 (2003).

[106] C. N. LaFratta, D. Lim, K. O'Malley, T. Baldacchini, and J. T. Fourkas, Chem. Mater. 18, 2038 (2006).

[107] L. Li, M. Hong, M. Schmidt, M. Zhong, A. Malshe, B. Huis in'tVeld, and V. Kovalenko, CIRP Ann.-Manuf. Tech. 60, 735 (2011).

[108] H. E. Williams, Z. Luo, and S. M. Kuebler, Opt. Express 20, 25030 (2012).

[109] Q. Z. Zhao, J. R. Qiu, X. W. Jiang, E. W. Dai, C. H. Zhou, and C. S. Zhu, Opt. Express 13, 2089 (2005).

[110] Tabrizi, S., Cao, Y., Lin, H. et al. Sci. China Phys. Mech. Astron. (2017) 60: 034201.

[111] J. K. Gansel, M. Thiel, M. S. Rill, M. Decker, K. Bade, V. Saile, G. von Freymann, S. Linden, and M. Wegener, Science 325, 1513 (2009).

[112] N. Liu, H. Guo, L. Fu, S. Kaiser, H. Schweizer, and H. Giessen, Nat. Mater. 7, 31 (2008).

[113] S. Maruo, and J. T. Fourkas, Laser Photon. Rev. 2, 100 (2008).

[114] Y. Y. Cao, N. Takeyasu, T. Tanaka, X. M. Duan, and S. Kawata, Small 5, 1144 (2009).

[115] T. Tanaka, A. Ishikawa, and S. Kawata, Appl. Phys. Lett. 88, 081107 (2006).

[116] J. Li, M. M. Hossain, B. Jia, D. Buso, and M. Gu, Opt. Express 18, 4491 (2010).

[117] Haes A J, Haynes C L, McFarland A D, Schatz G C, Van Duyne R P and Zou S 2005 MRS Bull. 30 368–75.

[118] Xia Y and Halas N J 2005 MRS Bull. 30 338–48.

[119] Park J, Kang H, Kim Y H, Lee S, Lee T G and Wi J 2016 Nanoscale 8 15514–20.

[120] Wi J, Tominaka S, Uosaki K and Nagao T 2012 Phys. Chem. Chem. Phys. 14 9131–6.

[121] Reichenbach P, Horneber A, Gollmer D A, Hille A, Mihaljevic J, Schäfer C, Kern D P, Meixner A J, Zhang D and Fleischer M 2014 Opt. Express 22 15484–501.

[122] Barbosa S, Agrawal A, Rodríguez-Lorenzo L, Pastoriza-Santos I, Alvarez-Puebla R A, Kornowski A, Weller H and Liz-Marzán L M 2010 Langmuir 26 14943–50.

[123] Soares L, Csáki A, Jatschka J, Fritzsche W, Flores O, Franco R and Pereira E 2014 Analyst 139 4964–73.

[124] Wu H, Kuo C and Huang M H 2010 Langmuir 26 12307–13.

[125] Luan J, Liu K, Tadepalli S, Jiang Q, Morrissey J J, Kharasch E D and Singamaneni S 2016 ACS Appl. Mater. Interfaces 8 23509–16.

[126] Chen, H., et al. "Direct Laser Writing of Microstructures on Gold Nanoparticle/PMMA Composites", NSTI-Nanotech 2007, Vol. 4, 2017.

[127] Nguyen, Dam Thuy Trang, et al. "Coupling of a single active nanoparticle to a polymer-based photonic structure." Journal of Science: Advanced Materials and Devices 1.1 (2016): 18-30.

[128] K. Kaneko, H. B. Sun, X. M. Duan, et al., “Two-photon photoreduction of metallic nanoparticle gratings in a polymer matrix,” Appl. Phys. Lett. 83(7), 1426–1428 (2003).

[129] Y. Y. Cao, N. Takeyasu, T. Tanaka, X. M. Duan, and S. Kawata, Small 5, 1144 (2009).

[130] W. E. Lu, Y. L. Zhang, M. L. Zheng, Y. P. Jia, J. Liu, X. Z. Dong, Z. S. Zhao, C. B. Li, Y. Xia, T. C. Ye, and X. M. Duan, Opt. Mater. Express 3, 1660 (2013).

[131] I. Izquierdo-Lorenzo, S. Jradi, and P. M. Adam, RSC Adv. 4, 4128 (2014).

[132] Y. Y. Cao, X. Z. Dong, N. Takeyasu, T. Tanaka, Z. S. Zhao, X. M. Duan, and S. Kawata, Appl. Phys. A 96, 453 (2009)

[133] Sakamoto, M.; Fujistuka, M.; and Majima, T. Light as a construction tool of metal nanoparticles: Synthesis and mechanism. J.Photoch. Photobio. C 2009. 10, 33–56.

[134] Kimling, J., et al. "Turkevich method for gold nanoparticle synthesis revisited." The Journal of Physical Chemistry B 110.32 (2006): 15700-15707.

[135] Tribuzi, Vinicius, et al. "Indirect doping of microstructures fabricated by two-photon polymerization with gold nanoparticles." Optics express 20.19 (2012): 21107-21113.

[136] J. G. Ng, D. E. G. Watson, J. Sigwarth, A. McCarthy, H. Suyal, D. P. Hand, and M. P. Y. Desmulliez, An Additive Method for Photopatterning of Metals on Flexible Substrates, in Proceedings of the 36th International MATADOR Conference (Springer, London, 2010), pp. 389-392.

[137] J. A. Huang, Y. L. Zhang, H. Ding, and H. B. Sun, Adv. Opt. Mater. 3, 618 (2015).

[138] B. B. Xu, H. Xia, L. G. Niu, Y. L. Zhang, K. Sun, Q. D. Chen, Y. Xu, Z. Q. Lv, Z. H. Li, H. Misawa, and H. B. Sun, Small 6, 1762 (2010).

[139] B. B. Xu, Y. L. Zhang, H. Xia, W. F. Dong, H. Ding, and H. B. Sun, Lab Chip 13, 1677 (2013).

[140] C. H. Lin, L. Jiang, Y. H. Chai , H. Xiao, S. J. Chen, and H. L. Tsai, Opt. Express 17, 21581 (2009).

[141] S. J. Lee, B. D. Piorek, C. D. Meinhart, and M. Moskovits, Nano Lett. 10, 1329 (2010)

[142] S. Y. Kang, K. Vora, and E. Mazur, Nanotechnology 26, 121001 (2015)

[143] K. Vora, S. Y. Kang, S. Shukla, and E. Mazur, Appl. Phys. Lett. 100, 063120 (2012).

[144] R. Ameloot, M. B. J. Roeffaers, G. De Cremer, F. Vermoortele, J. Hofkens, B. F. Sels, and D. E. De Vos, Adv. Mater. 23, 1788 (2011).

[145] A. Ishikawa, JLMN 7, 11 (2012).

[146] Palpant, B.; Photothermal properties of gold nanoparticles. In Gold nanoparticles for physics, biology and chemistry, 2nd ed.; Louis, C., Pluchery, O., Imperial College, UK, 2012; Volume 3, pp. 75–102.

[147] Richardson, H. H.; Carlson, M. T.; Tandler, P. J.; Hernandez, P.; & Govorov, A. O. Experimental and theoretical studies of light-to-heat conversion and collective heating effects in metal nanoparticle solutions. Nano letters, 2009, 9(3), 1139-1146.

[148] Xiaohua, H.; and M. A. El-Sayed. Plasmonic photo-thermal therapy (PPTT). Alexandria Journal of Medicine 2011. vol. 47, no.1, 1-9.

[149] Abadeer, Nardine S., and C. J. Murphy. C. J. Recent Progress in Cancer Thermal Therapy Using Gold Nanoparticles. The Journal of Physical Chemistry C 2016. 120.9, 4691-4716.

[150] Liu, G. L.; Kim, J.; Lu, Y. U.; & Lee, L. P. Optofluidic control using photothermal nanoparticles. Nature materials, 2006. 5(1), 27-32.

[151] Tohmyoh, H., Imaizumi, T., Hayashi, H., & Saka, M. Welding of Pt nanowires by Joule heating. Scripta Materialia, 2007. 57(10), 953-956.

[152] Challener, W. A., Peng, C., Itagi, A. V., Karns, D., Peng, W., Peng, Y., ... & Ju, G. Heat-assisted magnetic recording by a near-field transducer with efficient optical energy transfer. Nature photonics, 2009. 3(4), 220-224.

[153] Jain, P. K.; Lee, K. S.; El-Sayed, I. H.; & El-Sayed, M. A. Calculated absorption and scattering properties of gold nanoparticles of different size, shape, and composition: applications in biological imaging and biomedicine. The Journal of Physical Chemistry B, 2006. 110(14), 7238-7248.

[154] Pissuwan, D.; Valenzuela, S. M.; & Cortie, M. B. Therapeutic possibilities of plasmonically heated gold nanoparticles. TRENDS in Biotechnology, 2006 24(2), 62-67.

[155] G Baffou, R Quidant, and C Girard. Heat generation in plasmonic nanostructures: Influence of morphology. Applied Physics Letters, 94(15):153109, 2009.

[156] Kim, Pilnam, et al. "Soft lithography for microfluidics: a review." (2008).

[157] Beebe, David J., Glennys A. Mensing, and Glenn M. Walker. "Physics and applications of microfluidics in biology." Annual review of biomedical engineering 4.1 (2002): 261-286.

[158] Whitesides, George M. "The origins and the future of microfluidics." Nature 442.7101 (2006): 368-373.

[159] Anderson, Janelle R., et al. "Fabrication of topologically complex three-dimensional microfluidic systems in PDMS by rapid prototyping." Analytical chemistry 72.14 (2000): 3158-3164.

[160] Psaltis, Demetri, Stephen R. Quake, and Changhuei Yang. "Developing optofluidic technology through the fusion of microfluidics and optics." Nature 442.7101 (2006): 381-386.

[161] Testa, Genni, et al. "A hybrid silicon-PDMS optofluidic platform for sensing applications." Biomedical optics express 5.2 (2014): 417-426.

[162] Leclerc, Eric, Yasuyuki Sakai, and Teruo Fujii. "Microfluidic PDMS (polydimethylsiloxane) bioreactor for large-scale culture of hepatocytes." Biotechnology progress 20.3 (2004): 750-755.

[163] Hanna, J. "Towards a new horizon of optoelectronic devices with liquid crystals." OPTOELECTRONICS REVIEW 13.4 (2005): 259.

[164] Xia, Younan, and George M. Whitesides. "Soft lithography." Annual review of materials science 28.1 (1998): 153-184.

[165] Bratton, Daniel, et al. "Recent progress in high resolution lithography." Polymers for Advanced Technologies 17.2 (2006): 94-103.

[166] Mack, Chris. Fundamental principles of optical lithography: the science of microfabrication. John Wiley & Sons, 2008.

[167] Göppert-Mayer, Maria. "Elementary processes with two quantum transitions." Annalen der Physik 18.7-8 (2009): 466-479.

[168] Kaiser, W., and C. G. B. Garrett. "Two-photon excitation in Ca F 2: Eu 2+." Physical review letters 7.6 (1961): 229.

[169] Reichelt, Rudolf. "Scanning electron microscopy." Science of microscopy. Springer, New York, NY, 2007. 133-272.

[170] Eaton, Peter, and Paul West. Atomic force microscopy. Oxford University Press, 2010.

[171] Prost, Jacques. The physics of liquid crystals. Vol. 83. Oxford university press, 1995.

[172] Sutkowski, Marek, and Malgorzata Kujawinska. "Application of liquid crystal (LC) devices for optoelectronic reconstruction of digitally stored holograms." Optics and Lasers in Engineering 33.3 (2000): 191-201.

[173] Monat, C., P. Domachuk, and B. J. Eggleton. "Integrated optofluidics: A new river of light." Nature photonics 1.2 (2007): 106-114.

[174] Berreman, Dwight W. "Optics in smoothly varying anisotropic planar structures: application to liquid-crystal twist cells." JOSA 63.11 (1973): 1374-1380.

[175] Doane, J. W., et al. "Polymer dispersed liquid crystals for display application." Molecular Crystals and Liquid Crystals 165.1 (1988): 511-532.

[176] Chigrinov, Vladimir G. Liquid crystal devices: physics and applications. 1999.

[177] Sengupta A. (2013) Liquid Crystal Theory. In: Topological Microfluidics. Springer Theses (Recognizing Outstanding Ph.D. Research). Springer, Cham.

[178] Landau, L. D. In "Collected papers", edited by Haar, D. T., p. 193, Gordon and Breach, New York, 1965

[179] Maurice Kleman. Oleg D. Lavrentovich. "Soft Matter Physics: An Introduction", Springer, 2003.

[180] Wang, Xiaoxiao. "Phases of Liquid Crystals and Their Transitions."

[181] Dierking, Ingo, and Shakhawan Al-Zangana. "Lyotropic Liquid Crystal Phases from Anisotropic Nanomaterials." Nanomaterials7.10 (2017): 305.

[182] Iam-Choon Khoo. Liquid crystals: physical properties and nonlinear optical phenomena, volume 64. John Wiley & Sons, 2007.

[183] Lev M Blinov. Structure and properties of liquid crystals, volume 123. Springer Science & Business Media, 2010.

[184] Yang, D-Ke. & Wu, S-Tson. Fundamentals of Liquid Crystal Devices, Wiley-SID, Chichester, 2006.

[185] I. Nishiyama, A. Yokoyama, M. Fukumasa, A. Yoshizawa and T. Hirai. Jap. J. Appl. Phys., 10, 1851 (1989)

[186] R. S. Zola, Y. C. Yang and D.-Ke. Yang, J. of the SID, 19/5, 410 (2011).

[187] Dreher, R., G. Meier, and A. Saupe. "Selective reflection by cholesteric liquid crystals." Molecular crystals and liquid crystals13.1 (1971): 17-26.

[188] Mulder, D. J., A. P. H. J. Schenning, and C. W. M. Bastiaansen. "Chiral-nematic liquid crystals as one dimensional photonic materials in optical sensors." Journal of Materials Chemistry C2.33 (2014): 6695-6705.

[189] M. Sakamoto, M. Fujistuka, and T. Majima, ”Light as a construction tool of metal nanoparticles: Synthesis and mechanism,” J. Photoch. Photobio. C 10, 33–56 (2009).

[190] Harada, Masafumi, and Hisahiro Einaga. "In situ XAFS studies of Au particle formation by photoreduction in polymer solutions." Langmuir 23.12 (2007): 6536-6543.

[191] Maruo, Shoji, and Tatsuya Saeki. "Femtosecond laser direct writing of metallic microstructures by photoreduction of silver nitrate in a polymer matrix." Optics express 16.2 (2008): 1174-1179.

[192] Shukla, Shobha, et al. "Subwavelength direct laser patterning of conductive gold nanostructures by simultaneous photopolymerization and photoreduction." Acs Nano 5.3 (2011): 1947-1957.

[193] Wildman, Ricky, et al. Combining Two-Photon Polymerisation and Photoreduction to Enable the Manufacture of Metamaterials at the Nanosale. University of Nottingham Nottingham NG72RD United Kingdom United States, 2016.

[194] Fick, Adolph. "V. On liquid diffusion." Philosophical Magazine Series 4 10.63 (1855): 30-39.7

[195] Comyn, John. "Introduction to polymer permeability and the mathematics of diffusion." Polymer permeability. Springer, Dordrecht, 1985. 1-10.

[196] Yarin L.P. (2012) Drag Force Acting on a Body Moving in Viscous Fluid. In: The Pi-Theorem. Experimental Fluid Mechanics, vol 1. Springer, Berlin, Heidelberg.

[197] Jones, A. M., and James George Knudsen. "Drag coefficients at low Reynolds numbers for flow past immersed bodies." AIChE Journal 7.1 (1961): 20-25.

[198] Jenkins, Francis A., and Harvey E. White. Fundamentals of optics. Tata McGraw-Hill Education, 1937.

[199] Kamada, Kosuke, et al. "Surfactant-induced friction reduction for hydrogels in the boundary lubrication regime." Journal of Physics: Condensed Matter 23.28 (2011): 284107.

[200] Sun, Hongtao, et al. "Effective temperature sensing by irreversible morphology evolution of ultrathin gold island films." The Journal of Physical Chemistry C 117.7 (2013): 3366-3373.

[201] Ramaiah, M. "Chemistry and Applications of Leuco Dyes." (1997): 159.

[202] Martynov, Georgij A., and Robert R. Salem. Electrical double layer at a metal-dilute electrolyte solution interface. Vol. 33. Springer Science & Business Media, 2012.

[203] Gotti, Guillaume, et al. "Electrodeposited gold nanoparticles on glassy carbon: Correlation between nanoparticles characteristics and oxygen reduction kinetics in neutral media." Electrochimica Acta 128 (2014): 412-419.

[204] Sevenler, Derin, Neşe Lortlar Ünlü, and M. Selim Ünlü. "Nanoparticle biosensing with interferometric reflectance imaging." Nanobiosensors and Nanobioanalyses. Springer Japan, 2015. 81-95.

[205] Mayer K M and Hafner J H 2011 Chem. Rev. 111 3828–57

[206] Bohren C F and Huffman D R 1983 Absorption and Scattering of Light by Small Particles (New York: Wiley-Interscience)

[207] Jain, Prashant K., et al. "Calculated absorption and scattering properties of gold nanoparticles of different size, shape, and composition: applications in biological imaging and biomedicine." J. Phys. Chem. B 110.14 (2006): 7238-7248.

[208] K. Kneipp, M. Moskovits, and H. Kneipp, Surface- Enhanced Raman Scattering: Physics and Applications (Springer, 2006)

[209] Schatz G C, Young M A and Van Duyne R P, Electromagnetic Mechanism of SERS, Top. Appl. Phys. 103, 2006.

[210] Etchegoin P G and Le Ru E C, Surface Enhanced Raman Spectroscopy: Analytical, Biophysical and Life Science Applications (Weinheim: Wiley-VCH) pp. 1–37, 2011.

[211] Pettinger B, Picardi G, Schuster R and Ertl G., Surface-enhanced and STM-tip-enhanced Raman spectroscopy at metal surfaces, Single Mol. 5 285–294, 2002.

[212] Steidtner J and Pettinger B, Tip-Enhanced Raman Spectroscopy and Microscopy on Single Dye Molecules with 15 nm Resolution, Phys. Rev. Lett. 100, 236101–236104, 2008.

[213] Prodan E, Radloff C, Halas N J and Nordlander, A hybridization model for the plasmon response of complex nanostructures, P Science 302, 419–422, 2003.

[214] Etchegoin P, Cohen L F, Hartigan H et. al., Electromagnetic contribution to surface enhanced Raman scattering revisited, 2003 J. Chem. Phys. 119, 5281–5289

[215] Nafy L A, Recent advances in linear and nonlinear Raman spectroscopy. Part VI, J. Raman Spectrosc. 43 1845, 2012.

[216] Le Ru E C and Etchegoin P G, Quantifying SERS enhancements, MRS Bull. 38 631, 2013.

[217] Kiefer, Wolfgang. Surface enhanced Raman spectroscopy: analytical, biophysical and life science applications. John Wiley & Sons, 2011.

[218] Kandyala R, Raghavendra S P C and Rajasekharan S T 2010 J Oral Maxillofac Pathol. 14 1–5

[219] Palpant, Bruno. "Photothermal properties of gold nanoparticles." Gold nanoparticles for physics, chemistry and biology (2012): 75-102.

[220] Baffou, Guillaume, Romain Quidant, and F. Javier García de Abajo. "Nanoscale control of optical heating in complex plasmonic systems." ACS nano 4.2 (2010): 709-716.

[221] James R Adleman, David A Boyd, David G Goodwin, and Demetri Psaltis. Heterogenous catalysis mediated by plasmon heating. Nano letters, 9(12):4417–4423, 2009.

[222] Suljo Linic, Phillip Christopher, Hongliang Xin, and Andiappan Marimuthu. Catalytic and photocatalytic transformations on metal nanoparticles with targeted geometric and plasmonic properties. Accounts of chemical research, 46(8):1890–1899, 2013.

[223] David Boyer, Philippe Tamarat, Abdelhamid Maali, Brahim Lounis, and Michel Orrit. Photothermal imaging of nanometer-sized metal particles among scatterers. Science, 297(5584):1160–1163, 2002.

[224] David Lasne, Gerhard A Blab, St´ephane Berciaud, Martin Heine, Laurent Groc, Daniel Choquet, Laurent Cognet, and Brahim Lounis. Single nanoparticle photothermal tracking (snapt) of 5-nm gold beads in live cells. Biophysical journal, 91(12):4598–4604, 2006.

[225] Alexander S Urban, Tom Pfeiffer, Michael Fedoruk, Andrey A Lutich, and Jochen Feldmann. Single-step injection of gold nanoparticles through phospholipid membranes. ACS nano, 5(5):3585–3590, 2011.

[226] Adam J Gormley, Nate Larson, Shraddha Sadekar, Ryan Robinson, Abhijit Ray, and Hamidreza Ghandehari. Guided delivery of polymer therapeutics using plasmonic photothermal therapy. Nano today, 7(3):158–167, 2012.

[227] Adam J Gormley, Khaled Greish, Abhijit Ray, Ryan Robinson, Joshua A Gustafson, and Hamidreza Ghandehari. Gold nanorod mediated plasmonic photothermal therapy: a tool to enhance macromolecular delivery. International journal of pharmaceutics, 415(1):315–318, 2011.

[228] Ryan Huschka, Jorge Zuloaga, Mark W Knight, Lisa V Brown, Peter Nordlander, and Naomi J Halas. Light-induced release of dna from gold nanoparticles: nanoshells and nanorods. Journal of the American Chemical Society, 133(31):12247–12255, 2011.

[229] Claire M Cobley, Leslie Au, Jingyi Chen, and Younan Xia. Targeting gold nanocages to cancer cells for photothermal destruction and drug delivery. Expert opinion on drug delivery, 7(5):577–587, 2010.

[230] Xiaohua Huang, Prashant K Jain, Ivan H El-Sayed, and Mostafa A El-Sayed. Plasmonic photothermal therapy (pptt) using gold nanoparticles. Lasers in medical science, 23(3):217– 228, 2008.

[231] Erin B Dickerson, Erik C Dreaden, Xiaohua Huang, Ivan H El-Sayed, Hunghao Chu, Sujatha Pushpanketh, John F McDonald, and Mostafa A El-Sayed. Gold nanorod assisted near-infrared plasmonic photothermal therapy (pptt) of squamous cell carcinoma in mice. Cancer letters, 269(1):57–66, 2008.

[232] S. Lal, S. E Clare, and N. J. Halas. Nanoshell-enabled photothermal cancer therapy: impending clinical impact. Accounts of chemical research, 41(12):1842–1851, 2008.

[233] Guillaume Baffou, Pascal Berto, Esteban Bermúdez Ureña, Romain Quidant, Serge Monneret, Julien Polleux, and Herv´e Rigneault. Photoinduced heating of nanoparticle arrays. Acs Nano, 7(8):6478–6488, 2013.

[234] Baffou, Guillaume, and Romain Quidant. "Thermo-plasmonics: using metallic nanostructures as nano-sources of heat." Laser & Photonics Reviews 7.2 (2013): 171-187.

[235] J Kimling, M Maier, B Okenve, V Kotaidis, H Ballot, and A Plech. Turkevich method for gold nanoparticle synthesis revisited. The Journal of Physical Chemistry B, 110(32):15700–15707, 2006.

[236] Edward Harrison. Darkness at night: A riddle of the universe. Harvard University Press, 1989.

[237] Pezzi, Luigia, et al. "Photo-thermal study of a layer of randomly distributed gold nanoparticles: from nano-localization to macro-scale effects." Journal of Physics D: Applied Physics 50.43 (2017): 435302.

[238] Schneider, C.A.; Rasband, W.S.; Eliceiri, K.W. NIH Image to ImageJ: 25 years of image analysis. Nat. Methods 2012, 9, 671–675

[239] Schneider, C.A.; Rasband, W.S.; Eliceiri, K.W. NIH Image to ImageJ: 25 years of image analysis. Nat. Methods 2012, 9, 671–675.

[240] Ramon-Gimenez, Laura, et al. "Reactive mesogen based polymer particles." U.S. Patent No. 9,598,587. 21 Mar. 2017.

[241] Festag, Grit, et al. "Single particle studies of the autocatalytic metal deposition onto surface-bound gold nanoparticles reveal a linear growth." Nanotechnology 18.1 (2006): 015502.

[242] R. Zanella, and C. Louis, “Influence of the conditions of thermal treatments and of storage on the size of the gold particles in Au/TiO2 samples,” Catal. Today 107(8), 768–777 (2005).

[243] M. I. A. Umar, C. C. Yap, R. Awang, A. A. Umar, M. M. Salleh, and M. Yahaya, “Formation of gold-coated multilayer graphene via thermal reduction,” Mater. Lett. 106, 200–203 (2013).

[244] Thanamongkollit, Narin, Kent R. Miller, and Mark D. Soucek. "Synthesis of UV-curable tung oil and UV-curable tung oil based alkyd." Progress in Organic Coatings 73.4 (2012): 425-434.

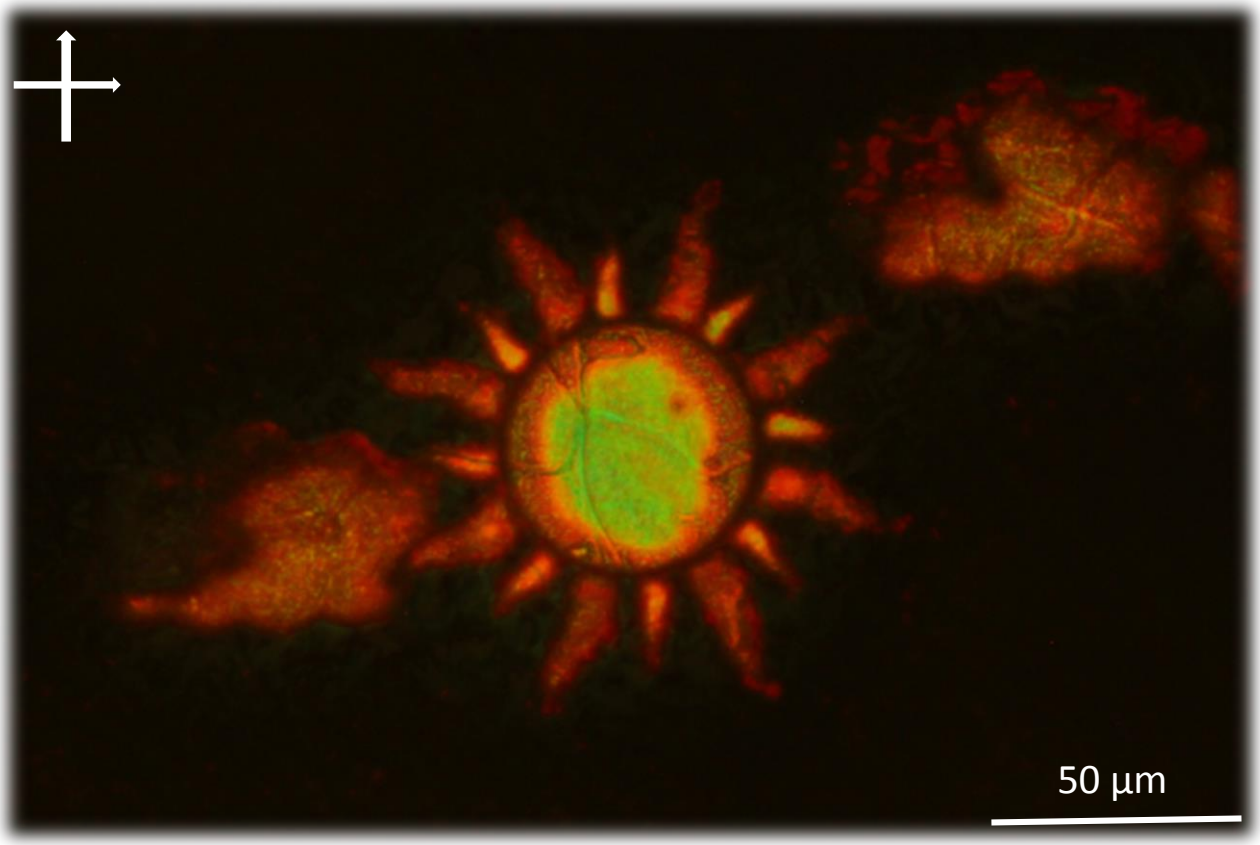

Remember that the sun will always rise even after the darkest of nights.
Even if it is a sun made through two-photon direct laser writing in chiral reactive mesogens,
observed between crossed polarized, with diameter of 50 µm, height 4 µm, with sunbeams of 5 µm.
Even if it presents a photonic band gap ranging from 520 nm to 590 nm.
Even if it is surrounded by clouds made in the same material.
The sun will rise.